A Perpendicular Biased 2nd Harmonic Cavity for the Fermilab Booster

Edited by C.Y. Tan

Contributors: J.E. Dey, K.L. Duel, M.R. Kufer, J.C. Kuharik, R.L. Madrak, A. Makarov, R. Padilla-Dieppa, W.A. Pellico, J.S. Reid, G. Romanov, R.G. Scala, B.A. Schupbach, M.H. Slabaugh, D. Sun, C.Y. Tan & I. Terechkine.

15 September 2020

A perpendicular biased 2nd harmonic cavity for the Fermilab Booster is currently being designed and built. The goal for the cavity design is to have 100 kV in the gap that works at both injection and at transition. This is the technical document that describes the measurements, simulations and decisions that were made for this cavity.

A Perpendicular Biased 2nd Harmonic Cavity for the Fermilab Booster

Edited by C.Y. Tan

Table of Contents

1 Introduction

It is well known for a long time that by flattening the bucket at injection, it is possible to increase the capture efficiency because of increased bucket area and a reduction in space charge density. See, for example, Ref. [1]. Although beam capture efficiency in Booster is already quite efficient, > 90% for 5.3×10^{12} protons, there is still an activation problem in Booster from beam loss. Therefore, even a gain in efficiency of a few percent can help mitigate this problem. This is the main motivation for the installation of 2nd harmonic cavities in the Booster.[1]

The addition of 2nd harmonic cavities also opens up the possibility of using it at transition to help the beam cross it and linearization of the accelerating voltage for bunch rotation at extraction.

At transition, the main mechanism for beam loss is bucket mismatch and not from space charge. See Ref. [2]. The 2nd harmonic cavity can be used to shape the bucket so that the beam is better matched to it before and after transition.

At extraction, the 2nd harmonic cavity can be used to linearize the voltage during bunch rotation so that there can be a reduction in the tails of the rotated distribution. [3]

The above three requirements for the cavity opens up technical challenges that have to be met:

1. The cavity that operates at $(2 \times 37.865) = 75.73$ MHz at injection, $(2 \times 52.25) = 104.5$ MHz at transition and $(2 \times 53.18) = 105.63$ MHz at extraction. This means that this cavity must be able to track the main frequency ramp that goes between these three frequencies in approximately 33 ms.
2. There must be sufficient volts on the cavity to effectively shape the bucket so that capture can be improved. ESME simulations show that for improved capture, the voltage on the 2nd harmonic cavity must be at least 100 kV, although optimally it should be 50% of the fundamental accelerating voltage. Capture efficiency improves slightly with higher voltage. See section 1.2.1.3
3. The voltage required for transition crossing depends on the method used. For example, if focus free transition crossing is selected, the optimum voltage ratio between the fundamental and the 2nd harmonic voltages is $\frac{815\text{ kV}}{224\text{ kV}} = 3.64$. This means that at least two cavities are required for this scheme to work optimally. See section 1.2.2.
4. For extraction, the required voltage ratio between the 2nd harmonic to the fundamental is 1/8 for canceling the cubic term. Presently (2016), the extraction voltage is 240 kV and thus only 30 kV is required for the 2nd harmonic cavity during bunch rotation.

[1] In this report, 2nd harmonic means twice the fundamental frequency.

These technical challenges imply that the cavity must be tunable and thus a ferrite loaded cavity must be used in the design. The high voltage requirement for one cavity means that high Q is necessary. In order to satisfy these requirements, a perpendicular biased cavity is proposed.

1.1 Historical perspective

Perpendicular biased cavities were proposed as a scheme for achieving higher Q and thus higher voltages compared to parallel biased cavities back in the 1980s. [4] And although this type of cavity has been designed and built for rapid cycling synchrotrons in the past, for example, for TRIUMF and the SSC [5], none of them became operational. The most successful cavity to date has been the TRIUMF cavity [6] that reached its design voltage of 65 kV. However, this cavity subsequently developed a problem and never did see beam.[2] This is not to say that perpendicular biased cavities are a pipe dream. In the subsequent years, perpendicular biased cavities have been successfully built, commissioned and made operational. However, these cavities typically have a small frequency sweep of < 1 MHz. For example, the Recycler 53 MHz cavities are perpendicularly biased and have a frequency sweep of 10 kHz [7].

Thus, if successful, the cavity that is being proposed for Booster will be the first perpendicular biased cavity that has a large frequency sweep range of about 30 MHz that will be installed into a rapid cycling synchrotron.

1.2 ESME simulations

We have used ESME [8] simulations to test out a series of voltage settings on the 2nd harmonic cavity to see its effect on capture efficiencies at injection. For these simulations, we will use PIP (Proton Improvement Plan) proton intensities, i.e. 5×10^{12} protons at injection. Note: PIP specifications require 4.2×10^{12} protons at extraction. We will assume that the total voltage available from the fundamental RF is 1 MV.

In the case of transition crossing, we have used the "focus free" method [9, 10] in the simulations as an example. This is just a particular choice that we have chosen because there are other methods to achieve matching of the beam to the bucket before and after transition.

[2] There is a vacuum leak from a crack in the ceramic window in the tuner [34], but the exact cause of the window failure has been lost in the mists of time. This cavity was shipped from TRIUMF to FNAL and it is stored at MI-60 now (2015).

1.2.1 Injection

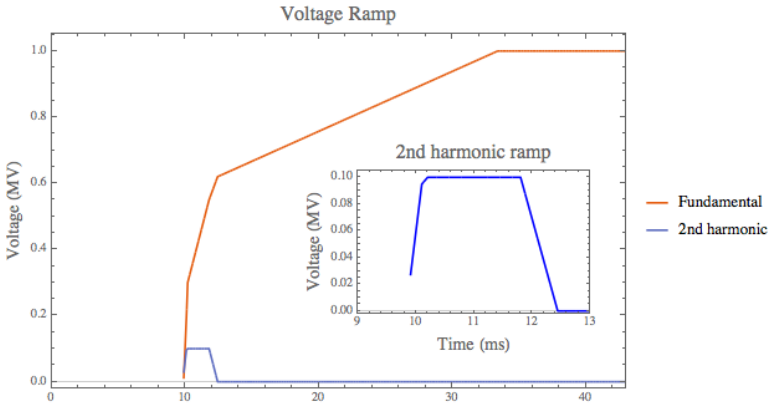

Figure 1: The voltage ramp on the fundamental and the 2nd harmonic used in the ESME simulations. In this example, the maximum 2nd harmonic voltage is 100 kV. The beam is injected at 0 ms and allowed to debunch. The RF voltage ramps start at 9.9 ms.

In our injection simulation, 200 MHz structured beam is injected into Booster from Linac at 0 ms. The RF is not ramped from zero volts until 9.9 ms later, this is to allow time for the beam to debunch. After 9.9 ms, the fundamental RF is ramped up to 1 MV using its nominal ramp profile, while the 2nd harmonic RF is ramped up and down in 2.54 ms. The ramp profiles of both RF systems used in the simulations are shown in Figure 1. The injected beam and flattened bucket when the 2nd harmonic voltage is at 100 kV are shown in Figure 2. Besides being flattened, the bucket area is also slightly increased with the 2nd harmonic turned on.

Table 1 summarizes the results when we change the voltage on the 2nd harmonic cavity. These simulations were done with 10500 macro particles and the number of macro particles that remained alive just before transition was counted. From this table, we can see that there is a point of diminishing returns in the capture efficiency after 100 kV. Of course, the efficiencies do not quite correspond to reality but these results give us a notion as to what value to set the voltage on the 2nd harmonic cavity. Using these results, we have specified that the voltage on the 2nd harmonic cavity should be 100 kV for an improvement of ~90% (1.8% loss to 0.2% loss).

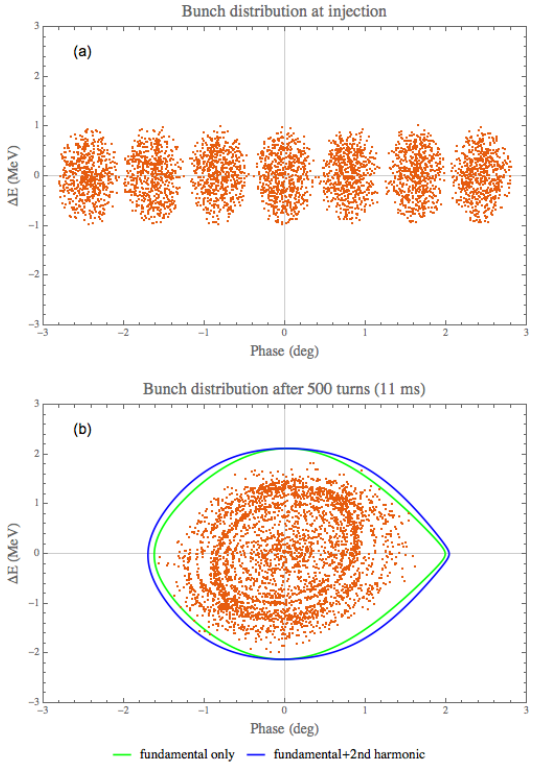

Figure 2: (a) The initial distribution of the injected beam that has 200 MHz structure. (b) The captured beam at 11 ms with 2nd harmonic at 100 kV.

2nd harmonic voltage (kV)	Number alive	% alive
0	10318	98.2
50	10417	99.2
100	10483	99.8
200	10488	99.9

Table 1: Summary of capture efficiency results.

1.2.2 Transition crossing

The natural problem in transition crossing is matching the beam to bucket right after transition. Any mismatch causes a quadrupole oscillation [11] of the beam that dilutes its longitudinal emittance. See Figure 3. There is a number of solutions to fix this mismatch besides just damping out the

oscillations, for example with a γt jump system [12] or with RF methods discussed in references [9, 10, 13]. But, in the end, all these methods require more volts from the cavities, whether this comes from the fundamental cavities alone or from a combination of fundamental and higher harmonics cavities. We discuss one particular method here, called "focus free" for crossing transition. This method, in principle, only works if the space charge induced instabilities is not a problem. And from ESME simulations for the beam charge of 4.2×10^{12} protons in PIP (and 6.4×10^{12} protons in PIP II), space charge has negligible effects.

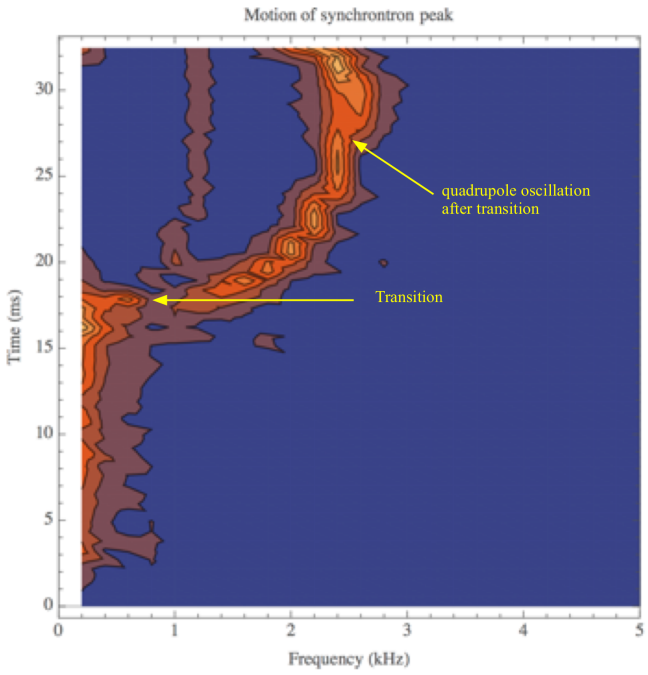

Figure 3: There is a quadrupole oscillation due to bucket mismatch after transition crossing in the Booster. Data was taken on 04 Nov 2015 for 4.5e12 protons.

For the focus free method to work, we must flatten the peak accelerating voltage so that the head and the tail of the bunch both see *the same accelerating voltage as the synchronous particle* – in effect the bunch looks like it is "drifting" through transition albeit being accelerated. A quick calculation shows that the ratio between the fundamental voltage and the 2nd harmonic voltage that creates a flatness variation of 0.6% is $\frac{816\text{ kV}}{224\text{ kV}} = 3.64$. This means that bunches which have a length of ± 49 degrees or less will see at most $\pm 0.30\%$ variation in voltage in this optimized case. See Figure 4. Since the required voltage on the 2nd harmonic is 224 kV, we would need at least 2 cavities in this method.

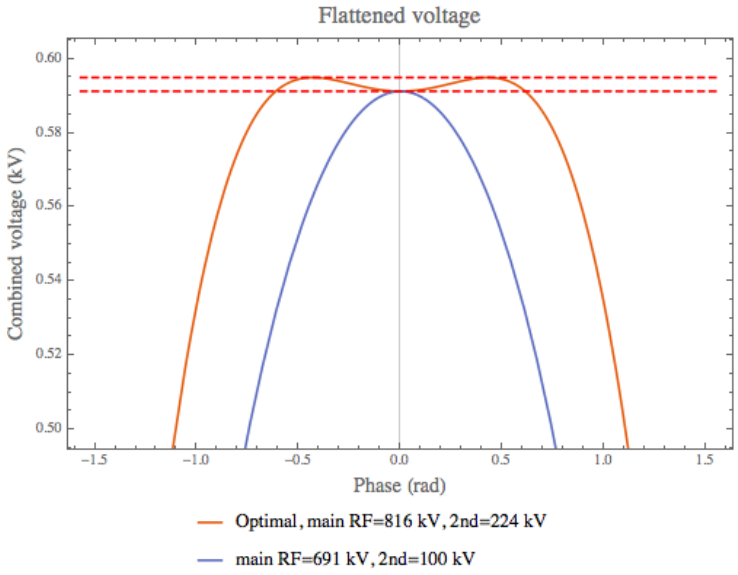

Figure 4: This graph shows the flattened voltages that can be used for going through transition. The dashed red lines on the graph indicate ±0.3% variation in the voltage variation on the optimized flat voltage curve (red). The blue curve is when the 2nd harmonic voltage is limited to 100 kV.

1.2.3 Bunch rotation at extraction

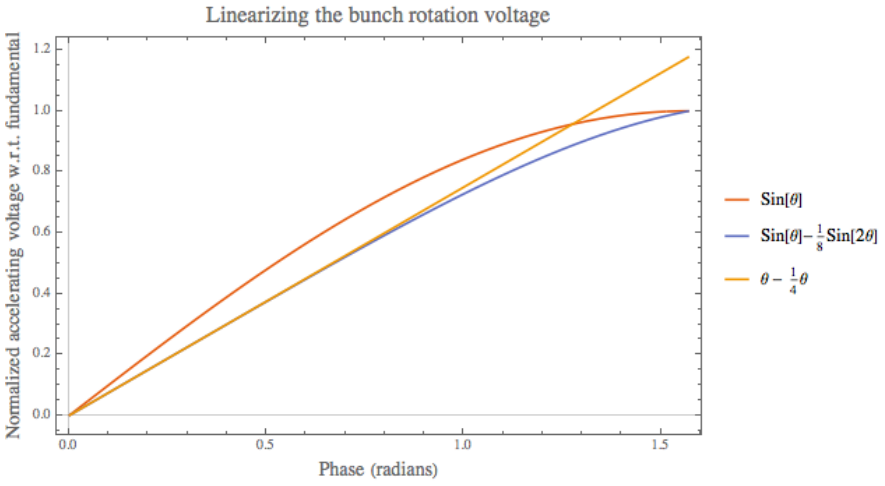

Figure 5: Linearizing the bunch rotation voltage.

Booster uses bunch rotation at extraction to reduce the bunch length of the beam before it is injected into the Recycler. It is trivial to show that the required 2nd harmonic voltage to cancel out the cubic term

of the fundamental sinusoid voltage is 1/8th its peak voltage. The normalized voltage w.r.t. the fundamental with and without the 2nd harmonic cavity compared to a pure linear voltage is shown in Figure 5. However, for operations, a higher voltage is required because of beam loading and the bunch distribution.

The results from the ESME simulations with and without the 2nd harmonic cavity are shown in Figure 6. The optimized voltages are 130 kV for the fundamental and 30 kV for the 2nd harmonic, and thus the voltage ratio is just below ¼. The improvement in rms energy spread is about 17% with this ratio.

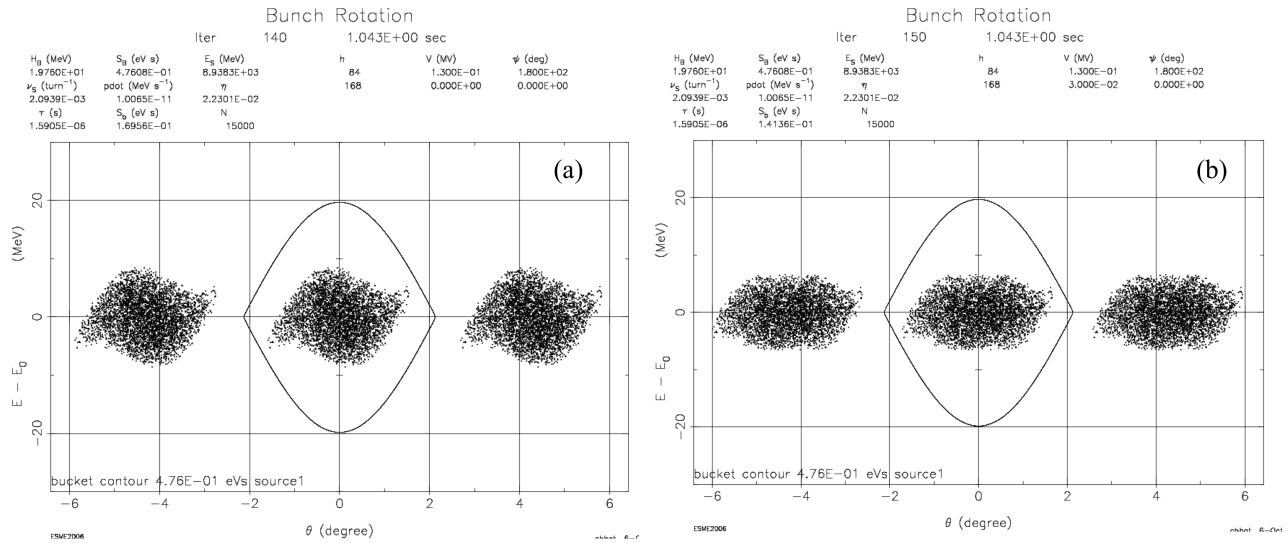

Figure 6: This is the 8 GeV bunch rotation simulated with ESME. (a) Only the fundamental cavity is used here. The rms energy spread after rotation is 3.44 MeV. (b) This time, the 2nd harmonic is turned on. The voltage ratio between the two cavities is 0.23. The rms energy spread after rotation is 2.85 MeV [14].

1.3 The voltage ramps

The proposed ramps are shown in Figure 7. The goals are:

1. Improve both injection and transition efficiencies. It is proposed that the cavity be "on" for 3 ms at injection and at transition.
2. Improve both injection and extraction efficiencies. It is proposed that the cavity be "on" for 3 ms at injection and 1 ms at extraction. It is expected that the required voltage for bunch rotation is < 50 kV.

The duty factor of the RF system is 10% or less which helps to reduce the power losses in the garnet. The injection frequency is at 75.73 MHz, the transition frequency is 104.5 MHz and the extraction frequency is 105.6 MHz. The heating and cooling of the garnet and the identification of the local hotpots are discussed in section 8.3.

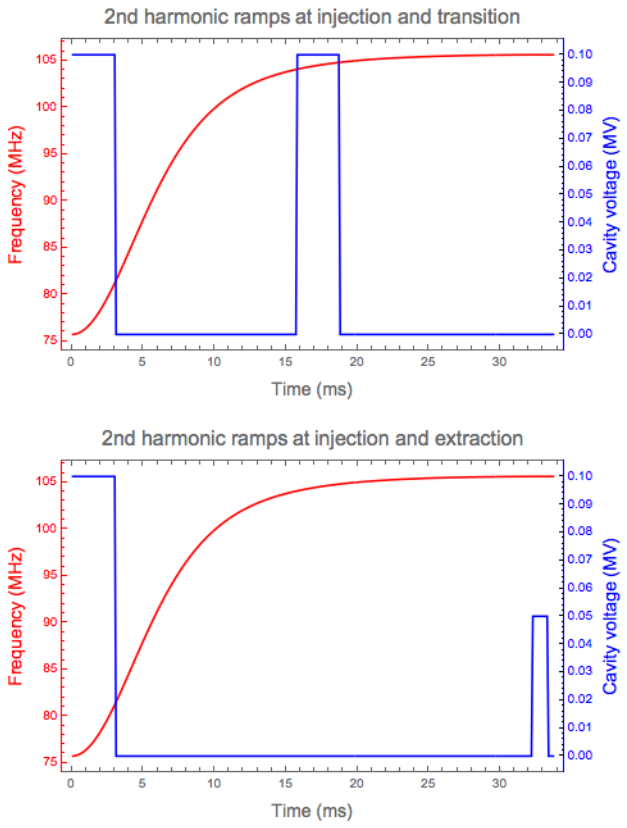

Figure 7: The proposed 2nd harmonic voltage ramp. The cavity is "on" during injection and transition or extraction and "off" otherwise.

2 The 2nd harmonic cavity

The NX9 model of the cavity is shown in Figure 8. We have used the experiences from both TRIUMF and SSC to improve the design. Our goals for the new design are:

1. Double both the operating and frequency swing ranges.
2. Improvement of the cooling of the garnet.
3. Removal of BeO cooling disks.

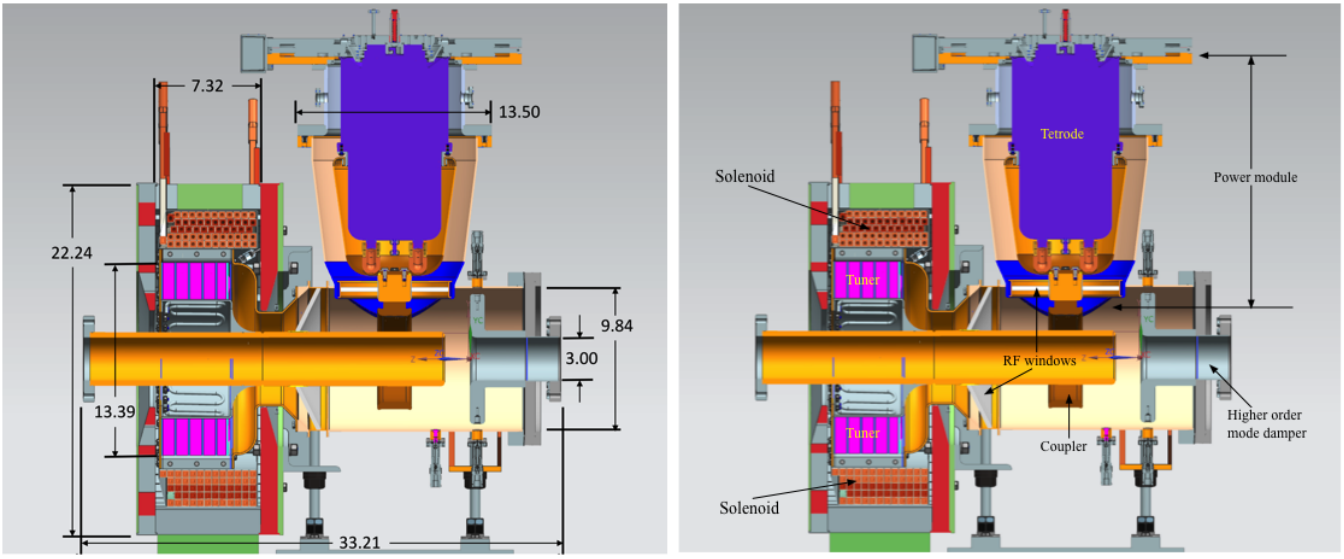

Figure 8: A cross sectional view of the 2nd harmonic cavity. All dimensions are in inches.

It turns out that cooling the local hotspots in the garnet is very important because these hotspots can cause a fracture in the garnet and destroy the cavity. See Ref [5, 15] where the authors state that some of the garnet literally melted at the hotspot. Learning from this lesson, we have used MWS (Microwave Studio) and COMSOL to help us locate where these hotspots are so that we can take care of them before any disaster strikes.

The use of BeO as the material for cooling disks is troublesome because there are significant safety requirements for handling them. Our design uses Al_2O_3 instead which, although, has a conduction coefficient 30 W/m K that is ten times worse than BeO (265 W/m K), MWS simulations show that when we use Al_2O_3 cooling disks, the garnet is better cooled than without.

Furthermore, the geometry of the cavity that holds the garnet has been shaped so that cooling channels can be embedded at both the inner and outer radii of the shell that holds the garnet. Thus, this new geometry also increases cooling of the garnet.

The garnet material that we have chosen for our cavity is AL800. It is necessary to use garnet rather than ferrite material, like NiZn ferrite, for perpendicular biasing because in this scheme, the cavity operates near saturation magnetization. As a comparison, AL800 saturates at 800 G (CGS units), while NiZn ferrite saturates at 3.2 kG. Thus, it is much easier to design a magnet that can saturate AL800 when compared to NiZn ferrite.

Another garnet material, AL400, is also a possible choice for the tuner. It has a lower saturation magnetization of 400 G compared to AL800. But its Curie temperature is 130°C which is too low because local hot spots can have temperatures that exceed 100°C. Contrast this to AL800 which has a Curie temperature of 200°C. Thus, AL800 is a good compromise between saturation magnetization and Curie temperature [16].

Parameter	Value	Units
Frequency range	75.7 – 105.6	MHz
R/Q	> 30	Ω
Higher order modes impedance	$\lesssim 2$	kΩ
Gap voltage	100	kV
Average garnet permeability (μ)	$1.3 < \mu < 3.5$	-
Anode impedance	1200 – 5000	Ω
Tube efficiency in class B operations	> 60	%
Repetition rate	15	Hz
Duty factor (66 ms cycle)	~10	%
Diameter of beam pipe	3	inches

Table 2: The specifications of the 2nd harmonic cavity

The loss tangent, $\tan \delta_m$, of AL800 is a critical parameter for calculating heating in the garnet. Unfortunately, all the published literature that we have found does not give an accurate parameterization of it. We have spent a lot of effort in measuring $\tan \delta_m$ to get it right. Our measurements are described in section 3. We have also measured the loss tangent of the glue that binds the AL800 sectors together and to the alumina cooling ring in section 4.

The garnet is biased with a solenoid so that its average permeability over the entire tuner volume can span the range from 1.3 to 3.5. The solenoid design will be discussed in section 9. Since the B-field will be ramped at 15 Hz, eddy currents induced on the surfaces of the metal shell of the cavity is a major concern. Eddy current mitigation will be discussed in section 8.6.

The specifications of the cavity are summarized in Table 2.

2.1 RF power

In order to save costs on the required infrastructure to power this cavity, we have decided to use the same tetrode tube, the Y567B[3] that is used to power the Booster RF cavities, to power our cavity. The only caveat is that although the Y567B is specified to work to 108 MHz, it has never been used at Fermilab at the required frequency range for the 2nd harmonic. In order to verify that the Y567B is capable of working in this frequency range, a test stand has been built to check its operating characteristics. The results from these tests will be discussed in section 14.

2.2 RF windows

In order to separate the vacuum from air, RF windows are required. There are two AL_2O_3 windows in this design. One window in the power module separates the tetrode cavity from the vacuum and another window separates the garnet section from the vacuum. The final location of the second window is a compromise between minimizing the following effects:

1. Multipacting
2. E-field on the surface of the window
3. Heating of the window

and ease of assembly of the cavity.

A consideration in the design of the RF window is how it impacts the length of the RF power module. Since the RF power module is strongly coupled to the accelerating cavity, the RF window has to be designed to not impact the input impedance seen by the Y567B. Small changes in the length of the RF module have a significant impact on the input impedance, and some care has to be exercised in its design.

The design of the windows will be discussed in section 12.

---

[3] Although the tube is generically called the Y567B, the actual tube used in the Booster cavities is a mechanically modified version of the Eimac 4CW150000.

2.3 Cavity design

The optimization of the cavity is an iterative process: the dimensions of the garnet and the non-garnet parts are optimized so that the cavity resonance spans the required frequency range for $\mu = 1.3$ to 3.5. The value of the coupling capacitor, which affects the resonant frequency range, is chosen so that both the step up ratio is reasonable for the range of μ's, and the Y567B sees the required anode impedance for it to operate. The iterative optimization of the dimensions, value of the coupling capacitor, and anode impedance continues until the specifications of the cavity summarized in Table 2 are satisfied. The results of the MWS simulations and the transmission line model of the cavity that are used in the cavity optimization will be discussed in section 6. The anode impedance and step up ratio that will allow the Y567B to drive the cavity will be discussed in section 7.2.

2.3.1 Tuner assembly

The tuner consists of a sandwich of 5 rings of garnet and alumina cooling rings. The garnet ring that is farthest from the shorted end of the cavity is thinner than the rest of the garnet rings and has a garnet shim glued on top of it. With the shim, the bias magnetic field is more uniform than without. Thus, the shim lowers the RF power losses, which in turn lowers the temperature on this garnet face during operations. As was discussed earlier, cooling of the tuner assembly is critical for preventing runaway heating. The design of the tuner assembly will be discussed in sections 8 and 17.11.

2.3.2 Power module

Since the power module and the cavity are strongly coupled, there are two normal modes in the system. Computer simulations have found that for the RF cavity to work properly, these two normal modes must be separated by at least 30 MHz so that the excitation of the cavity does not cause the power module to oscillate as well. This is because power will be wasted exciting the power module. This is an important criterion in the design of the power module. Its design will be discussed in sections 6.1.2 and 6.2.1.

2.3.3 HOM damper

The HOM (higher order mode) damper is a Smythe style damper [17]. This type of HOM damper is required because it needs to be broad band because of the large frequency swing of the fundamental, which means that the HOM modes will as well. The HOM damper is discussed in section 7.

2.3.4 Mechanical design and solenoid construction

The mechanical design is critical for realizing the virtual model that we found from simulations. During the assembly of the cavity, we had to make modifications to the original mechanical design because of tolerances that were not met during manufacture or errors on our part. The choices that were made for the fixes will be discussed in section 17. Also discussed was the assembly process, which

was challenging to say the least. At every step, the cavity seemed to want to thwart our best efforts. It was only through the concerted effort of the skilled technicians and the knowledgeable mechanical engineers that overcame those problems.

The solenoid is technically challenging to build because of its small size and high field. And because of the rapid cycling nature of the Booster, its yoke has to be laminated. Building a laminated solenoid is a very labor intensive process. The construction of the solenoid will be discussed in section 19.

2.4 Other details

There are a lot of details that have to be worked out to ensure the success of operating this cavity. Low power and high power tests will be discussed in sections 19 and 22. The HLRF system that is necessary for operations will be discussed in section 23. Photographs of the installation of the cavity at L11 will be shown in section 24. And after the successful install, how the cavity is operated and its effect on the beam will be discussed in section 25.

Finally, the success of this project is only possible with the effort from the tireless and dedicated people both inside and outside Fermilab. We gratefully acknowledge their contributions in section 26 and show photos of some of the participants in this endeavor in section 26.1.

3 Measuring the static permeability and loss tangent of AL800 (I. Tereckhine, R. Madrak & G. Romanov)

The ability to accurately model the cavity is key to the success of the design. In particular, it is necessary to know the permeability as a function of the bias magnetic field. The tuning range and losses are determined by the real and imaginary parts μ' and μ'' respectively. The bias magnetic field in the tuner is never perfectly uniform, and in order to properly model the device, these properties must be known at every point in the tuner for all bias settings. In the following sections, we describe our measurements of the static permeability and the loss tangent using the available set of AL800 garnet rings, obtained from National Magnetics/TCI Ceramics. More details can be found in Ref. [18].

3.1 Static permeability

The static magnetization curve was extracted by iteratively adjusting the magnetization curve used in the simulation of the setup, until the simulation results matched measurements. The initial $\mu(B)$ curve was a guess based on the vendor's data for the initial permeability (~50) and a theoretical value for large bias magnetic field.

A sketch of the setup is shown in Figure 9. Ten stacked rings, each having the following dimensions: 3.0″ OD, 0.65″ ID, and 0.5″ thick, are placed inside the solenoid that has a flux return on the bottom and sides made from CMD-10 and G4 ferrite. The solenoid's length, ID and OD are 7″, 4″, and 12″, respectively. The number of turns is 112. A steel plug is inserted on top to improve the uniformity of the bias magnetic field within the samples.

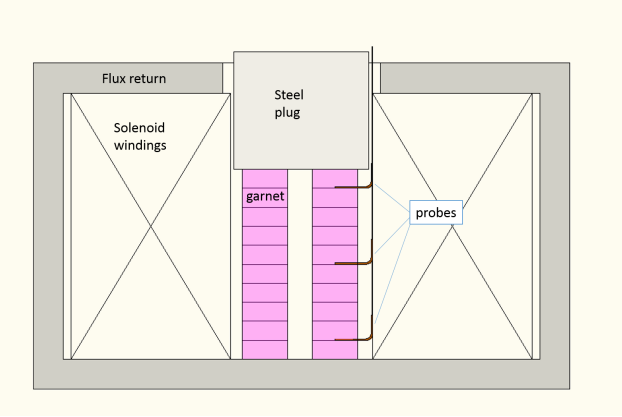

Figure 9: Setup concept for the measurement of the static magnetization.

Three different magnetometer/Hall probe pairs were available for measurement, and they were cross calibrated inside of the solenoid with no garnet. The Hall probes were placed between rings, on the top, bottom, and middle of the stack. The bias magnetic field was measured with each probe as a function of solenoid current.

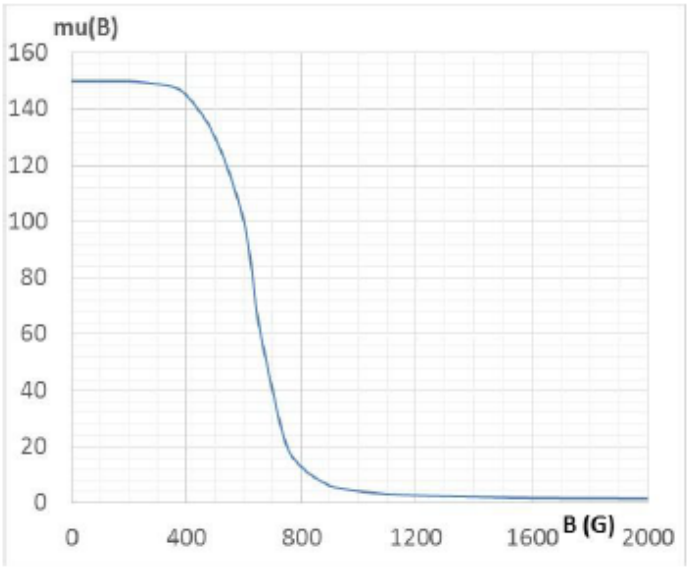

Figure 10: The extracted magnetization curve $\mu(B)$.

The iteratively obtained magnetization curve was gradually changed starting with low current. At each new current level, changes to the magnetization curve used at the previous level were made until the modeling result matched the measurement data. The existence of 1 mm gaps between rings (due to the presence of the probes) had a significant impact on the field distribution within the sample material, especially near the edges of the rings. It was necessary to take this into account in the modeling. The iterative modeling was accepted as converged when changes to the curve $\mu(B)$ become smaller than the spread in the measurement data. The final magnetization curve is shown in Figure 10. A comparison between the magnetic probe readings and the simulated bias magnetic field at the same locations (using the final magnetization curve) is shown in Figure 11.

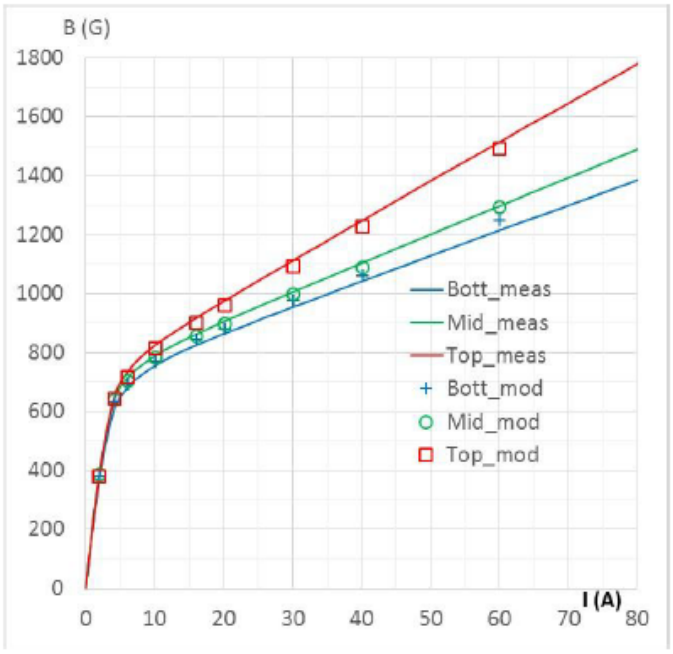

Figure 11: Comparison between measured values and values predicted by a model using the extracted magnetization curve. Values are *B* as a function of solenoid current.

Note that for the real cavity being designed, the maximum (averaged over the garnet) value of μ~3.5. Although this is the average value, the local value of the permeability, being a function of the local bias magnetic field, can be significantly greater. Thus the full magnetization curve is needed for the cavity modeling, unless one can make sure that the bias magnetic field is sufficiently uniform.

More details can be found in Ref. [19].

3.2 Loss tangent

To measure the magnetic loss tangent of the garnet, $\tan\delta_m = \mu''/\mu'$, a test resonator was constructed using the same set of garnet rings used for the static permeability studies. The measurement setup is shown in Figure 12. The cavity was the quarter-wave coaxial type with the garnet rings as a filler material. The resonator is placed inside the same solenoid that was used for the static permeability measurements, which allowed measurements for a range of frequencies. Again, a steel plug was placed on top of the cavity, to help with field uniformity. The quality factor Q of the cavity was measured at various settings of the bias current. As the Q is an integrated quantity, and the loss tangent depends on the magnitude of the bias magnetic field and the frequency, an iterative approach is used, as before, since the field in the sample is not uniform.

Weakly coupled probes were used for the excitation and for measurement of s21 with a network analyzer.

Figure 13 shows a field map in the sample for $I_{sol} = 30$ A current in the solenoid. The frequency of the cavity is 84 MHz, which means the gyromagnetic resonance would occur is at 30 Oe. The minimum field in the sample is ~50 Oe. Note that, without the steel plug, even for $I_{sol} = 40$ A, a large fraction of the sample was in gyromagnetic resonance, and similar resonances were observed, although in smaller volumes, up to near the maximum value of the current.

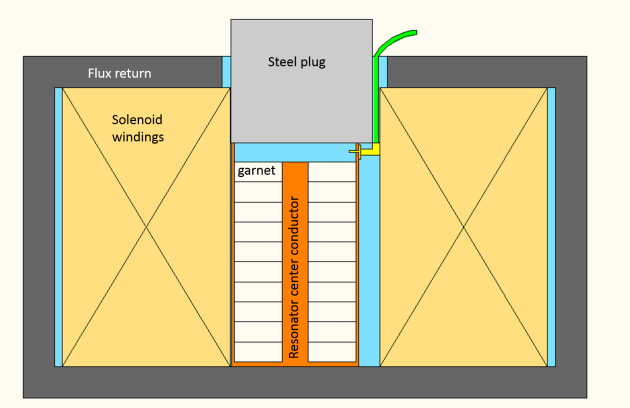

Figure 12: Measurement setup for measuring tan δ_m.

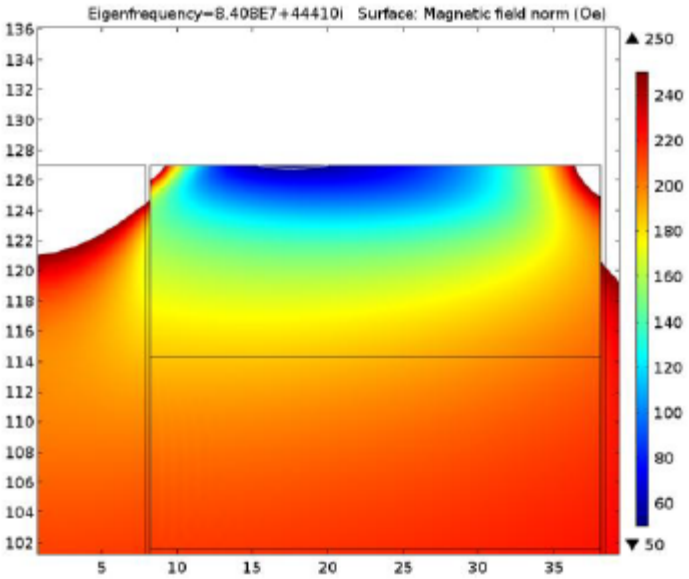

Figure 13: The field map in the sample for I_{sol} = 30 A. The horizontal axis is the radial coordinate, and the vertical axis is the longitudinal symmetry axis of the cavity and cylindrical ring stack. Only one half of the cavity/sample (in the radial direction) is shown.

Figure 14 shows measured values of Q as a function of I_{sol}. Resonant frequencies of the cavity range between 78 and 121 MHz. The significant increase in power loss at currents below 35 A can be attributed to onset of gyromagnetic resonance somewhere in the sample. Power losses in the cavity are resistive (copper), dielectric ($\tan\delta_\epsilon$) and magnetic ($\tan\delta_m$). The resistive losses can be calculated without difficulty since the conductivity of copper is well known. National Magnetics has supplied a measurement of $\tan\delta_\epsilon = 0.0001$.

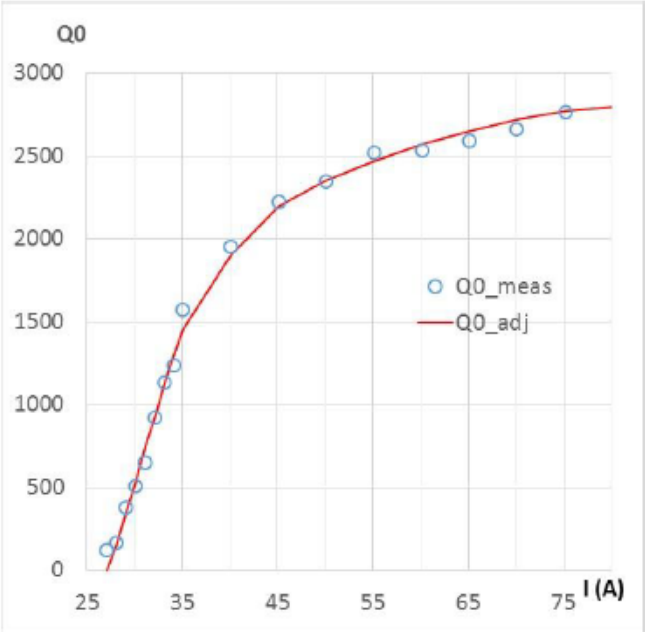

Figure 14: The measured Q of the resonator as a function of I_{sol}.

Magnetic power losses are traditionally characterized by the loss coefficient [20]. Since $\alpha \ll 1$, neglecting terms proportional to α^2:

$$\tan\delta_m = \frac{\mu'}{\mu''} = \frac{\alpha\omega\omega_M(\omega_0^2+\omega^2)}{(\omega_0^2-\omega^2)(\omega_0^2-\omega^2+\omega_M\omega_0)} \quad (1)$$

where ω is the frequency of interest, $\omega_0 = \mu_0\gamma H_0$ is the precession frequency for a given bias magnetic field, H_0, in the material, $\gamma = e/m_e$ is the gyromagnetic ratio, $\omega_M = \mu_0\gamma M_s$, and M_s is the saturation magnetization. For AL800, $\mu_0 M_s \approx 0.08$ T or 800 G.

The expression in Eq. (1) is accurate when $\omega_0 \gg \omega$, and this imposes a lower limit on H_0. Assuming that this requirement is satisfied, for a material with properties parameterized by ω_m at a point with field given by ω_0, and RF frequency ω, the loss tangent is proportional to α. It is unclear as to whether α itself has a dependence on the bias magnetic field. Some sources argue that it is a constant [20] while others dispute this [21].

Values of α for the AL800 sample were determined for each value of I_{sol} by adjusting its value in the model until the model predicted the same values for Q and frequency that were seen in the data.

Copper and dielectric losses are easily calculated by simulation. Inputs to the simulation were manufacturer measured values of dielectric constant $\epsilon = 13.8$, $\tan\delta_\epsilon = 0.0001$, and $4\pi M_s = 764$ G. In addition, the static permeability curve described in the previous section was used. Results are shown in Figure 15. The sharp rise of α at low currents can be explained by either (a) the onset of the resonant condition in some (initially small) parts of the sample or (b) that α has a dependence on the field or frequency. With the relatively low excitation current in the current experimental setup, the local power loss can be orders of magnitude higher than the averaged one. Results can be trusted only for the cases were resonance is nowhere within the material, i.e. when $I_{\text{sol}} \geq 40$ A.

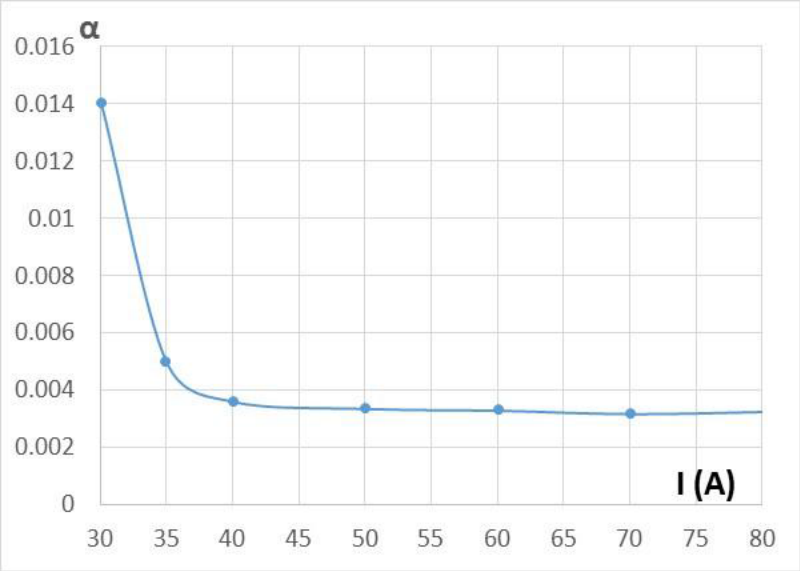

Figure 15: Extracted value of the loss coefficient α as a function of solenoid current. The rise at lower currents is likely due to an onset of gyromagnetic resonance.

As an initial assumption, α (used in Eq. (1) to calculate $\tan\delta_m$) was accepted to be constant over a wide range of frequencies, with $\alpha = 0.0033$. This assumption will be verified later by direct measurements. **Editor's note: Measurements with a garnet loaded cavity discussed in section 16.2.3 indicates that α cannot be a constant at low fields when $\mu' > 3.5$.**

For a comparison, α can also be calculated using the following formula with the line width data, $\Delta H = 24$ Oe, supplied by the vendor

$$\Delta H = \frac{2\alpha\omega_0}{\mu_0\gamma} \tag{2}$$

The above gives $\alpha = 0.0036$. Thus the vendor's α agrees to within 10% of the α found in these measurements.

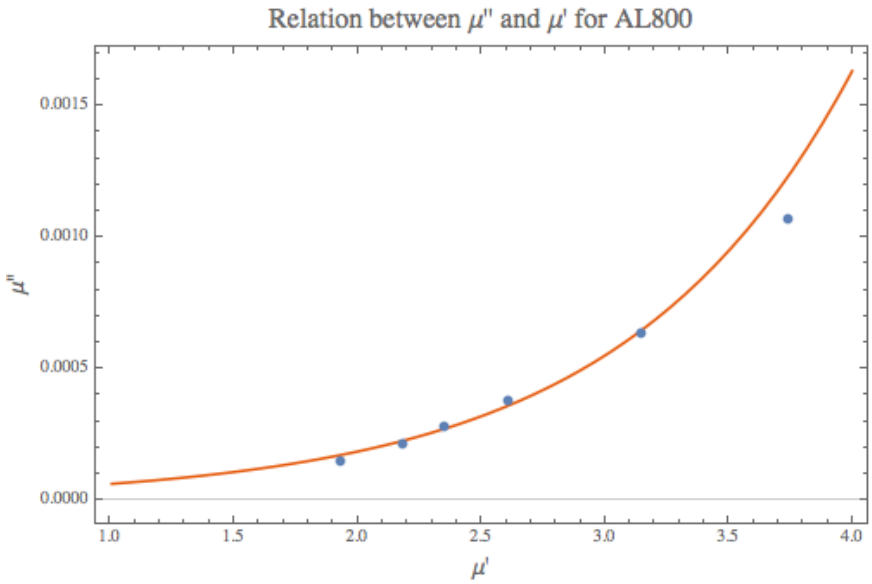

Figure 16: The relationship between μ'' and μ' for AL800.

Given the above-mentioned onset of gyromagnetic resonance, the biasing field equipment for devices that contain garnets should be designed to avoid field non-uniformity and the resulting onset of this resonance. Taking this into consideration, a more refined setup for permeability measurements has been built. This has been used to measure parameters of witness samples of the material that will be used in the 2nd harmonic cavity. See section 16.1. In addition, a test system (a cavity and a bias

magnet) has been used to perform measurements on the actual garnet rings that will be used in the cavity. See section 16.2.

More details can be found in Ref. [18].

Furthermore, from the damping constant α, the μ'' as a function of μ' curve can be generated. The result is shown in Figure 16. This curve is how the losses in the garnet of the transmission line model of the cavity, discussed in section 6.1, is calculated. The non-linear least squares fit to the measured data n that relates μ'' to μ' is

$$\mu'' = 0.211 \times 10^{-4} e^{1.088\mu'} \tag{3}$$

4 Measuring the loss tangent of Stycast epoxy (R. Madrak & I. Terechkhine)

It was decided to use Stycast 2850FT with Catalyst 9 [22] to join the sectors of AL800 to form a ring, and to attach the AL800 rings to the alumina cooling rings. The manufacturer specifies the dielectric constant as 5.01 and the dissipation factor as 0.028 at 1 MHz. It was necessary to measure the loss factor in the frequency range at which the harmonic cavity will operate.

A 76 MHz quarter wave resonator was constructed from standard 3-1/8" transmission line. A 2" thick ring of epoxy with an OD/ID of ~3"/1.375" was made to fit into the end of the resonator. A model of the setup is shown in Figure 17. The Q was measured with and without the epoxy sample. Without epoxy, Q was 1628, though the simulation predicted 2342. The conductivity of copper in the simulation was scaled down until the measured and simulated values of Q with no epoxy agreed. An analytical approximation of Q resulted in $\tan \delta_e = 0.017$. This value was then used in the simulation with epoxy, in which case the measured and simulated values were 235 and 230. The conclusion was $\tan \delta_{e\varepsilon}$ from this measurement is 0.017, substantially smaller than the vendor's value of 0.028 at 1 MHz. As a check of the sensitivity, the value of $\tan \delta_{e\varepsilon}$ in the simulation was increased to 0.03, in which case the simulation predicted Q = 138.

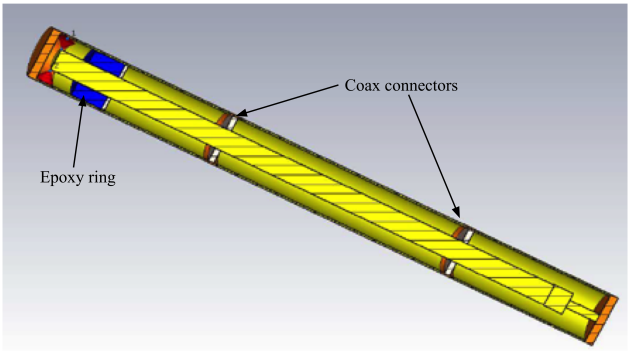

Figure 17: A sketch of the 76 MHz quarter wave resonator made from 3-1/8" transmission line. The measurement of tan δ_ε for a 2" thick ring of epoxy, and no garnet was done in this setup.

5 Measuring the loss tangent and dielectric constant of thermal grease (R. Madrak)

To make good thermal contact between the garnet-alumina rings and the outer and inner conductors of the cavity, thermal grease will be used. This is crucial because heat is removed by cooling lines on the outer and inner conductors. In addition, the grease will fill in small air gaps which could enhance the local electric field and cause sparking. The same grease will also be used between rings for the latter reason.

The grease that was chosen is MG Chemicals® Super Thermal Grease II 8616 [23]. The grease has a base of synthetic oil, and its principal components are aluminum oxide and zinc oxide. Values quoted in the technical data sheet for the dielectric constant were 6.77 and 6.69 at 1 and 10 kHz, respectively. At these frequencies, the dissipation factor is 0.01.

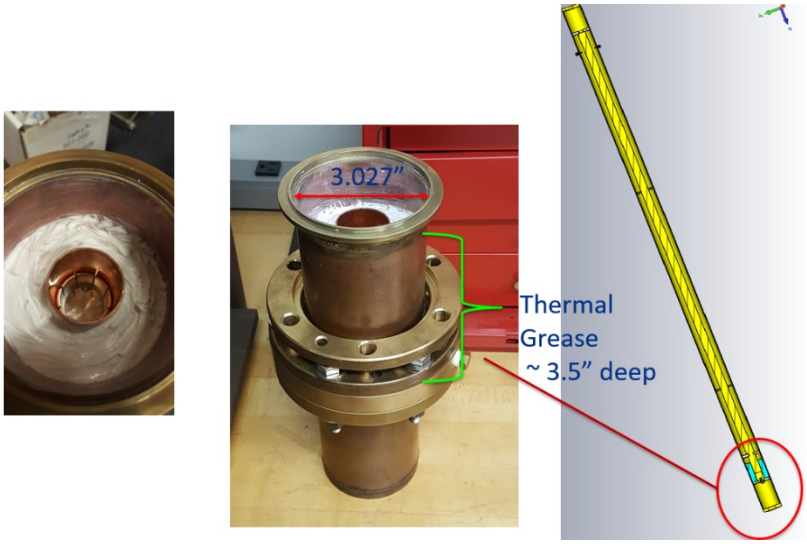

Figure 18: The half-wave resonator containing the thermal grease.

The properties of the grease were measured at low (kHz) frequencies, and also in the MHz range. In the first measurement, a half resonator was constructed from standard 3-1/8" transmission line. Thermal grease was added to a section of the line as shown in Figure 18. The frequency and Q of the resonator were measured with a network analyzer (S21). The setup was simulated in CST Microwave Studio. First, the conductivity of the metal outer and inner conductors was tuned so the Q values of the empty resonator matched in simulation and data. Using the tuned value for the conductivity, the setup with grease was simulated. The dielectric constant was tuned in the simulation the make the frequencies match in data and simulation, and then tan was tuned to make the values of Q match. The

resonant frequencies with and without grease were ~68 and 59 MHz, respectively. The values obtained for ε and $\tan\delta$ were 5.2 and 0.03. These were not what was given by the data sheet at lower frequency, but still considered acceptable given the relatively thin layer of grease that is expected to be used.

The value of ε was also measured at lower frequency by measuring the capacitance of a layer of grease sandwiched between two metal plates. The distance between the plates was maintained using small G10 spacers, and the capacitance was measured using a HP4263 LCR meter with and without the grease. The value of ε was obtained from the ratio of these two measurements, after correcting for the presence of the G10. The values obtained were between ~5.8 and 5.5 for 100 Hz to 100 kHz, which were again considered acceptable, though they did not agree well with specifications quoted in the data sheet.

6 Modeling the cavity

The simulations can be divided into two major parts: those that were done using a transmission line (TL) model and those that were done using a MWS model. Although MWS is the final arbiter on the behavior of the cavity, the TL model serves as a sanity check of the MWS results. Another advantage of the TL model is that calculating the results from any change in the model is relatively fast compared to MWS and thus besides serving as a sanity check, it also guides changes to the MWS model for it to achieve the desired cavity characteristics shown in Table 2.

6.1 The transmission line model (C.Y. Tan & R. Madrak)

The TL model that we have used in our *Mathematica* [24] calculations is shown in Figure 19. This is a simplified model of the MWS model shown in Figure 8 and described in section 6.2. A more complex Advanced Design System (ADS) [25] TL model has also been made, but the results are essentially the same when compared to the model shown here. And thus, we will only talk about the simplified TL model here. The ADS model is described in section 6.1.3.

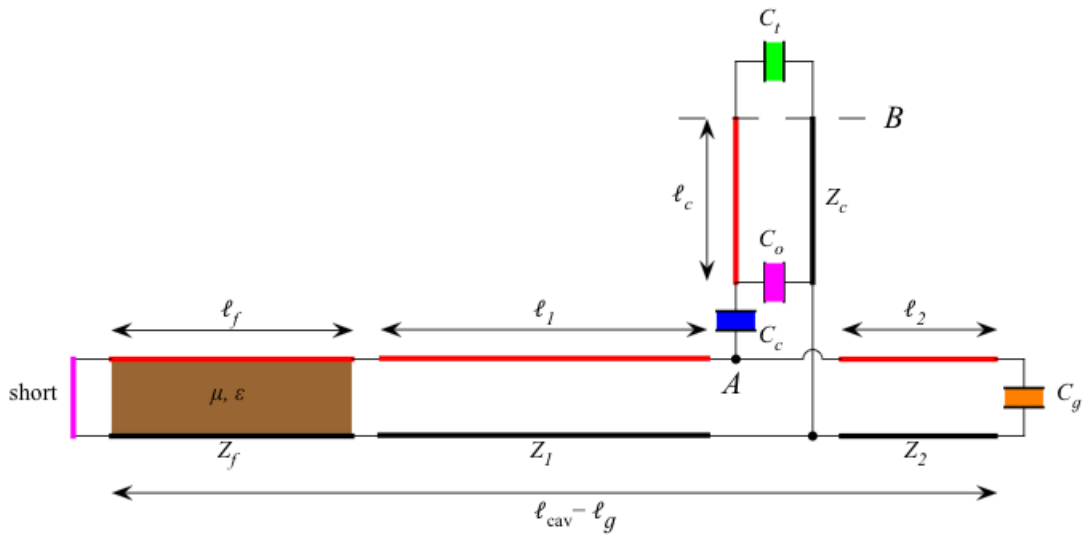

Figure 19: The TL model of the 2nd harmonic cavity.

The TL model is shown in Figure 19. Going from left to right, we will discuss the approximations that we have used in this model which are:

1. We have ignored the Al_2O_3 cooling plates that are sandwiched between the garnet rings, i.e. our model assumes a continuous cylinder of garnet material.

2. We have ignored the neck between the garnet and the main body of the cavity.
3. We have ignored the taper of the power module and approximated it as a uniform cylinder.
4. We model the Y567B as a capacitor $C_t = 60$ pF. C_t is the output capacitance of the Y567B in the grounded grid configuration.
5. C_o is the sum of the outer capacitance between the coupling capacitor and the outer wall of the transmission line and the capacitance of the RF window between the power module and the cavity.
6. We have neglected the impedance of the stem that connects power module to the coupling capacitor.

Parameter	Value	Units
Garnet part		
inner radius of transmission line r_{fi}	170	mm
outer radius of transmission line r_{fo}	105	mm
Vacuum part		
l_1	291	mm
l_2	100	mm
inner radius of transmission line r_i	45	m
outer radius of transmission line r_o	125	m
Power module		
l_c	339.2	mm
inner radius of transmission line r_{ci}	100.85	mm
outer radius of transmission line r_{co}	203.2	mm
Capacitors		
gap capacitance C_g	2.9	pF

coupling capacitance C_c	8.0	pF
outer capacitance C_o	4.5	pF
anode capacitance C_t	60	pF
Power module RF window capacitance	3.4	pF
relative permittivity of garnet	14.4	-
dielectric loss tangent $\tan\delta_e$	0.0001	-

Table 3: The parameters of the TL model.

A summary of the parameters of the used in the TL model that come from the MWS model discussed in section 15 are shown in Table 3. Notice that the length of the garnet l_f is not in Table 3 because we have varied this length to get the cavity to resonate at 76 MHz when $\mu = 3.5$. Our optimization found that $l_f = 112.46$ mm.

Using this length and the parameters in Table 3, we can calculate various cavity parameters of interest. These parameters are plotted in the next section.

6.1.1 Plots

We show in Figure 20 the frequency range of the cavity as a function of permeability of the garnet. It is clear from this figure that the TL model covers the required frequency range for $1.25 < \mu \leq 3.5$.

The shunt impedance[4] as a function of the resonant frequency calculated with the TL model is shown in Figure 21. We can calculate R/Q of the cavity using the shunt impedance and the following formula that we will derive in Appendix B

$$R/Q = 2\left(\omega_0 \frac{dB}{d\omega}\Big|_{\omega=\omega_0}\right)^{-1} \quad (4)$$

[4] We will use the RF engineer's definition of shunt impedance throughout this report rather than the accelerator physicist's definition of shunt impedance. See Appendix A for an explanation of the differences between the two definitions.

where B is the imaginary part of the admittance of the parallel RLC circuit model of a resonator and ω_0 is the angular resonant frequency of the circuit. The R/Q of the TL model is shown in Figure 22. Once we have R/Q, we can calculate the Q of the cavity and the result is shown in Figure 23. From this figure, we can see that at low frequencies, the garnet dominates the losses, while at high frequencies, the losses are dominated by the copper part of the cavity.

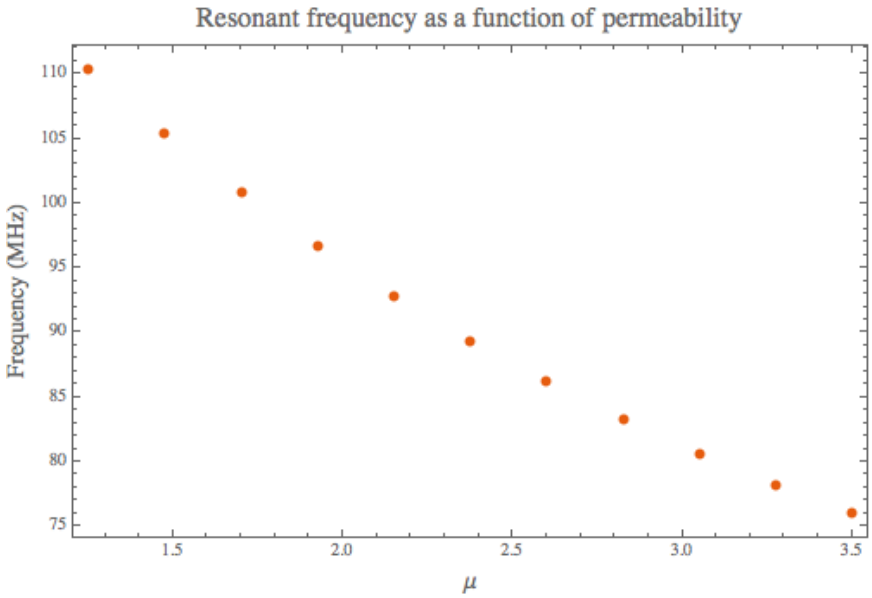

Figure 20: This figure shows the resonant frequency as a function of permeability. The cavity clearly covers the required frequency range.

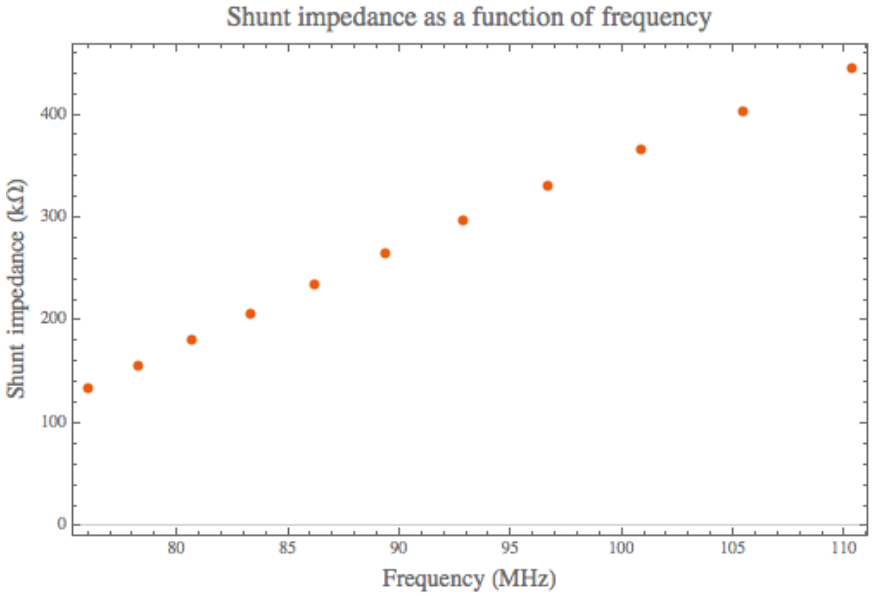

Figure 21: This is the shunt impedance of the TLM model cavity as a function of its resonant frequency.

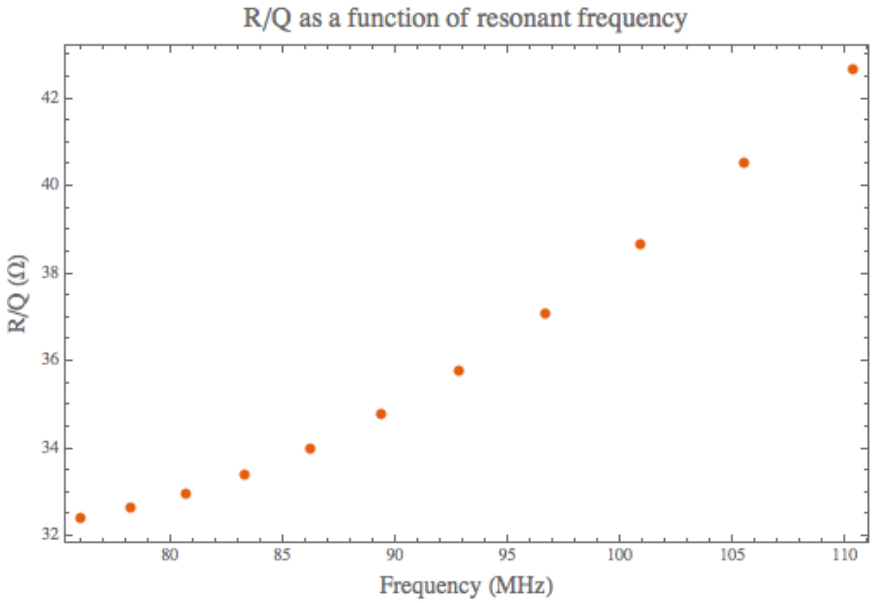

Figure 22: R/Q of the TL model cavity.

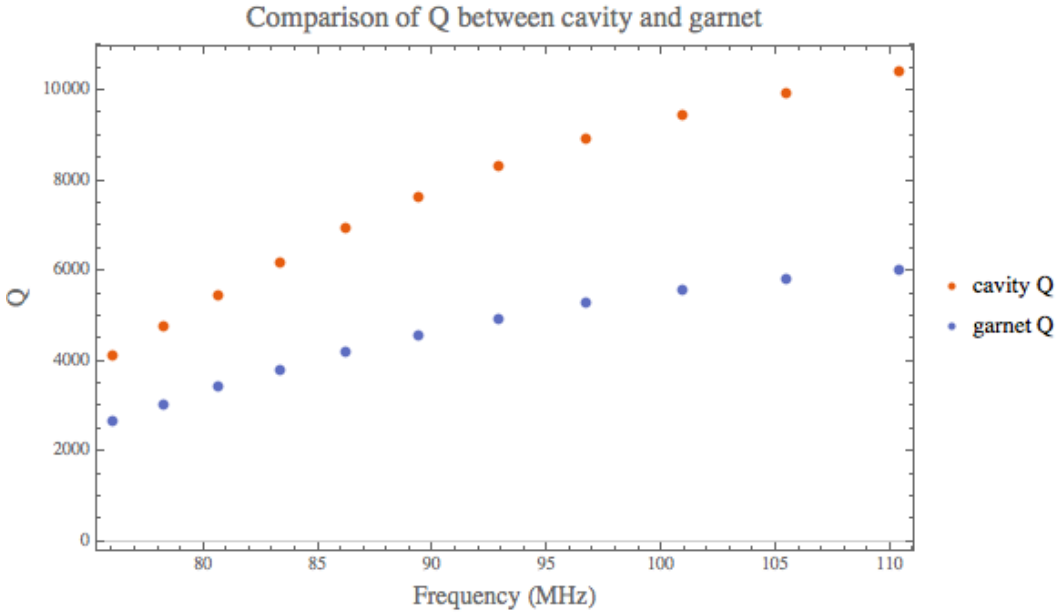

Figure 23: The Q of the TLM cavity and the garnet is shown here. At low frequencies, the losses in the cavity is dominated by the garnet while at high frequencies, it is dominated by losses in the copper.

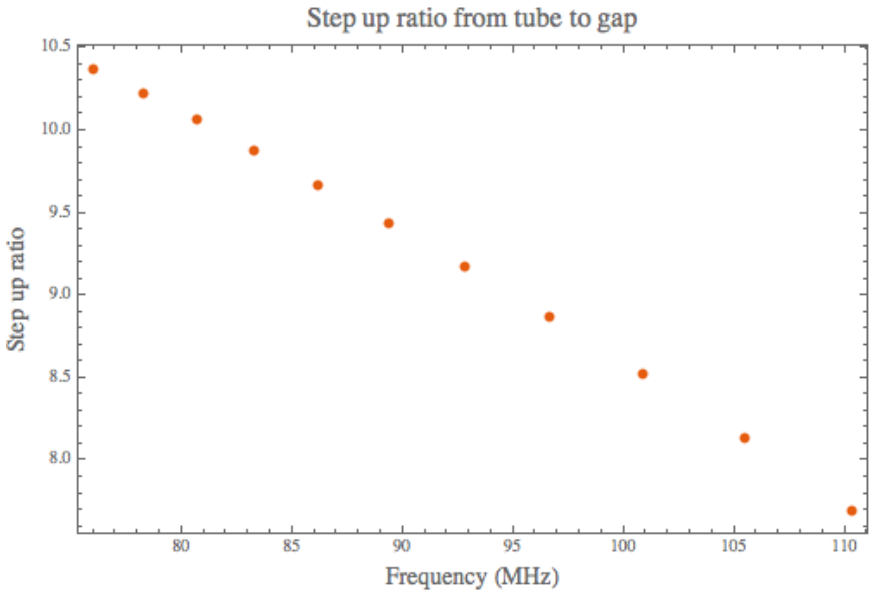

Figure 24: The step up ratio as a function of resonant frequency.

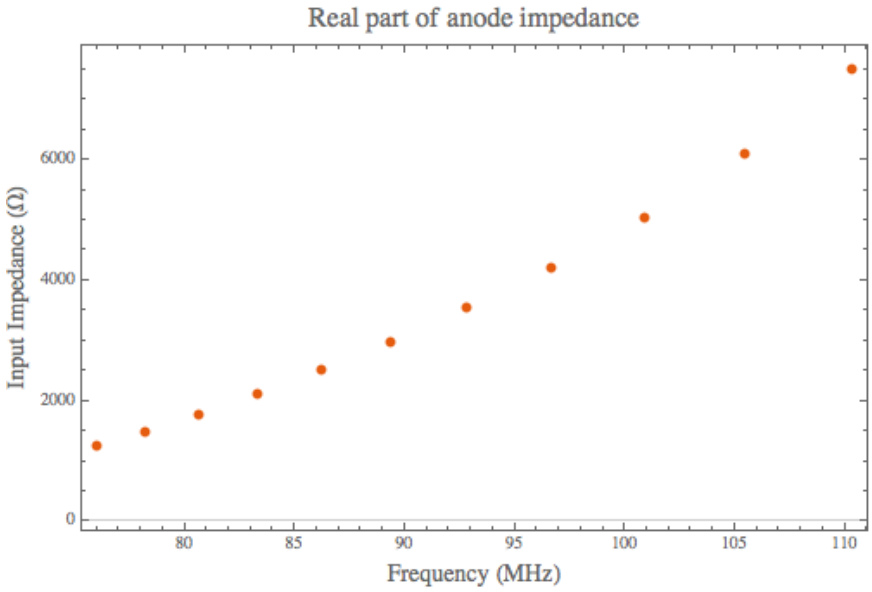

Figure 25: The impedance seen by the tube as a function of resonant frequency.

The step up ratio of the cavity is shown in Figure 24. We define the step up ratio to be $V_{\text{gap}}/V_{\text{anode}}$, where V_{gap} is the voltage across the accelerating gap and V_{anode} is the voltage at the power input of the cavity, marked with "B" in Figure 19.

The impedance seen by the anode of the tube, shown in Figure 25, is an important parameter because it determines whether the cavity can be driven by the Y567B. We can see that the TL model predicts that the anode impedance $>$ 1.3 kΩ for the entire frequency range of interest. The determination of the tube efficiencies will be discussed in section 7.2.

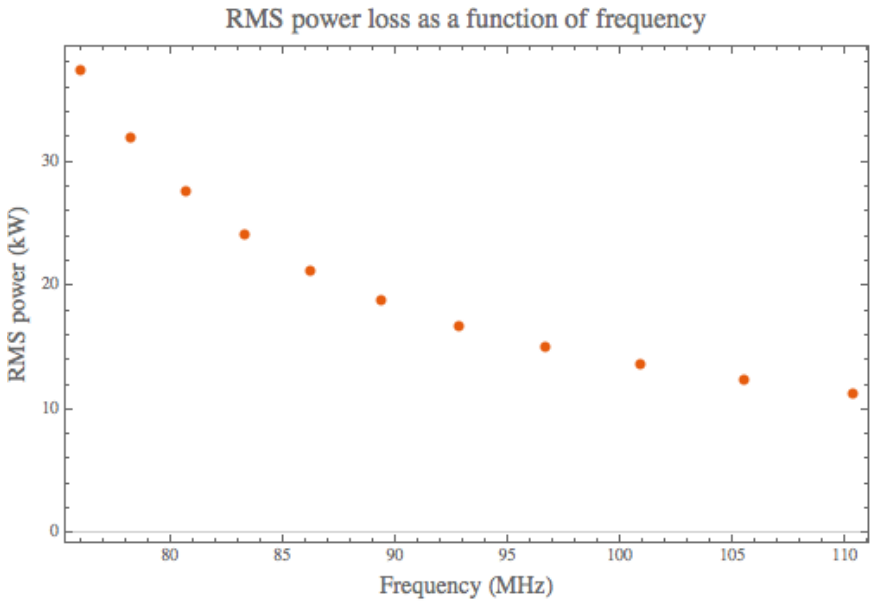

Figure 26: The rms power loss of the TL model cavity assuming a 100 kV gap voltage.

The rms power loss in the cavity assuming a 100 kV gap *peak* voltage is shown in Figure 26. We constructed this figure using the gap peak voltage and the shunt impedance of the cavity shown in Figure 21. At low frequency, most of the power is lost in the garnet (See Q plot in Figure 22) while at high frequency most of the power is lost in the copper.

6.1.2 Power module

The power module is capacitively coupled with C_c to the cavity at point "A" shown in Figure 19. At the end of the power module transmission line is a capacitor, C_t, which is used to model the Y567B tube. C_t is the output capacitance of the tube. The power module structure will resonate by itself and thus when it is coupled to the cavity resonator there are two normal modes (and their harmonics) in the structure. The natural resonant frequency of the module alone in this case is ~200 MHz and it is

sufficiently far away from the natural frequency of the cavity in the required $\mu < 3.5$ range that the power module itself does not resonate and take away power from exciting the accelerating gap.

6.1.3 ADS model

The ADS model of our cavity is shown in Figure 27. It is a more detailed transmission line model than the TL model shown in Figure 19. The main improvements in the ADS model that we have made over the TL model are the inclusion of the tapers and the Al_2O_3 garnet stack. We model the taper by joining transmission lines that have successively smaller radii to mimic the taper. Despite adding in the details, we have found that the results from the ADS model and the TL model give nearly the same results, and thus all the essential physics are captured with the TL model.

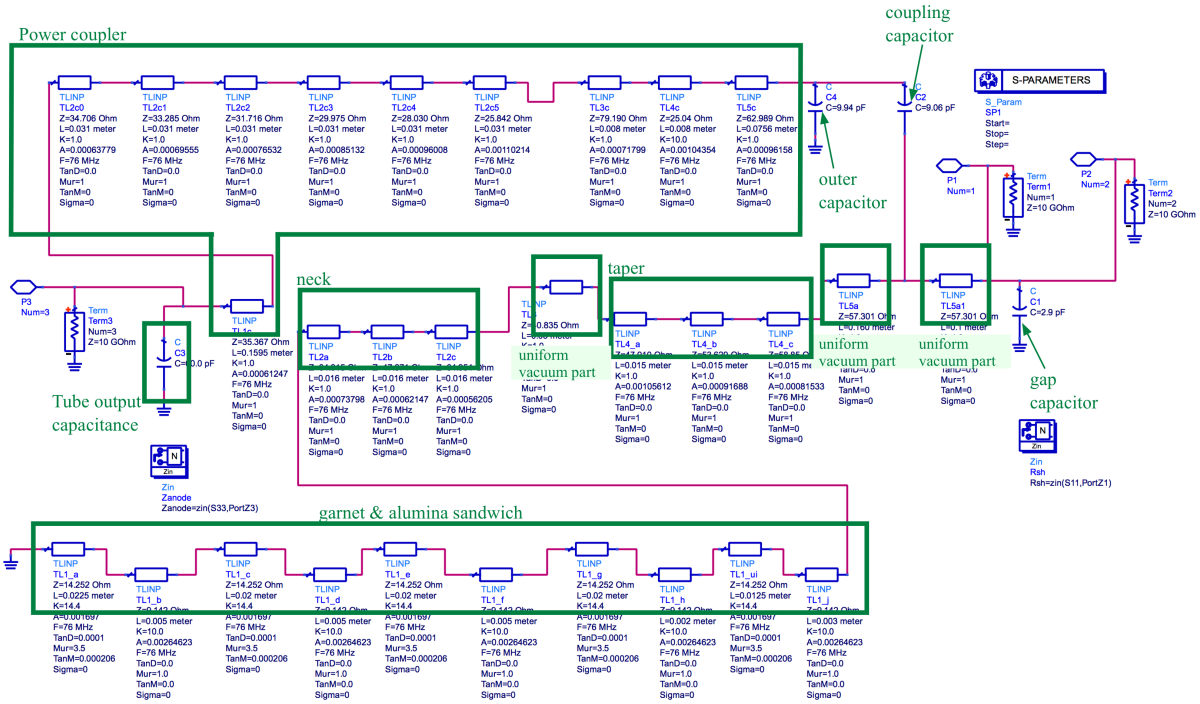

Figure 27: The ADS model of our cavity. It is a much more detailed transmission line model.

6.2 The CST Microwave Studio model (G. Romanov)

The CST Microwave Studio model of the 2nd harmonic cavity has gone through many iterations. The first model simply scaled the dimensions of the TRIUMF KAON cavity [6] to get the required frequency range of 75.7 MHz to 105.6 MHz. The final model shown in Figure 28 took into account the measured properties of the garnet, solenoid field, power amplifier (PA) and the higher order mode (HOM) cavity. In this section, we will only summarize the results that are not covered in the later chapters. The evolution of the model can be found by reading the presentations given in the fortnightly meetings on http://beamdocs.fnal.gov/AD-public/DocDB/DocumentDatabase (search for `2nd harmonic`).

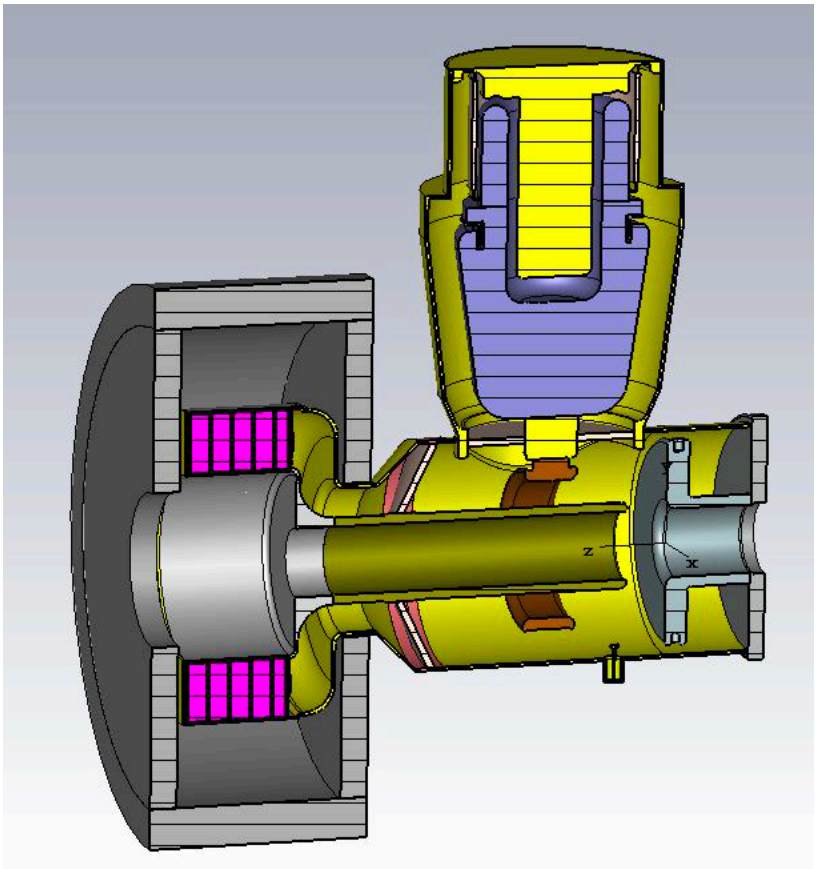

Figure 28: The final MWS model that includes every component.

6.2.1 Power amplifier model

We define the power module (shown in Figure 8) to be the part that contains the PA and the shell that houses it. The PA is capacitively coupled to the accelerating cavity with a ring. The power module of the 2nd harmonic cavity is strongly coupled to the accelerating cavity and thus any changes to the power module strongly affects the RF characteristics of the cavity. In fact, due to the strong coupling, the power module and the accelerating cavity cannot be considered as two separate entities and must always be treated as a multi-modal resonant structure in all optimizations.

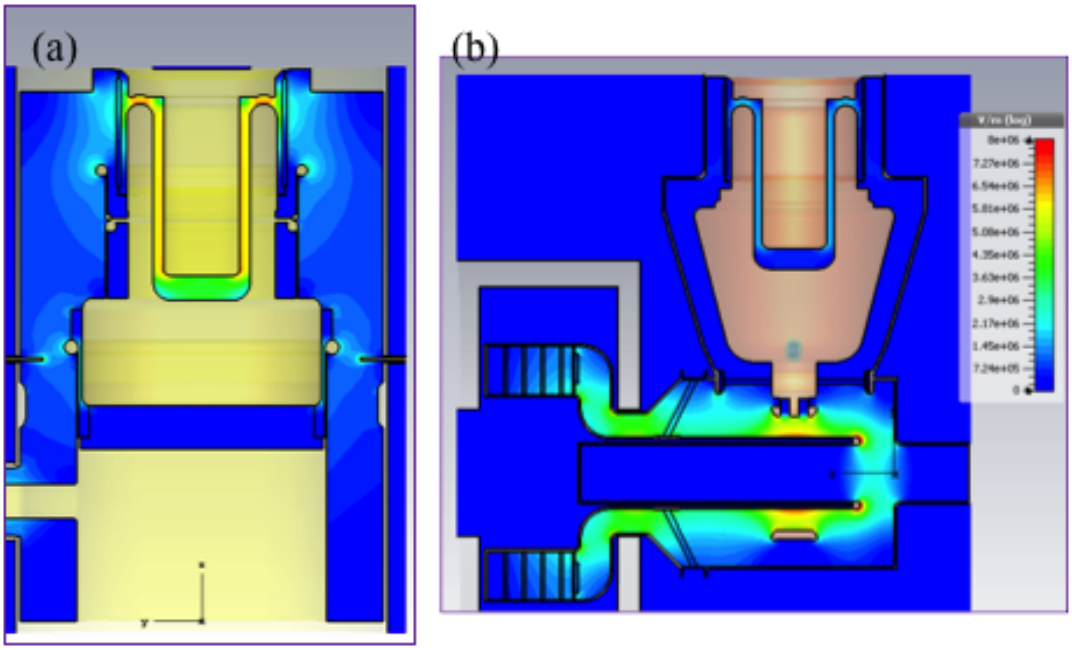

Figure 29: These pictures show the E-fields when the PA installed in (a) the PA test cavity and (b) the 2nd harmonic cavity.

Our early simulations simply modeled the PA as a 60 pF capacitor. This proved to be insufficient because the RF characteristics of the cavity are very sensitive to the shape and length of the power module. Small changes to the dimensions of the shell to accommodate water pipes and electrical connections have non-trivial RF consequences. Therefore, a good MWS model of the PA was made so that it could be synchronized with the mechanical model. This meant that we could verify that any mechanical changes would not have detrimental effects on the RF characteristics. In order to assure ourselves that the PA model was done correctly, it was verified by checking that the resonant frequency that MWS found for the PA test cavity (see section 14) was the same as the measured one [26]. Figure 29 shows the PA model installed in both the test cavity and the 2nd harmonic cavity.

We also studied where the simulation port should be placed in the PA model so that the anode impedance can be calculated. Our studies (See references [27, 28]) showed that the exact location of the port within the PA was not critical for evaluating the value of the anode impedance. We chose the port location shown in Figure 30.

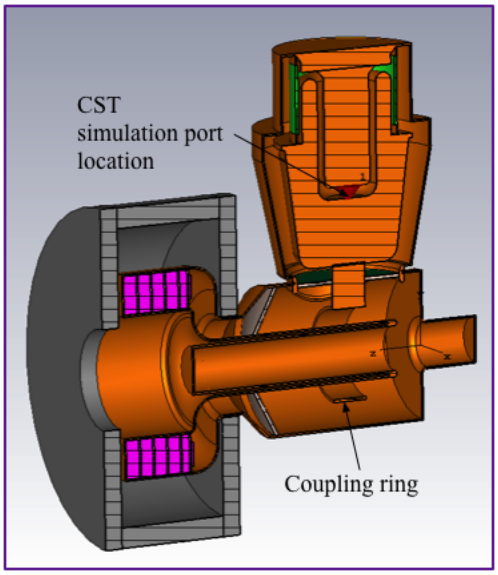

Figure 30: Location of CST simulation port in PA and the coupling ring.

6.2.2 Capacitive coupling ring

The capacitive coupling ring, shown in Fig 30, couples the power from the PA to the accelerating cavity. It is necessary to properly shape the coupling ring so that sparking does not occur. The screws that hold the coupling ring to the stem are recessed as well so that the fields are always below the Kilpatrick and W. Peter *et al* limits [29]. The limits in the frequency range from DC to 100 MHz are shown in Figure 31. From this plot, we will limit the surface fields to between 10 and 12 MV/m (or 100 kV/cm and 120 kV/cm). This is a very conservative limit because from the experiments that were conducted by W. Peter *et al*, they showed that the surface fields can be a factor of 2 higher before surface breakdown occurs.

The surface fields calculated by MWS after appropriately shaping the coupling ring and the edge of beam pipe at the accelerating gap are shown in Figure 32. The maximum surface field on the coupling ring is less than 59 kV/cm and on the beam pipe at the accelerating gap is less than 66 kV/cm. These two values are much less than the surface field limits and thus should not present sparking problems.

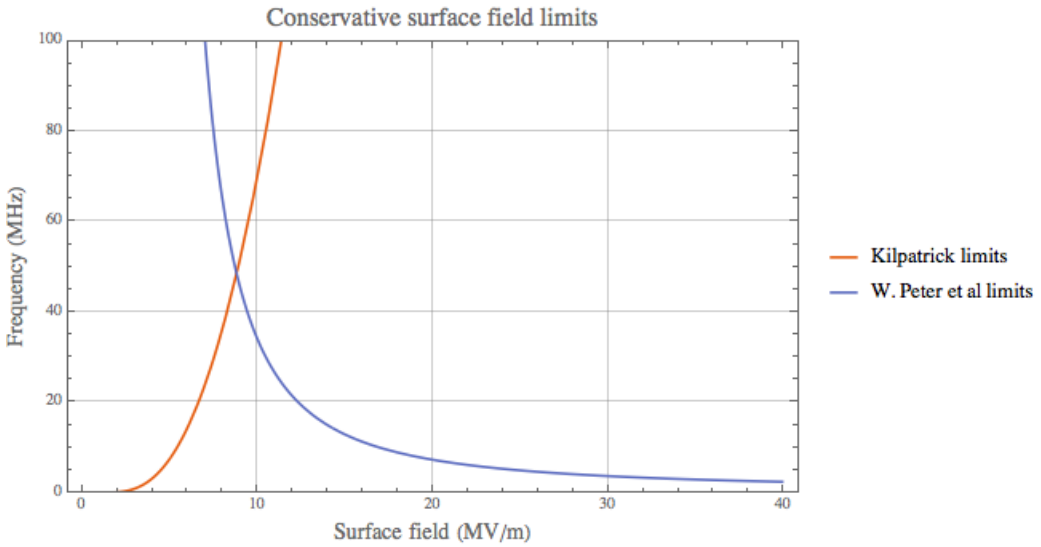

Figure 31: The curves show the conservative limits for surface fields. The limits for our cavity are between 10 to 12 MV/m.

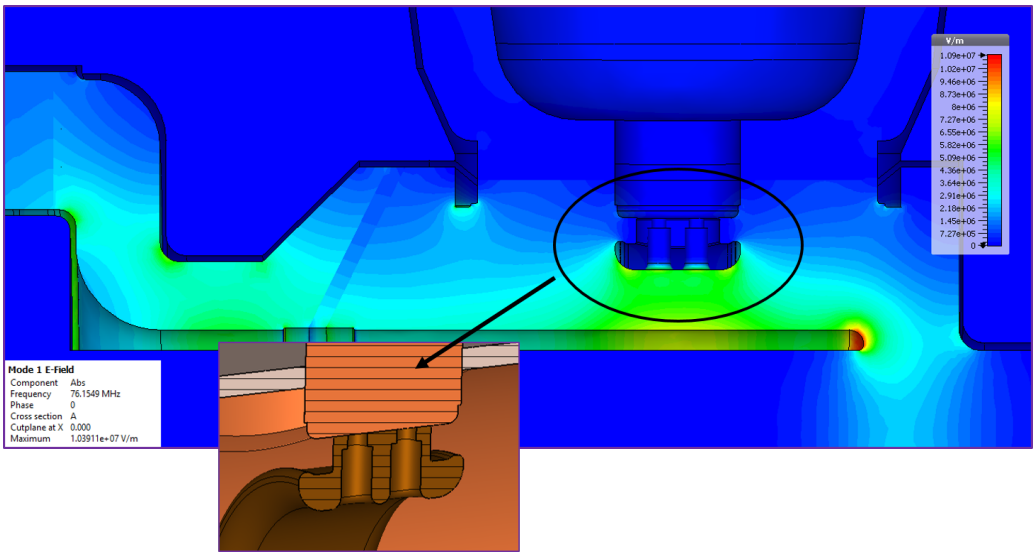

Figure 32: This is the E-field distribution in the cavity. The areas of concern are at the coupling ring and the beam pipe edge of the accelerating gap. The zoomed in view shows how the ring is connected to the stem via recessed screws.

6.2.3 Field probes

A pair of field probes will be placed near the accelerating gap. These field probes will be placed orthogonally at the gap. The locations of these probes will give 10 V when the gap voltage is 100 kV (**Editor's note: measurements show a slightly lower gain of 78 to 79 dB rather than 80 dB from simulations at injection. The gain is also a function of frequency. See section 21.2.4**). There is minimal effect on the resonant frequency with the addition of these probes [30]. The probe is made from a Type-N connector [31] and a button. See Figure 33.

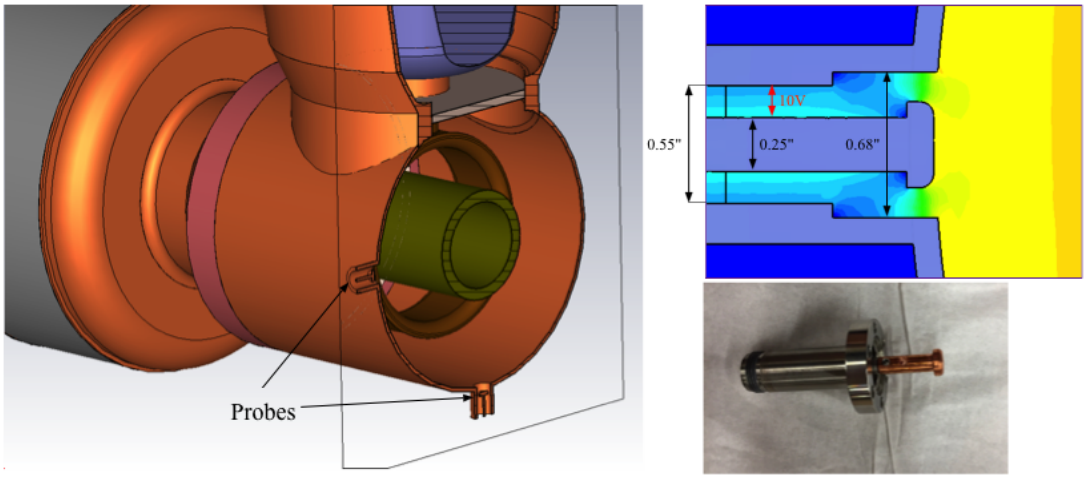

Figure 33: The field probes are installed near the accelerating gap. The field probe that is installed in the cavity is shown on the bottom right.

6.2.4 Calculated RF parameters

The RF parameters that MWS calculated for the cavity are shown in Figure 34 and Figure 35. These values will be used in the subsequent analysis of the cavity power requirements. These curves came from the MWS calculations dated 22 May 2017, MWS model file `2Dto3D_FD_CutOff_20170509`. The DC part of the solenoid current is 745 A into 11 solenoid turns which keeps the cavity at the injection frequency of 75.7 MHz at all times. The AC part of current ramps the solenoid to produce the magnetic field necessary to bias the tuner for higher frequencies. **Editor's note: The results here assume that the solenoid is divided into a DC coil with 11 turns and an AC coil with 48 turns. The actual as built solenoid will have 60 (not 59) turns connected electrically in series.**

Note: The Engineer's definition of the shunt impedances are used here. See Appendix A .

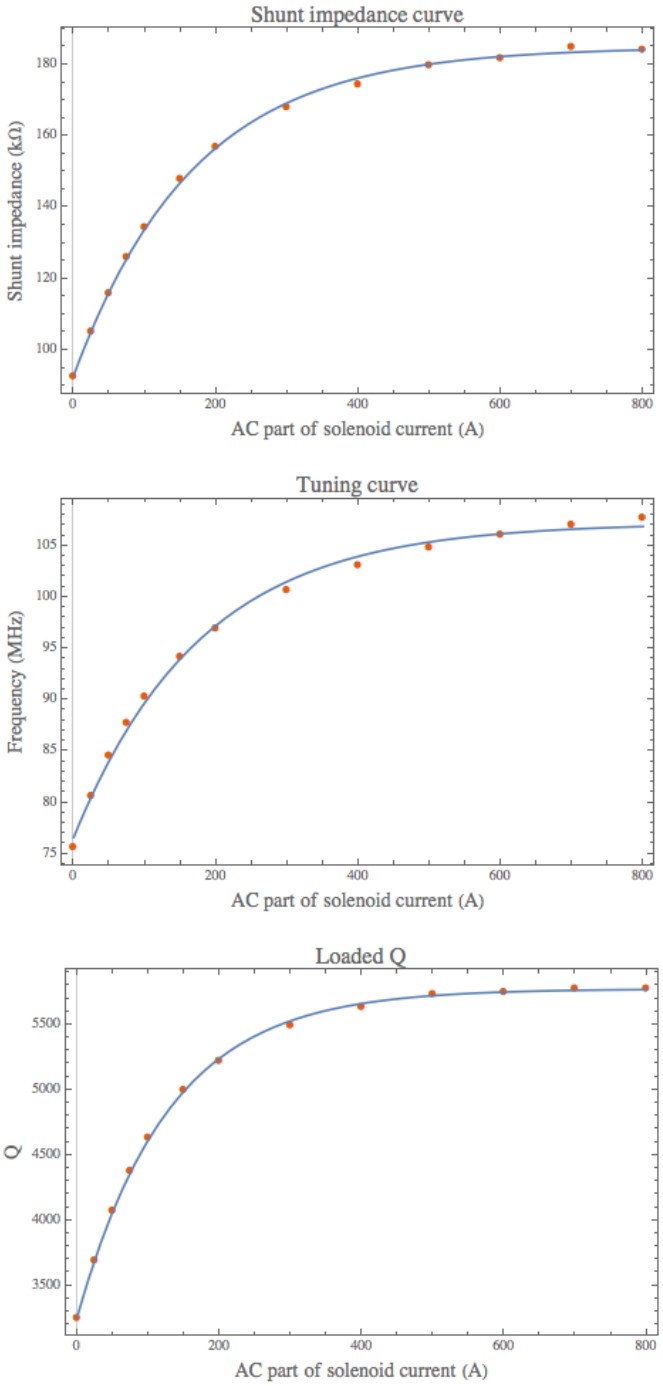

Figure 34: The shunt impedance, resonant frequency and loaded Q as a function of the solenoid current going into 48 solenoid turns.

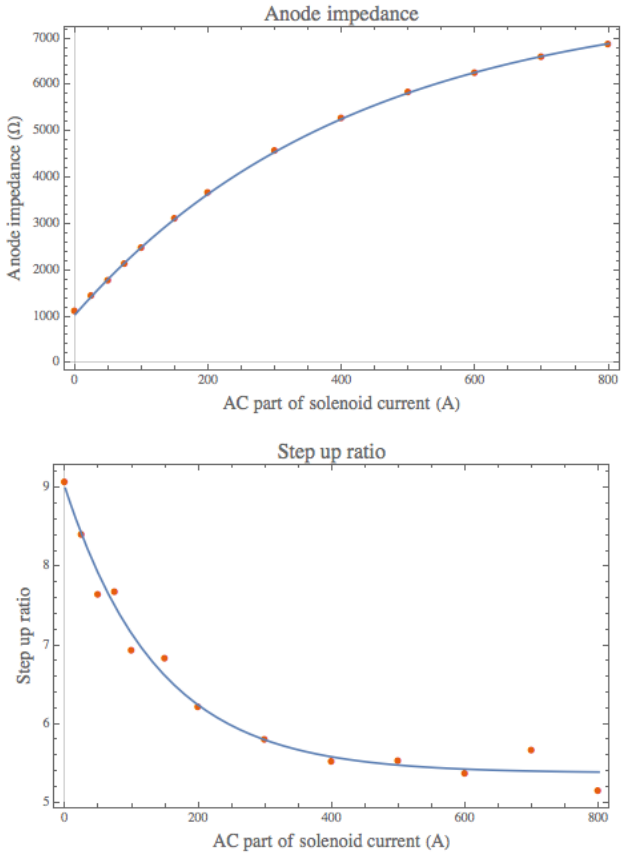

Figure 35: The anode impedance and the step up ratio.

See Table 5 for the MWS numerical results that compares the cavity with and without the HOM cavity.

7 HOM damper

The HOM (higher order mode) damper is an important part of the cavity design to lower the HOM modes of the cavity so that they do not become the source of beam instabilities. The HOM damper design is a modification of the Smythe style HOM damper cavity [17] that was used in both the TRIUMF cavity and the SSC [32] LEB cavity. The damping characteristics of the HOM damper have been calculated with a semi-analytic approximation and with MWS. Both methods are presented here. The goal is to have the higher order modes have impedances less than 2 kΩ. (This is very conservative because there are more than 20 fundamental cavities and their impedances can, in principle, add up to a lot more than 2 kΩ.)

7.1.1 Semi-analytic approximation (C.Y. Tan)

This semi-analytic approximation of the Smythe style damper cavity comes from Smythe [17] and Paramonov [33]. The reasons for using the semi-analytic approximation are that

1. Quick optimization of the geometry of the damper cavity.
2. Superfish [34] does not have the capability of calculating the effects of a resistive load.

Figure 36 shows the cavity + HOM damper cavity approximation. The cavity impedance is Z_1, Z_2 is the impedance of the HOM damper cavity, C is the gap capacitance, R is the load resistor, and I_b is the beam current. Z_g is the total impedance from the R, C and Z_2 contributions.

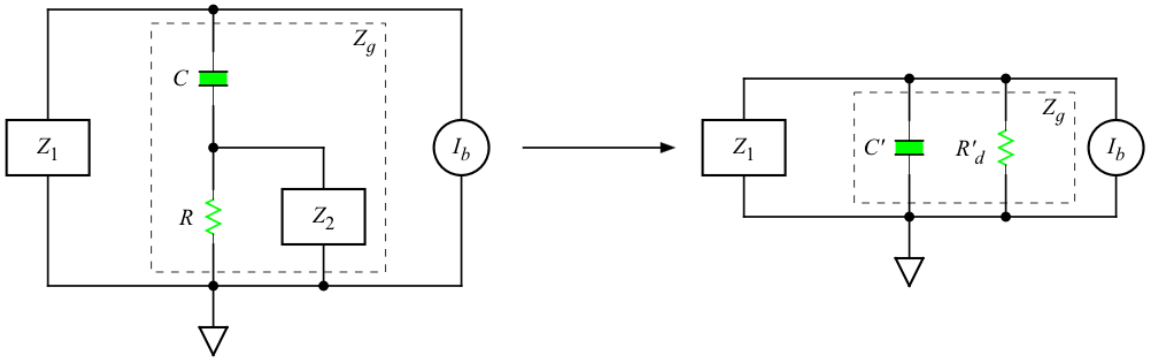

Figure 36: On the left is the cavity+HOM damper equivalent circuit. The symbols are explained in the text. On the right is the Smythe approximation where he introduces the equivalent damping resistor R'_d.

Smythe then asserts that Z_g can be made to look like a circuit that consists of a new gap capacitor C' and a damping resistor R'_d in parallel. Again see Figure 36. Since C' and R'_d are in parallel, we have

$$\frac{1}{Z_g} = \frac{1}{R'_d} + \frac{1}{Z'_c} \quad \Rightarrow \frac{1}{R'_d} = \frac{1}{Z_g} - \frac{1}{Z'_c} \tag{5}$$

where $Z'_c = 1/i\omega C'$. But Z'_c is completely imaginary and R'_d is completely real and thus

$$R'_d = \frac{1}{\mathrm{Re}[1/Z_g]} \tag{6}$$

Since Superfish does not have the capability of calculating the effects of the load resistor, we have to use R'_d that was found in Eq. (6) to calculate the effect on the shunt impedance. This is what we will do below.

Now, since Superfish can calculate both the voltage V_g across the accelerating gap, i.e. across Z_g without any resistors, and the voltage V_d across the HOM cavity gap, i.e. at the same location where R will be attached, we can these values to relate R to R'_d. We do this by assuming that the damper resistor R only perturbs the voltage across the accelerating gap and the HOM cavity gap, thus we can assume that both V_g and V_d are the same with it is attached. When this approximation holds, we must have the rms power lost through R equal to the power lost through R'_d, i.e.

$$\frac{V_d^2}{2R} = \frac{V_g^2}{2R'_d} \tag{7}$$

Therefore, the relationship between R and R'_d is

$$R'_d = R\left(\frac{V_g}{V_d}\right)^2 \tag{8}$$

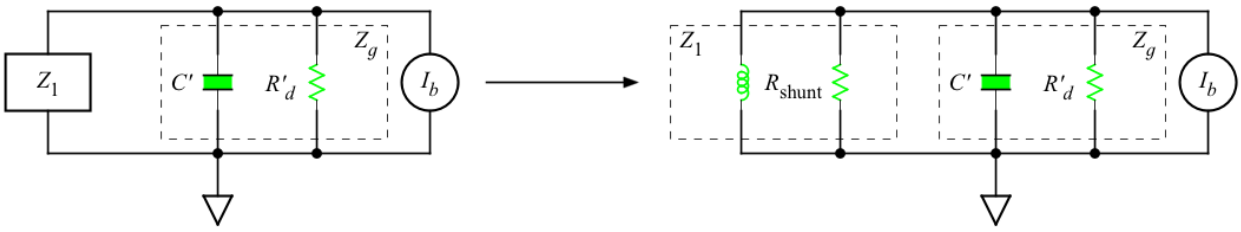

Figure 37: The cavity impedance Z_1 can be broken up into an inductance (and perhaps a capacitance as well) and the shunt impedance R_{shunt} that is the impedance without the HOM damper.

Finally, using Figure 37, we can calculate the shunt impedance R_{shunt} of the cavity without the HOM damper is in parallel with R'_d, the reduced shunt impedance of the cavity R'_{shunt} is simply given by

$$R'_{\mathrm{shunt}} = \frac{R_{\mathrm{shunt}}R'_d}{R_{\mathrm{shunt}}+R'_d} \tag{9}$$

• • •

7.1.1.1 Simple HOM damper

We have the required equations to calculate the shunt impedance of the cavity from the previous section after we calculate V_g and V_d for a given model from Superfish. We show the results of a Smythe style HOM damper cavity attached to the accelerating cavity shown in Figure 38.

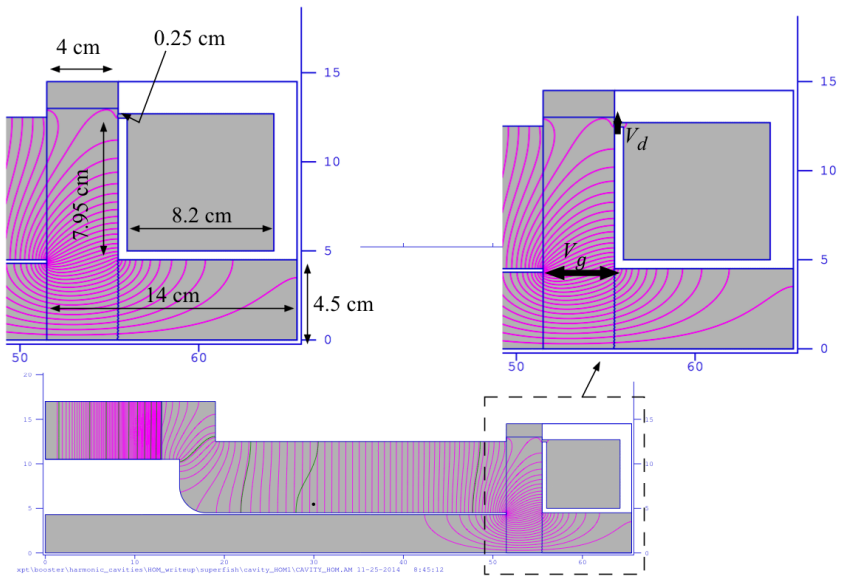

Figure 38: The accelerating cavity with a Smythe style damper cavity attached. The insets show where the voltages will be calculated and its dimension.

The dimensions of this simple HOM cavity are summarized in Figure 38. We point out that the HOM gap is ridiculously small at 0.25 cm. In the final design this gap will have to be optimized to give us the required impedance of each HOM.

When the load resistance $R = 50\Omega$, the HOMs of the accelerating cavity are damped. The results are quite good: although the impedance of the fundamental is reduced by 11% from 494 kΩ to 440 kΩ, the next higher harmonic, which has the highest impedance, is reduced by 93.3% from 228 kΩ to 1.6 kΩ. The comparison between the impedances with and without the HOM cavity is shown in Figure 39.

Figure 39: The shunt impedance of the cavity with and without the HOM cavity is shown here.

7.1.2 Microwave studio model (G. Romanov)

The MWS model of the HOM cavity connected to the accelerating cavity is shown in Figure 40. Using MWS, the HOM cavity dimensions were optimized to suppress the HOM modes while minimizing the effect on the fundamental. The initial HOM cavity dimensions came from the semi-analytic approximation discussed in the previous section. The optimized parameters are shown in Table 4 for a damping resistance of 21.875 Ω (Four 87.5 Ω resistors in parallel). In later MWS calculations, realistic resistor values are used: four 80 Ω resistors in parallel to give 20 Ω. Figure 40 illustrates the locations of these parameters. (Results are from 16_November_2016_2ndHarm.pptx).

Parameter	Description	Value (cm)
H_L	Cavity length	7.2
H_R_in	Inner radius	5.0
S_L	Coupling gap length	2.5
d_slot	Coupling gap width	1.0

S_R_in	See Figure 40	11.5
S_R_out	See Figure 40	12.5
H_R_out	See Figure 40	12.5
S_tip	See Figure 40	0.0

Table 4: The dimensions of the HOM cavity after optimization

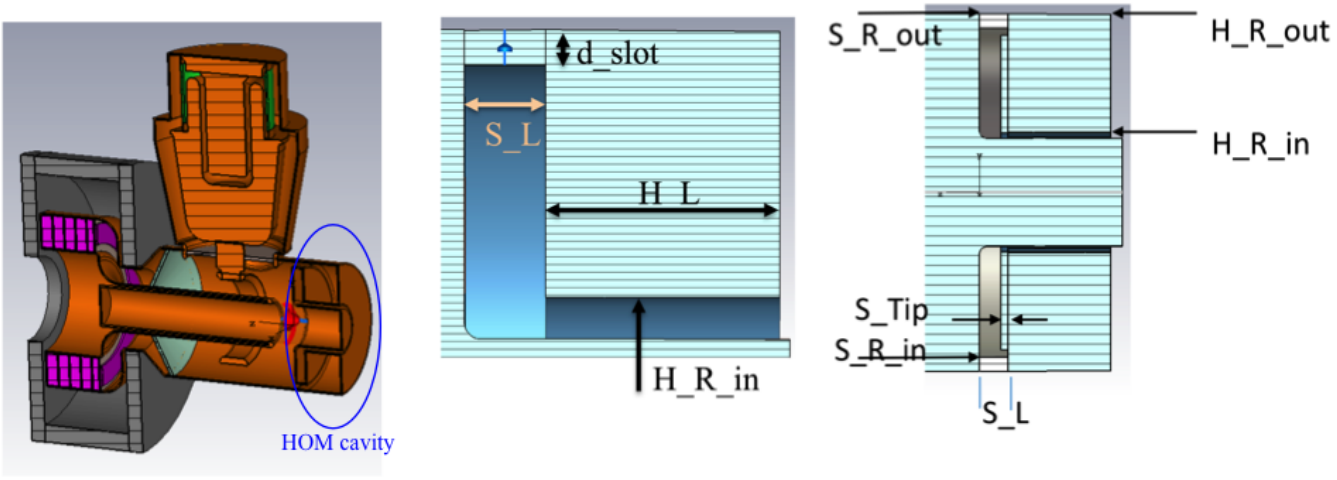

Figure 40: The HOM cavity is attached to the gap end of the cavity. The parameters shown in Table 4 to optimize the size of the HOM cavity are shown here.

The higher order modes of the cavity without the HOM cavity are calculated with two different MWS tube models and the semi-analytic model is shown in Figure 41. In all three cases

- The R/Q of the operating mode is almost the same in all three models.
- The HOMs associated with the tuner are nearly unchanged.
- The HOMs associated with the tube cavity go to higher frequency.
- The tube cavity provides additional damping of the HOMs.

The fundamental operating mode and HOM 1, 2 and 4 when the HOM cavity is connected (without damping resistors) are shown in Figure 42. These HOMs are well separated from the fundamental operating mode by >30 MHz and so do not interfere with the fundamental. However, the Q of the fundamental operating mode is lowered with the addition of the HOM cavity *without* damping resistors. Its impact is the greatest at the high frequency end where the Q is lowered by 10%. See Figure 43. The effect on the shunt impedance is minimal.

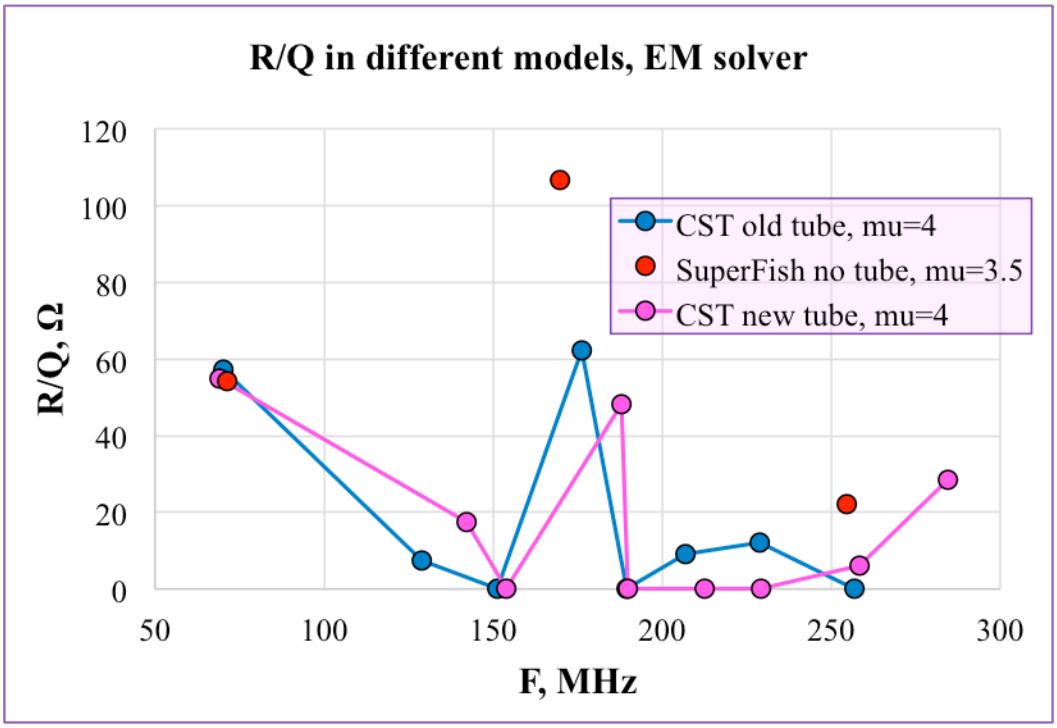

Figure 41: The R/Q of the cavity without the HOM cavity from three different models. Note: HOM 1 is not seen in the Superfish model.

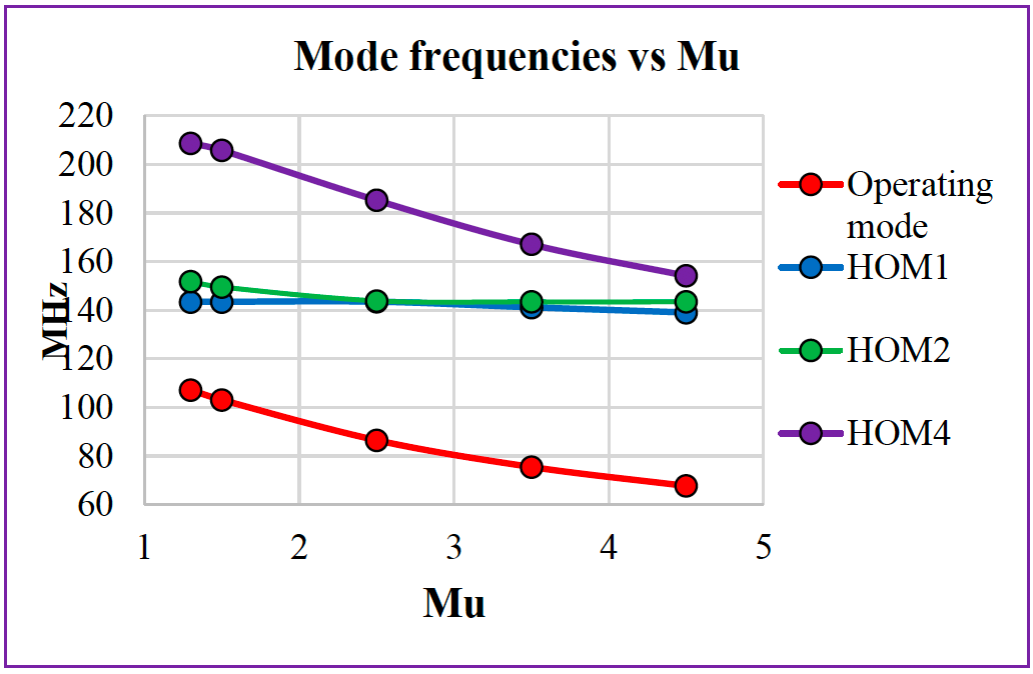

Figure 42: The behavior of the modes of the cavity with the HOM cavity without damping resistors.

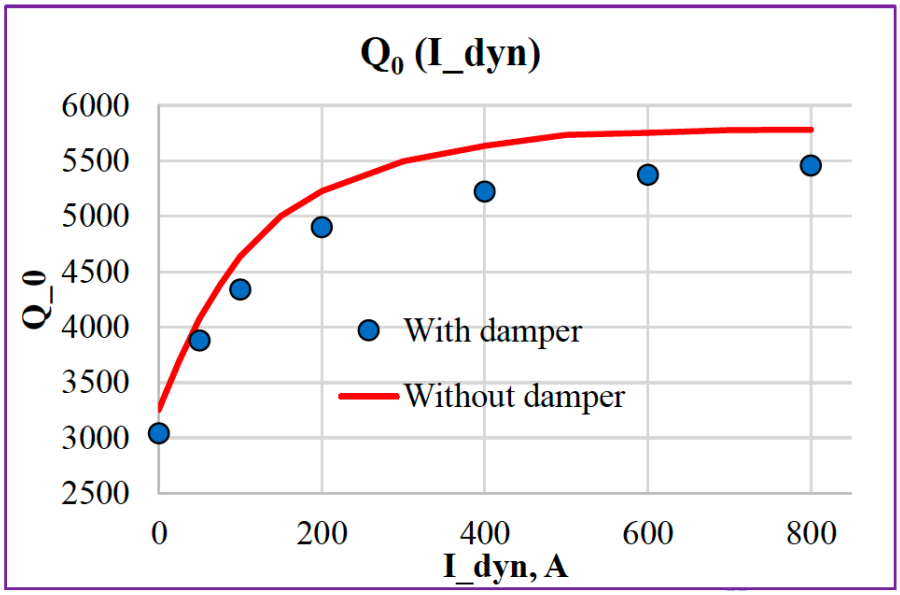

Figure 43: The Q of the cavity with and without the HOM cavity. Editor's note: The current required assumes 48 turns for AC and 11 turns for DC. See section 6.2.4.

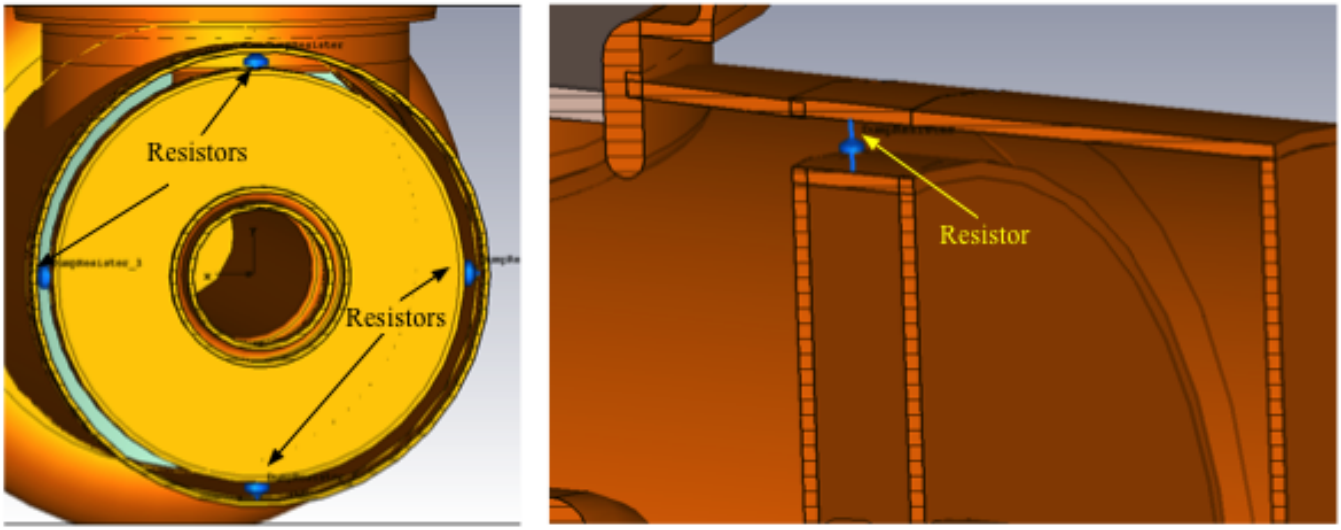

Figure 44: The location of the four damping resistors used in the MWS model. These four resistors are effectively in parallel.

The HOM mode that gives us the greatest concern is HOM 2 (HOM 1 is not seen in the Superfish calculation). When the damping resistance is 20 Ω (four 80 Ω in parallel shown in Figure 44), the impedance of HOM 2 seen at the MWS port at the accelerating gap is 2 kΩ while the fundamental is 12 kΩ. See Figure 45. The behavior of HOM 2 as a function of bias current is shown in Figure 46. **Editor's note: The current version of MWS Frequency Domain Solver seems to not calculate Q or the shunt**

impedance correctly with non-linear magnetic materials, like the garnet. This is why we are only plotting Z11 here. Z11 is the impedance seen at the MWS port at the accelerating gap. Z11 is not the shunt impedance.

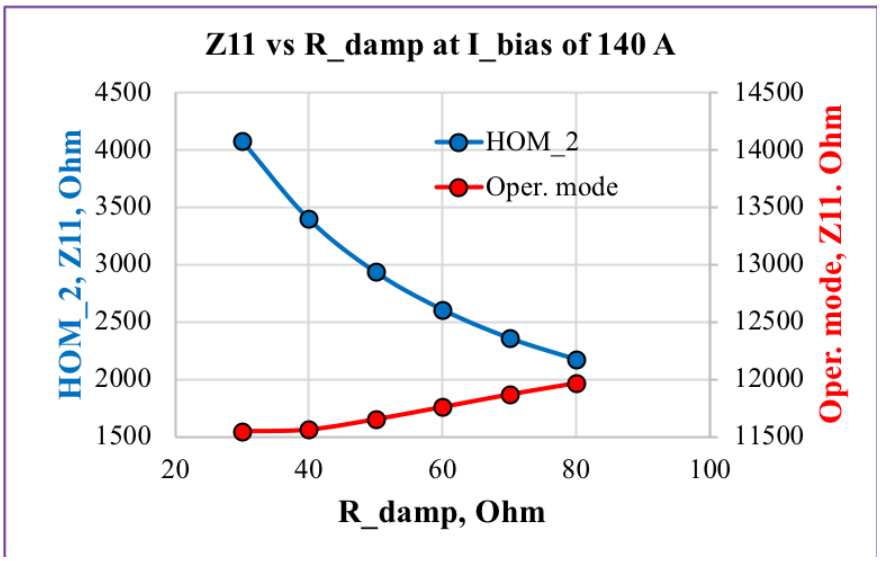

Figure 45: Optimizing the damping resistance. Z11 is the impedance seen by the MWS port at the accelerating gap. Z11 is not the shunt impedance.

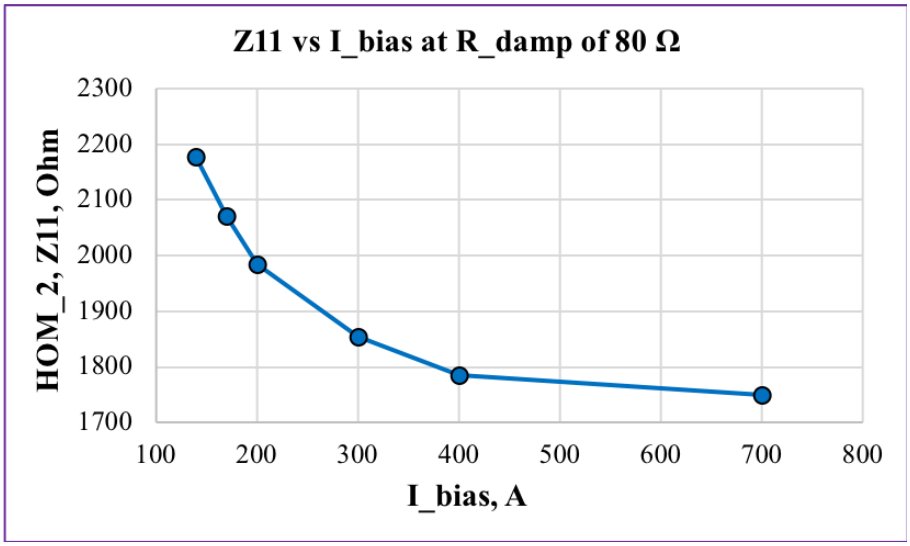

Figure 46: The behavior of HOM 2 seen at the pickup port as a function of the solenoid bias into 48 solenoid turns.

	No HOM cavity (Figure 47(a))			HOM cavity with 50 ohm terminations on HOM cavity (Figure 47(b))		
Mode	**Frequency (MHz)**	**Shunt impedance (kΩ)**	**Q**	**Frequency (MHz)**	**Shunt impedance (kΩ)**	**Q**
Fundamental	71.232	80.1	2544	71.224	80.7	1978
1	140.2	25.4	3895	140.1	25.7	1459
2	187.604	114.9	3608	187.43	117.5	282
3	262.3	3.5	3857	262.05	3.2	978

Table 5: Some modes and their properties with and without the HOM cavity. The excitation of the cavity in MWS uses the same pickup ports used for measurements that will be discussed in section 21.2. The garnet has uniform μ=4 and tan δ = 0.00026 in these simulations. Editor's note: MWS says that the shunt impedance does not depend on the load while the semi-analytic model claims otherwise.

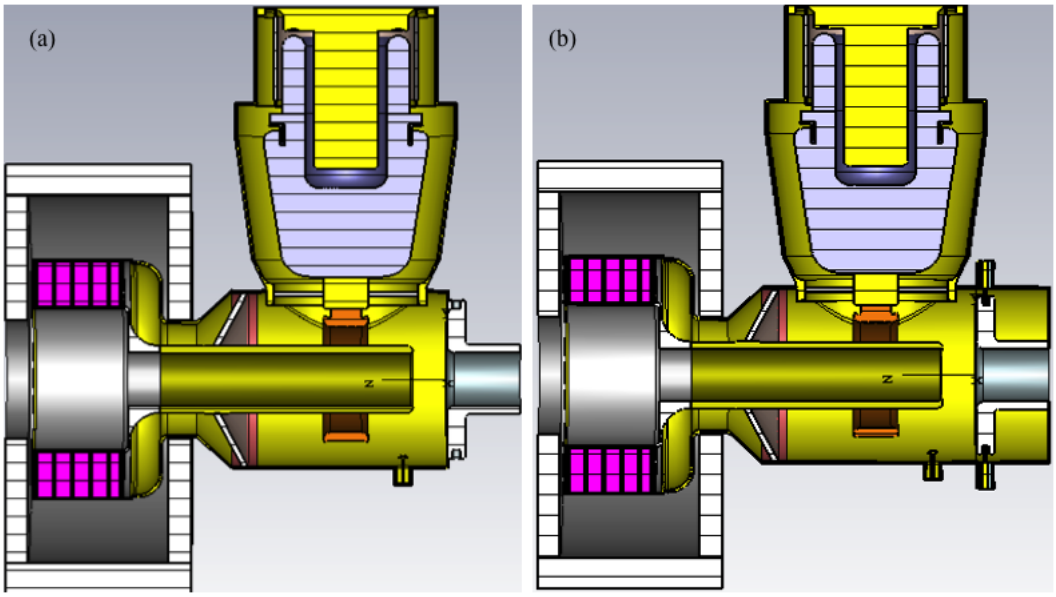

Figure 47: (a) The MWS model without the HOM cavity. (b) The MWS model with the HOM cavity and 50 Ω loads.

The results from Table 5 comes from MWS model files LindaSAT_FD_50_Ohms_20180824.cst and LindaSAT_FD_50_Ohms_20180826.cst.

7.1.3 HOM resistor power requirements (C.Y. Tan)

The details of this "back of the envelope" calculation can be found as a supporting document for this report [35].

The power that is dumped into the HOM resistor comes from the bunch train that is in Booster itself. This means that we have to consider how the how the charge is distributed in the bunch train that has 84 buckets. The most obvious way to do this is to consider δ-function bunches that have unequal charges circulating in Booster. In this case, it is trivial to show that for N δ-function bunches, with each having a charge q_k, for $k = 1, \ldots, N$ that the current, I, measured at any time t is give by

$$I(t) = \sum_{n=-\infty}^{\infty} \sum_{k=1}^{N=84} q_k \delta\left(t - nT_{\text{rev}} - (k-1)\frac{T_{\text{rev}}}{N}\right) = \frac{1}{T_{\text{rev}}} \sum_{n=-\infty}^{\infty} e^{in\omega_{\text{rev}}t} \sum_{k=1}^{N=84} q_k e^{-in(k-1)2\pi/N} \tag{10}$$

where T_{rev} is the revolution period and $\omega_{\text{rev}} = 2\pi/T_{\text{rev}}$ is the angular revolution frequency.

We note that Booster notches three of the 84 bunches for the transfer/abort kickers. We can easily take the notch into account by setting the charge $q_{82,83,84} = 0$. However, for simplicity, we will assume that all the bunches are filled with nearly the same amount of charge, i.e.

$$q_k = q_0(1 + \epsilon_k) \tag{11}$$

where $q_0 = Q_B/N$ if all the buckets are equally filled from a total charge of Q_B and ϵ_k is the variation parameter. Our requirement on ϵ_k is that

$$\sum_{k=1}^{N} \epsilon_k = 0 \tag{12}$$

so that Eq. (11) sums to the total charge, Q_B, that is in Booster.

When we substitute Eq. (11) into Eq. (10), we find that

$$I(t) = \frac{q_0}{T_{\text{RF}}} \sum_{p=-\infty}^{\infty} e^{ip\omega_{\text{RF}}t} + \frac{q_0}{T_{\text{rev}}} \sum_{n=-\infty}^{\infty} e^{in\omega_{\text{rev}}t} \sum_{k=1}^{N=84} \epsilon_k e^{-in(k-1)2\pi/N} \tag{13}$$

where $T_{\text{RF}} = NT_{\text{rev}}$ is the period of the fundamental RF, and $\omega_{\text{RF}} = 2\pi/T_{\text{RF}}$ is the angular RF frequency.

We can see from the above that the first sum is the contribution that comes from having Q_B equally distributed among all the bunches. The second sum gives me both the correction for having an unevenly filled bunch train and the size of the revolution harmonics that are also not multiples of the RF frequency.

7.1.3.1 Power dissipated from RF harmonics

The next step is to put in some numbers to calculate the expected power that will be dissipated in the HOM resistor. We will calculate the power loss from modes 1, 2, and 4 for the configuration where 6 dB attenuators are connected to the HOM cavity. Each 6 dB attenuator contributes 83.5 Ω to ground and so with four atttenuators, the total load in parallel is 20.875 Ω. The choice of an ~80 Ω load comes from the MWS results shown in section 7.1.2.

We will use the measured Q's and shunt impedances of modes 1, 2 and 4 in this calculation. Mode 3 should not be excited by the beam from our stretch wire measurements. Table 17 shows the required HOM parameters for this worst case back of the envelope calculation when 6 dB attenuators are used for the loads. Figure 48 shows the evolution of the HOMs during the ramp.

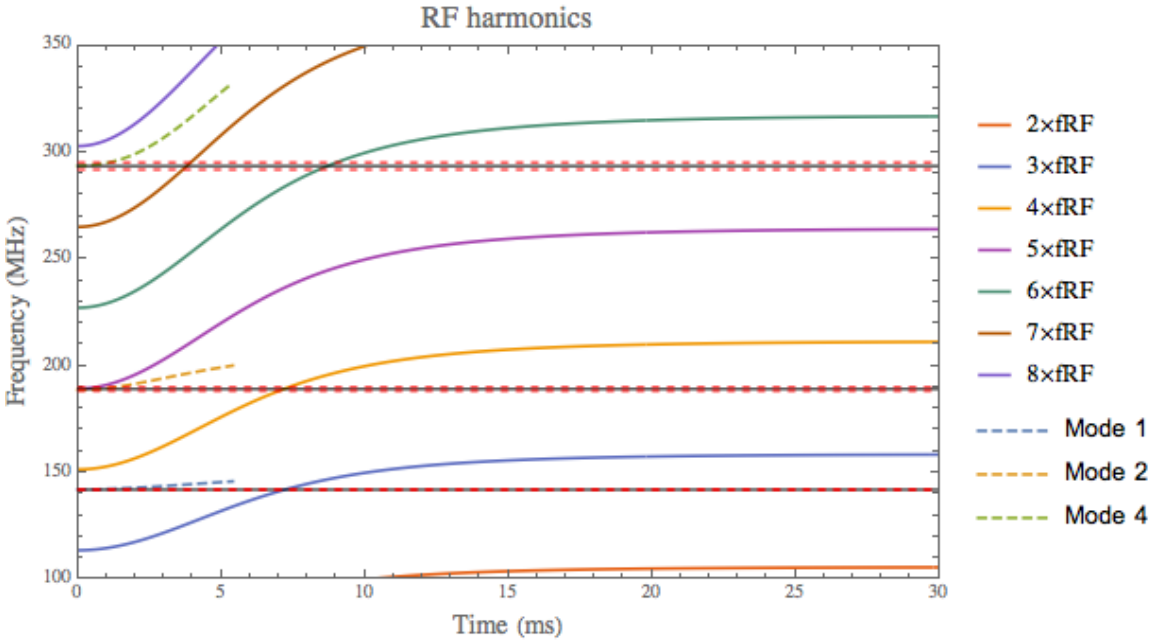

Figure 48: The measured modes (dashed lines) superimposed onto RF harmonics during the Booster ramp. The red dashed lines show the width of the mode if it is held constant during the ramp. The width is given by $\Delta f = \frac{f\text{res}}{Q}$ where $f$res is the resonant frequency of the mode and Q is the quality factor. Unfortunately, due to power supply constraints (see section 10.1), we can only measure the behavior of the modes up to about 5 ms (dashed lines that stop at around 5 ms).

We will perform a worst-case calculation. The following are our assumptions:

1. We will use the injection shunt impedance and Q of each HOM. These parameters improve as the bias is increased.
2. We will assume that $T_{\text{RF}} = 1/(53\ \text{MHz})$. This maximizes the amount of current in each RF harmonic.

3. The HOM modes are held at a constant frequency. This is a reasonable assumption for the worst case because it tells us that the modes cross the RF harmonics at most twice from Figure 48.
4. Each RF harmonic takes between 0.5 to 1 ms to cross the twice. We will use 1 ms for the total time for two crossings.

To calculate the power deposited into the HOM load resistor, we will use the first sum of Eq. (13). The current is simply the coefficient of this sum and it is

$$I_{\mathrm{RF}} = \frac{2q_0}{T_{\mathrm{RF}}} \tag{14}$$

where the "2" comes from the positive and negative frequencies in the first sum of Eq. (13).

Therefore, the static rms power for any HOM that the RF harmonic crosses is

$$P_{\mathrm{RF}} = \frac{I_{\mathrm{RF}}^2 R_s}{2} = 2\left(\frac{q_0}{T_{\mathrm{RF}}}\right)^2 R_s \tag{15}$$

For this static case, and by using the above assumptions for the worst case, we can calculate the power deposited into the load resistor when the number of protons in Booster is 6×10^{12} for each mode:

$$\left.\begin{aligned} P_{\mathrm{mode1}} &= 2\left(\frac{q_0}{T_{\mathrm{RF}}}\right)^2 R_s = 2\left(\frac{1.1 \times 10^{-8}\ \mathrm{C}}{1/(53 \times 10^6\ \mathrm{Hz})}\right)^2 \times (3700\ \Omega) = 2.7\ \mathrm{kW} \\ P_{\mathrm{mode2}} &= \left(\frac{q_0}{T_{\mathrm{RF}}}\right)^2 R_s = 2\left(\frac{1.1 \times 10^{-8}\ \mathrm{C}}{1/(53 \times 10^6\ \mathrm{Hz})}\right)^2 \times (6700\ \Omega) = 4.9\ \mathrm{kW} \\ P_{\mathrm{mode4}} &= \left(\frac{q_0}{T_{\mathrm{RF}}}\right)^2 R_s = 2\left(\frac{1.1 \times 10^{-8}\ \mathrm{C}}{1/(53 \times 10^6\ \mathrm{Hz})}\right)^2 \times (6300\ \Omega) = 4.6\ \mathrm{kW} \end{aligned}\right\} \tag{16}$$

because $q_0 = 6 \times 10^{12} \times 1.6 \times 10^{-19}/84 \ = 1.1 \times 10^{-8}$ C and "84" is the Booster harmonic number.

The above solution only applies to RF harmonics that that is sits on the HOMs indefinitely. To correct for this, we can zoom into Figure 48, and use the worst-case assumption of 1 ms crossings (point 3 and 4 above). We will assume 15 Hz ramps and so the duty factor is

$$\eta = (1 \times 10^{-3}\ \mathrm{s}) \times 15\ \mathrm{Hz} = 0.015 \tag{17}$$

Therefore, the power that is deposited into the HOM resistors in the worst case for this duty factor is

$$P_{RF}(1.5\%) = \eta(P_{\mathrm{mode1}} + P_{\mathrm{mode2}} + P_{\mathrm{mode4}}) = 0.015 \times (2.7 + 4.9 + 4.6)\ \mathrm{kW} = 183\ \mathrm{W} \tag{18}$$

If the HOMs are 4-fold symmetric, then $P_{RF}(1.5\%)$ equally divides among the four HOM load resistors. This means that each resistor sees 45 W. However, if the HOM modes are all dipole modes then the power is divided into two resistors and is about 90 W. Thus 150 W load resistors should be more than sufficient for our purposes.

7.1.3.2 Power dissipated from revolution harmonics

The contribution of power from the revolution harmonics come from the double sum of Eq. (13)

$$I_\epsilon(t) = \frac{q_0}{T_{\text{rev}}} \sum_{n=-\infty}^{\infty} e^{in\omega_{\text{rev}}t} \sum_{k=1}^{N=84} \epsilon_k e^{-in(k-1)2\pi/N} \tag{19}$$

which in general can only be calculated numerically. However, we can consider a special case by looking at the nth revolution harmonic. It has the following strength

$$I_\epsilon(n) = \frac{q_0}{T_{\text{rev}}} \sum_{k=1}^{N=84} \epsilon_k e^{-in(k-1)2\pi/N} \tag{20}$$

Let us consider the special case where $|\epsilon_k| = \varepsilon$, this means that

$$I_\epsilon(n) = \frac{q_0}{T_{\text{rev}}} \varepsilon \sum_{k=1}^{N=84} \mathcal{P}_k e^{-in(k-1)2\pi/N} \tag{21}$$

Where we have introduced $\mathcal{P}_k$ that has a 50/50 chance for being either -1 or $+1$ with the requirement that $\sum_{k=1}^{N} \mathcal{P}_k = 0$ because of Eq. (12).

For $n = pN$, i.e. RF harmonics, it is easy to show that $I_\epsilon(pN) = 0$. This means that there are no corrections to the strengths of the δ-functions of the RF harmonics.

For the remaining revolution harmonics, in principle, the only way to calculate the value of I_ϵ by numerical methods. However, since every injection into Booster has a different current distribution, we can use this information to find the average power from an infinite number of injections. This average power will be the power requirement for the HOM resistor contributed by the revolution harmonics.

Let us define a new variable $J_n = \frac{q_0}{T_{\text{rev}}} \varepsilon \sum_{k=1}^{N=84} \mathcal{P}_k e^{-in(k-1)2\pi/N} = |J_n| e^{i\theta_n}$, we can show that the rms power is given by (see the supporting document [35] for the derivation)

$$P_{\text{harmonics}} = \frac{N}{2} \left(\frac{q_0}{T_{\text{rev}}}\right)^2 \varepsilon^2 \sum_{n=-\infty}^{+\infty} \text{Re}[Z(n\omega_{\text{rev}})] \tag{22}$$

where $Z(\omega)$ is the shunt impedance of the chosen HOM. We have modeled $Z(\omega)$ as an RLC circuit. There is sufficient information given in Table 17 to calculate the inductance and capacitance of the HOM.

We have numerically calculated for a constant variation $\varepsilon = 10\%$, and $q_0 = 6 \times 10^{12} \times 1.6 \times 10^{-19}/84 \ = 1.1 \times 10^{-8}$ C, that the power contributed by the revolution harmonics for an infinite number of turns averaged over an infinite number of injections is less than 1 W. Therefore, the contribution to the heat load is small from revolution harmonics. Thus, the earlier statement that 150 W loads are more than sufficient for the HOM load still applies.

Figure 49: Two different styles of 150 W, 6 dB attenuators (API/Weinschel) that will be used as loads for the HOM cavity.

7.2 Y567B load lines (C.Y. Tan)

In order to drive the cavity, we have to check that the impedance seen by the Y567B is within its range so that it can power it efficiently. In our setup, the Y567B is in the "grounded grid" configuration for powering the cavity. It is also operated approximately as a class B amplifier. Our analysis of the power efficiency comes from Carter [36, 37]. We will assume that the tube is operated as a class B amplifier in the following analysis. And, in this operating mode, the best-case theoretical amplifier efficiency is 75% where power efficiency is defined to be the ratio P_{rf}/P_{DC}, and P_{rf} is the power going into the wanted RF part of the half sine wave and P_{DC} is the power going into the DC component of the half-sine wave.

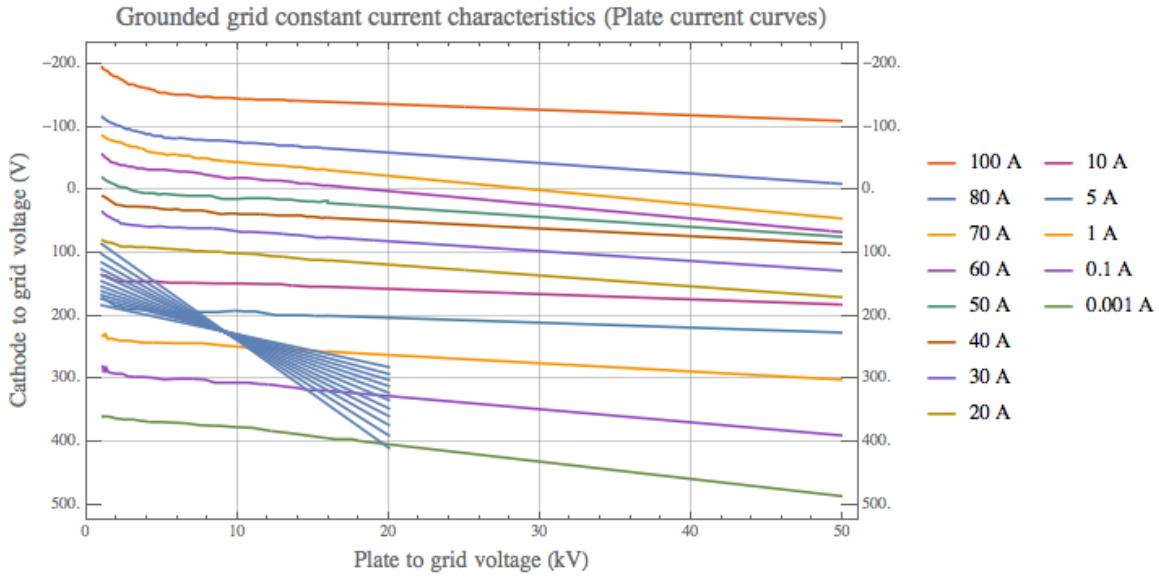

Figure 50: A set of load lines (blue) is plotted against the grounded grid constant current curves of the Y567B.

We determine the required anode voltage from the tube to get 100 kV gap voltage with the step up ratios shown in Figure 25. (Note: At the time when this calculation was made, the MWS model was not mature enough to be used and so the TLM was used instead. The final results from MWS shown in Figure 35 for the anode impedance and the step up ratios are close enough to the TLD model that a recalculation was not done.) We increase the required voltage by 1 kV to take into account the screen voltage. We then use the anode voltage and the power loss (shown in Figure 26) and 75% power efficiency to calculate the anode current. From here, we multiply the anode current by 4 (rather than π to take into account non-linearities of the tube) to obtain the peak anode current.

Using the method described by Carter, we use the peak current found above, minimum cathode to grid bias of 250 V, minimum anode voltage of 1 kV, to get the end points of the load lines. An example

of load lines that we have used the data from Figure 25 and Figure 26 is plotted against the grounded grid constant current characteristic curves of the Y567B is shown in Figure 50. And from these load lines, we can calculate the tube efficiency as a function of anode impedance shown in Figure 51. As we can see from this figure, the tube is most efficient at 1.3 kΩ, i.e. at injection. This is exactly where we would want the highest tube efficiency because this is where the tube is required to output the highest power. Therefore, from these calculations, the Y567B is able to drive our cavity because the power required is always $<$ 50 kW for the entire frequency range.

There are two observations that we would like to point out:

1. The anode impedances calculated by the load lines are different compared to the TL model at high frequency. For example at 110 MHz, the anode impedance calculated by the load lines method gives 5.5 kΩ while the TL model gives 7.5 kΩ. However, at 76 MHz the results are much closer: the load lines method gives 1.1 kΩ and the TL model gives 1.2 kΩ.
2. The anode impedance does not only determine the efficiency. The efficiency also depends on the step up ratio, and thus the value of the anode voltage and current. Therefore, it is insufficient to just specify the anode impedance to have an idea of what the efficiency is, i.e. the anode voltage also matters.

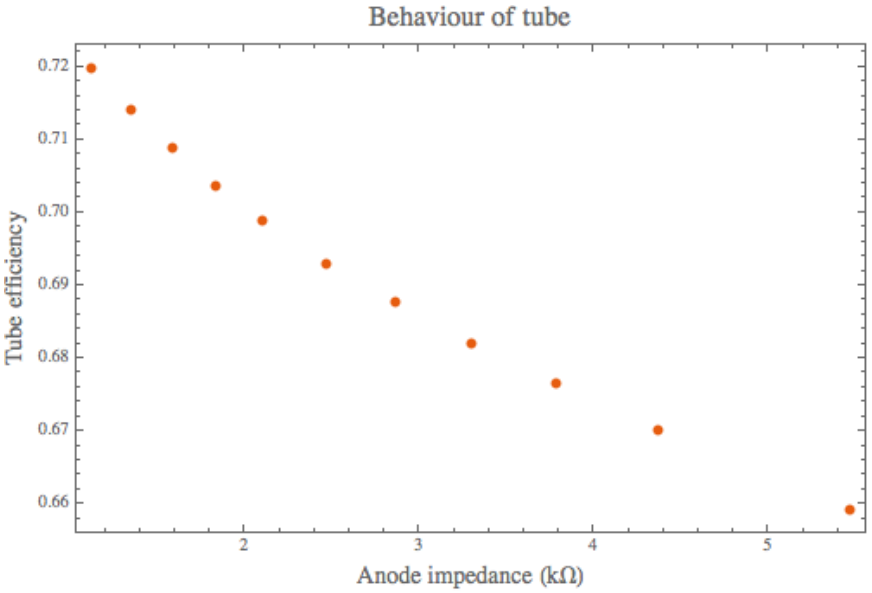

Figure 51: The tube efficiency as a function of anode impedance.

8 Tuner (I. Terechkine, G. Romanov)

The accelerating cavity is loaded with garnet which is a gyromagnetic material. The permeability of the garnet is a function of the bias magnetic field. The part of the cavity that is the garnet is placed within the bias magnetic system is called the tuner. Five garnet rings with a specially shaped shim piece form the tuner stack. The shim piece is there to improve the bias magnetic field uniformity at the transition between the loaded and unloaded parts of the transmission line. Each of the 21 mm thick garnet rings have a thin alumina ring glued to it, while the 16 mm thick garnet ring has two thin alumina rings glued to it. The alumina rings enable the heat that is generated by the RF to be conducted out to the shell of the tuner. The shell of the tuner is copper plated stainless steel with water cooling pipes brazed to it. The thickness of the shell and the thickness of the copper coating has been chosen to reduce eddy currents without compromising the RF properties of the cavity. Figure 52 shows a cross-sectional view of the tuner assembly.

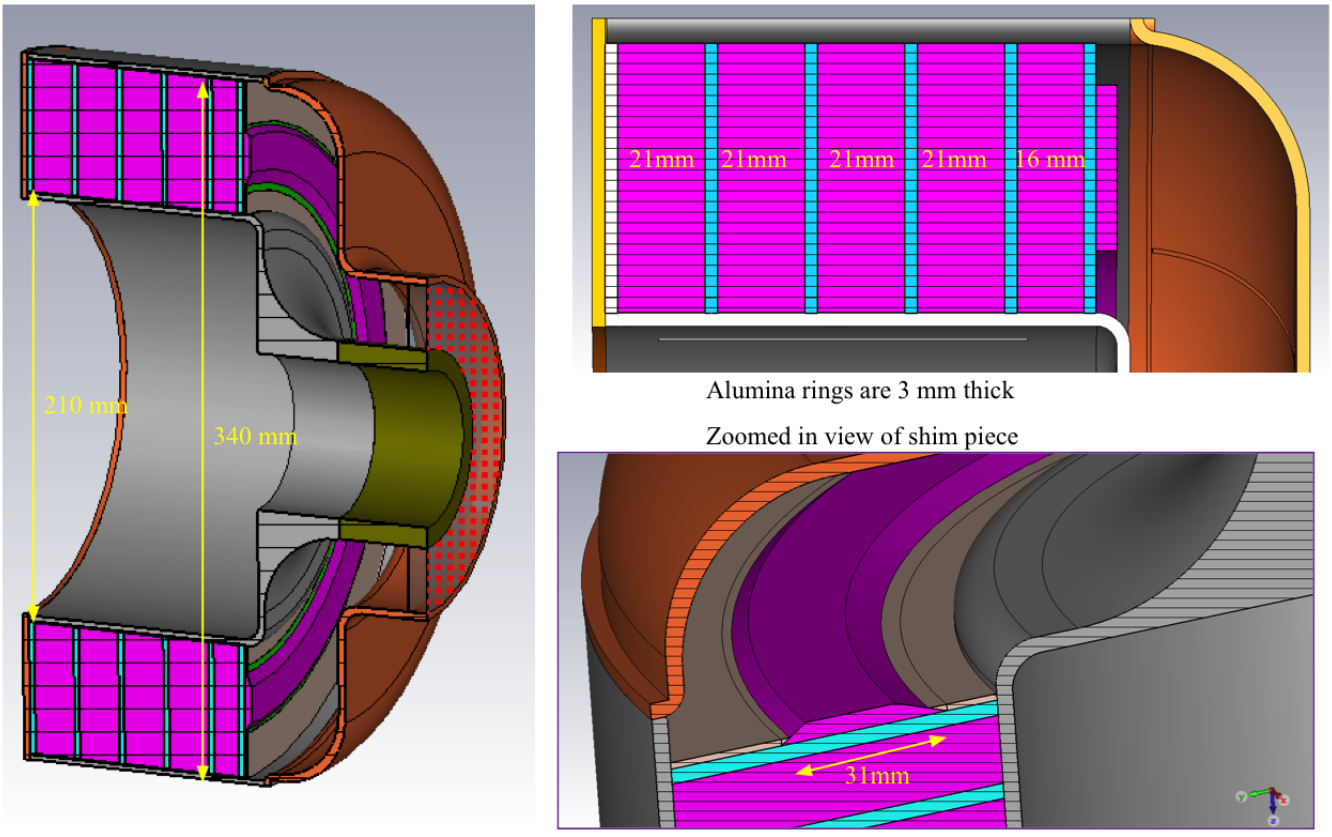

Figure 52: The tuner assembly consists of 5 garnet rings that are glued to an alumina substrate and a specially shaped shim piece. The shell is made of copper plated stainless steel with slits to reduce eddy currents.

8.1 Garnet ring

Each garnet ring is made of 8 sectors of garnet glued together and then glued onto an alumina substrate. See Figure 53. The reason why the ring cannot be made as one contiguous piece of garnet is because currently (as of 2016), the only known vendor for garnets, National Magnetics, does not have a large enough oven to make anything bigger.

For quality assurance, each garnet sector is accompanied with a witness piece. Every witness piece and ring undergoes RF tests. The results of these tests will be discussed in section 16.

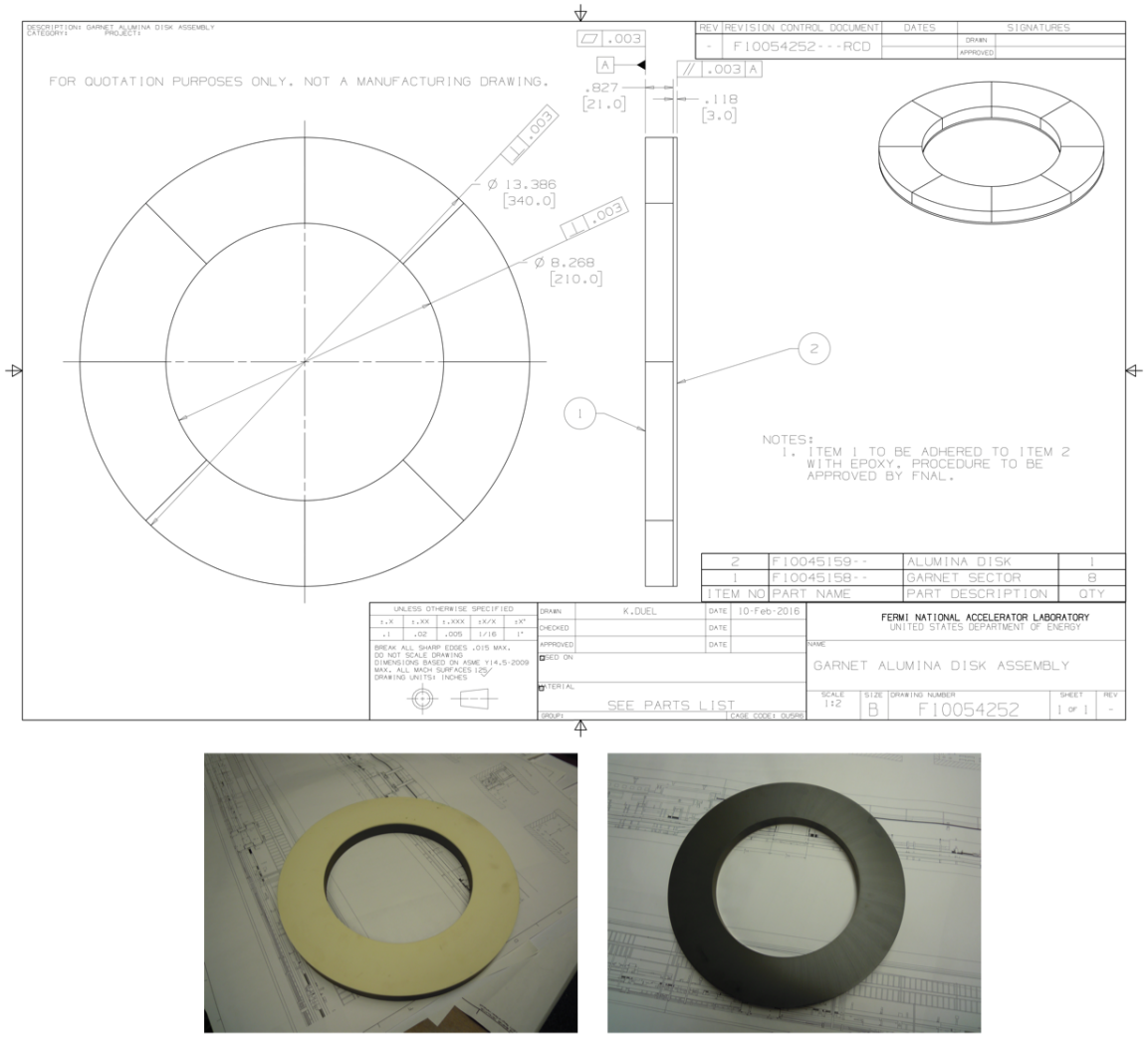

Figure 53: Each garnet ring is made from 8 sectors of garnet glued together and then glued onto an alumina substrate.

8.1.1 Stycast 2850FT epoxy

The epoxy used to glue the ring together is Stycast 2850FT [22]. The procedure for gluing the garnet sectors together is detailed in section 17.1.1. The RF properties of Stycast have been measured and was discussed in section 5.

8.2 Shim

A shim ring has been added to the front of the tuner stack to improve the bias magnetic field uniformity at the transition between the loaded and unloaded parts of the tuner [38]. The shim ring like the garnet ring, is made of 8 sectors of garnet glued to an alumina substrate. See Figure 54.

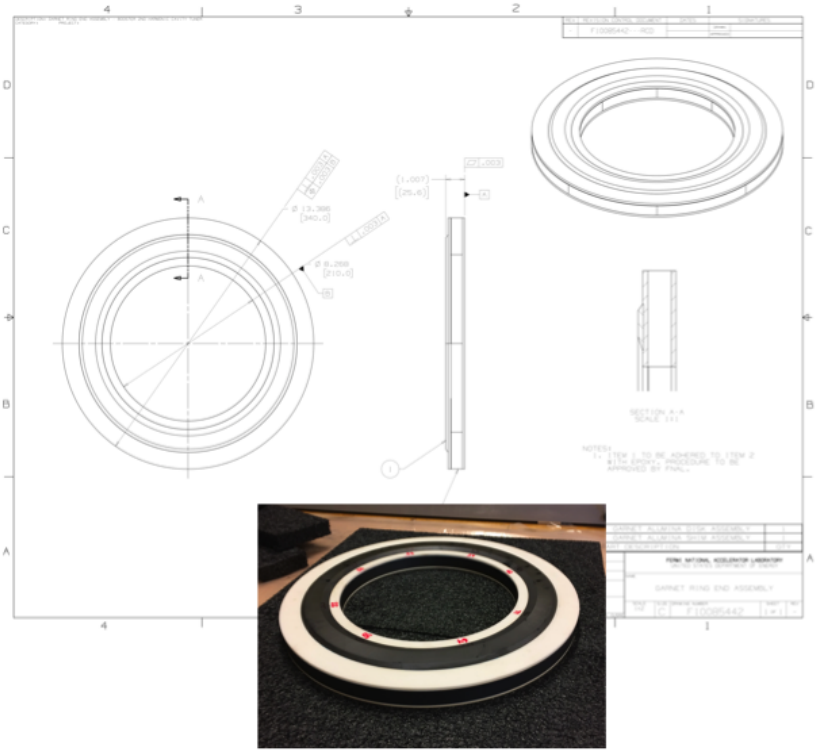

Figure 54: The shim ring consists of 8 sectors of garnet glued onto two alumina rings. A shim alumina ring is glued to the top surface.

8.3 RF thermal analysis

The region where there is high RF power loss is closely associated with the regions where the bias magnetic field is at its weakest. From our simulations, the transition region between the loaded and unloaded transmission line is where there is a sharp increase in the complex magnetic permeability. There are several ways to improve the field quality at the transition. The option that is chosen is to add a shim on this transition surface. The result of adding a shim to the tuner greatly improves the uniformity of the field in the tuner as shown in Figure 55.

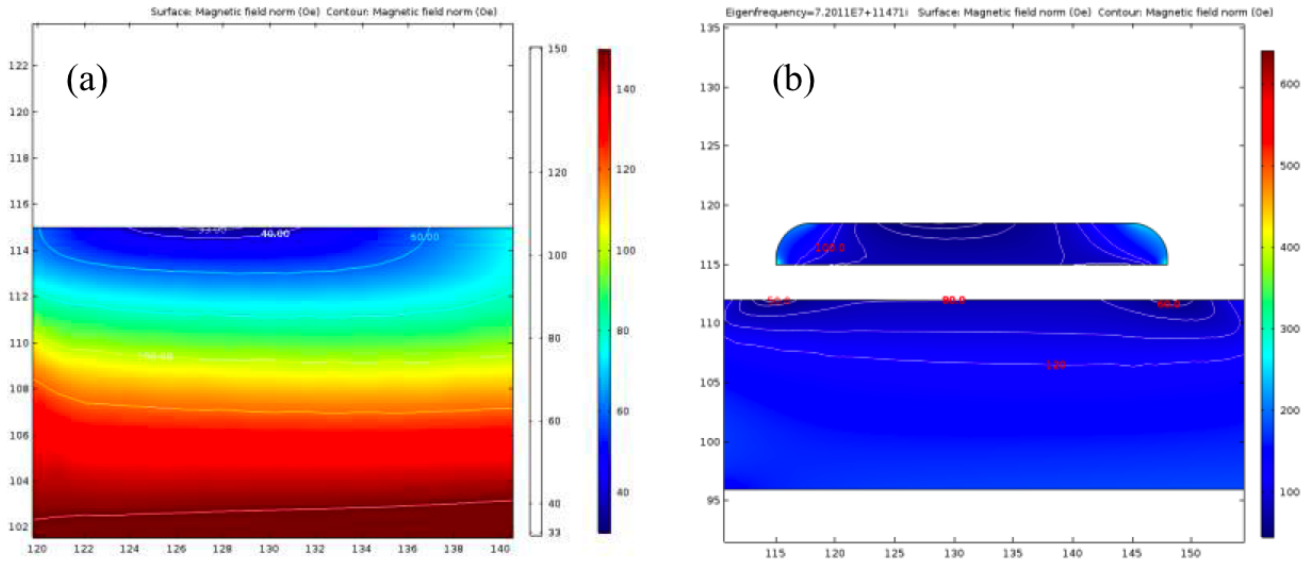

Figure 55: The magnetic field density and contour plots in the tuner (a) without the shim and (b) with the shim. It is clear from these results that the magnetic field is a lot more uniform when the shim is added.

If we call the garnet at the transition surface the top ring, then due to the lower power loss on the top surface with the addition of the shim ring, its thickness of the top ring has been increased from 13.5 mm (without the shim ring) to 16 mm. The rest of the rings are 21 mm thick.

There are two 3 ms intervals of interest during the ramp: injection and transition where the gap voltage is at 100 kV. See Figure 7. The power dissipation in the top ring during these two active intervals are shown in Figure 56. The time averaged heat deposition is ~300 W during injection and ~115 W during transition. Thus, thus the total heat dissipated is ~415 W. For the shim, the heat deposition is 21 W during injection and 15 W during transition. This gives a total of 36 W.

To evaluate the temperature in the top portion of the tuner, we have to use the average power density distribution in those parts of the tuner. The RF power loss density in the top two alumina rings and the RF losses at the top of the tuner stack are shown in Figure 57.

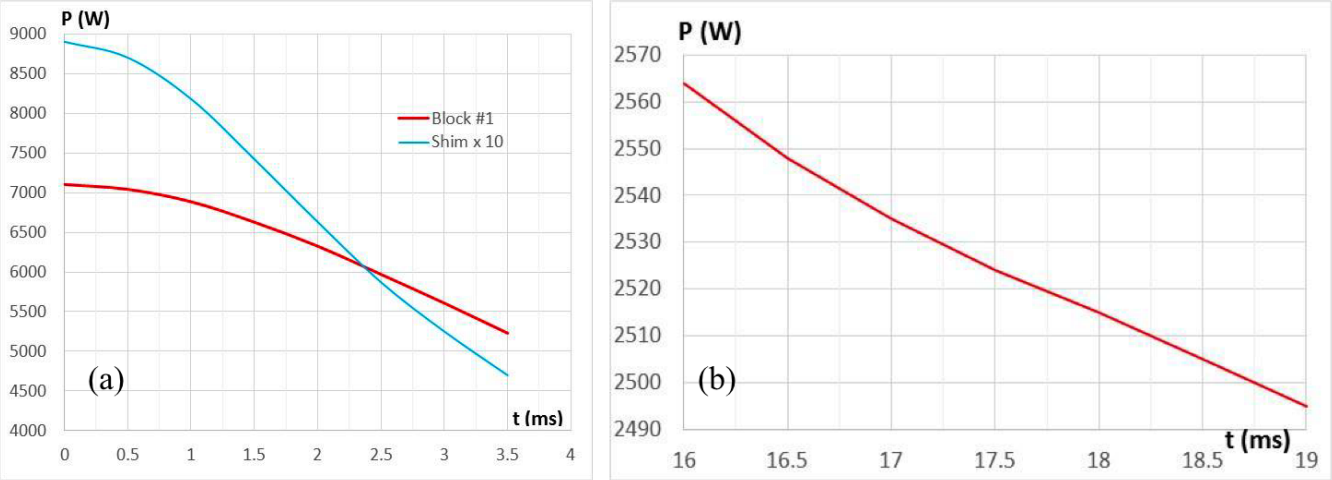

Figure 56: The power dissipated in (a) the top ring and shim during injection and (b) in the top ring during transition.

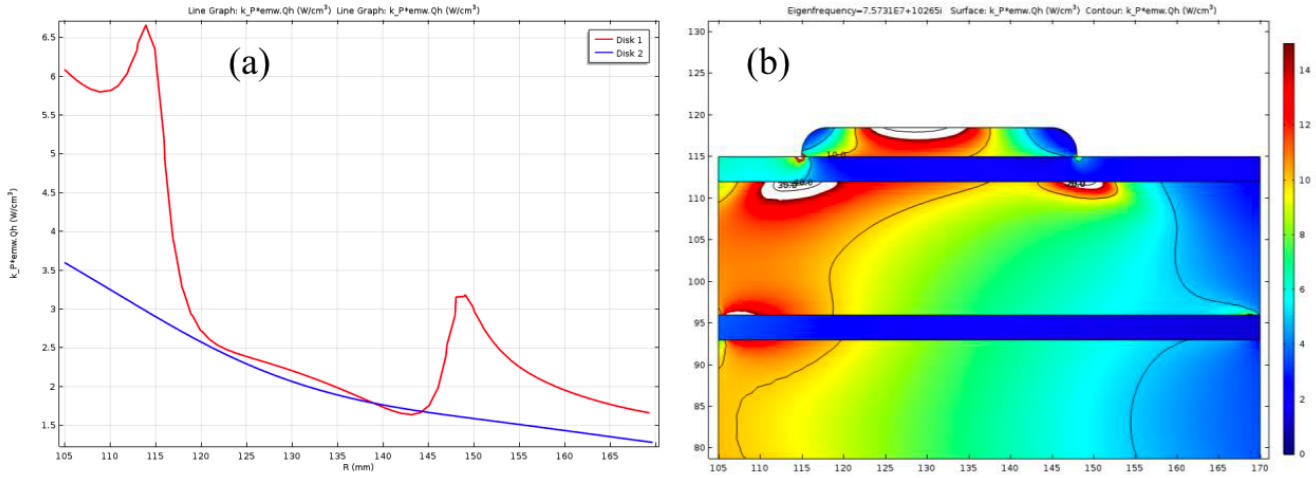

Figure 57: (a) The RF power loss density in the top two alumina rings and (b) the density map of the RF losses at the top of the tuner.

The temperature distribution map of the top part of the tuner with and without thermal contact on the inner and outer cylindrical surfaces are shown in Figure 58. The details of how these maps were created from the power loss distribution can be found in Ref. [38]. The maximum temperature rise is 49°C without thermal contact for the garnet rings but thermal contact for the alumina rings. And it is 44°C when there is contact on both the garnet and alumina rings.

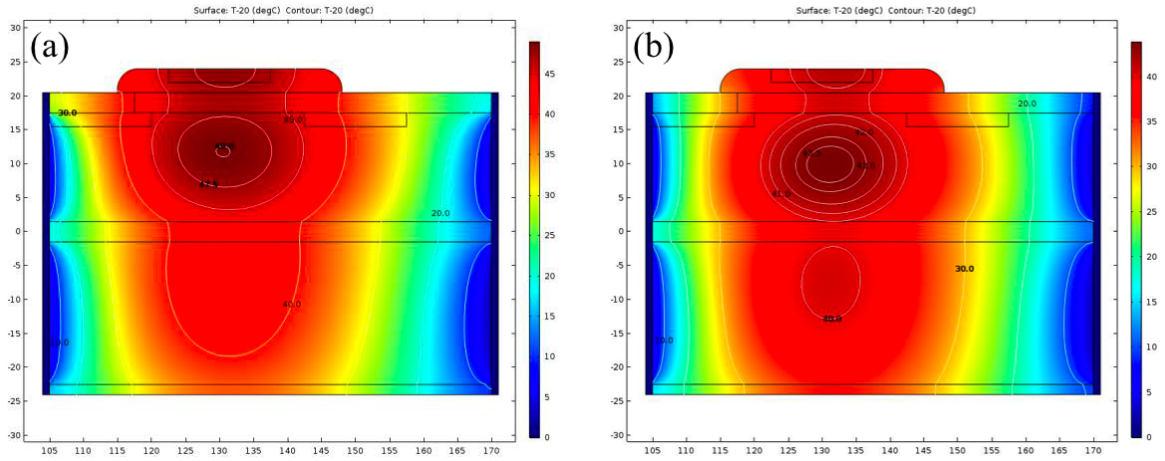

Figure 58: The temperature map when (a) the garnet ring does not have thermal contact with the walls both the inner and outer cylindrical surfaces while the alumina rings do; (b) all both the garnet and alumina rings have thermal contact. The maximum temperature is lowered by 5°C between cases (a) and (b).

8.4 Optimizing the shape of the shim

Although a rounded shim with straight edges was used in the thermal analysis in the previous section, we found that there is anomalous heating of the top alumina disk. Our analysis showed that this was due to an elevated electric field between the shim and the inner electrode of the cavity. Figure 59 shows the static RF power loss density in the alumina (a) and the values of the electric field in the area (b).

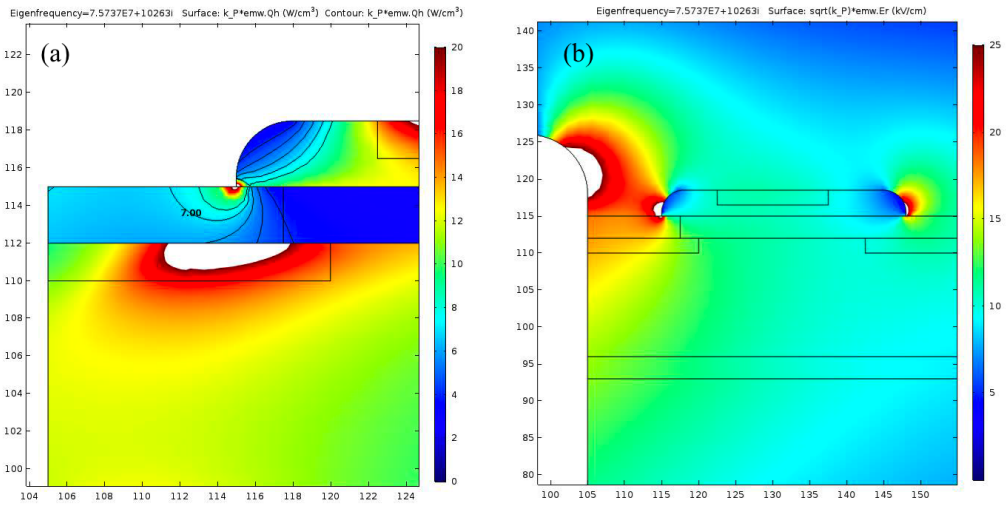

Figure 59: (a) RF power loss density and (b) the electric field.

The maximum value of the radial component of the electric field on the surface of the alumina at the triple point is ~40 kV/cm. However, this value can be reduced to 27.5 kV/m by simply reshaping the shim. An added advantage after the modification is that the minimum bias magnetic field is slightly increased from 67.3 Oe to 69.3 Oe and the localized permeability decreased from 12 to 11.75. Figure 60 shows the before and after results.

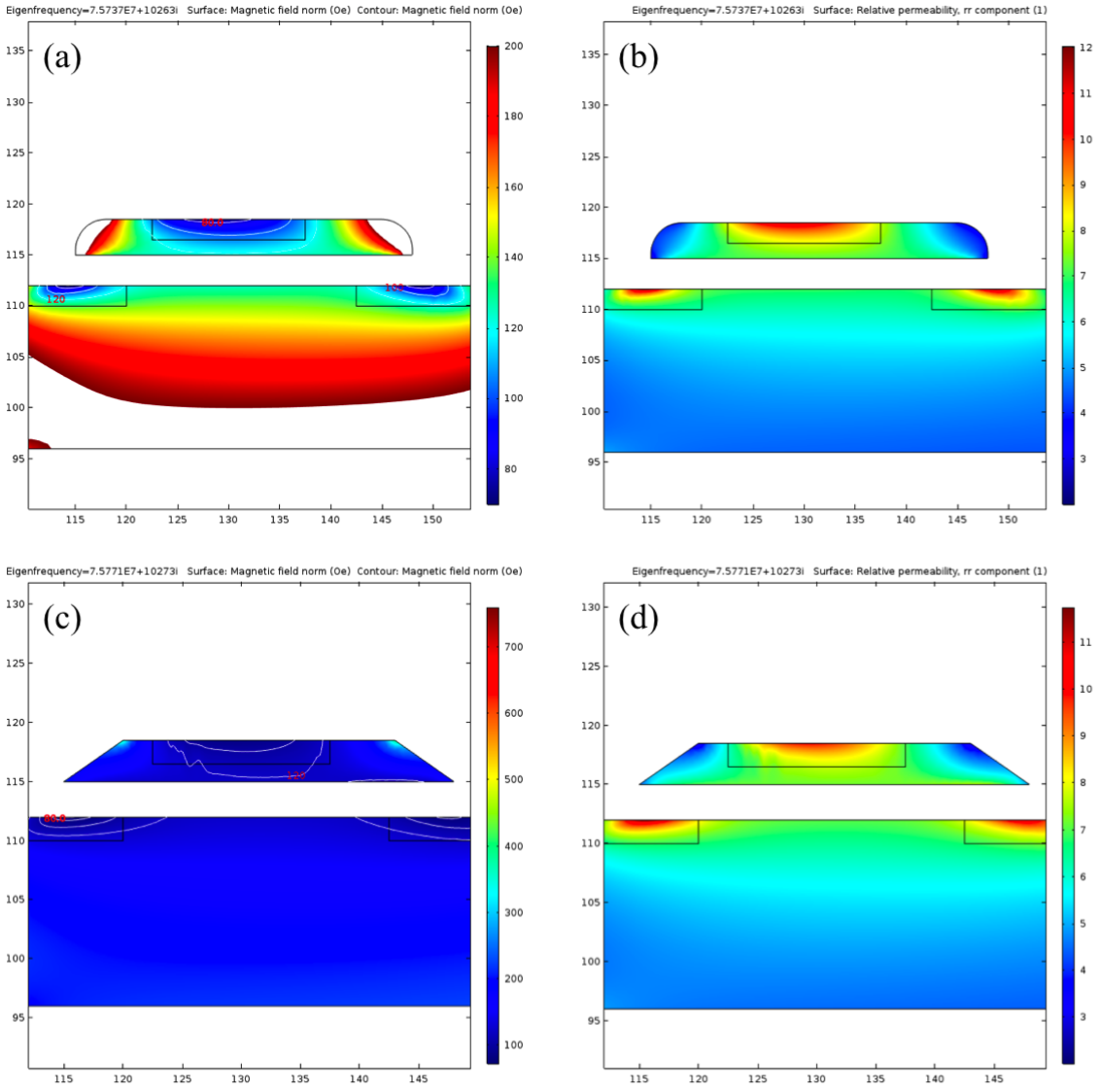

Figure 60: (a) and (b) show the magnetic field density and the relative permeability of the top of the tuner stack with a rounded shim. (c) and (d) shows the same plots for an angled shim.

8.4.1 Total RF power loss

The total RF power loss in the tuner for the ramp shown in Figure 7 (injection and transition with two 3 ms pulses) has been evaluated. It is about 3 kW. Details of the calculation can be found in Ref. [39].

8.5 Thermal grease

Thin layers of thermal grease will be applied between all contact surfaces in the tuner stack. The grease that will be used is Super Thermal Grease II 8616 [23] which is a mixture of alumina and zinc oxide suspended in non-silicon based oil. We chose this grease because

1. It has acceptable thermal conductivity of 1.78 W/m·K.
2. It has a high dielectric constant of 6.77 at 1 kHz. The high dielectric constant is desirable because the grease will be used to fill in the air gaps between copper and garnet or copper and alumina which reduces the electric field at the triple points of contact. Its dielectric property at our frequency of interest has been measured and was discussed in section 5.
3. It does not contain silicon which can contribute to mixed waste in a radioactive environment.

Its RF properties in our frequency of interest were measured and was discussed in section 5.

8.6 Eddy currents

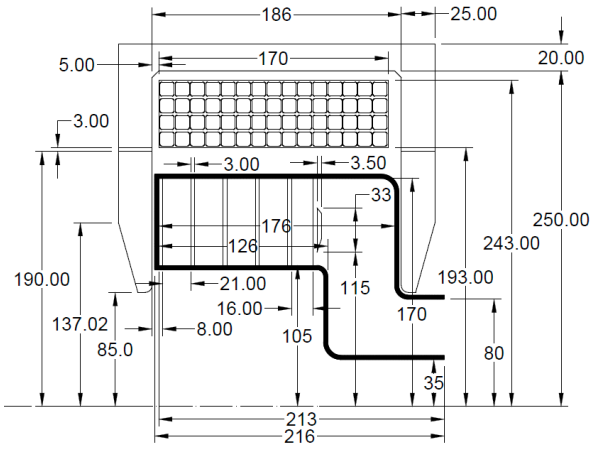

Figure 61: This is the solenoid geometry used in the 2D analysis. Note: This is not the final solenoid design.

The details of the Eddy current analysis can be found in Ref. [40]. **Warning: This analysis was done before the solenoid design was finalized. In this study, the solenoid has 50 turns rather than 60 turns as in the as-built solenoid.** Nonetheless the results apply for how the tuner shell should be made.

The solenoid and tuner geometry that is used in this analysis is shown in Figure 61. A simplified current pulse for this study is shown in Figure 62. In this study, We will assume that the solenoid has 50 turns and has this current pulse at a repetition rate of 15 Hz.

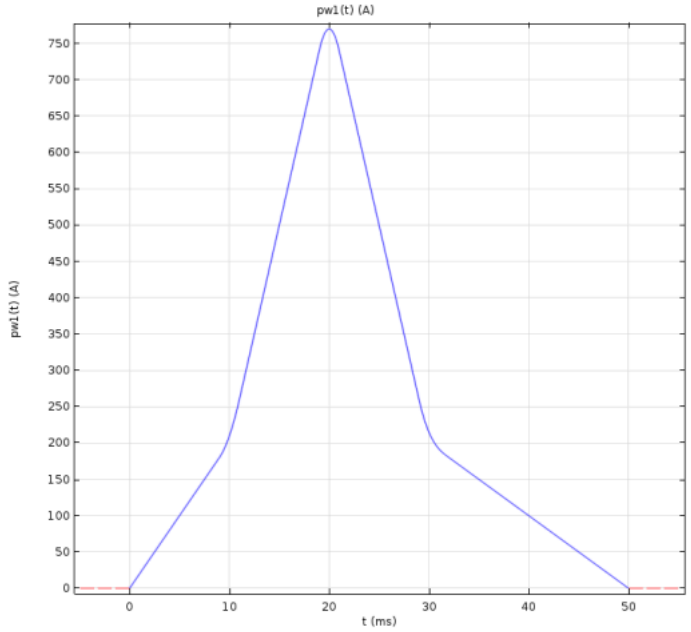

Figure 62: This is the simplified current pulse sued for the Eddy current impact study. In this study the number of solenoid turns used is 50.

The bias current pulse has been designed so that at injection, it is 168 A for the cavity to have a resonant frequency of 75.7 MHz. To reach the injection state, a "setting" current ramp is used with a ramp rate of 20 A/ms. After injection, the maximum current ramp rate is 60 A/ms. After the transition period, which ends at 19 ms, the current is brought back to zero before the next accelerating cycle. The ramp down rate is also 60 A/ms.

In the conceptual design of the tuner, the shell is made of 3 mm thick stainless steel with a 25 μm thick copper coating. Our 2D simulations of the Eddy current impact analysis concludes that the shell is magnetically semi-transparent. The Eddy current in the shell reaches 1200 A, which is about 14% of the total current turns at injection ($168\ \text{A} \times 50\ \text{turns} = 8400\ \text{A turns}$). The average heat generated in the shell with this current ramp can reach about 1.5 kW with most of the heat deposited in the outer part of the shell.

Besides heating, the Eddy current in the shell changes the spatial distribution of the bias magnetic field inside the tuner. Thus, both the redistribution of the bias magnetic field and the heating complicates the design of the cooling for the shell. The most natural way for increasing the

transparency of the shell to the changing magnetic field and decreasing the power loss is to interrupt the azimuthal component of the current flow by adding longitudinal slots to the shell. This analysis requires the use of a 3D model.

8.6.1 3D model

The geometry of the RF shell used for the 3D Eddy current impact analysis is shown in Figure 63. Although there are more design features than that used in the 2D model shown in Figure 61, this geometry is still simplified but captures the needed details for the Eddy current analysis. We will not consider RF performance at this stage.

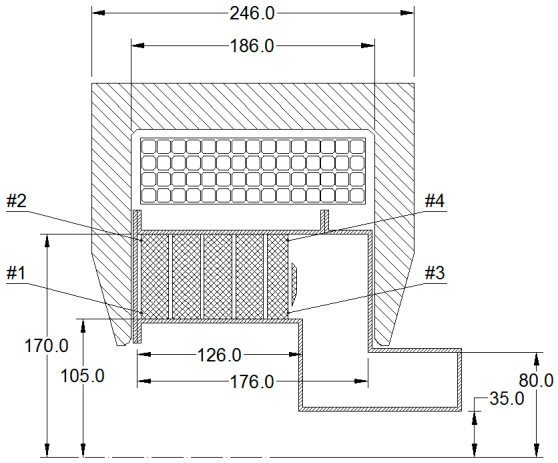

Figure 63: The geometry of the tuner and solenoid used for the 3D study. Note: This is not the final solenoid design.

We have found that the most challenging part of the accelerating cycle is at injection [39]. During this time, the bias magnetic field in the garnet can get dangerously close to the gyromagnetic resonance. Therefore, we will only study this part of the cycle. The results at injection can be used to evaluate the impact of the Eddy currents for the entire accelerating cycle because the bias current ramp rate reaches its maximum here. Figure 64 shows the bias current that we have constructed to ensure that we have the required frequency ramp for the tuner at injection only.

The 3D simulations discussed in Ref. [40] show that by splitting the tuner shell into four insulated sectors, the azimuthal component of the Eddy current is interrupted. In Figure 65, we show the current flow before and after segmentation. The new current flow pattern tells us how to add longitudinal slots to the shell if needed. When we add these slots, it will have to be done without disturbing the TEM-type mode in the tuner and compromising the structural integrity of the shell.

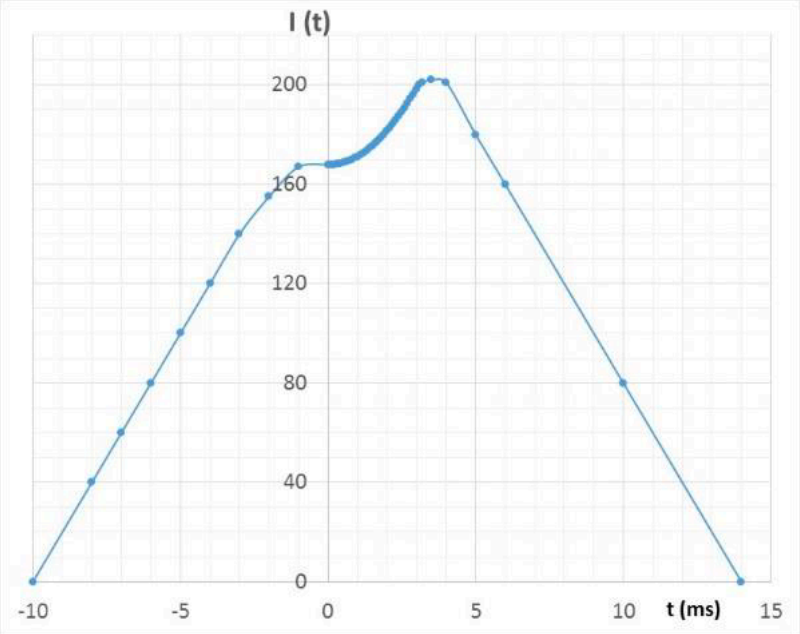

Figure 64: The current time profile for injection only. The darker part of the curve is the region where beam injection occurs.

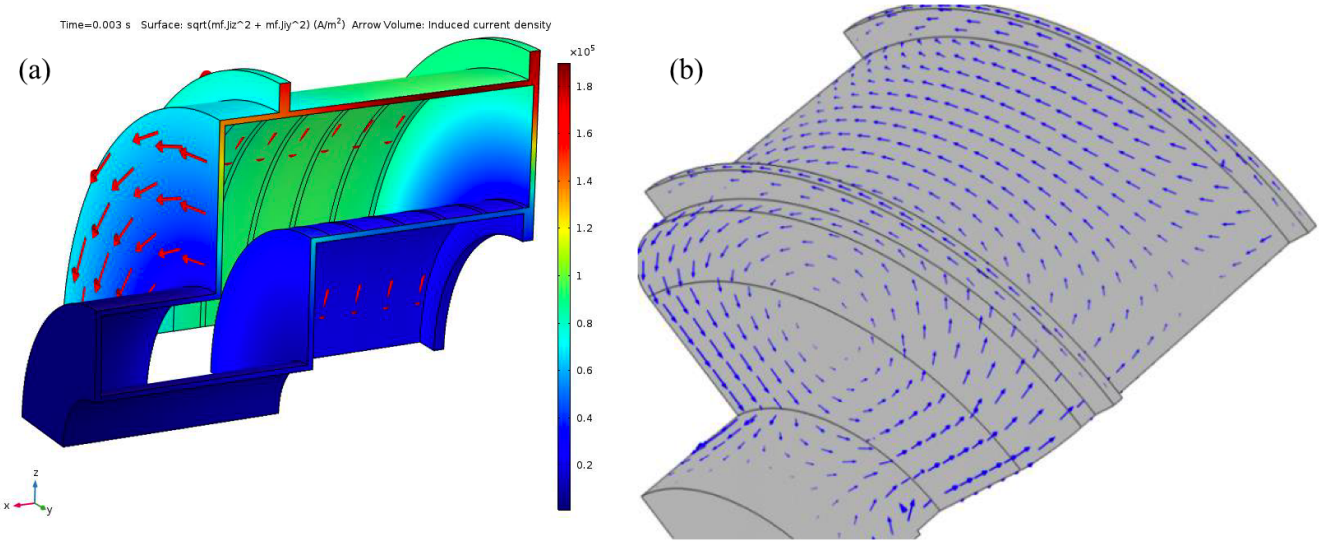

Figure 65: (a) shows the azimuthal Eddy current flow when the tuner has not been partitioned into 4 segments. (b) is the Eddy current flow after partitioning.

We made several shell models that had different longitudinal slot patterns to check their impact on the setting current rise rates and its effect on the bias magnetic field. We used the slot pattern shown in Figure 66 as the reference design. We found that the addition of more slots to the reference tuner shell and to the end plates only led to subtle changes in the distribution of the Eddy currents and fields. Increasing the number of segments from 4 to 8 also did not show any significant improvement of the bias magnetic field uniformity but only made the mechanical design more difficult. Therefore, we settled for just partitioning the tuner into 4 segments without any additional slots in the final design, i.e. Figure 65(b).

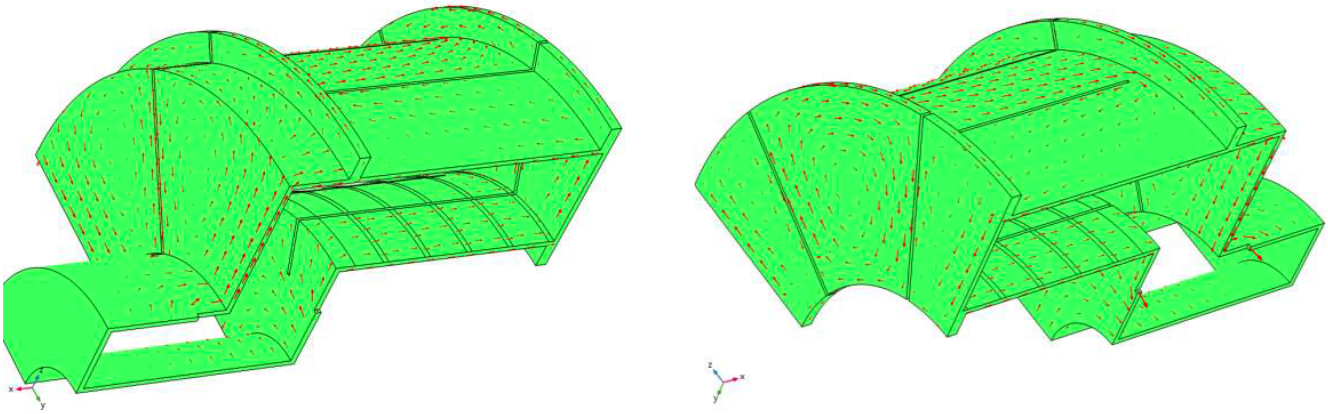

Figure 66: Two views of the reference tuner shell that show the slot patterns. Note: the final design does not have slots.

8.6.2 Bias magnetic field distribution

The magnetic properties of the garnet are highly non-linear. Its permeability and local magnetic field can have large variations in a small area. If the bias magnetic field becomes close to the gyromagnetic resonance at any RF frequency, then significant RF loss can result. It was shown in Ref. [39] that the part of the tuner closest to the accelerating gap is the most vulnerable part of the cavity that can be subject to the increase in RF power loss. And so, we must pay attention to the field at this location. We also have to pay attention to the field of the tuner at the end flange because of the segmentation. Here, the field is partly forced into the gap between segments of the shell. Figure 67 and Figure 68 show the bias magnetic field and permeability in these two regions.

We have found from the results shown in Figure 67 and Figure 68 that the volumetric average permeability of the tuner is 3.41 at injection. The minimum bias magnetic field in the tuner is about 200 G which is comfortably higher than the gyromagnetic resonance value of about 27 G at the injection frequency of 75.7 MHz.

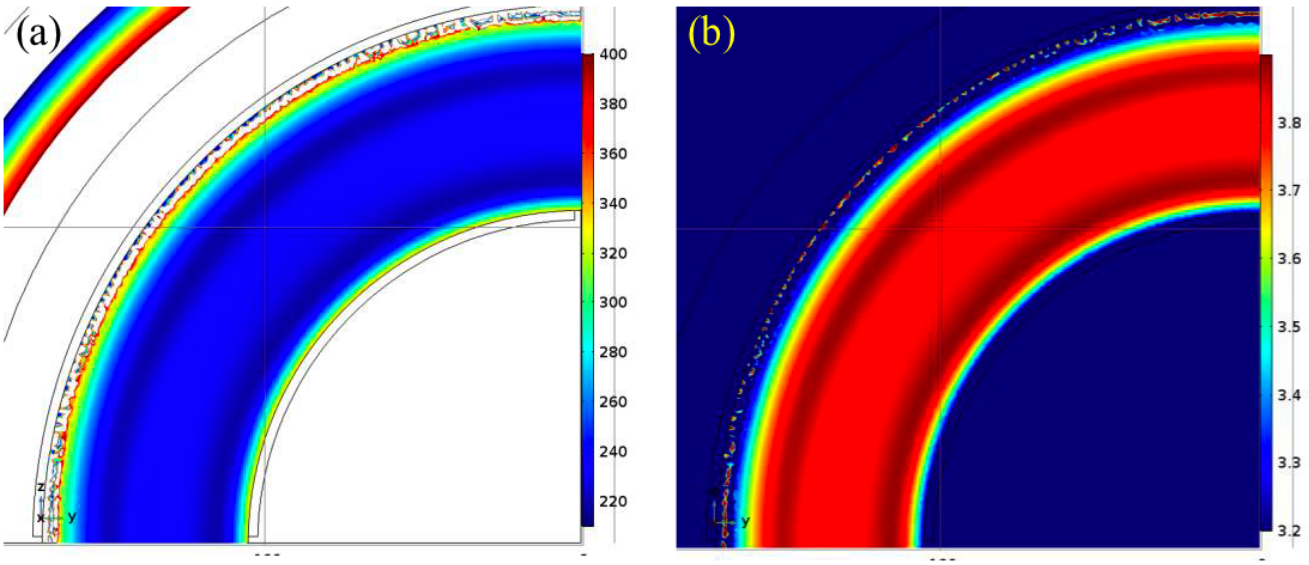

Figure 67: The maps of (a) the magnetic field in oersted (Editor's note: correcting an error in units from Ref. [38]) and (b) the permeability in the plane closest to the gap (z = 118 mm) at injection (3.75 ms).

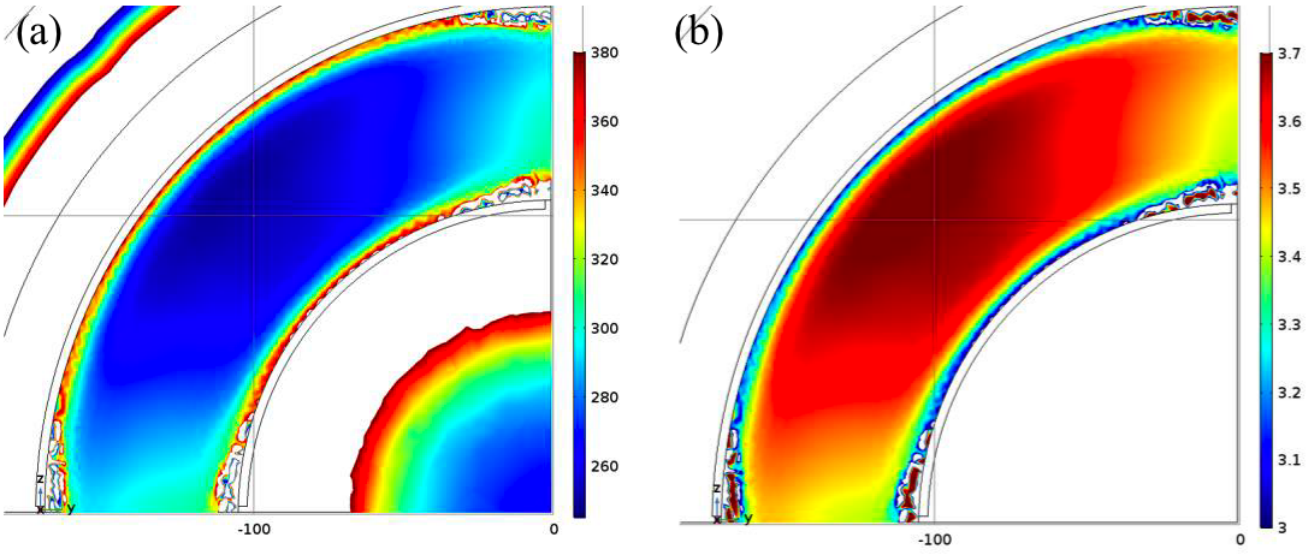

Figure 68: The maps of (a) the magnetic field oersted (Editor's note: correcting an error in units from Ref. [38]) and (b) the permeability in the plane closest to the end flange (z = 10 mm) at injection (3.75 ms).

8.6.3 *Tuner shell heating and cooling*

The RF loss in the garnet stack has been discussed in section 8.3 and Ref. [39] and the Eddy current distribution in the tuner has been found and so we can calculate the temperature distribution in the tuner. Figure 69 shows the tuner with the cooling channels in the inner surface of the shell with the solenoid removed. The outer shell has a similar cooling arrangement. Each segment will be cooled with its own electrically insulated cooling circuit. The cooling water is assumed to be 27°C in these simulations. The goal is to keep the temperature of the tuner shell below 100°C which became possible from the use of the thermally conducting grease between the shell and the rings.

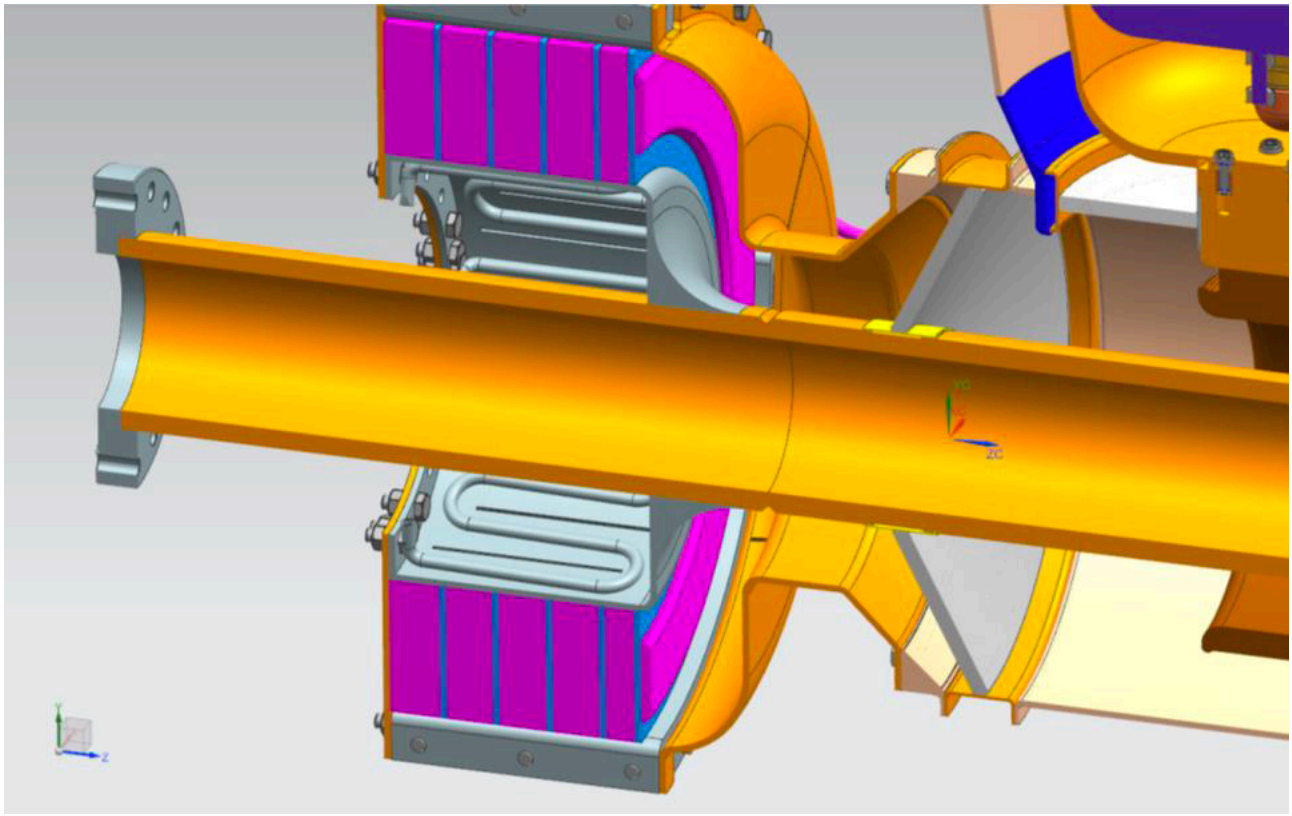

Figure 69: The tuner with the solenoid removed. The cooling channels on the inner surface of the shell can be clearly seen here. (Editor's note: there is an extra cooling disk between the end flange and the tuner stack that is not shown here).

After many iterations of the cooling design, we have found that by adding an alumina disk between the end flange and the tuner stack, we only need to apply cooling to the peripheral surfaces of the flange. In this case the temperature of the flange does not exceed 95°C. Cooling has to be applied to the neck region as well because we have found that Eddy current heating is high at the electrical connection of the neighboring segments. Figure 70 shows the proposed cooling scheme.

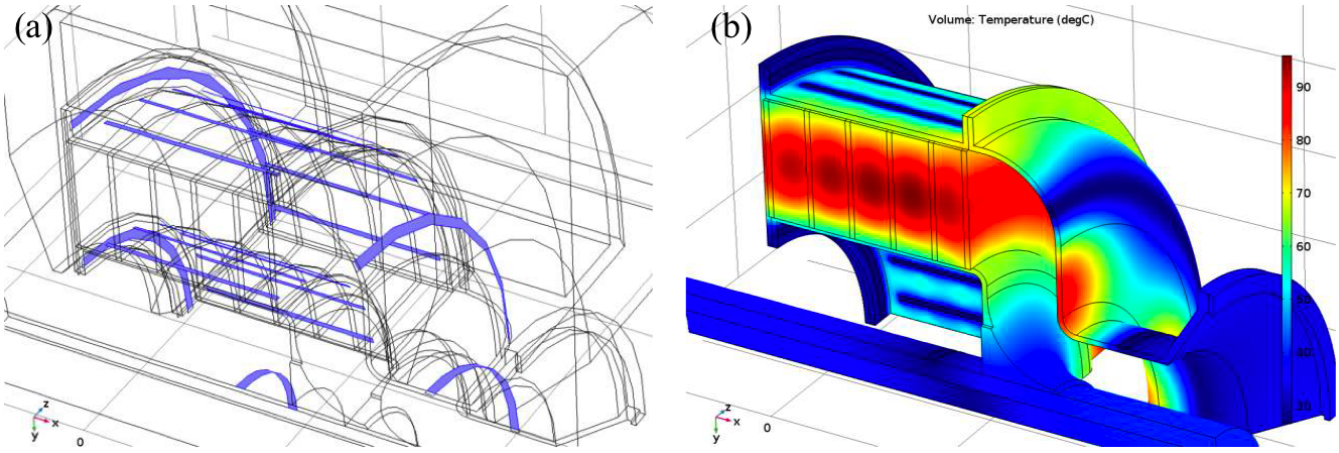

Figure 70: (a) is the proposed tuner cooling scheme and (b) the temperature map.

8.7 Triple points (G. Romanov)

We have to be very careful in the design and assembly of the tuner to avoid triple points where the E-field can be greatly enhanced. Areas where the garnet, alumina and metal shell meet must be carefully filled with thermal grease (See section 8.5). If we assume that the dielectric constant of the thermal grease is about 6 then the E-field can be reduced by a factor of between 6 and 7. See Figure 71. Another location of concern is the interface where the tuner shell segments are bolted together shown in Figure 72. The E-field is reduced by a factor of 3 to 3.5 without thermal grease but with straight edges. The addition of thermal grease should reduce the E-field even further.

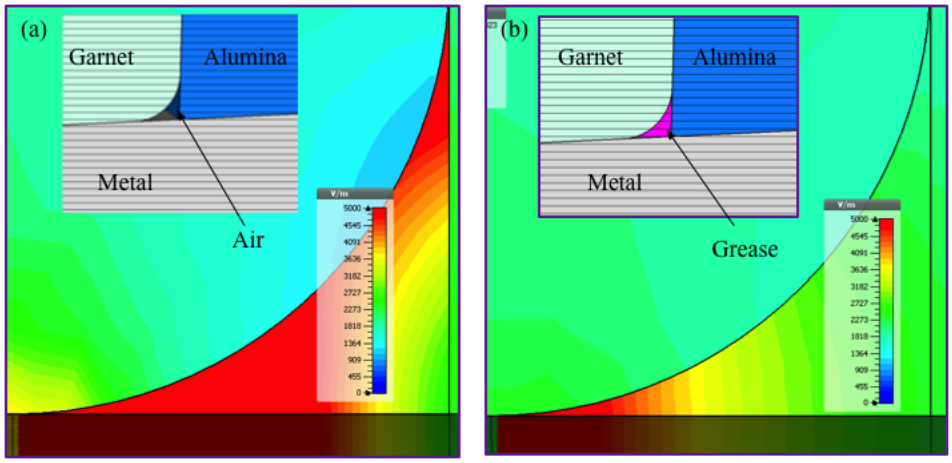

Figure 71: (a) shows the field with air in the gap and (b) with grease. The E-fields are reduced by a factor between 6 and 7 in (b).

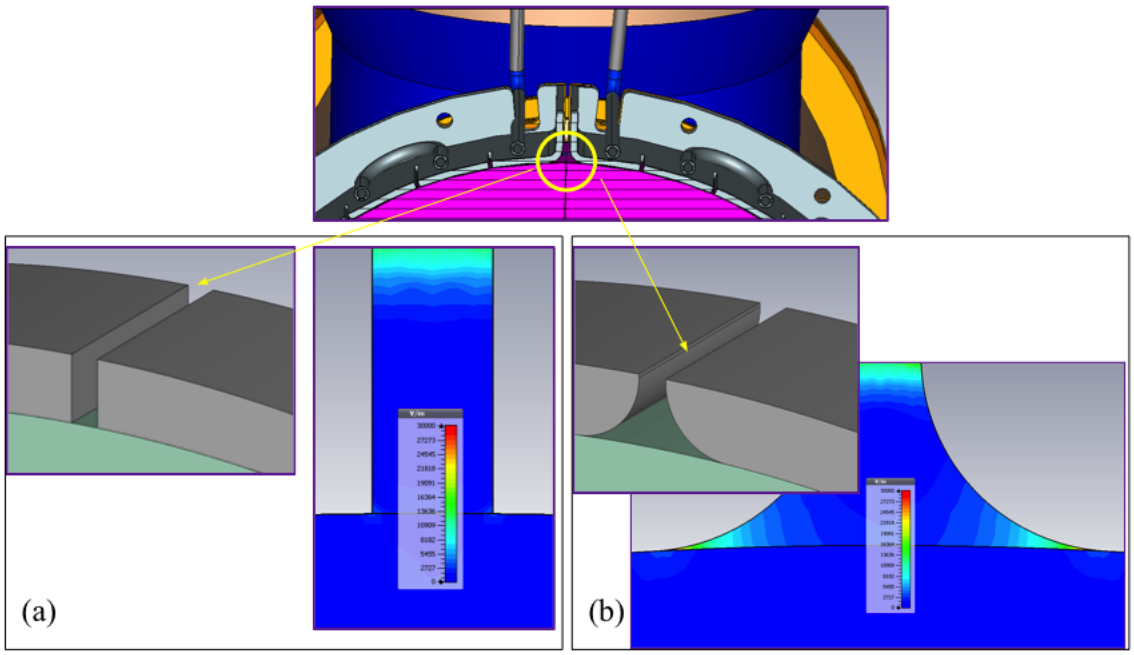

Figure 72: The gap at the location where the tuner segments are bolted together can have a lower E-field by a factor of 3 to 3.5 by having straight edges shown in (a) compared to straight edges shown in (b). In this comparison, there is no thermal grease filling the gap.

8.7.1 Total Eddy current power loss in shell

The total Eddy current power loss has been evaluated. Using Table 2 of Ref. [40] for the case where we have no slots but with 4 segments is about 530 W. This value was found for the simplified ramp shown in Figure 73. **(Editor's note: in the final ramp design, the starting and stopping points of the ramp is about ~140 A and not at 0 A. See Figure 77. Therefore, the power loss is smaller than 530 W.)**

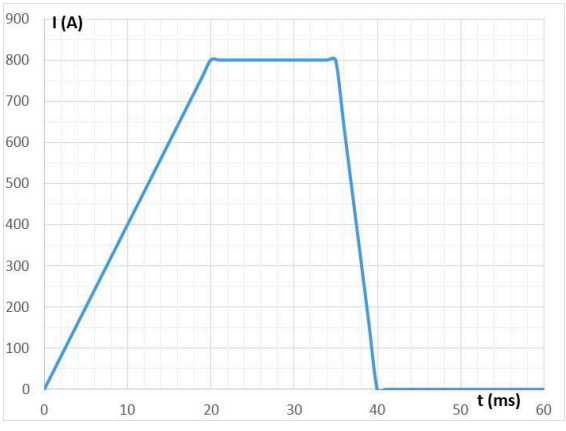

Figure 73: A simplified bias ramp for a 50 turn bias solenoid.

9 Bias solenoid (I. Terechkine)

The magnetic permeability of garnet in the tuner is determined by the bias magnetic field. In this design, the bias magnetic field is generated between the two poles of a magnet with a solenoid type winding. The central (axial) part of the dipole accommodates the beam pipe. The solenoid has been designed so that it can produce the necessary fields to bias the tuner so that it can follow the Booster ramp. The fast cycling of the Booster at 15 Hz means that the solenoid yoke has to be made of laminations to reduce the effects of Eddy currents. The cross-sectional view of the solenoid and tuner is shown in Figure 74.

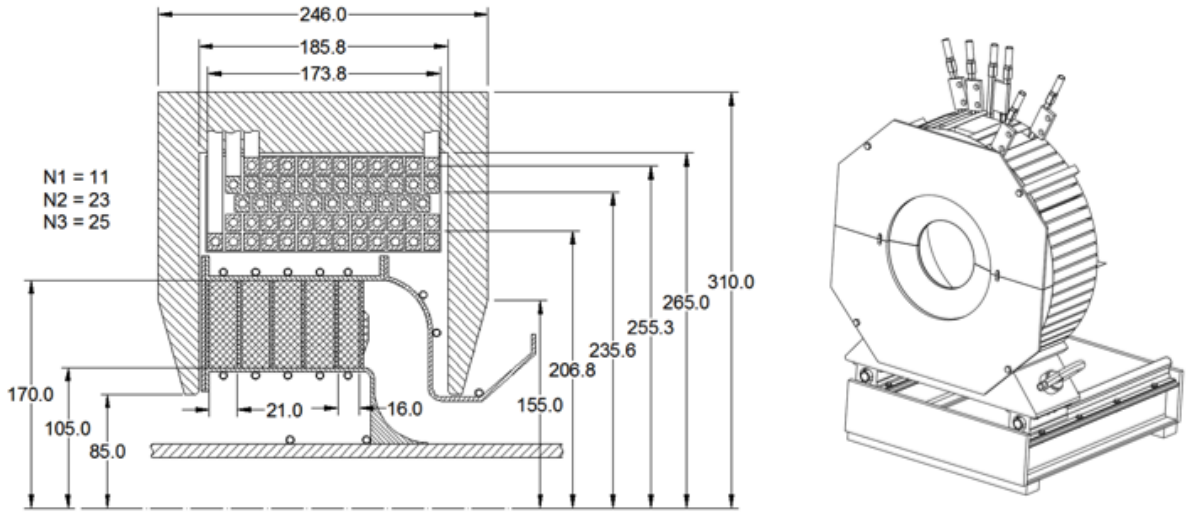

Figure 74: A cross sectional view of the bias solenoid and the tuner. All dimensions are in millimeters.

The winding is made of three coils. Depending on the chosen scheme to power the magnet, the coils can be connected in series or independently. In our design, the three coils are connected in series for a total of 59 turns. The coils are made from 10.4 mm square copper wire with 5.8 mm diameter cooling channel. **(Editor's note: In the final design, the coils are made from 0.460" square with 0.25" hole copper conductors. There are 60 turns in total and not 59 turns. See section 19.3. The measured inductances and resistances of the coils without the garnet tuner are shown in Table 13).** The calculated resistances of the coils are shown in Table 6. The inductances of the coils in series as a function of DC bias for two different coil excitations are shown in Figure 75 when the garnet tuner is within the solenoid. In particular, the inductance of the coils when they are biased at 100 A which is close to injection is 4.7 mH. (These results are from document `Bias_System_Parameters.docx` dated 20 Jul 2017, and private communications dated 08, 09 Aug 2017).

The DC current at injection is 139 A into 59 turns (8200 A·turns) so that the tuner is biased for a resonant frequency of 75.7 MHz.

Winding	Number of turns	Resistance (mΩ)
1	11	4.5
2	23	8.8
3	25	8.3

Table 6: Calculated resistance of the windings. All three windings will be connected electrically in series but cooled in parallel.

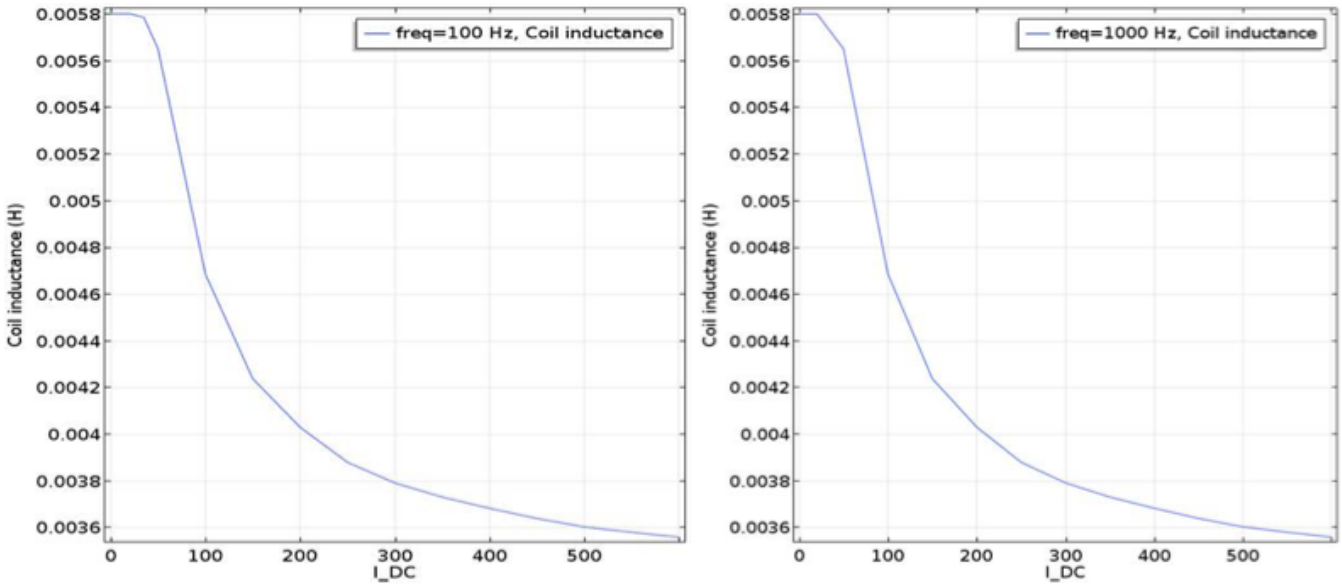

Figure 75: The inductance of the coils connected in series for two different coil excitations. These results show that the inductance is independent of the way the coils are excited. These results were done with the garnet tuner within the solenoid.

9.1 The current ramps

The required solenoid (59 turns) current ramps for the cavity to operate at injection, transition and extraction are shown in Figure 76. The maximum dI/dt and inductive voltages at these three breakpoints are summarized in Table 7. Note that the current ramp will follow some curve outside these regions in order to make sure that the revolution harmonics do not land on the fundamental or HOM resonances.

Booster breakpoint	Maximum dI/dt (kA/s)	Maximum inductive voltage
Injection	16	80
Transition	17	70
Extraction	1	3

Table 7: Maximum parameters in the three Booster break points.

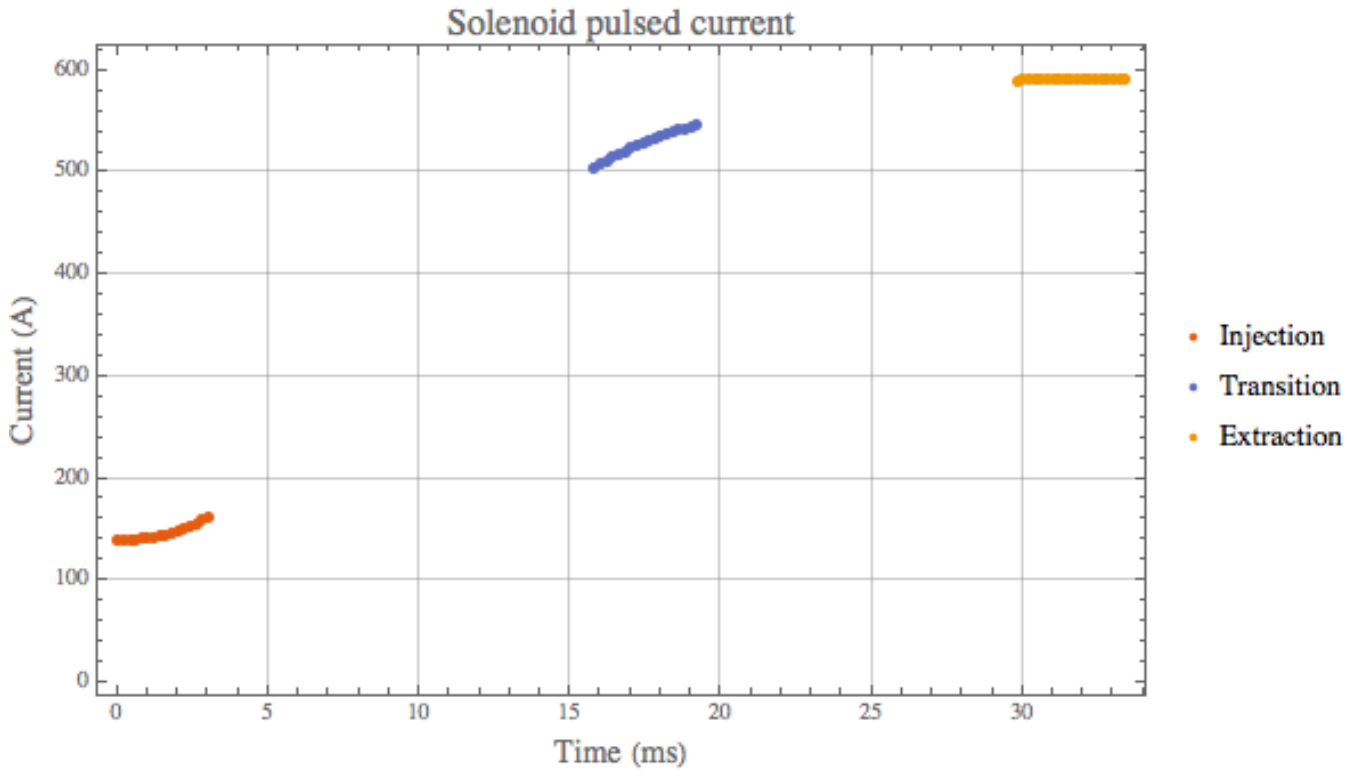

Figure 76: The current pulses required to bias the garnet. These current values assume that the solenoid has 59 turns. The current ramp outside these regions are not shown here. The exact ramp will be determined operationally.

9.2 Coil heating and cooling requirements

The coils will need to be cooled because heat will be generated by the current ramp. Using the fictitious ramp shown in in Figure 77, the power loss in the windings is 4.1 kW (derived below). This is a lot of power and so cooling of the windings is imperative. The exact current ramp need only be known in the three regions shown in Figure 76. The current outside these regions will be determined operationally to keep the revolution harmonics of the beam outside the fundamental and the HOM resonances. A fictitious current ramp shown in Figure 77 models the required ramp with sufficient precision for our thermal analysis.

The fictitious current ramp starts from 139 A at injection and rises linearly in 20 ms to 592 A. It stays constant until $T_{\text{pulse}} = 66$ ms before linearly ramping down to 139 A. The rms current,I_{rms}, for this ramp is simply

$$I_{\text{rms}} = \sqrt{\frac{1}{T_{\text{pulse}}}\int_0^{T_{\text{pulse}}} I_{\text{rms}}^2(t)\,dt} = 435 \text{ A} \tag{23}$$

where $I_{\text{pulse}}(t)$ is the current pulse shown in Figure 77.

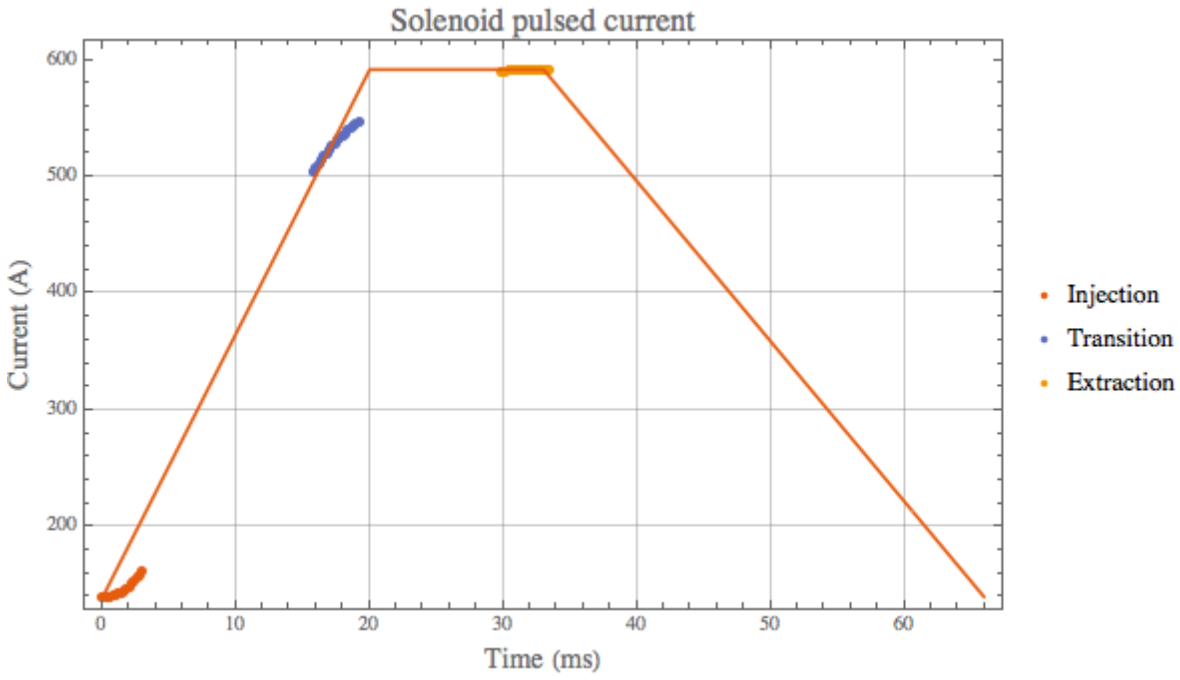

Figure 77: A fictitious ramp for the purpose of calculating the heating and required cooling of the coils. The required ramps for injection, transition and extraction are superimposed onto the fictitious ramp.

The resistance of the coils is the sum of the resistances in series from Table 6 and is $R_c = 21.6$ mΩ. Thus, the rms power, P_{rms}, deposited in the coils from the fictitious ramp is

$$P_{\text{rms}} = I_{\text{rms}}^2 R_c = 4.1 \text{ kW} \tag{24}$$

9.2.1 Flow rate

We can use the specific heat formula to calculate the energy required to raise the temperature of water by ΔT. If we assume that the water temperature rise is $\Delta T = 10°\text{C}$, then we have

$$\Delta E = mc_p \Delta T = 4.1 \text{ kJ in 1 second} \tag{25}$$

where m is the mass of water in kg, $c_p = 4.1813 \times 10^3$ J/kg/K is the specific heat of water at constant pressure. Solving for m, we get $m = 0.1$ kg. The volume, V, of water that corresponding to this mass in 1 second is

$$V = \frac{m}{\rho} = \frac{0.1[\text{kg/s}]}{1000[\text{kg/m}^3]} = 0.1\times10^{-3} \text{ m}^3/\text{s} \tag{26}$$

where ρ is the density of water. Thus the flow rate, f, is

$$f = 0.1\times10^{-3} \text{ m}^3/\text{s} = 0.1 \text{ L/s} = 6 \text{ L/min} \tag{27}$$

which is quite large for only 1 cooling channel with a narrow cross-sectional area.

9.2.1.1 3 cooling channels in parallel

The way the coils will be wound and connected, it is possible to have 3 cooling channels connected in parallel (but electrically in series). If we have 3 cooling channels then the cross-sectional area is increased by 3. Therefore, for a hole in the wire that has a diameter $d = 5.8$ mm, the cross-sectional area is

$$a = \pi(d/2)^2 = 0.26 \times 10^{-4} \text{ m}^2 \tag{28}$$

And by using 3 channels, the cross-sectional area is increased by this factor

$$a3 = 3 \times (0.26 \times 10^{-4})[\text{m}^2] = 0.8 \times 10^{-4} \text{ m}^2 \tag{29}$$

From the above, we can calculate the velocity of water and it is

$$v = \frac{V}{a3} = 0.1\times10^{-3} \left[\frac{\text{m}^3}{\text{s}}\right] / 0.8 \times 10^{-4}[\text{m}^2] = 1.2 \text{ m/s} \tag{30}$$

We can calculate the required differential pressure, Δp, that generates v. We do this by using the following formula is used at Technical Division for calculating the required water pressure [41]

$$\Delta p = \frac{v^2 L}{2d^{1.33}} \tag{31}$$

where Δp is the differential pressure in atm, v is the velocity of the water in m/s, L is the length of the pipe in m, and d is the diameter of the pipe in mm. When we substitute in the numbers we had shown above and set $L = 22$ m, we have

$$\Delta p = \frac{(1.2\ [\mathrm{m/s}])^2 (22\ [\mathrm{m}])}{2(5.8\ [\mathrm{mm}])^{1.33}} = 1.6\ \mathrm{atm} = 23.5\ \mathrm{psi} \tag{32}$$

Therefore, cooling of the coils is easily done.

9.3 The poles and flux return

The flux return of the solenoid (the detailed analysis of the flux return can be found in [42]) both closes the magnetic circuit and reduces fringe fields. Since the solenoid will have to ramp at 15 Hz, the flux return has to be laminated to minimize both Eddy current heating and its impact on the bias magnetic field. We have selected M15 silicon steel sheets that are 0.025″ thick to be the flux return material. **(Editor's note: In the final design, the actual thickness of the silicon steel is 0.014″. See section 19.1.).** Its magnetization curve is shown in Figure 78.

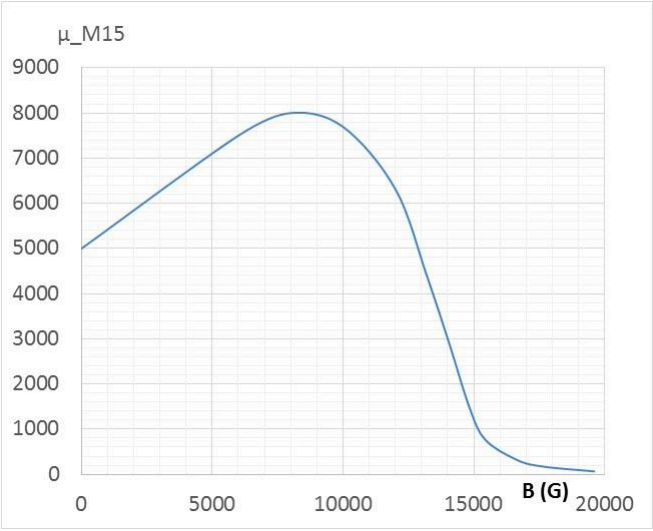

Figure 78: M15 silicon steel magnetization curve.

Both 2D and 3D modeling of the flux return were done. It was necessary to perform a 3D analysis of the poles and flux return because they are made from stacks of laminated steel and there are gaps between the stacks that cannot be accounted for in the 2D model. Figure 79 shows the configuration of the flux return and the poles and the 3D COMSOL model used to calculate the bias magnetic field.

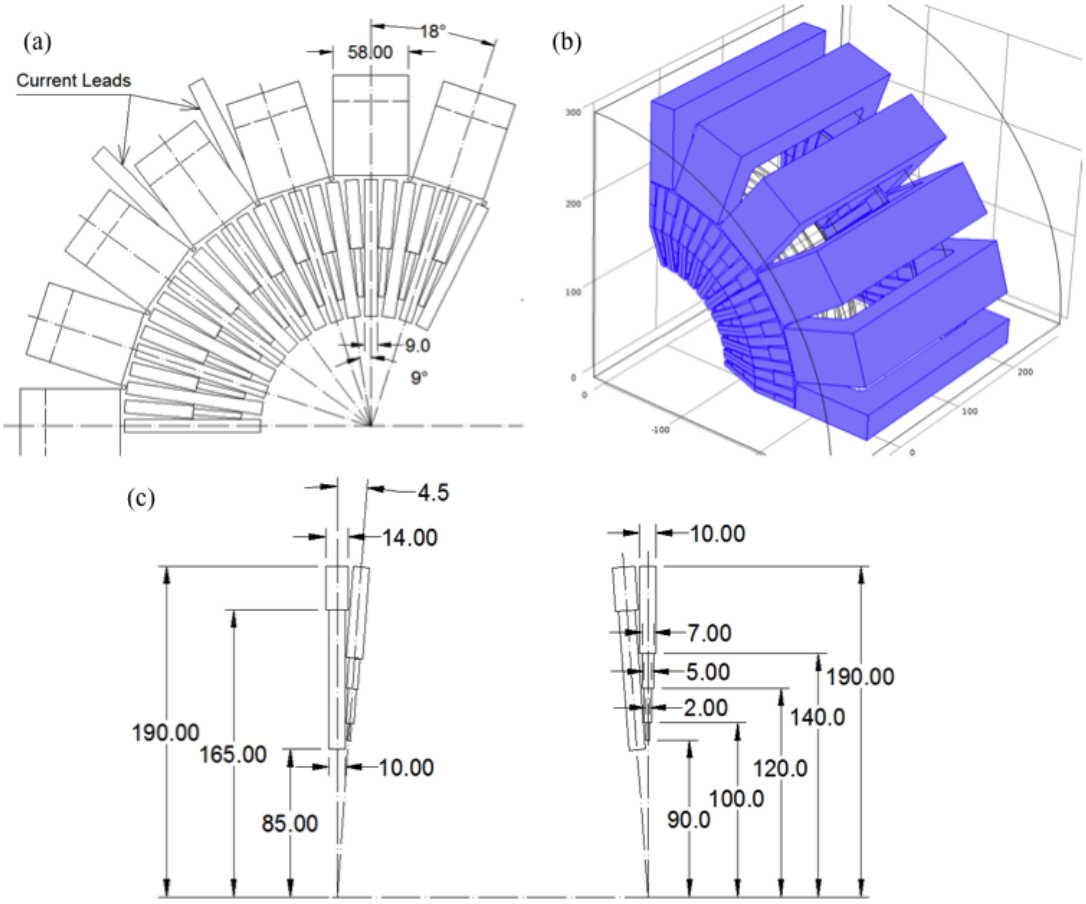

Figure 79: (a) and (c) show the cross-sectional views of the flux return and poles and the laminations. (b) is the 3D COMSOL model.

Figure 80 shows the map of the flux density in the flux return at the maximum current in two planes: the inner surface of the pole and the longitudinal cross section at zero degrees. The geometry of the laminations was chosen to avoid saturation at high current. At the design stage, further optimizations of the flux return were made with the goal of simplifying its fabrication and assembly. The discussion of the actual assembly of the solenoid is in section 19.

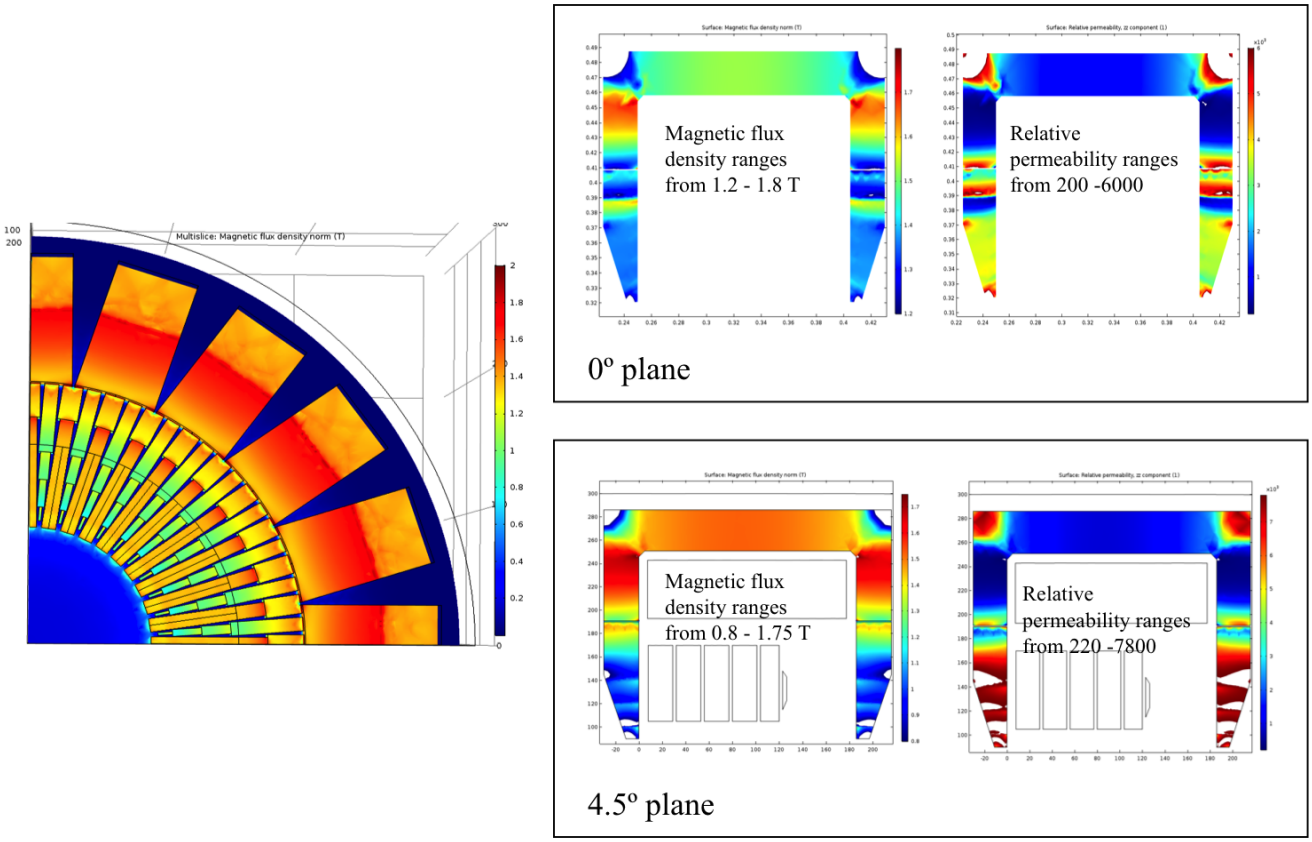

Figure 80: The magnetic flux density at high field is shown on the left. The flux returns in two planes are shown on the right.

9.4 Effect on the tuning stack

The effect on the permeability and bias magnetic field in the tuner stack at the maximum current before the flux return saturates is shown in Figure 81. At this bias current, the average permeability is significantly lower than the permeability required for the cavity to be resonant at transition, i.e. at 104.86 MHz.

At injection, the permeability and bias magnetic field in the garnet for the cavity to be resonant at 75.73 MHz is shown in Figure 82. And since the gyromagnetic resonance at 75 MHz is about 32 Oe, this calculation shows that the all low field regions in the tuner are still far away from the gyromagnetic resonance condition.

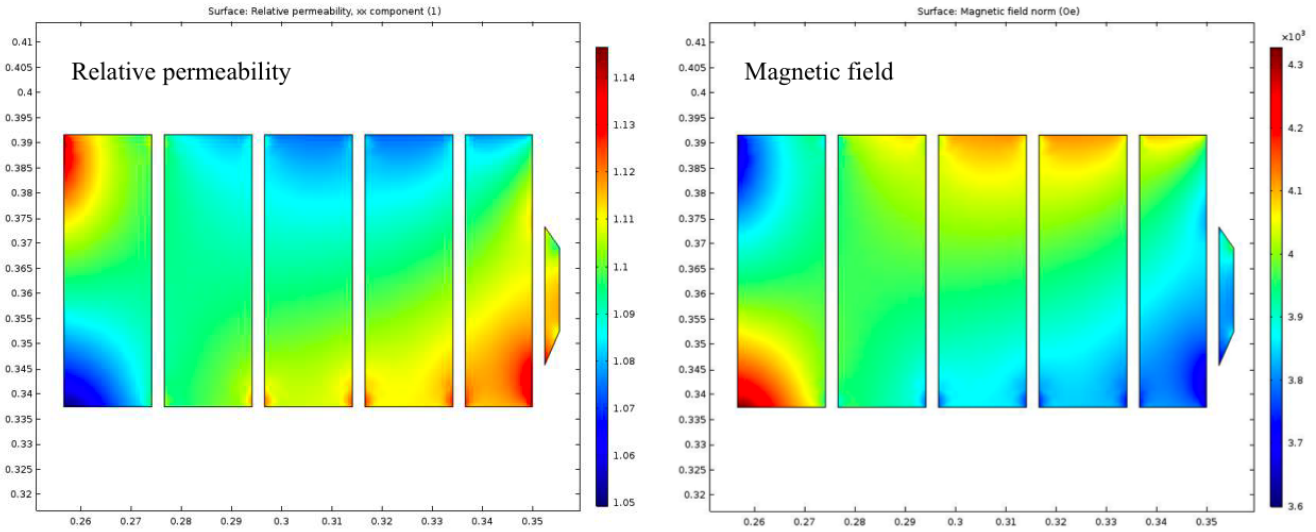

Figure 81: The relative permeability and bias magnetic field in the tuner at the maximum current in the solenoid before the flux return saturates.

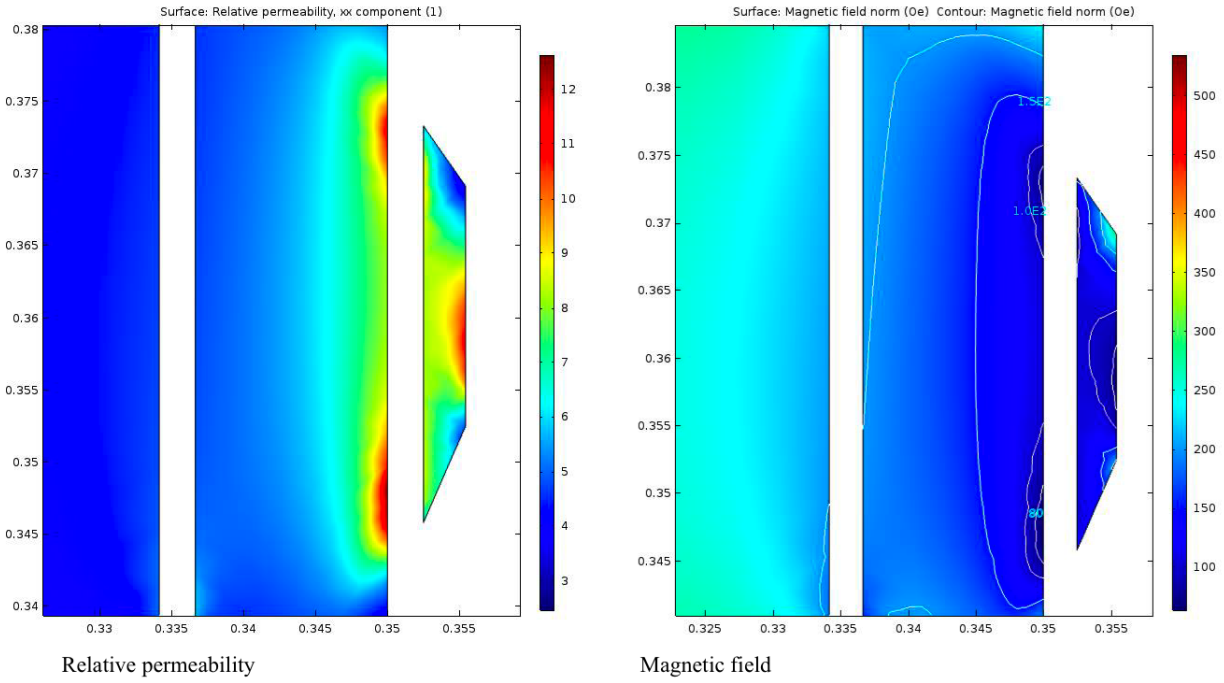

Figure 82: The relative permeability and bias magnetic field in the tuner at low field for injection. The magnetic field levels are 80, 100, 150 and 200 Oe for the contour plot on the right.

10 Bias solenoid power supply (M. Kufer)

The block diagram of the bias solenoid power supply is shown in Figure 83. It consists of a charging power supply and four Performance Controls GA301-P-002 gradient amplifiers [43] connected in parallel.

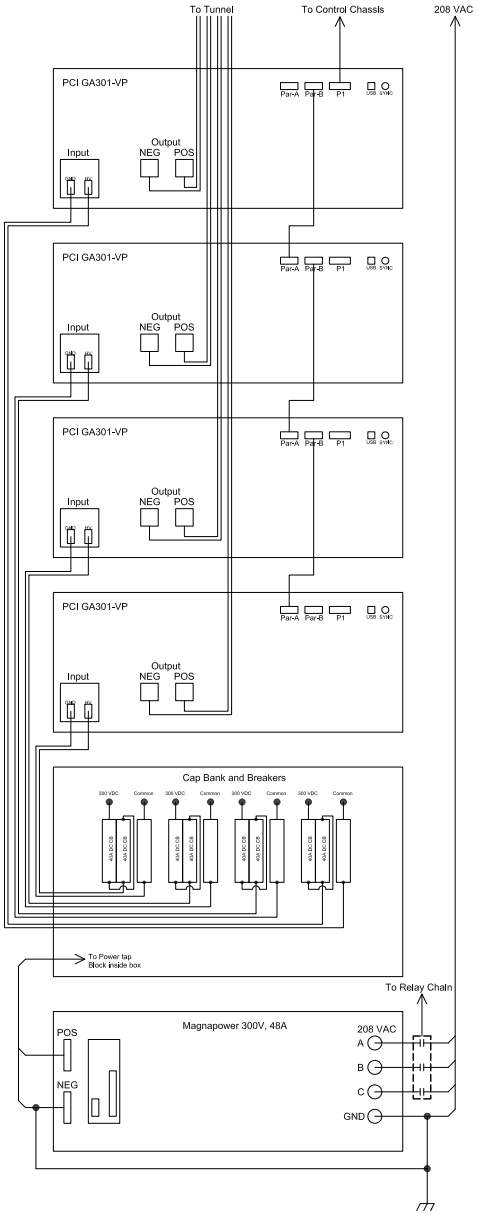

Figure 83: The block diagram of the bias solenoid power supply.

10.1 Bias ramp for operating at injection only (C.Y. Tan)

Due to funding constraints in FY2018, our cavity will only be "on" during injection for the first 3 ms. Therefore, for the rest of the ramp, the bias ramp has to be "parked" so that its fundamental resonance and HOMs lie between revolution harmonics as much as possible or to not be at any revolution harmonic for very long.

Our initial choice was to "park" the fundamental resonance at the "flat" part of the frequency ramp. Figure 84 shows a plot of several revolution harmonics as they evolve during the ramp. We can see that the flattest part of the frequency is after about 20 ms. The range of revolution harmonics that are available to us for parking is between 120th to 129th revolution harmonic. Higher revolution harmonics, like 130th, are unavailable to us at this time because of the constraints on the bias power supply.

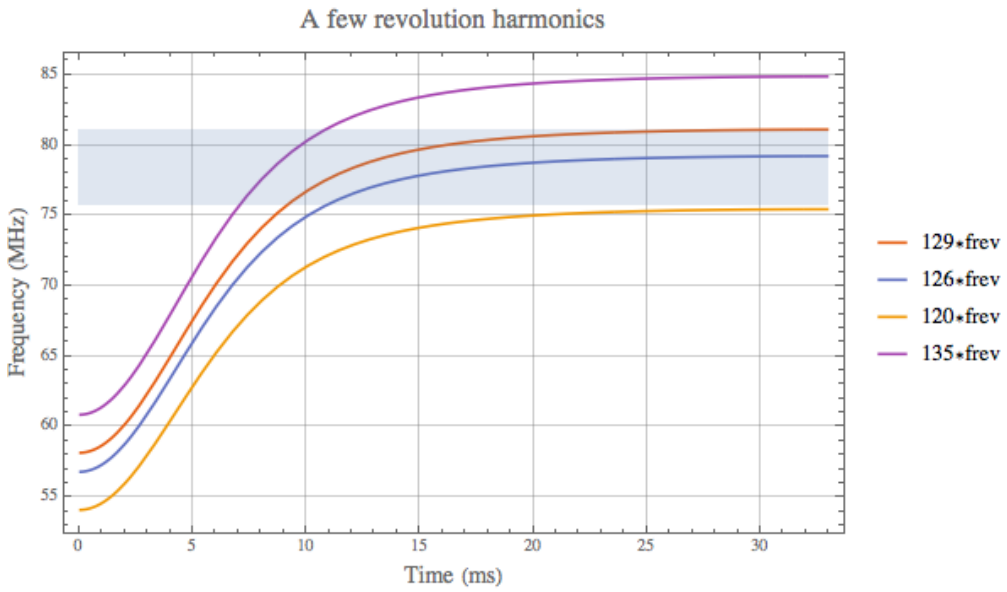

Figure 84: Plotted here are several multiples of the revolution frequency, frev. The shaded region is the range of frequencies that are allowed from the capabilities of the bias power supply. The flattest part of the frequency curve is above 20 ms.

Unfortunately, "parking" after 20 ms at around 78 MHz mid-way between 76 MHz and 81 MHz was deemed to be too close to the HOM resonance of the fundamental cavities. This resonance was the source of the coupled bunch mode instability at high field and so we decided not to use the parking scheme. So instead of parking, we will linearly ramp down the frequency back to 76 MHz.

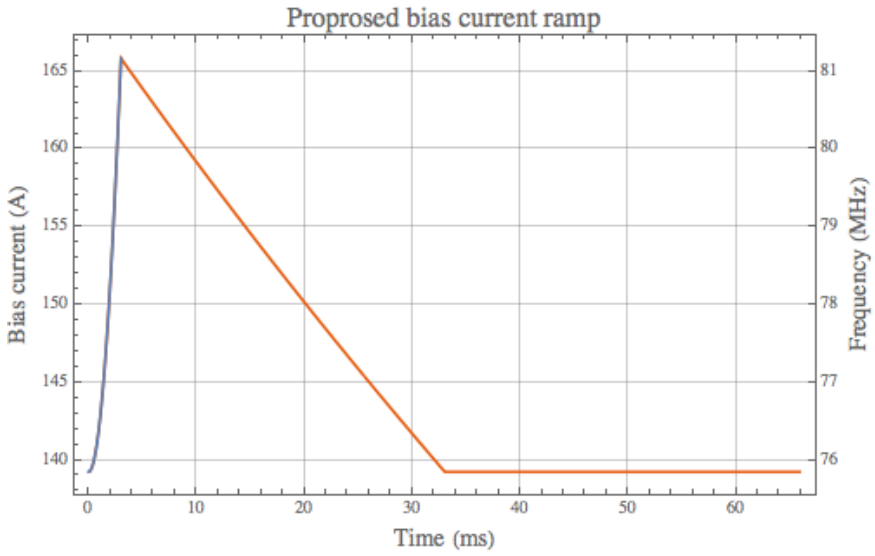

Figure 85: The proposed bias current and frequency ramp. The first 3 ms of the ramp must faithfully be 2× the fundamental.

The proposed current and frequency ramps are shown in Figure 85. We will faithfully follow the required frequency ramp that must be twice the fundamental frequency from 0 to 3. We will then linearly ramp down from 3 ms to 33 ms to the injection frequency 76 MHz and sit there until the beam is re-injected at 66 ms.

Note that the bias supply has a finite bandwidth and so the high frequency components of the current cannot be reproduced, i.e. all the sharp changes in current will roll off. The way that we plan to compensate for the roll off is to pre-shape the current ramp so that current output of the power supply will reproduce the required ramp especially between 0 to 3 ms. If we suppose that the bandwidth of the power supply is 1 kHz, our proposed pre-shaped current ramp is shown in Figure 86. After going through a 1 kHz low pass filter, the required current curve is recovered from 0 to 3 ms. But there is some overshoot after 3 ms that we can tolerate.

10.1.1 RMS current of the bias ramp

The rms current of the bias current ramps shown in Figure 85 and Figure 86 is 150 A. This current is within the specifications of the bias power supply.

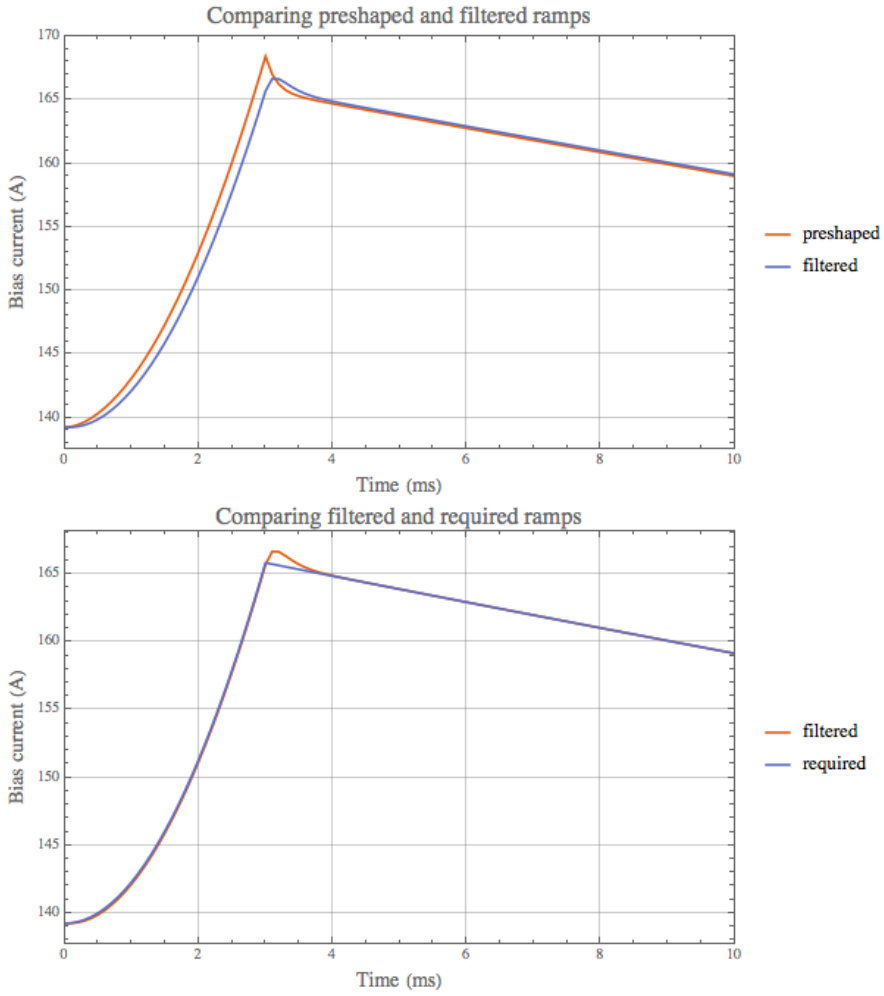

Figure 86: The current has to be preshaped so that after it passes through a bias supply that has a 1 kHz bandwidth, the output current has the required profile between 0 and 3 ms. There is a small overshoot of the current after 3 ms that can be tolerated.

11 Phase locked loop (C.Y. Tan)

A phase locked loop (PLL) is required to keep the RF at the correct point of the cavity phase when both the RF frequency and the cavity resonance are ramped. The block diagram of the PLL is shown in Figure 87.

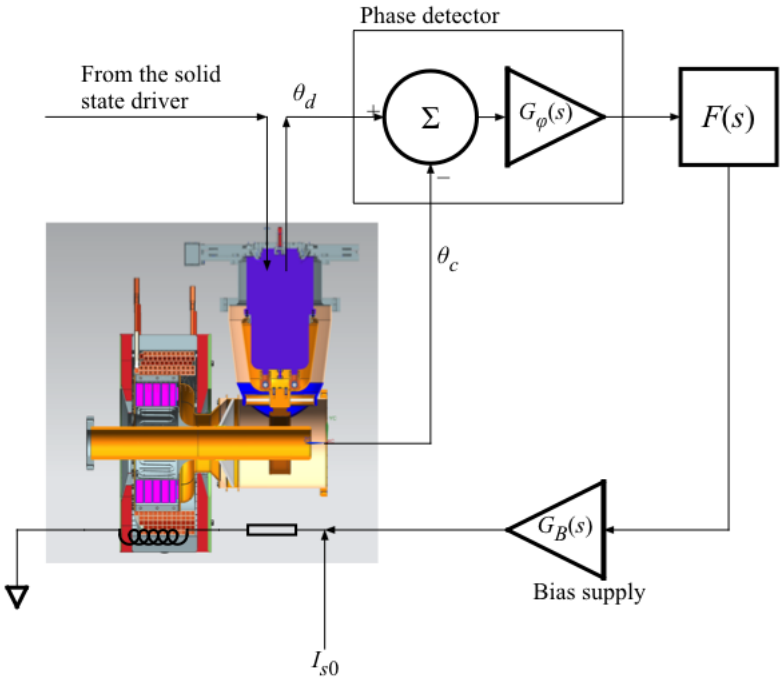

Figure 87: This is the block diagram of the PLL. There is a bias current I_{s0} that flows into the solenoid so that it always biased even when $(\theta_d - \theta_c)$ is zero.

In the analysis of the of the PLL model, the RF cavity is modeled as a parallel RLC circuit. Let I_s be the current in the bias solenoid. The impedance of the parallel RLC circuit is given by

$$Z_c[\Delta\omega, I_s] = \left(\frac{1}{R_c(I_s)} + \frac{1}{i\omega L_c(I_s)} + i\omega C_c(I_s)\right)^{-1} \tag{33}$$

where the shunt impedance, R_c, the cavity inductance L_c and capacitance C_c have explicit dependence on the bias current I_s. The above can be linearized to give

$$Z_c[\Delta\omega, I_s] \approx \frac{R_c(I_s)}{1 + 2Q_c(I_s)\Delta\omega/\omega_c(I_s)} \approx R_c\left(1 - i2Q_c\frac{\Delta\omega}{\omega_c}\right) \tag{34}$$

where $\omega_c = 1/\sqrt{L_c C_c}$, $\Delta\omega/\omega_c \ll 1$, and $Q_c = \omega_c R_c C_c$. And thus the linearized phase of the cavity impedance is

$$\arg[Z_c] = -\tan\left[2Q_c\frac{\Delta\omega}{\omega_c}\right] \approx -2Q_c\frac{\Delta\omega}{\omega_c} = -2R_c C_c \Delta\omega \tag{35}$$

In the time domain, how the cavity shifts the drive phase can be seen with the following equation

$$\theta_c(t; I_s) = \theta_d(t) - 2R_c(I_s)C_c(I_s)\left(\dot{\theta}_d(t) - \dot{\theta}_s(t; I_s)\right) \tag{36}$$

where θ_d and $\dot{\theta}_d$ are the phase and frequency of the drive applied to the cavity, and $\dot{\theta}_s$ is the resonant frequency of the cavity when the solenoid current is at I_s. The above can be further simplified for analysis if the following approximations are adopted

1. Both R_c and C_c are constant in the small range around the resonant frequency, $\dot{\theta}_{s0}$, of the cavity when the bias current is at I_{s0}.
2. If $K_d = d\dot{\theta}_d/dI_d$ then $\dot{\theta}_d(t) - \dot{\theta}_{s0} \approx K_d(I_d(t) - I_{s0})$.
3. With the above approximation for the slope, any frequency close to I_{s0} is given by $\dot{\theta}(I) = \dot{\theta}_{s0} + K_d(I - I_{s0})$.

Thus, by using the above approximations, Eq. (36) can be further simplified. It becomes

$$\theta_c(t; I_s) = \theta_d(t) - 2R_c C_c K_d(I_d(t) - I_s(t)) \tag{37}$$

In Laplace space, the above becomes

$$\Theta_c(s) = \Theta_d(s) - 2R_c C_c K_d(\tilde{I}_d(s) - \tilde{I}_s(s)) \equiv \Theta_d(s) - \mathcal{H}_c(\tilde{I}_d(s) - \tilde{I}_s(s)) \tag{38}$$

where $\mathcal{H}_c$ is the transfer function that relates how the cavity shifts the phase of the drive for a given change in bias current.

11.1 Output of phase detector and the transfer function of the PLL

The output of the phase detector in Laplace space is

$$\Theta_\varphi(s) = G_\varphi \Delta\Theta_d(s) \tag{39}$$

where G_φ has units of V/rad. And then through the rest of the block diagram up to the solenoid, the output voltage is

$$\tilde{V}_s = G_B F G_\varphi \Delta\Theta_d \tag{40}$$

At the solenoid, the bias current is

$$\tilde{I}_s = \tilde{I}_{s0} + \frac{G_B F G_\varphi \Delta\Theta_d}{sL_s + R_s} \tag{41}$$

where $\tilde{I}_{s0}$ has been added so that when $\Delta\Theta_d = 0$, there is current in the solenoid that keeps the resonance at $\dot{\theta}_{s0}$. When the above is substituted into Eq. (38), the amount the drive phase is shifted by the cavity resonance is

$$\Delta\Theta_d = 2R_c C_c K_d \left(I_d - I_{s0} - \frac{G_B F G_\varphi \Delta\Theta_d}{sL_s + R_s} \right) \tag{42}$$

In the simplified model described above,

$$\dot{\theta}_d = \dot{\theta}_{s0} + K_d (I_d - I_{s0}) \equiv \omega_0 + K_d (I_d - I_{s0}) \tag{43}$$

The ω_0 is troublesome, but is neglected in all VCO analysis (see For example Best [44] page 15). If this term is neglected, the phase variation of the drive is

$$\Delta\theta_d = \int_{-\infty}^{t} K_d [I_d(\tau) - I_{s0}(\tau)]\, d\tau \tag{44}$$

which has the Fourier transform

$$\Theta_d = \frac{K_d}{s} (\tilde{I}_d - \tilde{I}_{s0}) \;\; \Rightarrow (\tilde{I}_d - \tilde{I}_{s0}) = \frac{s\Theta_d}{K_d} \tag{45}$$

if $\Delta\theta_d(t = 0) = 0$.

After some algebra, the phase error between the cathode and anode is found to be

$$\Delta\Theta_d = \Theta_d - \Theta_c = \frac{2\tau_c Z_s s}{Z_s + 2\tau_c F G_B G_\varphi K_d} \Theta_d \tag{46}$$

Where $\tau_c = R_c C_c$ and $Z_s = sL_s + R_s$.

11.2 Loop performance analysis

In this section, the loop performance is analyzed. In order to proceed, the proportional-integral (PI) filter is chosen to be the loop filter so that a pole is introduced into the feedback loop. The PI filter is

$$F(s) = \frac{1 + s\tau_2}{s\tau_1} \equiv F'(s)/s \tag{47}$$

where τ_1 and τ_2 are the RC time constants that determine the shape of the filter response.

11.2.1 Phase step applied to Θ_d

When there is a drive phase step, $\Delta\Phi$, in the drive

$$\Theta_d = \Delta\Phi/s \tag{48}$$

By using Eq. (46),

$$\Delta\Theta_d = \frac{2\tau_c Z_s s^2}{sZ_s + 2\tau_c F' G_B G_\varphi K_d}\left(\frac{\Delta\Phi}{s}\right) \tag{49}$$

and applying the final value theorem to the above

$$\Delta\theta_d(t = \infty) = \lim_{s\to 0} s\Delta\Theta_d(s) = 0 \tag{50}$$

Thus, the phase step error approaches zero as $t \to \infty$.

11.2.2 Frequency step applied to Θ_d

When there is a frequency step, $\Delta\omega$, in the drive

$$\Theta_d = \Delta\omega/s^2 \tag{51}$$

By using Eq. (46),

$$\Delta\Theta_d = \frac{2\tau_c Z_s s^2}{sZ_s + 2\tau_c F' G_B G_\varphi K_d}\left(\frac{\Delta\omega}{s^2}\right) \tag{52}$$

and applying the final value theorem to the above

$$\Delta\theta_d(t = \infty) = \lim_{s\to 0} s\Delta\Theta_d(s) = 0 \tag{53}$$

Thus the frequency step error approaches zero as $t \to \infty$.

11.2.3 Frequency ramp applied to Θ_d

When there is a frequency ramp, $\Delta\dot{\omega}$, in the drive

$$\Theta_d = \Delta\dot{\omega}/s^3 \tag{54}$$

By using Eq. (46),

$$\Delta\Theta_d = \frac{2\tau_c Z_s s^2}{sZ_s + 2\tau_c F' G_B G_\varphi K_d}\left(\frac{\Delta\dot{\omega}}{s^3}\right) \tag{55}$$

and applying the final value theorem to the above

$$\Delta\theta_d(t=\infty) = \lim_{s\to 0} s\Delta\Theta_d(s) = 0 \tag{56}$$

Thus the frequency ramp error approaches zero as $t \to \infty$.

Therefore, in all three scenarios, the feedback loop is able to compensate for those errors and eventually reduce the phase error to zero.

11.3 PI-like filter

In real life, a PI filter is impossible to build because it has an infinite response at DC. A realizable PI filter will have a roll off. An implementation of a PI-like filter is shown in Figure 88.

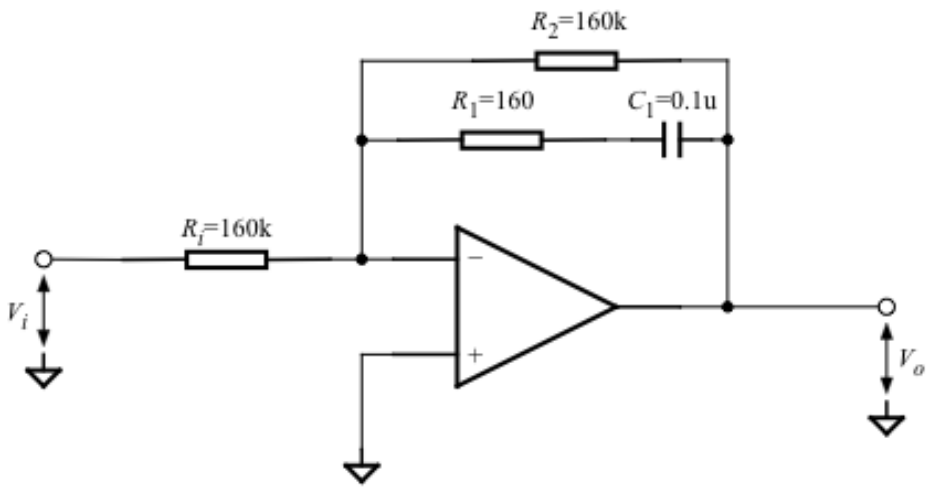

Figure 88: This is a PI-like filter that has the time constants $\tau_1 = R_1C_1 = 1.6 \times 10^{-5}$s and $\tau_2 = R_2C_2 = 0.016$ s.

The PI-like transfer function for an ideal opamp is

$$\mathcal{H}_{\text{PI-like}} = -\frac{1}{R_i\left(\frac{1}{R_2} + \frac{1}{R_1 + 1/sC_1}\right)} \tag{57}$$

The roll offs in this particular design are at $f_1 = 10$ Hz $\Rightarrow\ \tau_1 = \frac{1}{2\pi f_1} = 0.016$ s, and $f_2 = 10$ kHz $\Rightarrow$ $\tau_2 = \frac{1}{2\pi f_2} = 1.6 \times 10^{-5}$ s. The frequency response with these values are shown in Figure 89. The PI filter response from Eq. (57) when plotted together with this curve shows that between 10 Hz and 10 kHz, the PI-like filter acts like a PI filter and hence like an integrator.

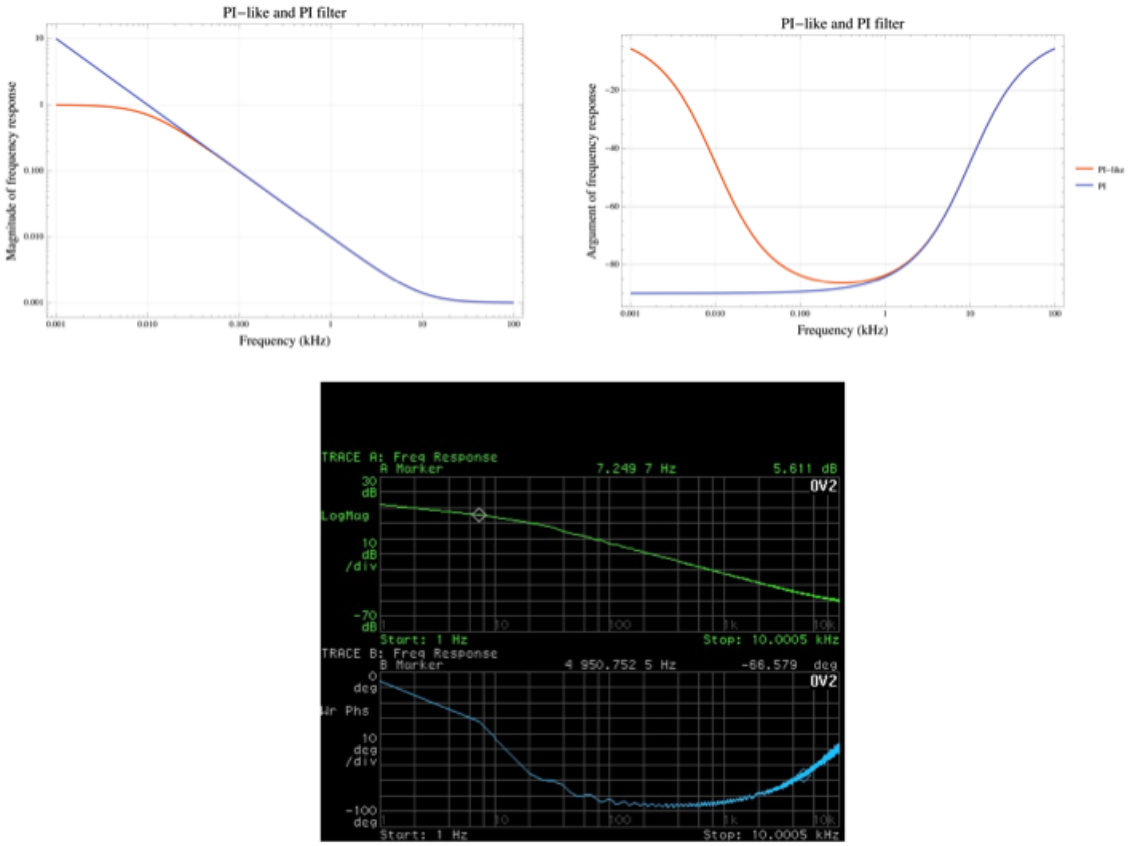

Figure 89: The PI-like and PI filter frequency responses that have the time time constants $\tau_1 = R_1C_1 = 1.6 \times 10^{-5}$s and $\tau_2 = R_2C_2 = 0.016$ s. The measured frequency response of an implementation of the PI-like filter shown in Figure 88 is also shown here. The behavior of the implementation is very similar to the theory.

11.4 Time domain analysis

In the time domain analysis, the goal is to determine the tracking error of the PLL during the ramp. The maximum loop error that is allowed comes from the available rms power from the PA. Therefore, given the maximum power $P_{\max}$ of the PA, the minimum allowable impedance can be found with the formula

$$P_{\max} \geq \frac{V_{\max}^2}{2R_{\min}} \tag{58}$$

If the maximum available power $P_{\max} = 100$ kW and the required gap voltage is 100 kV, then the minimum shunt impedance $R_{\min} = 50$ kΩ.

11.4.1 Allowable frequency error at injection

The first 3 ms at injection, the frequency sweep of the cavity is from 76 MHz to 81 MHz. The Q and shunt impedances of these two frequencies are summarized in Table 8.

Frequency (MHz)	Q_c	R_c (kΩ)	Max allowable freq error (kHz)
76	3200	92.75	±10.9
81	3800	110	±10.9

Table 8: The start and end point Q and shunt impedance for the first 3 ms of the ramp.

By using the linearized form of the cavity impedance from Eq. (34), the maximum allowable frequency error $\Delta f_{\max}$ from resonance given $R_{\min}$ is

$$R_{\min} = \mathrm{Re}\left[\frac{R_c}{1 + i2Q_c\,\Delta f_{\max}/f_c}\right] \tag{59}$$

Using the above formula and the numbers from Table 8, $\Delta f_{\max} = 10$ kHz when $R_{\min} = 50$ kΩ.

11.4.2 Numerical results

The shunt impedance, tuning curve and Q of the cavity calculated by MWS are shown in Figure 34. **Editor's note: The results here assume that the solenoid is divided into a DC coil with 11 turns and an AC coil with 48 turns. The final as-built solenoid will have 60 (not 59) turns connected electrically in series.** These curves are applied to the proposed AC part of the solenoid pulsed current shown in Figure 90. The tracking and the frequency error during the first (1 + 3) ms of the frequency ramp are shown in Figure 91 for $G_B G_\varphi = 5 \times 10^3$ for the proposed AC pulsed current. The first 1 ms of

the ramp is used to settle the PLL. It is clear that the frequency error is well within the required ±10 kHz frequency error.

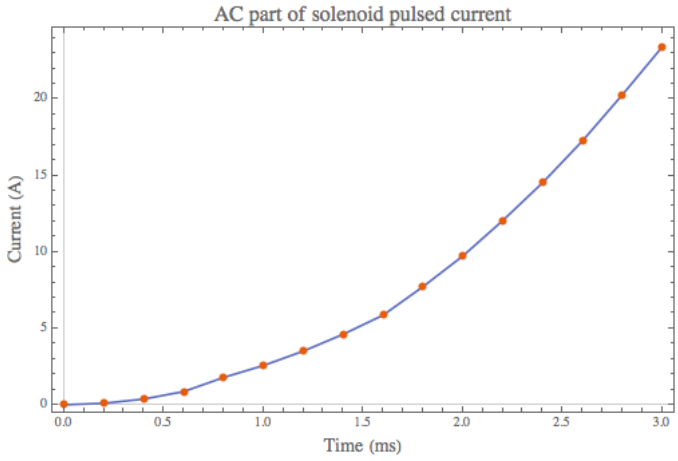

Figure 90: This is the proposed AC part of the solenoid current ramp at injection from 0 ms to 3 ms.

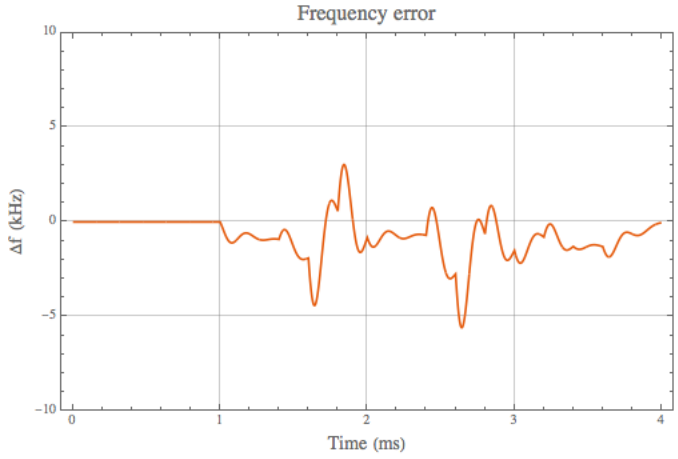

Figure 91: This is the PLL frequency error of the (1+3) ms ramp. It is well within the ±10 kHz requirement.

12 RF windows (D. Sun)

The 2nd harmonic cavity is made up of four parts: PA, garnet tuner, cavity, and HOM damper. The area of the cavity that hosts the power coupler and high voltage gap is under high vacuum of ~10^{-7} Torr or better. Two RF vacuum windows are used to seal this high vacuum area: a flat window (O.D. 7.48″) at the power input side and a conical window (O.D. 9.842″) at the tuner side of the cavity. Both windows are RF coaxial type windows.

There were several design challenges that had to be overcome during the design phase of these two windows. These difficulties arose from their location, manufacture, braze process and assembly. Our solutions will be described in detail in the subsequent sections.

12.1 Choice of flangeless design

For most RF cavities, the power input windows are traditionally located outside of the cavity body and are designed as stand-alone units with two RF flanges, i.e. one flange at the power input side and the other at the vacuum side. Furthermore, the cavity will have a neck and a mating flange onto which the window's flange is bolted. This arrangement allows a window to be mounted and dismounted from the cavity easily (non-destructively) for service or for any other reason.

But for the 2nd harmonic cavity, any large changes in the space between the PA and the cavity body is undesirable because it affects the designed resonant frequency. Extra space will be required with the addition of two flanges to the window. This increases the total length of the window assembly, which in turn, increases the length of the whole cavity assembly. The increased length pushes the resonant frequency to undesirable regions. For this reason, the stand-alone option was eliminated, and both windows are "bare" windows which have no mounting flanges and are welded to the cavity.

12.2 Location choices

Shown in Figure 92 are the three locations that were considered for the input window.

1. Location 1 The water tubes for cooling the PA would go through the vacuum area and their penetrations would need two additional air to vacuum seals. These penetrations should be avoided because of the risk of water leaking into the vacuum.
2. Location 2 There is not enough room because the ceramic surface is too close to the flat bottom surface of the inner conductor. There are water elbows for cooling the PA that stick out from underneath the inner conductor.
3. Location 3 This is the only possible place to install the input window because of the constraints discussed above. This location is unorthodox because it is located "inside" the tank of the cavity.

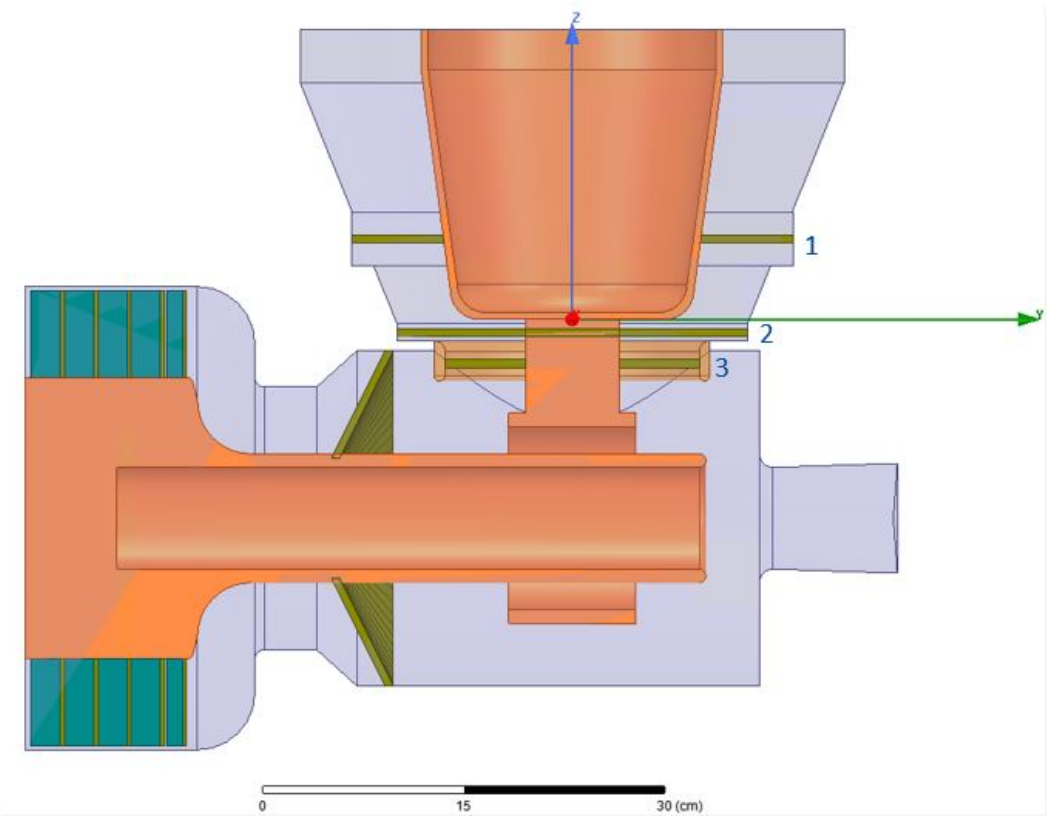

Figure 92: Three possible input window locations that have been considered.

HFSS simulations have been performed to check the effect of input window at those locations shown in Figure 92. The results are listed in Table 9. These results show that a window at location 2 or 3 does not increase the reflected RF power when compared to the same cavity without a window. HFSS simulations also show that the electric fields around the window at locations 2 and 3 are below those at two critical areas: coupler and gap.

Window location	No window	Location 1	Location 2	Location 3
Resonant frequency (MHz)	113.790	113.120	113.410	113.315
Return loss (dB)	24.24	21.3	34.46	25.39

Table 9: The effect on the resonant frequency and return loss due to window location.

For the conical window, it is located on the tuner end of the cavity because it is the only space that can host this window. The accelerating gap and coupler have to be on the high vacuum side because of the high electric fields.

12.3 Design choices

The two RF windows have features that create not only very challenging conditions for brazing but also tight mechanical tolerances for the parts. The main goal of the design is to ensure that the windows can be brazed successfully. The second goal in the design is to ensure that the windows can be successfully connected to the cavity and tuner.

1. Both windows are coaxial type windows which have both inner and outer conductors. Therefore, there are two separate brazed joints: ceramic disk to the copper inner conductor and ceramic disc to the copper outer conductor. This feature creates thermal expansion related problems during the brazing process which are described below:

   During the heating process, the inner conductor will expand more than the ceramic disk because of the difference in the thermal expansion coefficients of the ceramic and copper. This difference between the two materials is large which means that the copper compresses the ceramic. Meanwhile the outer conductor will expand more than the ceramic which pulls the outer conductor away from the ceramic. This force can create a gap between them. During cool-down, the same problems occur but in reverse: the inner conductor will contract more than the ceramic and may create gaps while the outer conductor will contract more than the ceramic which creates compression on the ceramic disk. These forces on the ceramic may cause it to break.

2. Both window assemblies are large in size for brazing: the outer diameter of the ceramic disks are 7.48″ and 9.842″ respectively. Their size makes the absolute thermal expansion differences even worse.
3. The large mass of the inner conductors of both windows makes the problem of the expansion force from the copper even more difficult to manage:
   a. The inner conductor of the input window is a solid cylinder (stem). The stem has to be made of solid copper and the diameter has to be at least 2.7″ because it has to have four bolt holes at each end. Bolts are used to hold the anode output on one end and the power coupling ring on the opposite end.
   b. The inner conductor of the conical window is the beam pipe with a 0.25″ wall. The beam pipe cooling mechanism comes from thermal conduction by the thick wall which means that the wall thickness cannot be reduced. Also, the length of the beam pipe to be brazed is 8″ long. This length increases the mass significantly which makes it difficult to get to thermal equilibrium and requires a large braze furnace.

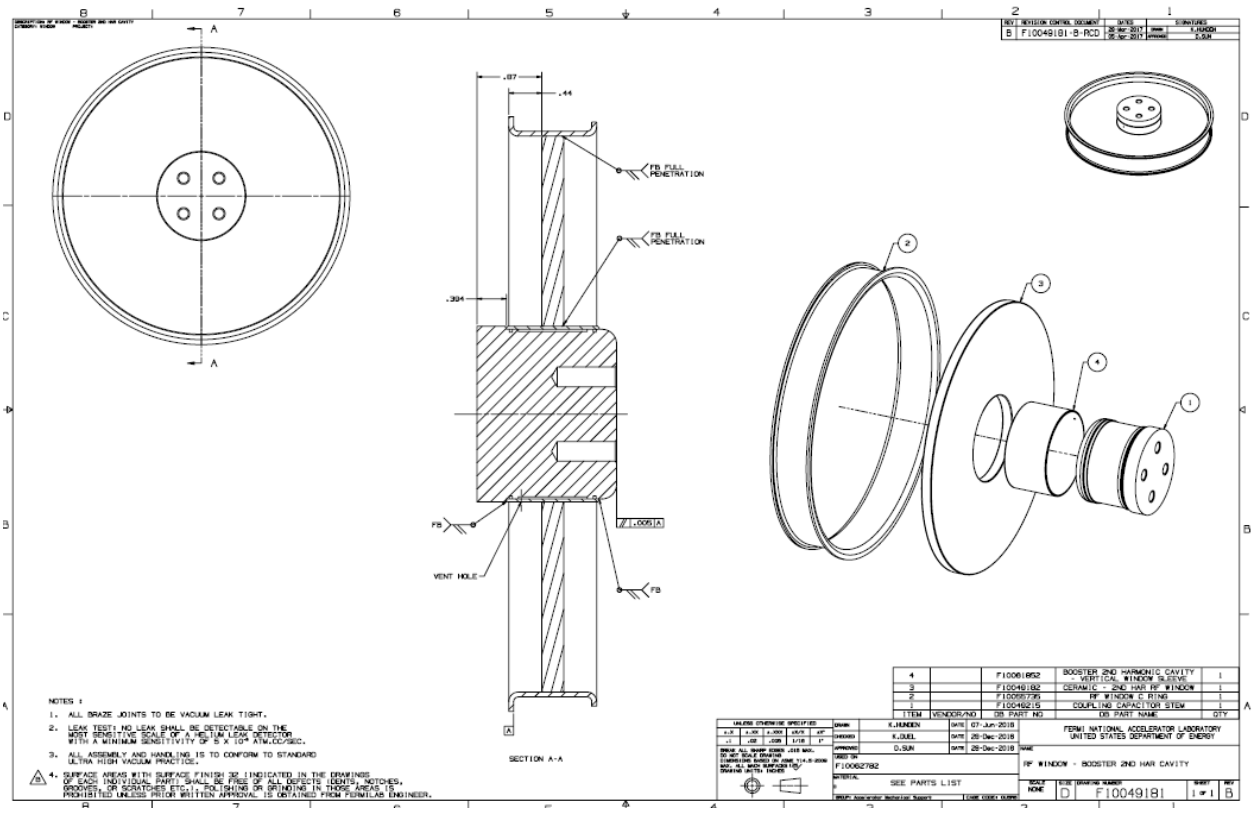

Figure 93: The input window.

To solve these thermal expansion difference problems, each window assembly was divided into four parts:

1. Inner conductor: A solid copper cylinder (stem) for the input window. A beam pipe for the conical window
2. Thin copper sleeve: A copper sleeve that is 1″ long with a wall thickness of 0.04″ between the ceramic disk and the inner conductor.
3. Ceramic disk.
4. Thin copper outer ring: A copper ring with a wall thickness of 0.05″. The thin wall makes it easier to constrain the effects of thermal expansion during brazing and welding in the assembly stage.

12.4 Assembly

Each thin copper sleeve is brazed onto their respective inner conductors only at two ends and in the middle area where there is a gap between the sleeve and the inner conductor. The thin sleeve will deform during brazing because of the difference in the thermal expansion rates between the sleeve and the ceramic disk. The deformation creates less force on the ceramic disk. Figure 93 and Figure 94 are the assembly drawings of these two windows.

The outer ring (also called as "flange") of the conical window is a thin copper ring whose cross section is "U" shaped. The outer ring is welded onto the cavity on one side and onto a thick copper disk (which will eventually be welded to the tuner outer shell) on the other side. See Figure 160.

The outer ring (also called "flange") of the input window is similarly designed with a "C" shaped cross section. This ring will form the weld lip during welding to the cavity body and tuner assembly. See Figure 177.

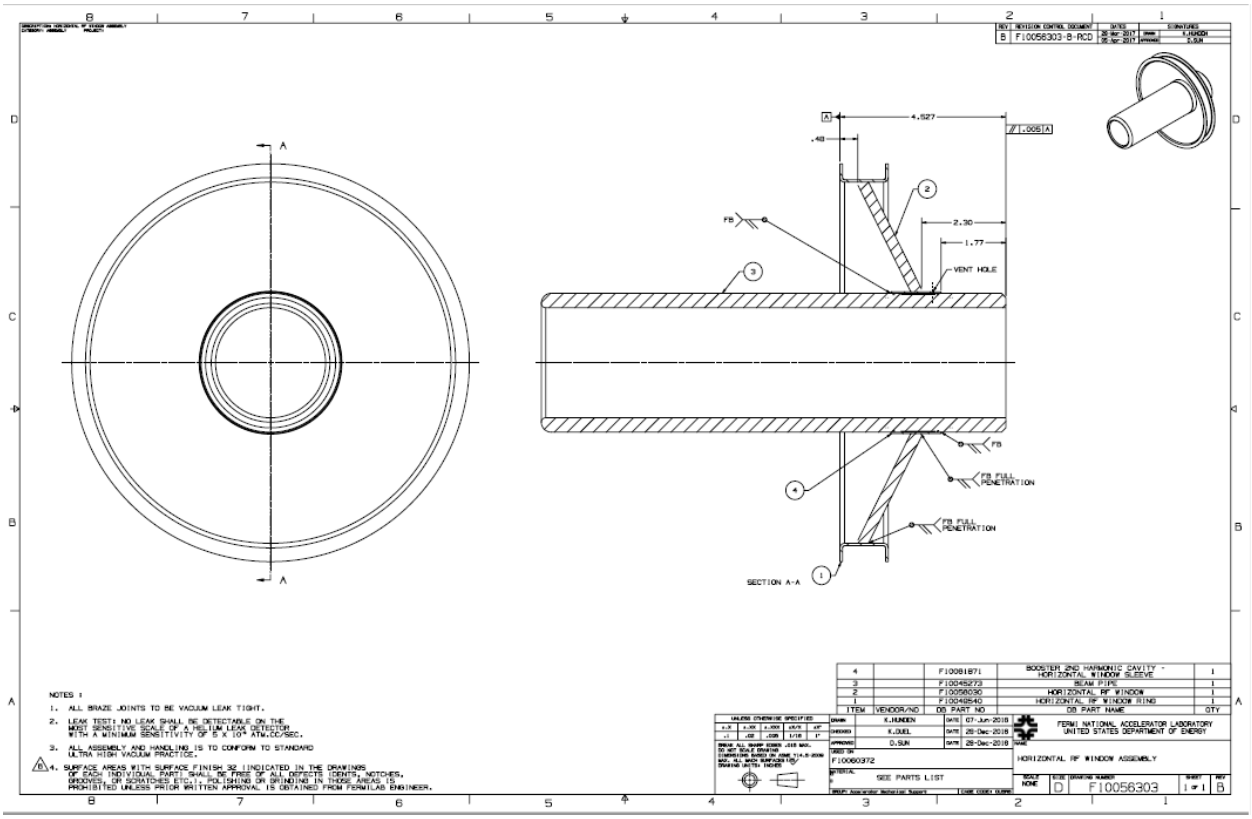

Figure 94: The conical window.

12.5 Cooling considerations

There is no provision for water cooling of either window at this time. The heat generated in the ceramic will be carried away by thermal conduction of the brazed solid (or thick) copper inner conductor and the cavity/tuner part brazed to the outer rings. CST MWS simulations show that the power lost in the input window is only 0.25 W and the power lost in the conical window is only 6.5 W under designed operating conditions (gap voltage: 100 kV, 3 ms injection, 3 ms extraction). [45] In the future, if necessary, the outer rings ("U" shaped or "C" shaped) can be converted into water cooling channels.

12.6 Machining of copper parts

An outside vendor was used for the machining of the copper parts. The copper parts were machined with a lathe. All parts were inspected by the Technical Division Quality Assurance Group (TD QA) at IB4. All the important dimensions of the parts are within the required tolerance.

The machined parts met the surface finish requirements but there were a couple of rough machining marks ("kinks") left on the tip area of the beam pipe. Unfortunately, they were at the high E-field region of the cavity which meant that polishing was required. The vendor was asked to perform diamond polishing to smooth them out. The diamond polished areas were then optically examined by the TD QA group.

12.7 Brazing problems

Figure 95: The window assemblies made by Company B had cracks and gaps.

Not many vendors have the appropriate capacity and interest in the job because of the brazing challenges these two large RF windows discussed in section 12.3 present. This is especially true for brazing the conical window to the beam pipe. Only two reputable brazing firms, Company A and Company B submitted reasonable quotes. Note: the quote from Company B was just a best effort offer. For risk management reasons, the brazing job was split and assigned to both companies. Company B

was given the task for brazing two input flat windows and Company A was given the task for brazing two input flat windows and two conical windows. Also, for risk control, both companies were required to braze one window at a time. The ceramic disks were made by each company.

Brazing work done by Company B completely failed (see Figure 95). There were gaps between the outer flange and ceramic disk after the first window was brazed. A repair attempt was made to fill in the gap with a liquid copper powder solution ("Cu drop"). The restraints on outer flange were also increased. After the assembly went through a second brazing, gaps still remained between the outer flange and ceramic disk. Finally, the ceramic cracked after the restraints were released. The second window assembly went through same brazing procedure and had the same problems. The team at Company B could not figure out what were the causes for the cracking, but they did not think that the "Cu Drop" was the cause.

Braze work by Company A was relatively successful. There were no cracked ceramic disks and the brazed joints were vacuum tight. The detected leak rate was ~2×10^{-10} mbar-L/s (test performed by Fermilab AD vacuum group).

One of the input windows and one of conical windows were inspected with a CMM by the TD QA group. Most of the dimensions achieved the given design specifications. The major deviations from the design specifications that were critical are:

1. The distance between the beam pipe tip and copper flange is ~0.006" – 0.035" shorter than the design specifications. This means that the high voltage gap will be longer by this amount if everything else was built exactly as designed.
2. The angle from the center line of the beam pipe to the ceramic outer ring plane is ~0.2° off 90°. When compared with the errors that are unavoidably introduced when assembling the cavity (including the garnet tuner), these deviations from the design value are very small and is acceptable.

The braze work from Company A was not perfect. There is a small overflow of the braze alloy (CuSi) on the ceramic surface near the ceramic-copper joint. This overflow forms a thin layered, circular metal "band" (about 0.03" wide) perpendicular to the inner and outer conductor which may cause sparking and/or local heating problems at high RF power levels. HFSS simulations have been performed to check the field enhancement effect of these metal "bands". The results may also apply to any tiny sharp spikes on the metal surfaces. The results of the HFSS simulations are discussed in section 12.9.

12.8 Shipping problems

Company A's packaging and shipping was extremely poor which caused the following problems:

1. There is minor damage on the surface of the tip of beam pipes (both windows). See Figure 96(a) for the damage on the first conical window from Company A. This damage was hand polished away.
2. The outer ring of both conical windows was bent. The outer ring of the second conical window was bent to an unacceptable level (see Figure 96(b)). This window assembly was returned to Company A. A repair was done where the "bend" was straightened out using a spinning process. After the repair, better packaging was used to ship the window back to Fermilab. This repaired window is now the spare.

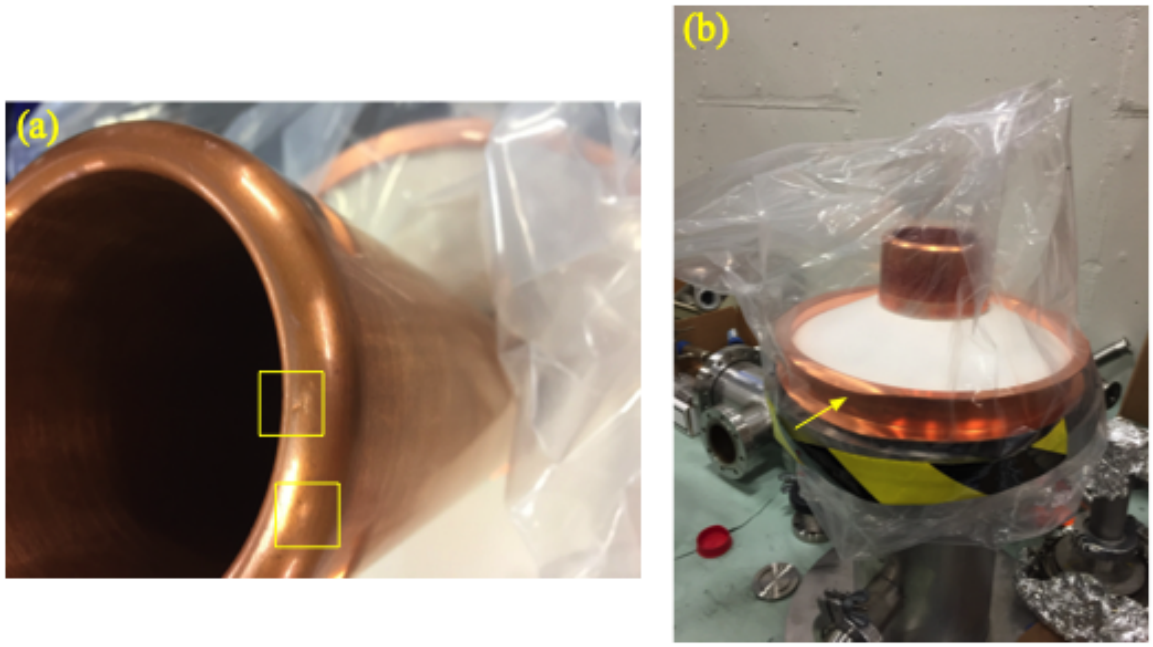

Figure 96: (a) The squares mark the regions on the beam pipe that had minor shipping damage. (b) The outer ring of the second conical window had a very serious bend.

12.9 HFSS simulations

HFSS simulations were performed to assess how the strength of the E-field can be affected by the braze material overflow. The overflow was a defect from Company A's brazing process. A very small portion of the metal overflow "band" was modeled as a sharp wedge that stuck out from the beam pipe surface that was adjacent to the surface of the ceramic disk. This was the area where fine mesh points were used. The sharp wedge was formed with a triangular cross section that swept 10° around the beam axis. As a result, the sharp wedge is ~7.8 mm long. Two base width to height ratios (sharpness ratio) were considered: (a) ~1 mm base width and 1 mm height, and (b) 1 mm base width and 1.9 mm height. The edges of the wedge were filleted with three different radii: 0.3 mm, 0.4 mm and 0.5 mm. These radii reduce its height and sharpness ratio. The edges of the wedge (a) were filleted with a

radius of 0.3 mm only to reduce its height and sharpness ratio. (Note: the wedge and the filleted wedge may not truly represent the real "bands".). See Figure 97 for the HFSS models of the wedges.

The maximum E-field that is on the surface of the beam pipe tip will be used as the base line reference. These results show that the maximum E-field on the wedge was increased significantly—the maximum E-field on a wedge is at least 12 times (for a 1mm x 1mm wedge) larger than the E-field on the smooth surface at the same location. It is 4.5 times larger than the maximum E-field on the surface of the beam pipe tip. If these simulated field enhancement numbers are true, it may indicate a sparking problem during high power operations. However, looking at wedges in detail shown in Figure 97(b) - (e), the maximum E-field on the wedge (whether filleted or not) is only at a few spots, and not the entire area. So, at this time it is unknown whether the singularity is real or an artifact from the simulation. Also, unexpectedly, filleting does not decrease the E-field enhancement. In the high sharpness ratio case, filleting actually increased the field enhancement by a factor of 4. For comparison, in the low sharpness ratio case, filleting only increased the E-field enhancement be 20%. This strange behavior may be caused by the fact that in the HFSS simulation, filleting always creates more lines and points.

Simulations of the filleted wedges also had another strange result: E-fields near the edge of the big inner conductor of the garnet tuner became larger than the maximum E-field on the surface of beam pipe tip. This anomaly needs to be further investigated.

However, despite some anomalous behavior of the simulations, these simulation results are correct overall. They show that the E-field at a sharp edge is much higher than in the smooth areas. For example, field enhancement factors of 10 or more was commonly used in research literatures. And the higher the sharpness ratio, the stronger the field enhancements when compared to the un-filleted cases.

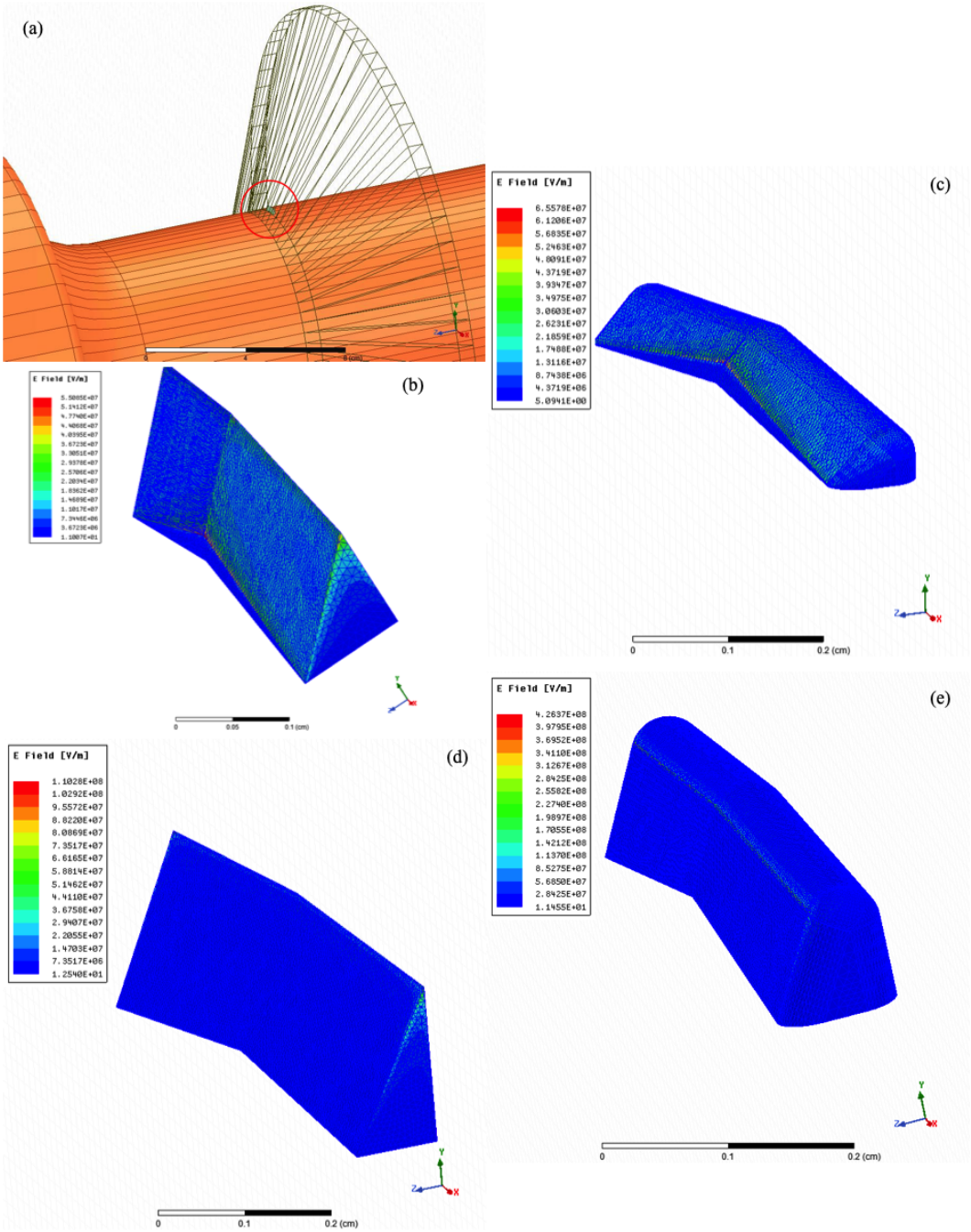

Figure 97: (a) The location of the wedge (green structure in the red circle) on the beam pipe surface (orange) and near the ceramic window (clear mesh) in the HFSS simulation. (b) Wedge (1 mm base width and 1 mm height). (c) Filleted wedge (1 mm base width, 1 mm height, 0.3 mm fillet on all edges. The height after filleting is 0.55 mm. (d) Not filleted wedge (1 mm base width, 1.9 mm height) (e) Filleted wedge (1 mm base width, 1.9 mm height, and 0.3 mm fillet on all edges.

13 Cathode resonator (R. Madrak, J. Dey, & C.Y. Tan)

A cathode resonator is required to match the output impedance of the solid-state amplifier (SSA) to the input impedance of the Y567B, which is mainly reactive due to the cathode-grid capacitance. However, due to the large frequency swing ~30 MHz requirement, the cathode resonator has to have a very low $Q < 10$, and thus the impedance match is far from perfect except at the peak frequency. Section 13.2 discusses the cathode resonator model that served as the starting point of the design. However, it was discovered soon after the first resonators were made that the model is too simplistic and did not adequately predict the matching impedance, and thus the VSWR. It was also found that the input capacitance of the Y567B is dependent on frequency, which was not known during the initial design stage. This meant that the size of the inductance required for resonance at the design frequency was wrong and had to be corrected in the final design. Although the model's usefulness is limited in scope, the relative changes it predicts can still be used as an aid in the "trial and error" method to arrive at the final design.

It was found that the cathode resonator, by itself, still presented a poor match to the SSA. A matching tuning stub was added between the SSA to the resonator to improve the VSWR. The details of the tuning stub are discussed in section 13.3.

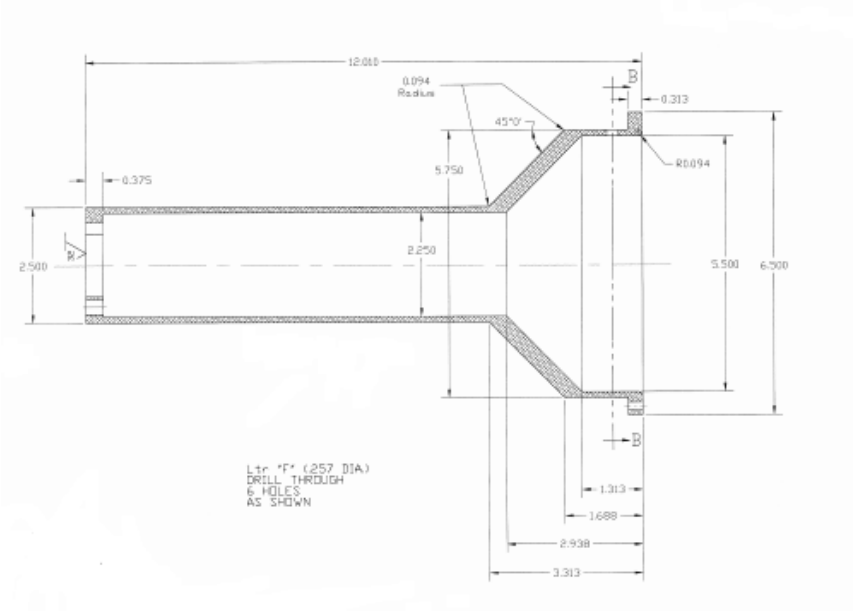

Figure 98: Center conductor of the cathode resonator for the Booster fundamental PA.

13.1 Modified Booster cathode resonator

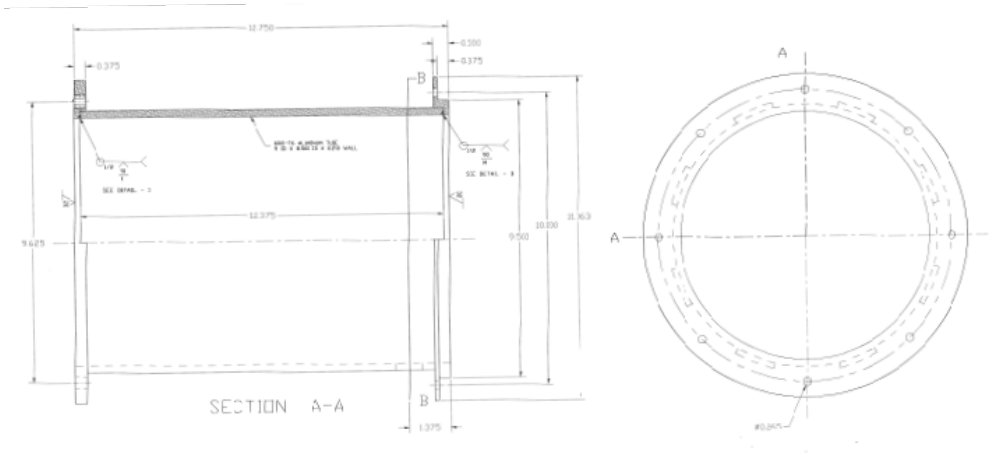

Figure 99: Outer conductor of the cathode resonator for the Booster fundamental PA.

The cathode resonator is a modified version of the fundamental Booster cathode resonator. Figure 98 shows the center conductor and Figure 99 shows the outer conductor. Since the harmonic cavities operate at a higher frequency, the inductance of the resonator must be smaller and therefore it must be shorter. A prototype version of the Booster fundamental cathode resonator was available to be modified. Both the center conductor and outer conductor were cut transversely by the same amount (to remove length), and re-welded. This is shown in Figure 100 for the center conductor.

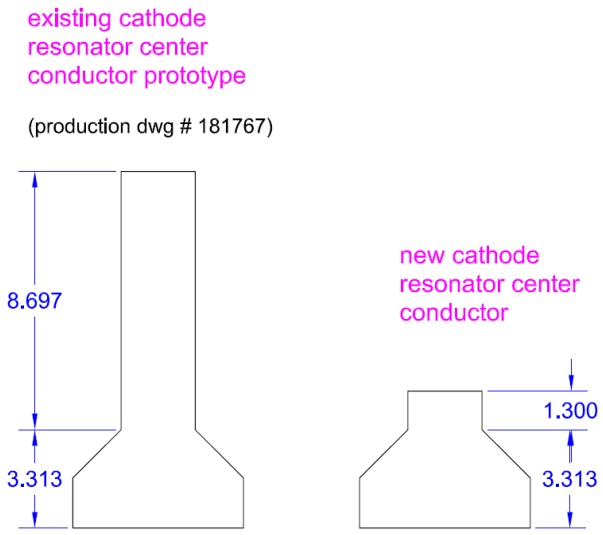

Figure 100: Modifications to the prototype Booster fundamental cathode resonator.

13.2 Cathode resonator model (R. Madrak & C.Y. Tan)

The cathode resonator model that we are using is based on the model developed by T. Berenc [46]. There are some major differences between our model and Berenc's model. The first difference is that we do not include transconductance, g_m, of the Y567B. Experimentally, we have found that $1/g_m$ in the frequency of interest is > 1 kΩ, and thus its contribution to the parallel RLC circuit is negligible when compared to the swamper resistors that contribute either 12.5 Ω or 25 Ω depending on the setup. The second difference is that we have added a series impedance, Z_b, in series with the RLC circuit. Z_b is the collective impedance of the banana plugs + adapters used to connect the solid state amplifier (SSA) to the cathode resonator. Our s11 measurements show that the banana plugs + type N to HN adapters together have a surprisingly large inductance of about 35 nH. The improved resonator model is shown in Figure 101. Although we have made a better model, and used it for our initial design, we have found that it is not very useful for absolute results. For example, the VSWR that the model calculates does not match measurement.

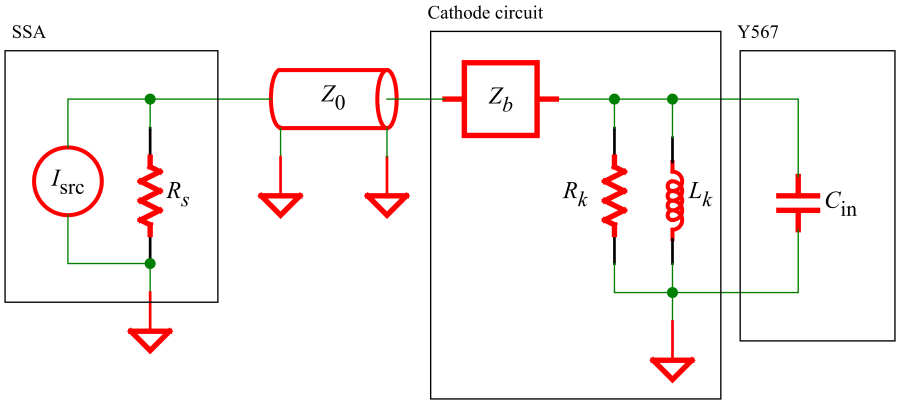

Figure 101: The resonator model for calculating the bandwidth of the cathode resonator. R_k comes from the swamper resistors, L_k is the inductance of the cathode resonator shown in Figure 100, and C_{in} is the cathode capacitance of the Y567B. Z_b is the inductive contribution from the banana plugs + adapters, Z_0 = 50 Ω is the characteristic impedance of the cable (note: In Booster fundamental cavities, Z_0 = 12.5 Ω) between the SSA and the resonator. R_s = 50 Ω is the SSA output impedance.

However, despite its shortcomings, we will continue with our analysis. The impedance of the cathode resonator shown in Figure 101 is

$$Z_c = Z_b + \frac{1}{\frac{1}{Z_{L_k}} + \frac{1}{R_k} + \frac{1}{Z_{C_{\text{in}}}}} \tag{60}$$

where $Z_{L_k} = i\omega L_k$ is the inductive impedance of the cathode resonator, and $Z_{C_{\text{in}}} = 1/i\omega C_{\text{in}}$ is the capacitive impedance at the input of the Y567B.

The input capacitance, C_{in}, has been measured as a function of frequency and is shown in Figure 102. This was done using three different cathode resonators that were connected to the Y567B for measuring the resonant frequencies. Weakly coupled probes were used in a transmission measurement (s21) so that the peak was narrow, and the resonant frequency was measured. Since the geometries of the cathode resonators are known, their inductances, L_k, are easily calculated. The Y567B input capacitance is then determined by the equation $C_{\text{in}} = \frac{1}{\omega^2 L_k}$. Since there is a large change in C_{in} in the frequency range of interest, our final choice of L_k has to be a compromise.

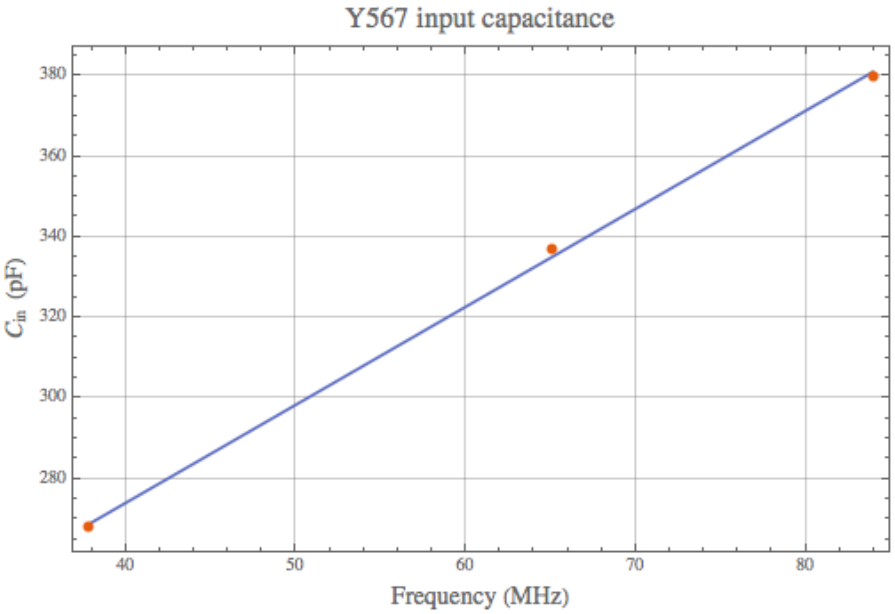

Figure 102: The measured input capacitance of the Y567B as a function of drive frequency. The red circles come from measurement.

13.2.1 VSWR example

We can use the model to calculate the VSWR so that the maximum power from the SSA is delivered to the cathode resonator. For these calculations, we will use $Z_b = i\omega \times (35 \times 10^{-9})$ Ω that was obtained from measurements. We will make the cathode resonator resonate at the midpoint between 76 and 106 MHz, i.e. 91 MHz. To do so, we must have $L_k = 7.6$ nH and $C_{\text{in}} = 361$ pF from Figure 102. The only variables left are the swamper resistance R_k that we can vary in integer fractions of 50 Ω and the characteristic impedance Z_0. An example of how the VSWR changes as function of these two variables is shown in Figure 103. The best VSWR is obtained when $R_k = 12.5$ Ω is when $Z_0 = 25$ Ω.

We have to emphasize here that the model is not that useful for predicting absolute values because it is too simplistic and does not capture the true behavior of the system. For example, we have found that when $Z_0 = R_k = 12.5\ \Omega$, the VSWR ≈ 6 at both 76 and 106 MHz, although our model says that the VSWR >10 at 76 MHz and VSWR ≈ 7 at 106 MHz.

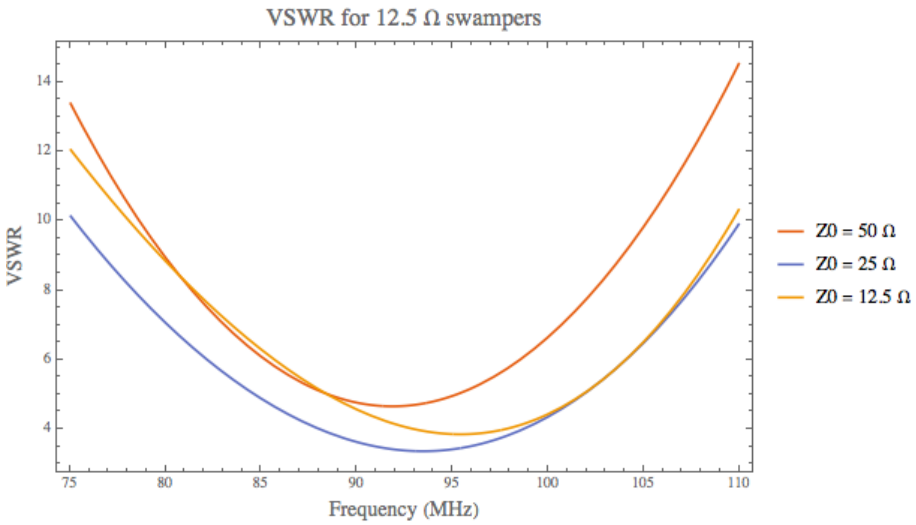

Figure 103: The VSWR calculated with the model. The VSWR predicted by the model is too pessimistic.

13.3 Matching tuning stub (J. Dey, R. Madrak & C.Y. Tan)

Note: High power tests with a newly designed cathode resonator (see section 14) demonstrated that the tuning stub is not needed. This section is left here, as is, for reference only.

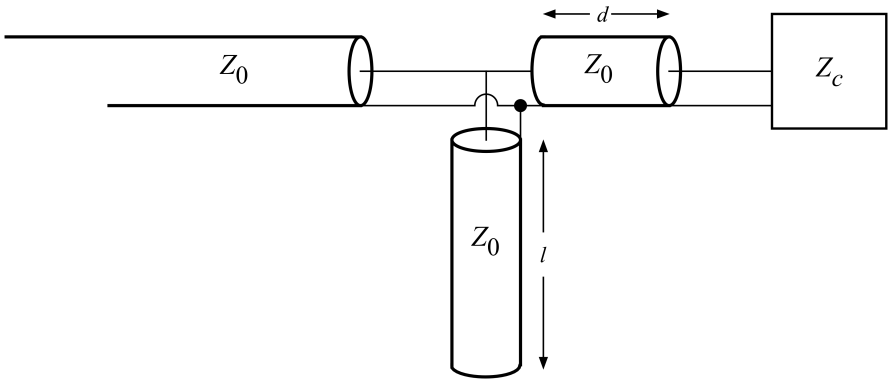

Figure 104: This is the diagram of the open tuning stub that is added before the cathode resonator Z_c for matching to Z_0. The two lengths d and l can be found so that VSWR=1 at one chosen frequency.

In order to reduce the reflected power from the cathode resonator so that the TOMCO solid-state amplifier (SSA) does not substantially de-rate (see section 13.4), it is necessary to either have a matching network or a circulator between the SSA and the cathode resonator. We choose to make an open stub tuner for matching, which is shown in Figure 104. Our requirement is VSWR ≤ 4 because this means that $\leq 36\%$ of the power is reflected. This is an acceptable limit for driving the Y567B so that it can output $>$ 100 kW. See section 13.4.

We measured the impedance of our test cathode resonator, Z_c, that has its center frequency at 94 MHz rather than at the mean frequency of $\frac{76+106}{2} = 91$ MHz. This cavity has $(4 \times 50)\ \Omega$ swamper resistors in parallel connected to it. The results are shown in Figure 106. We can use these results and together with the standard method used for tuning stub matching (for example in Pozar [20], section 5.2), to find d and l. We found that for $Z_0 = 50\ \Omega$ (see Figure 104) and choosing, by trial and error, the matching frequency, $f_0 = 105.5$ MHz, we have $d = 0.02$ m and $l = 0.59$ m (or equivalently an electrical length of 1.9 ns). The required bandwidth is 30 MHz and from our model, we have a VSWR of 3.3 at $(94 - 15) = 79$ MHz and 4.4 at $(94 + 15) = 109$ MHz. The trick that we have done here for increasing the bandwidth is that, instead of selecting f_0 to be in the middle of the required frequency range, we have chosen f_0 to be close to the outside of this range. This, then, allows the capacitive part of the length l transmission line below f_0 to cancel out more of the inductive contribution from the banana plugs + type N to HN adapters.

We have found experimentally that by starting with the d and l found from above, we can tune the stub so that the VSWR ≈ 4 with a 30 MHz bandwidth. Figure 106 is the comparison between theory and the measured VSWR of the cathode resonator with the tuning stub added. It is clear from this figure that we have the required bandwidth and the VSWR is better at 109 MHz and worse at 79 MHz. Our final cathode resonator with the correct center frequency and a high power tuning stub will need to be tuned so that the required VSWR ≤ 4 occurs at both 76 MHz and 106 MHz.

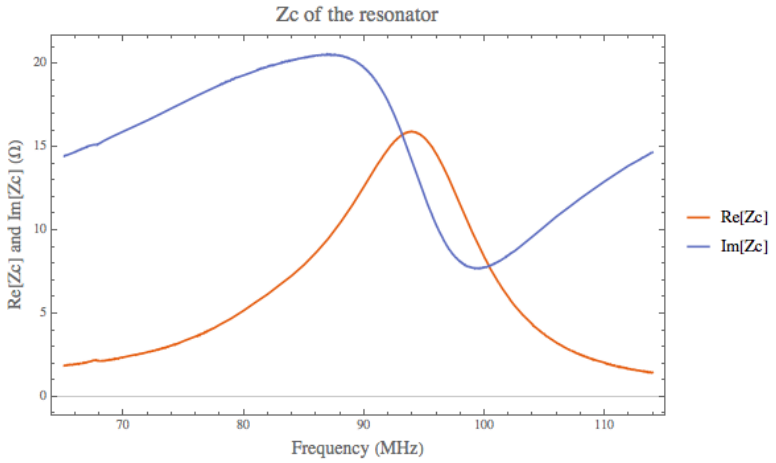

Figure 105: The impedance of the test cathode resonator with (4×50 Ω) swamper resistors in parallel. It resonates at 94 MHz.

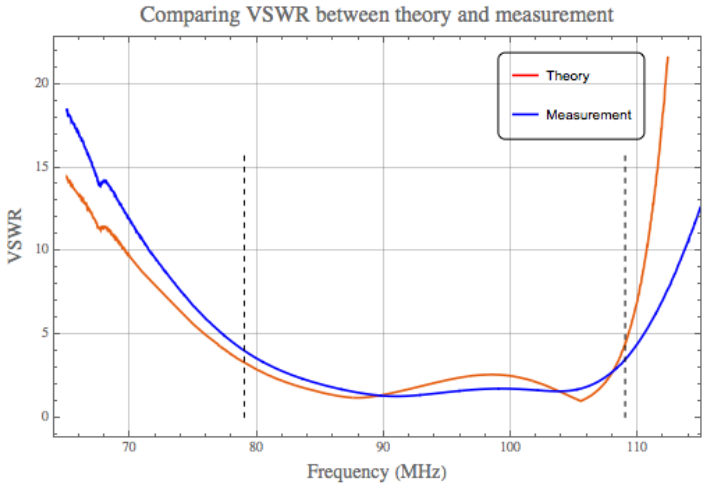

Figure 106: The measured VSWR versus the theoretical VSWR that has center frequency at 94 MHz. The dotted vertical lines indicate the locations of (94–15) MHz and (94+15) MHz. The measured VSWR at these two locations is approximately 4.

13.3.1 The matching tuning stubs

The low power matching tuning stub is shown in Figure 107. The open end of the tuning stub l consists of one 1 ns cable + 4 bullets + 4 barrels which together gives 1.8 ns of electrical length. This is about the same electrical length of 1.9 ns that was calculated in the previous section. Decreasing the length of the RF connection to about 0.06 ns (i.e. half a BNC tee because we will assume that the "parallel" connection happens in the middle of the tee), which was also calculated from the previous section, at the resonator itself increases the bandwidth of the match. This decrease was achieved by replacing the original HN connector with a BNC connector. The swamper resistance in this case is 12.5 Ω.

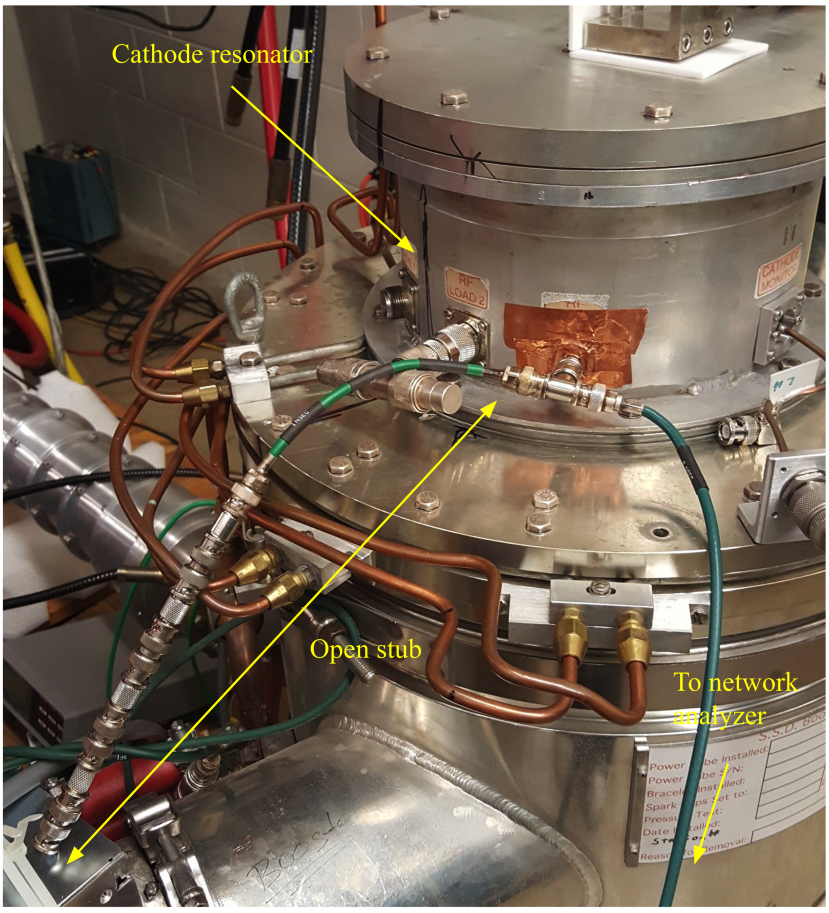

Figure 107: The low power open tuning stub. The open end of the stub consists of one 1 ns cable and 4 bullets + 4 barrels to give 1.8 ns of electrical length.

13.4TOMCO SSA de-rate table

The TOMCO SSA de-rates from 8 kW as a function of VSWR [47]. However, the amplifier does not limit output unless the amount of reflected power is above the threshold for 2 seconds, for which it can withstand 100% reflected power at full output. Since we operate in pulsed mode with pulse widths substantially less than 2 seconds, this situation will never be realized. See section 14.

Forward power degradation (VSWR)	Percent of full power
1	100
1.5	100
2	80
3	60
5	40
10	30
∞	20

Table 10: TOMCO SSA de-rate table. The SSA is capable of supplying 8 kW at full power.

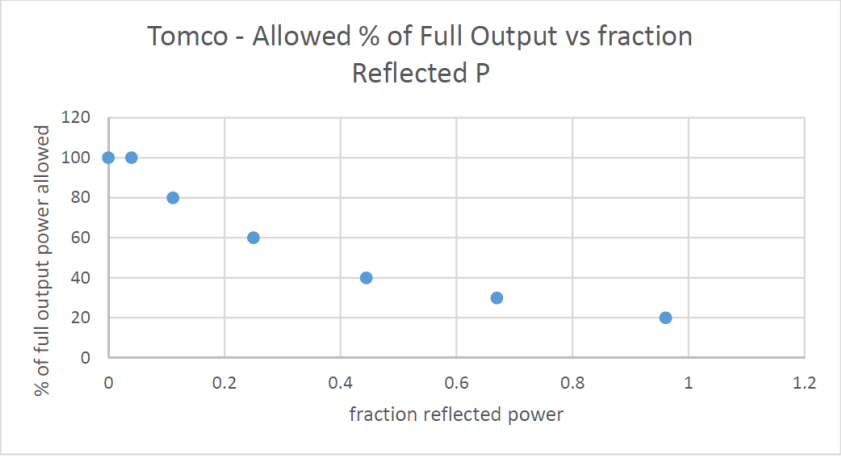

Figure 108: The de-rate table is plotted here.

14 Y567B measurements [48](R. Madrak & J. Reid)

We will use the same power tetrode (Eimac Y567B) which is used in the main (fundamental frequency) Booster cavities (~38 - 53 MHz), the Main Injector, and the Recycler (~53 MHz). According to the specifications for the Y567B (Eimac 4CW150000 [49],), it can operate with up to 150 kW of power dissipated in the anode, and up to 108 MHz. In present Booster cavities, the output maximum is 100 kW, with an efficiency of ~60 – 70%. The 2nd harmonic cavity is expected to have shunt impedances of 96 kΩ and 180 kΩ at 76 and 106 MHz, respectively. For the required peak voltage of 100 kV across gap, substantially less power will be needed by the Booster 2nd harmonic cavities when compared to the existing cavities operating at the fundamental frequency. Nevertheless, we must verify that the tetrode can produce the required output power at the frequencies of the 2nd harmonic.

14.1 The power amplifier and test station

Testing and use of the tetrode at a given frequency requires a module ("power module") to mechanically support the tube and supply voltage to its various electrodes, a drive resonator ("cathode resonator"), and an output resonator ("anode resonator"). The tetrode, power module, and cathode resonator together are referred to as the PA (power amplifier).

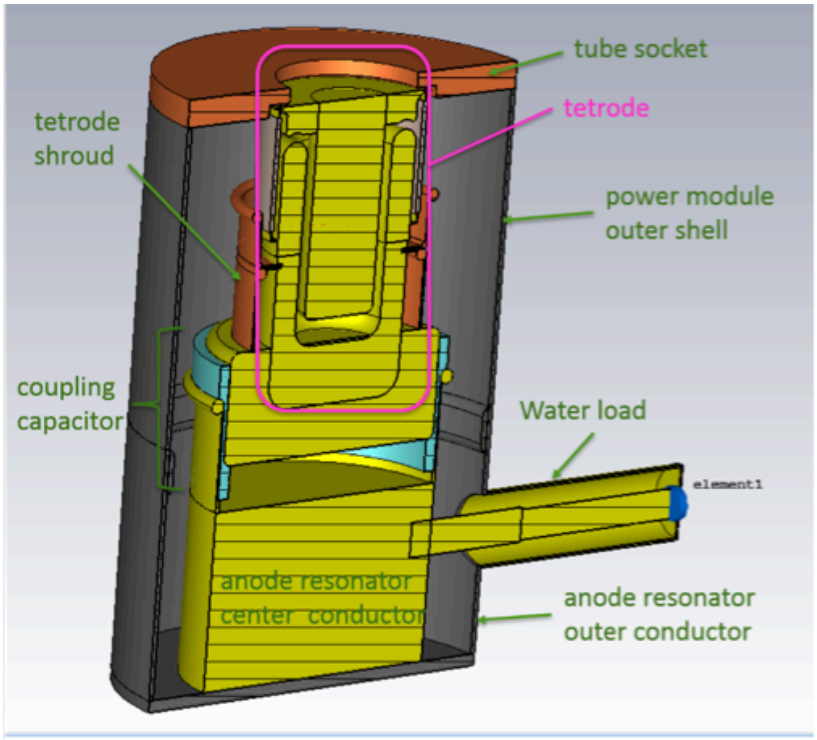

Figure 109: Drawing of the PA test setup.

The power module is essentially a shell with the tube socket. The drive resonator is a coaxial line which looks inductive. This ideally should cancel the imaginary part of the tube input impedance, which is capacitive. "Swamper loads" (two 50 Ω loads in parallel) are connected to it so that the resonance is broad, and the tube can be driven over a wide frequency range by a solid state amplifier which would ideally see a purely resistive 50 Ω load.

The anode resonator serves as a (non-tunable) stand-in for a real cavity during PA testing. A water cooled 50 Ω load is attached to it to mimic the power dissipation in the ferrite of a real cavity with a tuner. The resonator and power module form a shorted transmission line; a different resonator must be constructed for each frequency at which we want to test the tube. Since a spare Booster power module was available, we used this for our testing. In the case of the real 2nd harmonic cavity, the design for the power module is smaller so that the input part of the cavity does not excessively detune it. For the PA testing we also use the same coupling scheme as the main Booster PAs. That is, a shroud is attached to the anode of the tetrode and inserted into a blocking (coupling) capacitor which is mounted on the anode resonator center conductor. This scheme will also be different in the real 2nd harmonic cavity, but it is suitable for testing the tetrode.

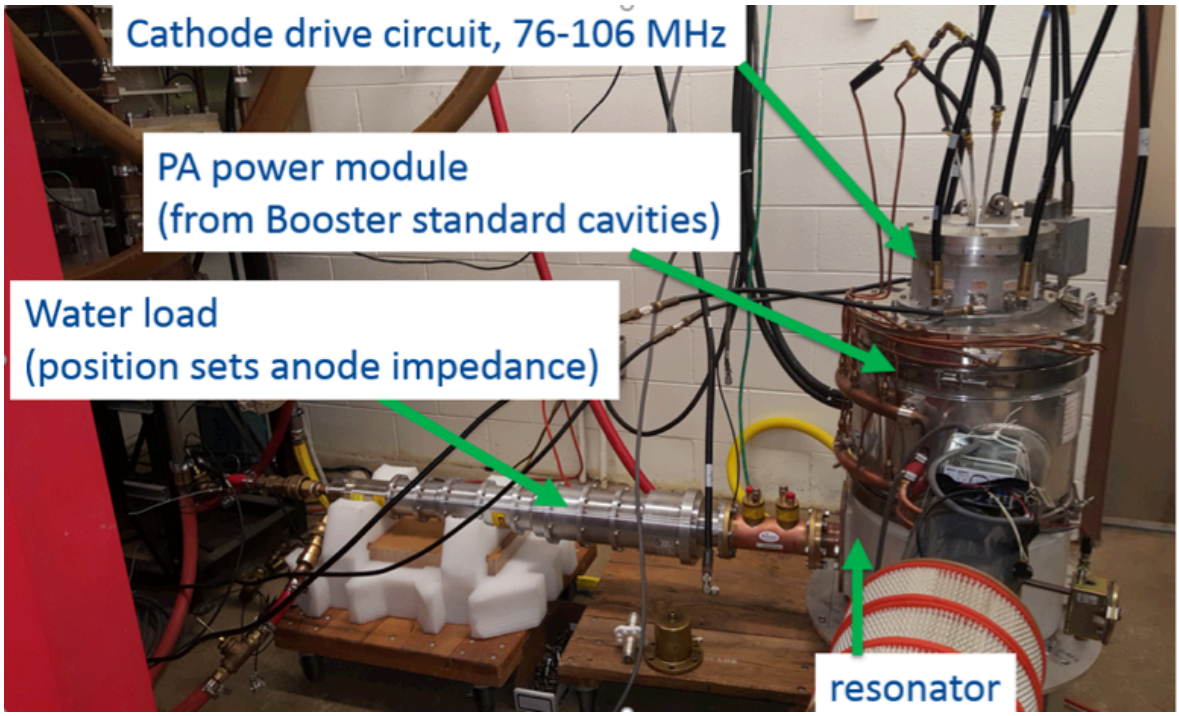

Figure 110: Photograph of the PA power test setup.

Given the components used, the 2nd harmonic test station looks very much like a fundamental Booster PA test station, except that the anode and cathode resonators are different sizes. The cathode resonator was constructed from a prototype fundamental cathode resonator by shortening it. (See section 13 for more details.) A new anode resonator was constructed so that the complete setup would resonate at 76 MHz. A drawing and photograph are shown in Figure 109 and Figure 110.

The first anode resonator was designed to test the PA at 76 MHz. The setup was modelled using a transmission line plus lumped circuit analysis with Agilent (now Keysight) Advanced Design System (ADS), and also with CST Microwave Studio. The simulations are discussed in section 14.2.

After construction of the first resonator, the measured frequency was only 71.7 MHz. Power tests were done at this frequency, and then later the resonator was modified to test at exactly 76 MHz.

The PA was also tested at 106 MHz. Since a quarter wave resonator would have been too small to be practical (for instance, to connect the load), the 106 MHz resonator plus PA form a 3 /4 resonator. A picture is shown in Figure 111(a).

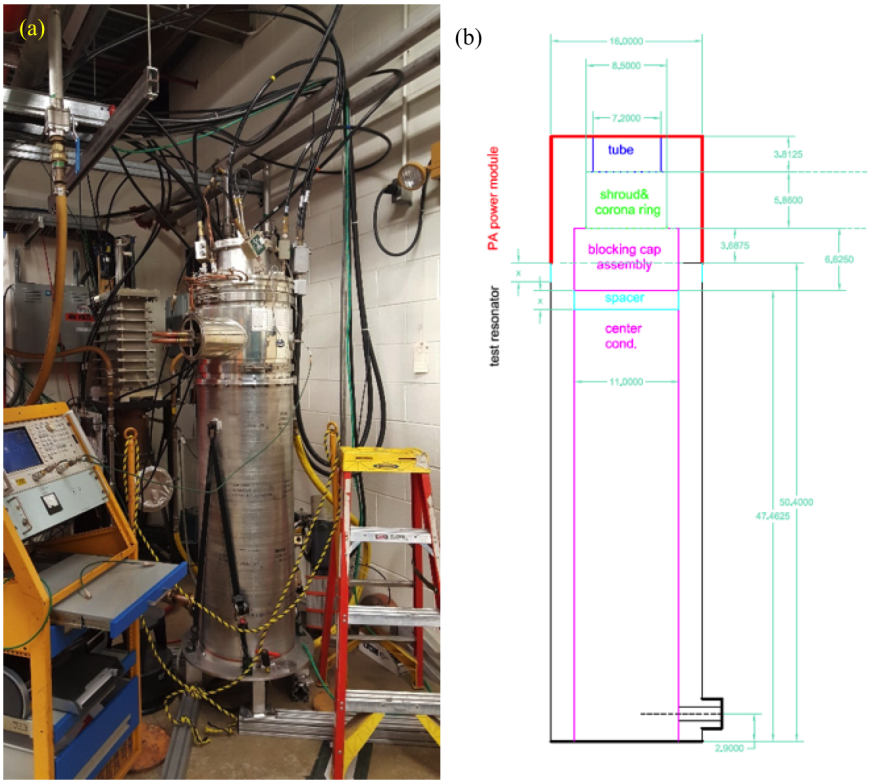

Figure 111: (a) Photograph of the 106 MHz PA test setup. (b) Drawing that shows a removable spacer (2" long) that was included in the design.

14.2 Simulations and anode resonator design

To determine the geometry of the anode resonator such that the system would resonate at 76 MHz, a transmission line model of the existing setup for the fundamental Booster PA tests was constructed. The transmission line dimensions are determined by the diameters and lengths of the anode resonator inner and outer conductors, tube anode diameter, and power module outer shell diameter. The resonator is shorted at one end and the other end is foreshortened by the tube output capacitance of ~60 pF. The blocking capacitor is represented by another lumped capacitance of 1000 pF. The model in the Keysight/Agilent Advanced Design System (ADS) software is shown in Figure 112. The simulation predicted a resonant frequency of 53 MHz and a Q of 60, which agreed with what was measured. The dimensions of the transmission line corresponding to the anode resonator part of the setup were then modified so that the frequency of the setup was 76 MHz. Changes are shown in Figure 113.

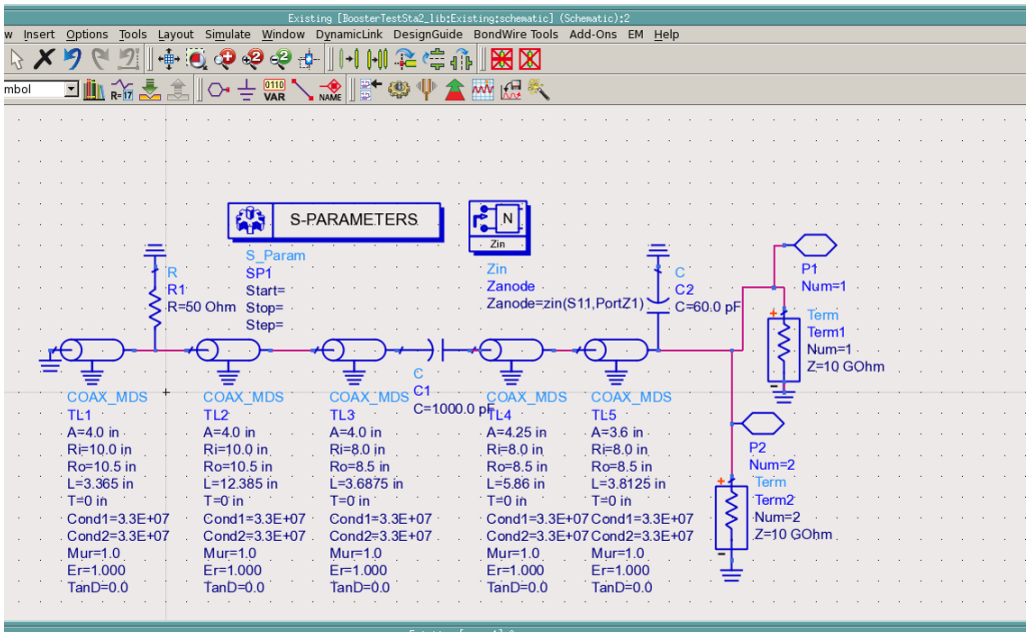

Figure 112: The transmission line model of the Booster fundamental PA test setup in Keysight/Agilent ADS.

As a check, the anode resonator and tube were also simulated in CST Microwave Studio. In the first (simplified) model the output capacitance of the tube was represented by a physical parallel plate capacitor at the end opposite the short. Again, the fundamental PA test station was modeled first and tuned (by adjusting the capacitor gap) until it predicted the correct resonant frequency. The model was then modified using the anode resonator dimensions which ADS had shown to give a resonant

frequency of 76 MHz. The CST model predicted 78 MHz. It was decided that this was sufficient agreement, especially since the simulations were both using simplified models of the tetrode. (The coupling capacitor was simplified as well).

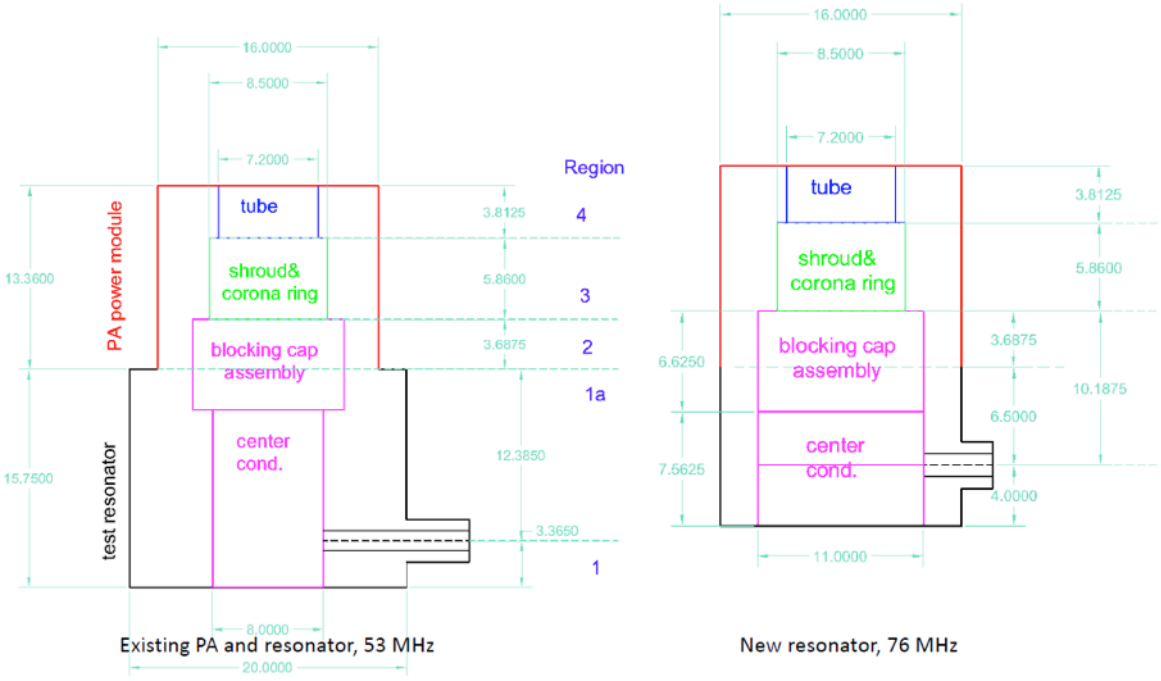

Figure 113: Modifications to the PA test setup.

The anode resonator was constructed according to the calculated dimensions, however, the resulting resonant frequency of the system was 71.7 MHz and not the desired 76 MHz. We proceeded with power tests since it was likely that it was sufficient to test the PA near 76 MHz. In order to test the PA at exactly 76 MHz, a modification to the setup was designed. A ring was manufactured and bolted to the bottom of the anode resonator, making it effectively shorter and higher frequency. A modification to the load connection scheme was also made. In order that the impedance seen by the tube was optimal and similar to that in the 71.7 MHz tests, the connection scheme for the load was changed from a direct straight across connection to one in which the conductor attached to the load loops up and back down again, as shown in Figure 114. (In order to maintain the same impedance with the added ring and a straight across connection, the connection point would have had to be moved up further than the end of the anode resonator center conductor, into the coupling capacitor region.)

For the design of the 106 MHz test station, we again used a model similar to that shown in Figure 112. The main differences were the following. First, the 106 MHz resonator and PA formed a three quarters wavelength resonator, instead of a quarter wavelength resonator. Second, the value of the tube output capacitance was changed from 60 pF to 73.1 pF, which is the capacitance, which, when used in

the model for the initial 71.7 MHz resonator, gave the correct measured frequency. Nevertheless, we had seen before that extrapolating from 53 MHz to 76 MHz gave a cavity with a low frequency. In anticipation that this might happen again, we designed the 106 MHz cavity to have 2 inch long removable spacers on the inner and outer conductors. The cavity nominal predicted frequency was 106 MHz with the spacers in. If the frequency was too low, the spacers could be removed or shortened. As it turned out, the test cavity was exactly on resonance at 106 MHz with the spacers removed. The change in the design to 106 MHz is shown in Figure 111(b) to be compared with Figure 113.

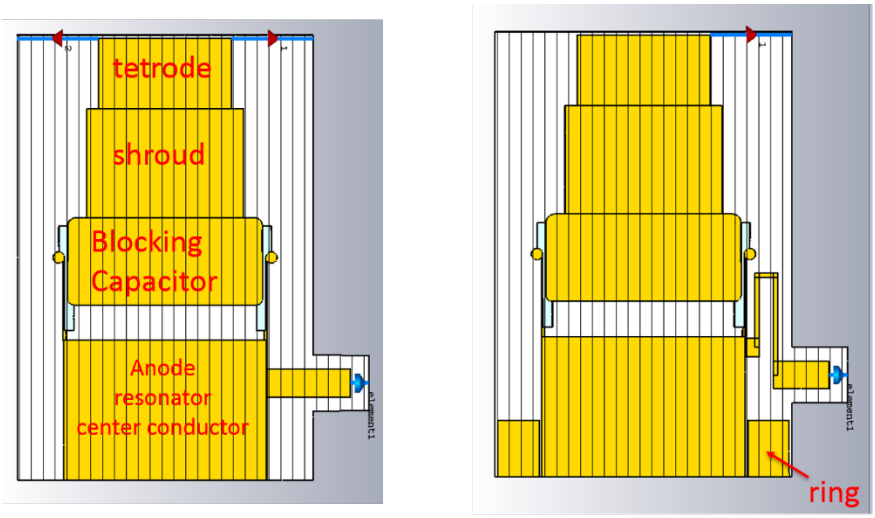

Figure 114: Original (left) and modified (right) anode resonator. The modified setup contains a ring at the bottom to increase the resonant frequency to from 71.7 to 76 MHz. In addition, the load connection geometry is changed so the tetrode sees the optimal impedance.

14.3 Cathode resonator

Editor's note: A more detailed discussion of the cathode resonator can be found in section 13.

A schematic of the drive circuit is shown in Figure 115. The amplifier, made by Tomco [47], has a maximum output power of 8 kW. It is meant to drive a 50 Ω load. To protect the amplifier components, forward output power is limited depending on the fraction of reflected power as shown in Figure 108 in section 13.4. However, the amplifier does not limit output unless the amount of reflected power is above the threshold for 2 seconds, for which it can withstand 100% reflected power at full output. Since we operate in pulsed mode with pulse widths substantially less than 2 seconds, this situation will never be realized.

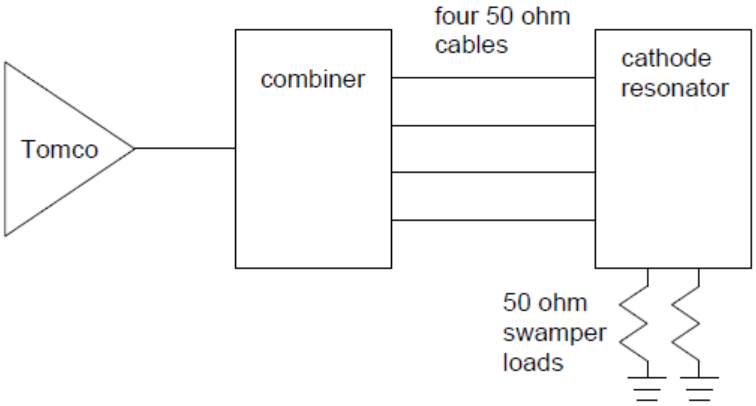

Figure 115: The schematic of the drive configuration.

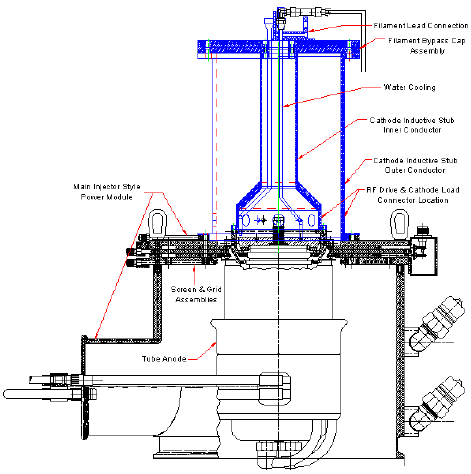

Figure 116: Cross section of the fundamental Booster PA. The cathode resonator is drawn in blue.

Four 50 Ω Heliax cables connect the combiner outputs to the cathode resonator, through HN connectors and banana plugs (inside the resonator).

The cathode resonator was modeled in a manner similar to that of the anode resonator, and is also discussed in Ref [46]. That is, it is essentially a shorted quarter wave resonator foreshortened by the tube input capacitance of 250 pF. Note, according to [46] this includes both the tube inter-electrode capacitance and the capacitance of the tube socket. The frequency of the new resonator, the "76 MHz

cathode resonator", was shifted up by shortening the Booster prototype fundamental resonator (see Figure 116 and Figure 100) so that its peak was near 76 MHz. As with the fundamental resonators, this frequency was chosen as the peak (as opposed to mid-range) since it is where the shunt impedance of the cavity is the lowest and thus where the most drive power would be needed.

The simulation predicted that the response would be down by only 1.1 dB at 106 MHz, compared to 76 MHz. Unfortunately, this turned out to not be true. In fact, with this cathode resonator, we have measured in low power tests that the fraction of reflected power is 77% at 106 MHz; at 76 MHz only 5 – 10% is reflected. The failure of the simulation to accurately predict the falloff in response and is larger than expected reflection is possibly due to a frequency dependence of tube input capacitance.

One way to improve the situation, which has been studied at low power levels and has shown promise (see section 13.3), is to attach an open stub (made from Heliax cable) to the resonator to adjust the impedance. Here, we are shaping the response curve as a function of frequency to something which is more desirable. It turned out to be sufficient to slightly modify the design of cathode resonator — this time, aiming for maximum response between 76 and 106 MHz as opposed to at 76 MHz. So the response at 76 MHz is inferior to that of the initial resonator, but is nevertheless workable at both frequencies. This "modified cathode resonator" was shorter than the 76 MHz cathode resonator by 0.18". Also, the center conductor was not tapered; the OD was constant (5.75"), and the same OD as the base (larger OD part) of the 76 MHz cathode resonator. Before building the modified cathode resonator, we constructed one out of sheet metal and measured the reflected power at low power levels. We then iterated upon this to obtain the best possible responses at both 76 and 106 MHz.

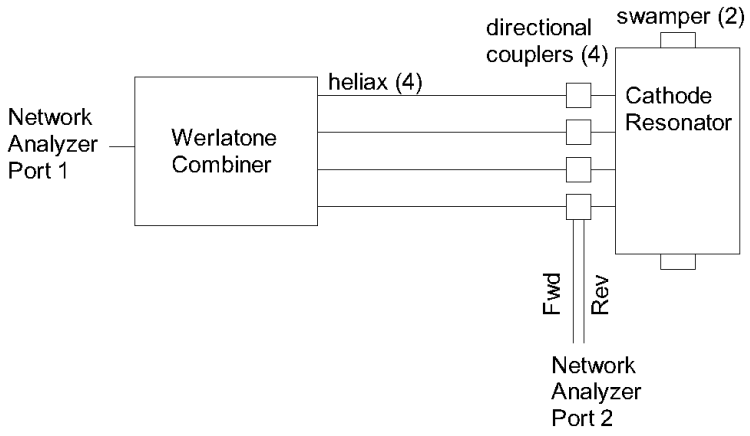

Figure 117: Low power measurement setup for 76 MHz for measuring the cathode resonator reflected power.

Figure 117 shows the setup used to measure the low power response of the cathode resonators with no high voltage on the tetrode. The filaments were on. Figure 118 shows the directional coupler measurements of the percentage of reflected power for the (1st) 76 MHz cathode resonator. As we will see in the next section, this is lower by up to around 5% when the tetrode is actually on, at 76 MHz. Figure 119 shows the response of the modified cathode resonator with the same low power setup. At 76 MHz ~32% of the power is reflected; at 106 MHz, ~59% of the power is reflected.

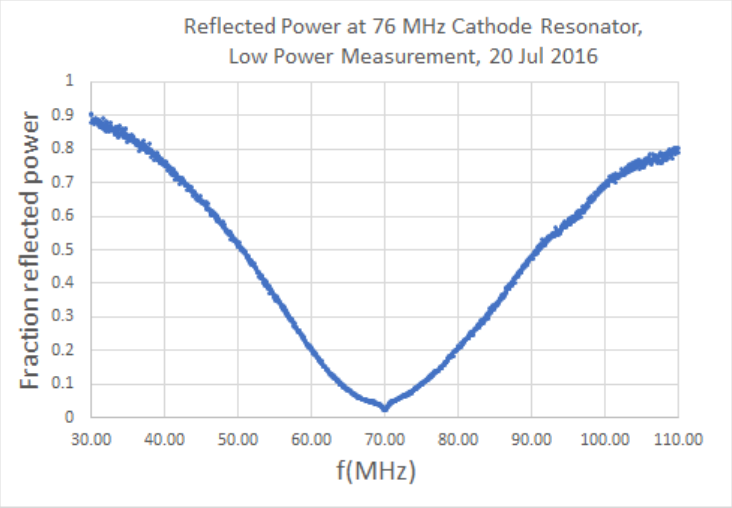

Figure 118: Measurement of the 76 MHz cathode resonator reflected power before modifying the resonator.

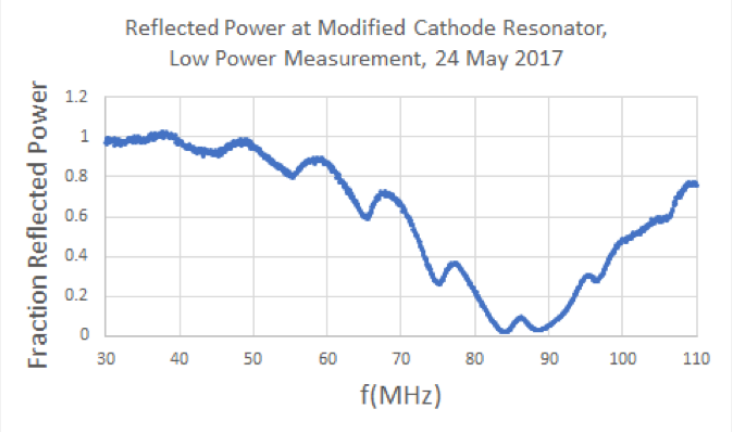

Figure 119: Measurement of the 76 MHz cathode resonator reflected power.

The modified cathode resonator was the one used in the power test at 106 MHz. For high power tests at 76 MHz, the PA was initially tested using the 76 MHz cathode resonator, and was then tested a second time with the modified cathode resonator. Again, in the high power tests, the measured reflected power was less than or equal to that measured in the low level tests. (See section 14.4 below.)

14.4 High power tests

The PA was first tested at 71.7 MHz in April 2016 and then at 76 MHz, with a modification to the anode resonator, in January 2017. The impedance seen by the tetrode is set by the vertical position of the 50 Ω water load, which is adjustable. We aimed for $Z_0 = \frac{V_a(DC)}{I_a(DC)} \approx 2$ kΩ where $V_a(DC)$ and $I_a(DC)$ are the DC anode voltage and current. Following Carter [36], by Fourier analysis for class B [5] operation, this corresponds to an impedance at the RF frequency of $Z_1 = {}^{2}/_{\pi}\, Z_0$.

The test was performed with 25 – 50% duty factor and 40 ms wide RF pulses. Power dissipated in both the anode and load were determined calorimetrically by measuring the flow to each and the temperature differential in the cooling water. As a cross check, power dissipated in the load was also measured using a directional coupler in line with it. Other measured quantities were DC anode voltage and current, forward and reflected drive power, and anode and cathode monitor response. Forward and reflected drive power were measured by one directional coupler on the output of the drive amplifier, and also by one of four directional couplers on the four inputs to the cathode resonator. A schematic of the test setup is shown in Figure 120.

For the main study, several data points were taken starting at an anode voltage of 12 kV and increasing it to 21 kV. At each point, the drive power was adjusted so that the screen current was 300 mA. In this case the tetrode was operating with an efficiency of $\geq 70\%$. For another study (only at 76 MHz), the anode voltage was kept constant at 21 kV and the drive power was varied, regardless of the screen current or efficiency. This was done in the interest of measuring output power in the case where the drive power is small due to poor impedance matching to the cathode resonator.

[5] Technically, the amplifier is operated as class AB, but since the conduction angle is not very much more than 180°, this estimate can be used.

For the main study, several data points were taken starting at an anode voltage of 12 kV and increasing it to 21 kV. At each point, the drive power was adjusted so that the screen current was 300 mA. In this case the tetrode was operating with an efficiency of 70%. For another study (only at 76 MHz), the anode voltage was kept constant at 21 kV and the drive power was varied, regardless of the screen current or efficiency. This was done in the interest of measuring output power in the case where the drive power is small due to poor impedance matching to the cathode resonator.

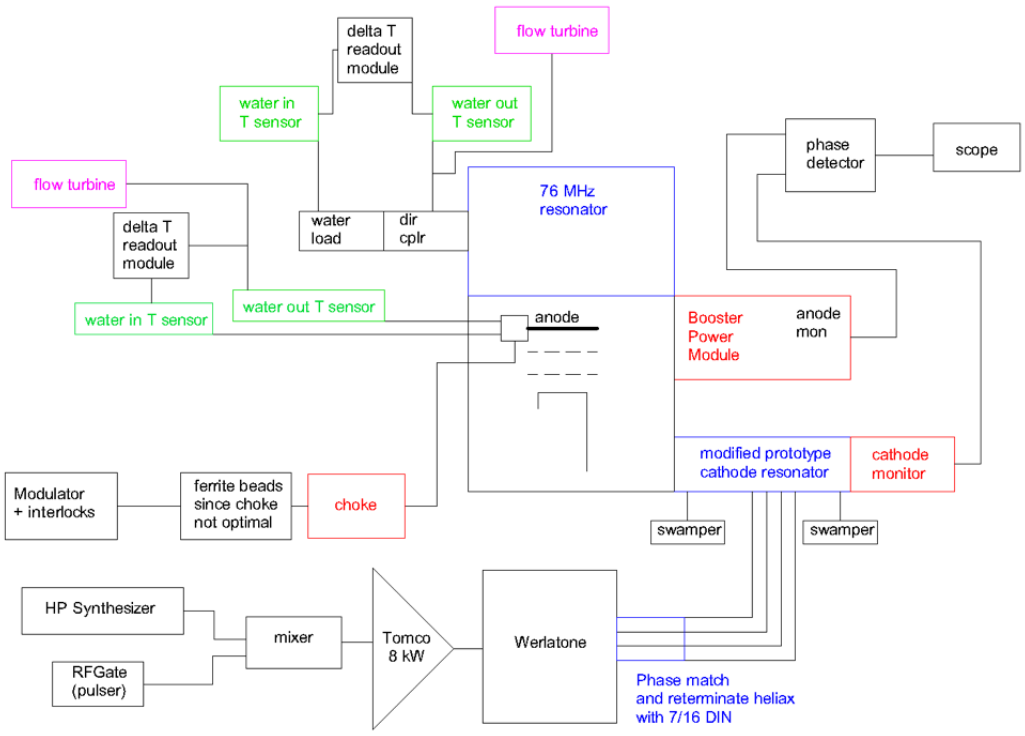

Figure 120: Schematic of the PA test setup.

For the main study, several data points were taken starting at an anode voltage of 12 kV and increasing it to 21 kV. At each point, the drive power was adjusted so that the screen current was 300 mA. In this case the tetrode was operating with an efficiency of 70%. For another study (only at 76 MHz), the anode voltage was kept constant at 21 kV and the drive power was varied, regardless of the screen current or efficiency. This was done in the interest of measuring output power in the case where the drive power is small due to poor impedance matching to the cathode resonator.

In the 76 MHz power test with the 76 MHz cathode resonator, A maximum output power of 138 kW was obtained with an anode voltage of 21 kV and forward drive power of 3 kW. The tube efficiency was 70%. Similar results were obtained in the 71.7 MHz test.

The tetrode was next tested at 106 MHz, with the modified cathode resonator (see section 14.3). Plots are shown in Figure 121 to Figure 124. In these plots, "dir cplr" refers to the directional coupler on the output of the drive amplifier. "DC 1/4 x 4" refers to the power at one of four directional couplers on the input to the cathode resonator. The power in one of these has been multiplied by four.

The final test conducted was again at 76 MHz, but this time with the modified cathode resonator. Plots are shown in Figure 125 to Figure 128.

Given the predicted shunt impedances of 96 kΩ and 180 kΩ at 76 MHz and 106 MHz, respectively, we expect we will need 52 kW and 28 kW to produce a peak voltage of 100 kV in the cavity. Technically, for, extraction, only 30 kV is needed, in which case the PA output is only 2.5 kW. For transition, it is likely that more than one cavity will be needed. As shown in the plots referenced above, the tetrode can produce more than the required amount of power at both frequencies, using the modified cathode resonator. In addition, the drive powers (and associated fraction of power reflected) required to produce these output power levels are within the safe operating range for the drive amplifier, as shown in Figure 108.

Additional plots and more detail can be found in Ref. [48].

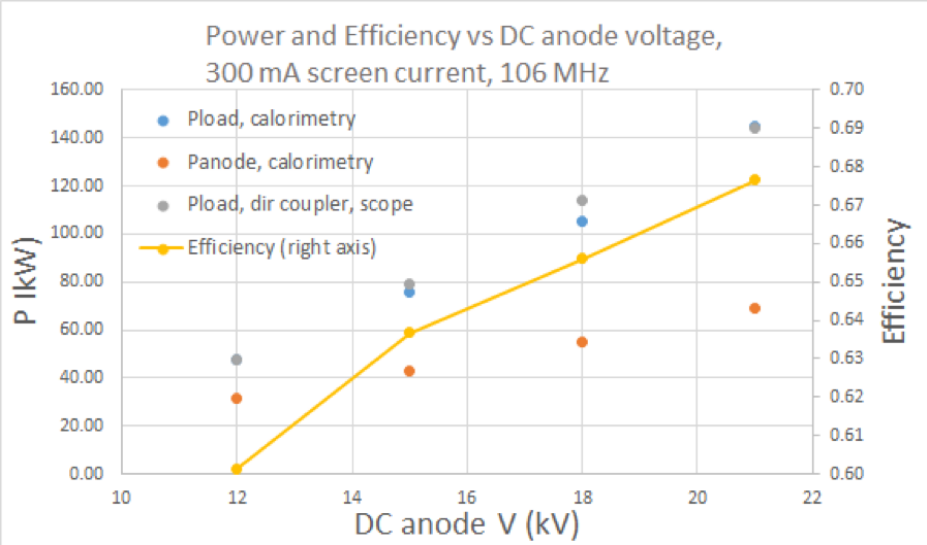

Figure 121: Output (load) power, power dissipated in anode, and efficiency for each value of DC anode voltage from the 106 MHz test. At each point the drive power was set to produce 300 mA of screen current.

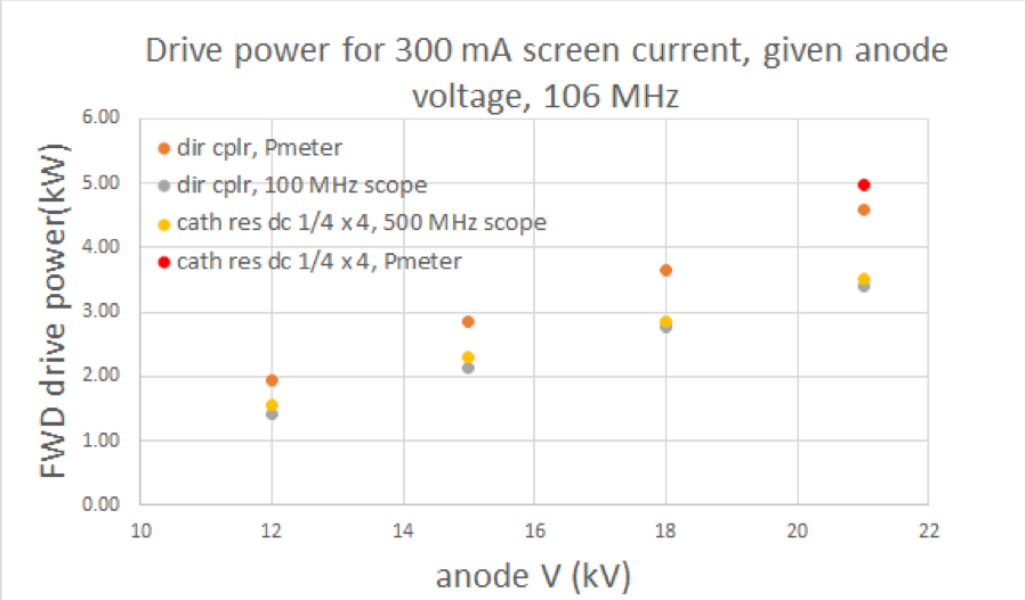

Figure 122: Drive power used at each anode voltage setting to produce 300 mA of screen current from the 106 MHz test. The measurements using the dedicated power meter (Pmeter) are more accurate. Additional measurements of the voltage were taken on the oscilloscopes, and power was calculated. This serves mainly as a cross check.

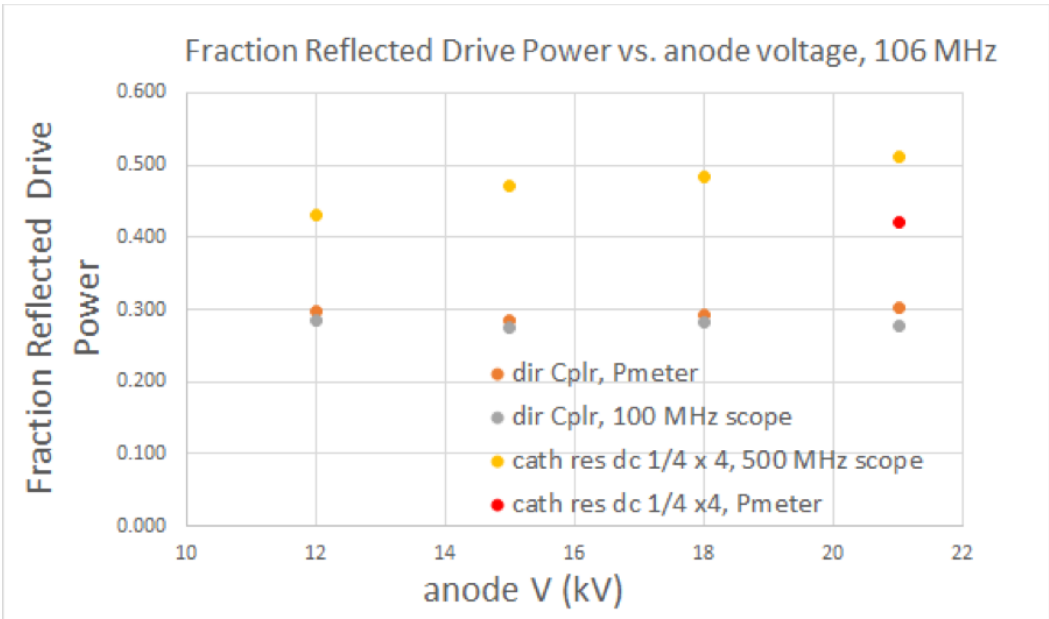

Figure 123: Fraction of reflected power, measured in several ways, for each DC anode voltage from the 106 MHz test.

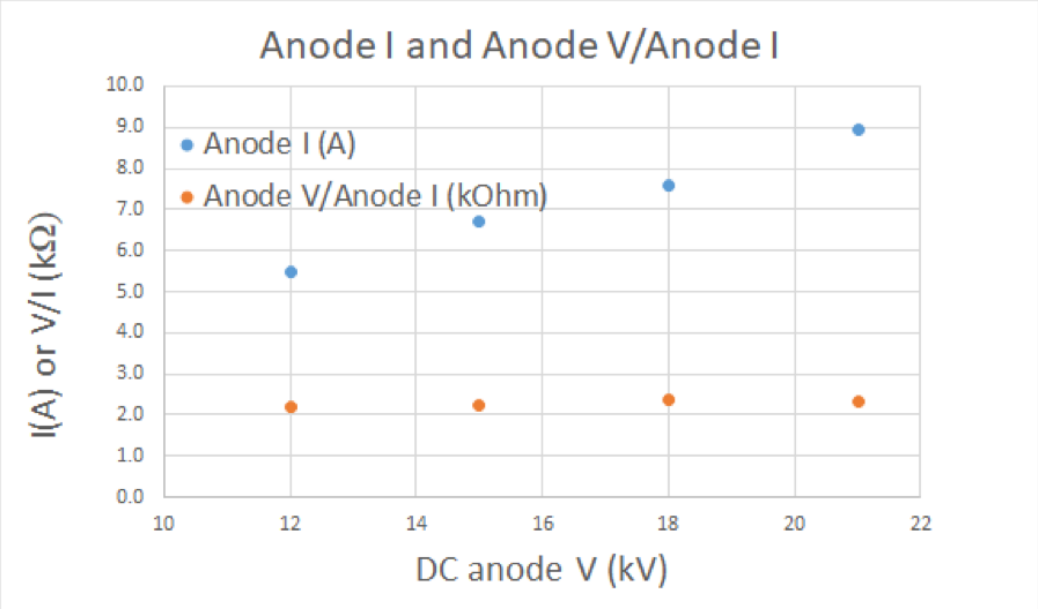

Figure 124: DC anode voltage and current for 300 mA screen current from the 106 MHz test.

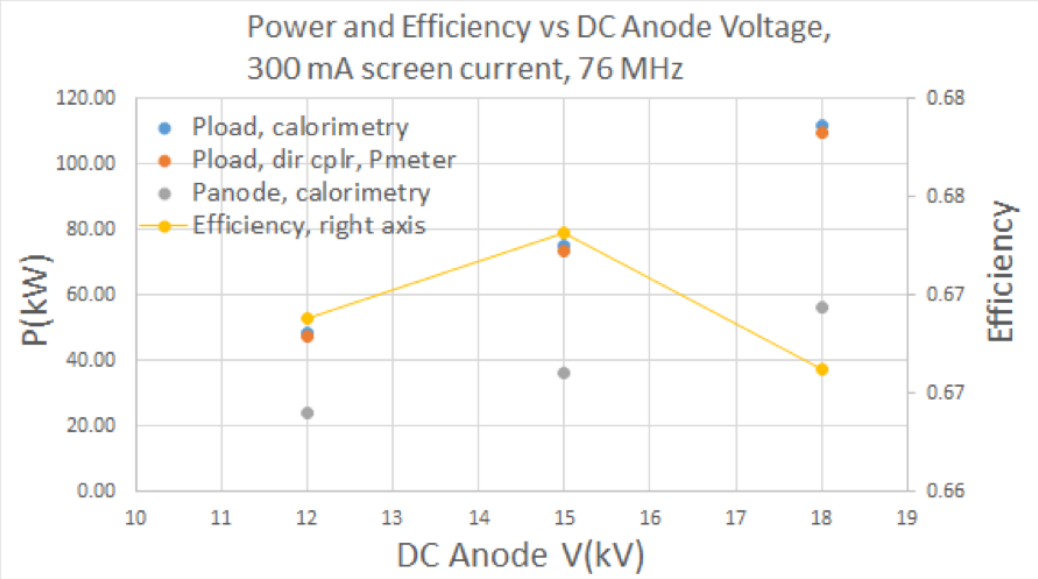

Figure 125: Output (load) power, power dissipated in anode, and efficiency for each value of DC anode voltage from the final 76 MHz test. At each point the drive power was set to produce 300 mA of screen current.

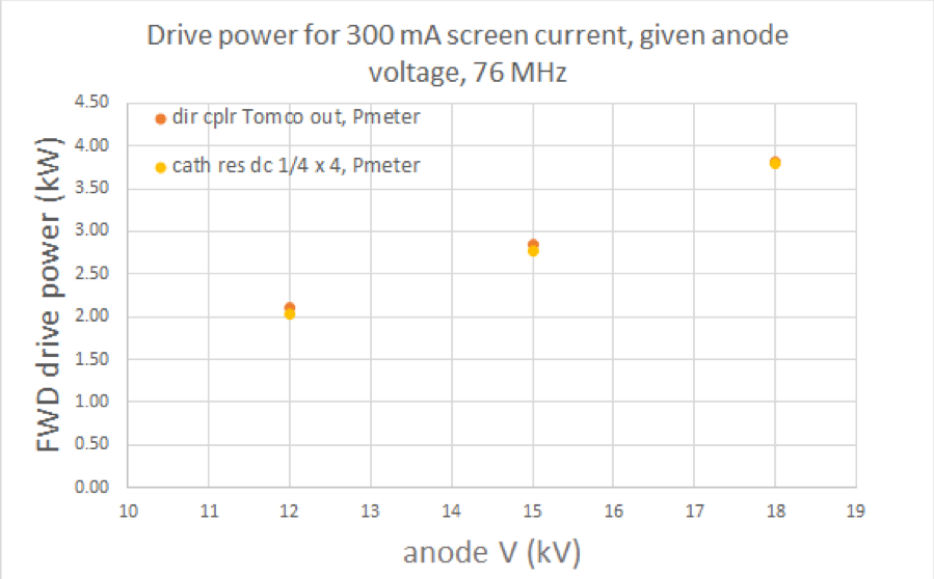

Figure 126: Drive power used at each anode voltage setting to produce 300 mA of screen current from the final 76 MHz test. The measurements using the dedicated power meter (Pmeter) are more accurate. Additional measurements of the voltage were taken on the oscilloscopes, and power was calculated. This serves mainly as a cross check.

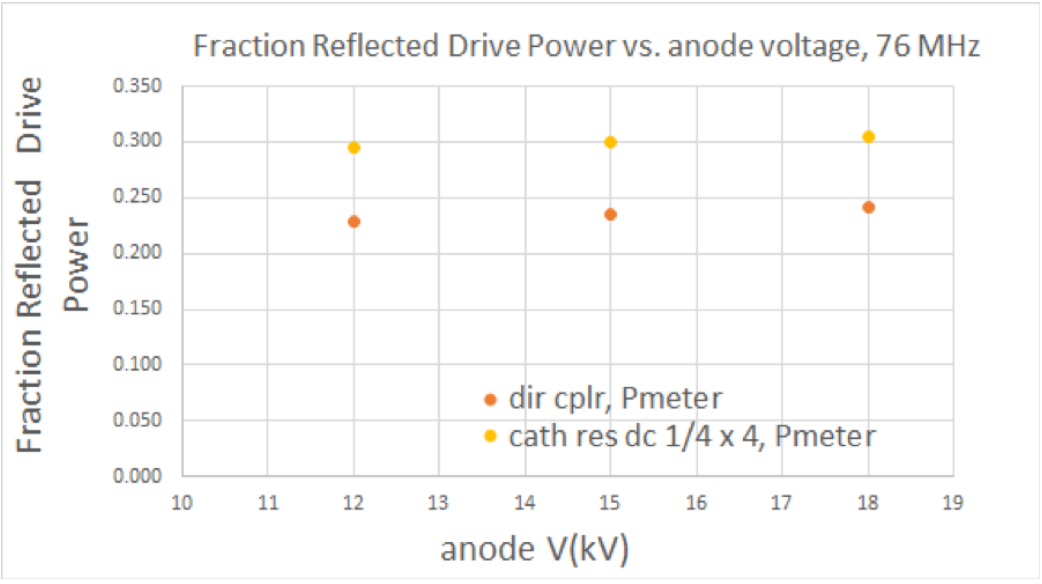

Figure 127: Fraction of reflected power, measured in several ways, for each DC anode voltage from the final 76 MHz test.

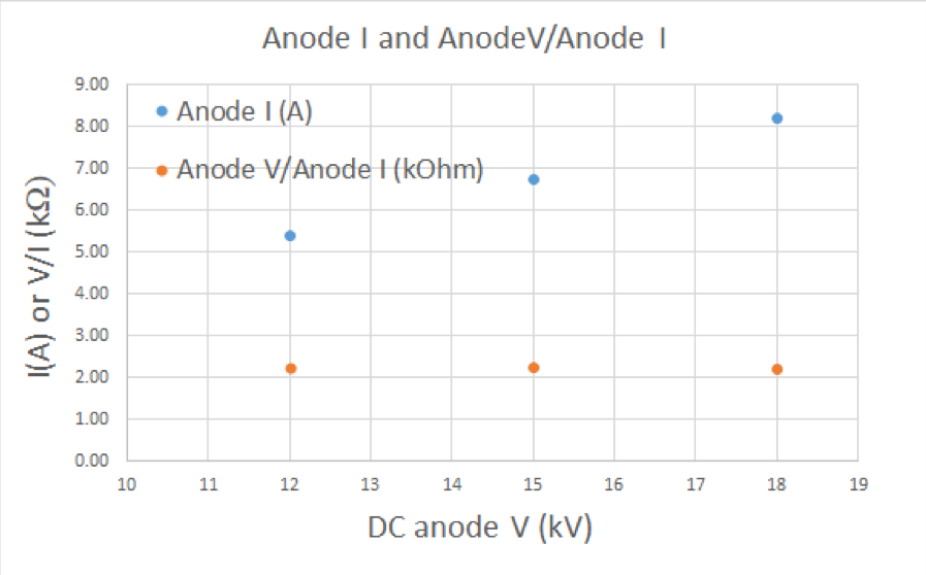

Figure 128: DC anode voltage and current for 300 mA screen current from the final 76 MHz test.

• • •

15 Mock cavity measurements (K. Duel, R. Madrak, G. Romanov, I. Terechkine)

In the interest of validating the simulations, a model cavity was constructed. The goal was to measure the frequencies of the fundamental and higher order modes, as well as the corresponding shunt impedances and Qs, as a function of magnetic field bias. For the simulation validation, the measurements were compared with the simulation's prediction. Input to the simulation characterizing the AL800 had already been made based on previous material measurements. See section 3.

A drawing of the model cavity assembly is shown in Figure 129. The outer conductors are made of sheet (0.010" or 0.013" thickness) copper. The center conductor is machined from solid copper. The model cavity dimensions were based on those of the real cavity at the time the model cavity was designed (the real cavity design has continuously evolved). In the larger OD section (without garnet), the center and outer conductor size, as well as the gap distance, are the same as in the real cavity.

The radial dimensions in the garnet section are much smaller than those in the real cavity. This is due to the fact that in order to perform measurements, an external field must be applied. The solenoid, which was available, has an inner bore of only 4". Thus, the radial dimensions of the inner and outer conductors in the garnet section were scaled down so that they would fit inside of the solenoid. The ratio of the outer to inner diameter was kept the same as in the real cavity so the model and real cavities still have the same characteristic impedance in that section.

Measurements of frequency and Q were performed using probes located near the gap, weakly coupled to the cavity electric field. A stretched wire measurement [50, 9] was also performed. In this case, a 0.028" diameter wire was stretched across the cavity gap, through the inside of the center conductor (the "beampipe"), and through electrically insulating bushings to the exterior of the cavity, as shown in Figure 24. More traditionally the wire would exit the cavity through the "beampipe" on the shorted end, but this was not practical in the present case because it was necessary to have the garnet as close as possible to the bottom of the solenoid. This is to reduce magnetic field non-uniformities inside the garnet, which lead to ambiguities when comparing measurement and simulation. Matching resistors were added to each end of the wire. This is to match a network analyzer's 50 Ω output to the characteristic impedance of the transmission line formed by the wire inside of the beampipe. While performing a S_{21} (transmitted power) measurement from one end of the wire to the other, the shunt impedance across the gap can be viewed as a resistive element in a voltage divider with the matching resistors and the network analyzer's 50 Ω termination. Measuring the value of S_{21} at the peak of the resonance and knowing the values of the resistors in the matching network allows for the calculation of the shunt impedance. For some modes, the presence of the stretched wire reduces the cavity Q and shunt impedance (though R/Q should be preserved [51]). Thus, the extracted

value of the shunt impedance, Rshunt, is scaled by Q_{probe}/Q_{sw}, where Q_{probe} and Q_{sw} are the measured values of Q from the probe measurement and the stretched wire measurement.

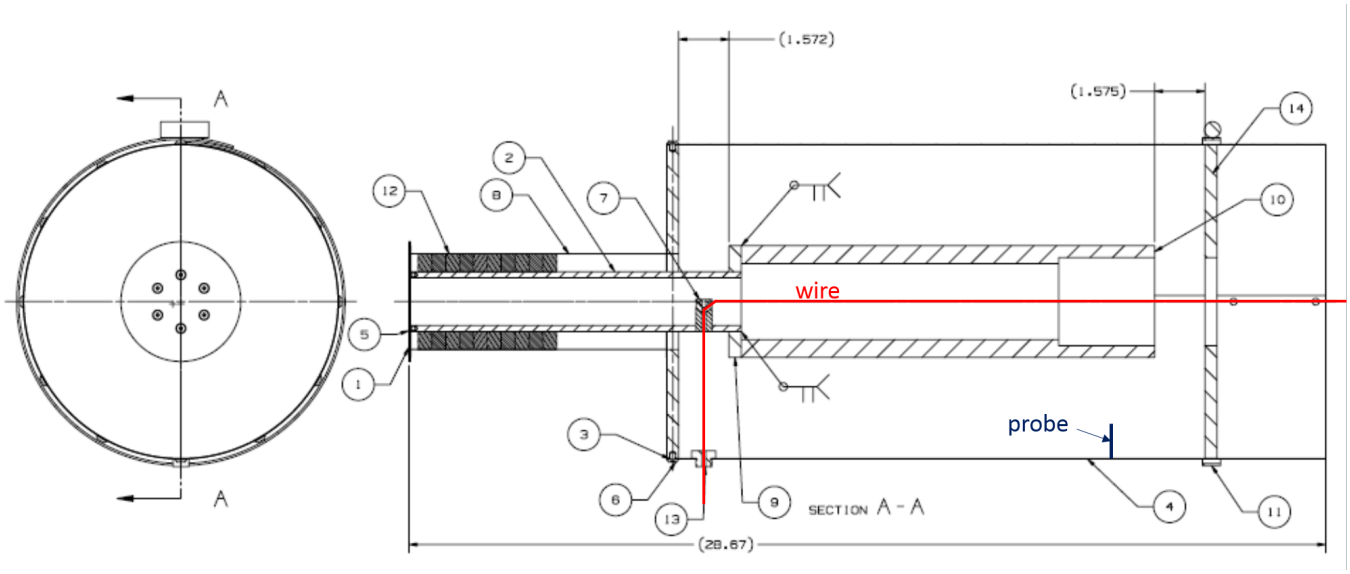

Figure 129: Drawing of the Model Cavity: 1) Cavity shorted end and shorting plate, 2) Garnet center conductor, 3) Transition plate, solid copper, 4) Outer conductor, 5) Screws connecting center conductor to shorting plate, 7) G10 bushing for stretched wire, 8) Garnet outer conductor, 10) Cavity gap end, 12) Garnet, 13) G10 bushing for stretched wire.

After the probe measurements and stretched wire measurements were performed with garnet, it was removed from the cavity, and the frequency and Q of the fundamental mode was measured. (Due to the nature of the construction of the cavity, it was not advisable to do this measurement first.) This allows us to separate any losses in the garnet from losses in the copper and any imperfect joints. While the predicted value of Q was ~3600 at ~135 MHz, the measured value was only ~1900. Not all of the joints were soldered, and after some manipulations it was seen that the Q could be temporarily increased to ~2500 by applying additional pressure or adding shielding to some joints. This indicates that there were losses due to imperfect joints between various parts of the cavity. For a more detailed discussion see [Yuri].

Figure 130 shows frequency as a function of bias for simulation and data. The data are from the measurements with the probes. (The stretched wire measurement is needed for Rshunt only). The agreement is good.

Figure 131 shows the quality factor, for data and simulation, where again the data is from probe measurements. Though it is not rigorously correct, the simulation uses an effective copper resistivity that is larger than nominal to mimic the effect of the losses due to poor RF joints. The resistivity used was that which resulted in the maximum observed Q in the bare cavity (~2500).

The main purpose of the cavity was to validate the modeling of the garnet which has been achieved.

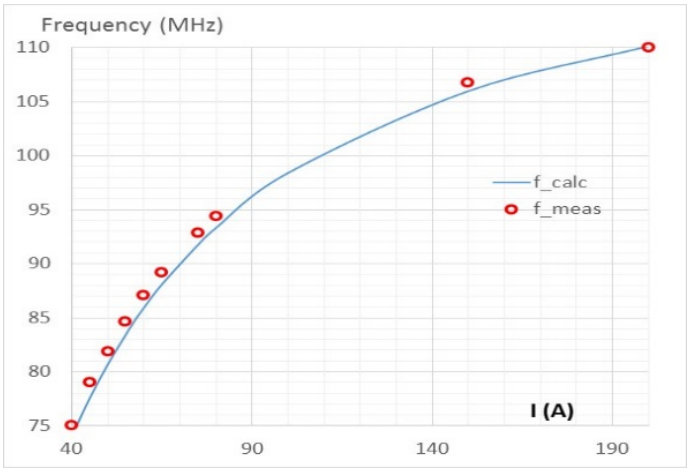

Figure 130: Frequency as a function of solenoid bias from measurements (probe data) and simulation (labeled as "f_calc" in the plot).

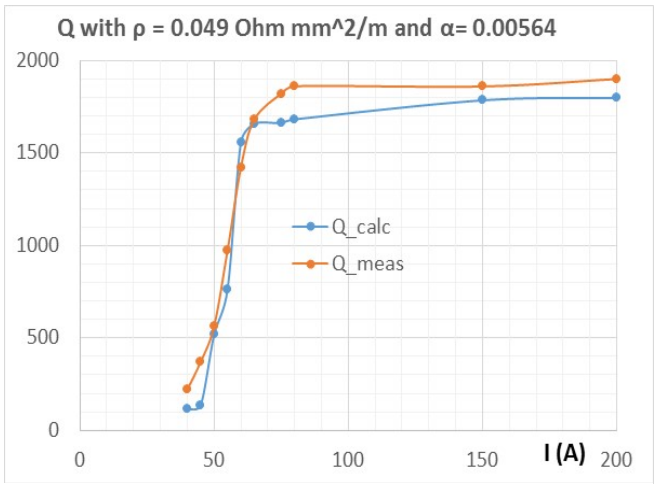

Figure 131: The quality factor as a function of solenoid bias for data and simulation. The simulation uses an effective conductivity for the copper (lower than nominal) to mimic losses due to poor RF joints.

16 Garnet characterization (J. Kuharik, R. Madrak, G. Romanov, I. Terechkine & C.Y. Tan)

As part of the quality control process for building our cavity, we have to assure ourselves that the garnets and the garnet rings that were delivered by National Magnetics had consistent RF properties. One major reason for our caution was the reported measurements from the garnet ring test for the SSC LEB (Low Energy Booster). Their measurements showed that one ring out of five had μ'' that was substantially different from the batch [52]. Therefore, to ensure that the RF properties of our garnet rings are uniform, we have built two test systems for this purpose. The first is a garnet witness piece test stand and the second is a garnet ring test stand.

The garnet witness piece test stand is used to measure the permeability of the witness pieces. Witness pieces are small samples from the actual rectangular blocks that are used to manufacture each sector of the garnet ring. Each garnet sector and its corresponding witness piece are paired by their identification numbers.

The garnet ring test stand is used to measure the permeability and RF losses in each fully assembled garnet ring. The garnet ring test stand consists of a specially designed cavity and a solenoid to bias the garnet. After measuring the resonant frequency and Q of the empty test cavity, the same measurements are repeated with the cavity loaded with the garnet ring as a function of solenoid bias. The resonant frequency range of the loaded cavity is 60 MHz to 121 MHz.

16.1 Garnet witness pieces measurements (J. Kuharik & I. Terechkine)

Our goals for testing the garnet witness samples are to discover whether the magnetic permeability of the samples is near the predicted value and whether all of the samples have the same permeability within our measurement uncertainties.

16.1.1 Theory

In free space, the magnetic flux density $\boldsymbol{B}$ is related to the magnetic field strength $\boldsymbol{H}$ by the permeability of free space μ_0, i.e.

$$\boldsymbol{B} = \mu_0 \boldsymbol{H} \tag{61}$$

where $\boldsymbol{B}$ is the magnetic flux density in teslas, $\boldsymbol{H}$ is the applied magnetic field strength in amperes per meter and $\mu_0 = 4\pi \times 10^{-7}$ H/m is the permeability of free space.

In a magnetic material, such as the AL800 garnet,

$$\boldsymbol{B}_M = \mu_r \mu_0 \boldsymbol{H}_M \tag{62}$$

where μ_r is the relative permeability of material, and $\boldsymbol{B}_M$ and $\boldsymbol{H}_M$ are the magnetic flux density and field strength within the material respectively.

The above forms the basis for extracting μ_r once the magnetic field strength, $\boldsymbol{H}_M$ is known. This can be done for our setup shown in Figure 132. In this setup, a known current, I, is applied to an "excitation" coil which surrounds the sample. We then measure the induced voltage in a "measurement coil". Using Ampere's Law, the closed path line integral shown in red in the figure is

$$\oint \boldsymbol{H}_M \cdot d\boldsymbol{l} = N_e I \tag{63}$$

where N_e is the is the number of turns in the "excitation" solenoid. The integration path is chosen to be symmetric top and bottom and it is assumed that the field outside the box is zero, then the above integral can be written as

$$\frac{1}{\mu_{\text{yoke}}}\int_{\text{yoke top}} \boldsymbol{B}_M \cdot d\boldsymbol{l} + \frac{1}{\mu_{\text{garnet}}}\int_{\text{garnet}} \boldsymbol{B}_M \cdot d\boldsymbol{l} + \frac{1}{\mu_{\text{yoke}}}\int_{\text{yoke botom}} \boldsymbol{B}_M \cdot d\boldsymbol{l} = \mu_0 N_e I \tag{64}$$

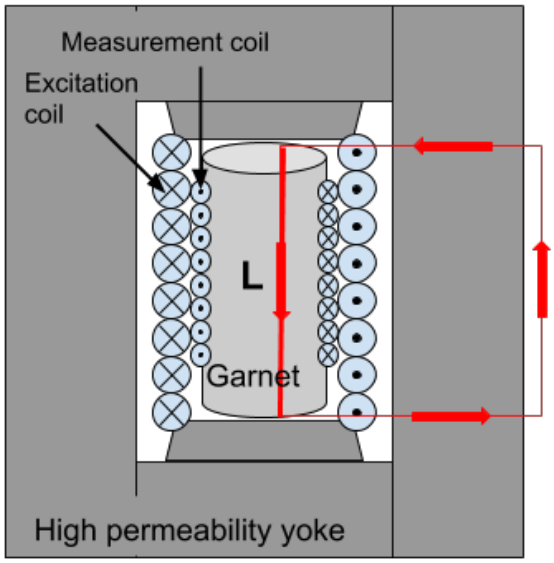

Figure 132: A cross-sectional view of our flux return box, solenoid and witness sample. The red rectangle is the closed loop integration path for applying Ampere's Law. The tightly fitted pole pieces at the end of the solenoid ensures that no field leaks into air gaps between the solenoid and the yoke.

Since the top and bottom paths are symmetric but opposite in sign, the path integrals cancel. We are left with

$$\frac{1}{\mu_{\text{garnet}}}\int_{\text{garnet}} \boldsymbol{B}_M \cdot d\boldsymbol{l} = \frac{B_M L}{\mu_{\text{garnet}}} = \mu_0 N_e I \tag{65}$$

Now, we have to determine B_m. We can do this by using both Faraday's Law and Lenz's Law, i.e.

$$V = -\frac{d\phi}{dt} \tag{66}$$

where ϕ is the magnetic flux and V is the induced voltage. In our setup, the relationship between ϕ and $\boldsymbol{B}_M$ is

$$\phi = N_m \int_A \boldsymbol{B}_M \cdot d\boldsymbol{A} = N_m B_M A \tag{67}$$

because $\boldsymbol{B}_M$ is parallel to the "measurement" solenoid coil which has N_m turns and cross-sectional area $\boldsymbol{A}$. When we substitute the above into Eq. (66), we have

$$V = -N_m A \frac{dB_M}{dt} \tag{68}$$

because A is a constant. B_M is found by integrating the above

$$B_M = -\frac{1}{N_m A}\int_0^t V\, dt \tag{69}$$

Finally, we can substitute the above into Eq. (65) to get

$$\mu_{\text{garnet}} = -\frac{1}{\mu_0 \left(\frac{N_e}{L}\right) N_m I A}\int_0^t V\, dt \tag{70}$$

which, in principle, is the equation that is used to determine the relative permeability of the garnet. This equation will have to be modified to include the correction for the air gap between the garnet and the coils. This correction will be discussed in section 16.1.4.

16.1.2 The witness pieces and measurement setup

Each garnet ring is made up of eight sectors glued together with a 3 mm thick alumina ring base. See Figure 53 and Figure 54. Witness samples have been paired with each sector piece and individually numbered by the manufacturer. The samples are 17.8 mm in diameter and 16 mm long. Figure 133

shows an example of a witness sample. The samples are tested in an apparatus designed to provide a uniform magnetic field within the sample throughout the tested range of bias current between 0 to 19.1 A.

Figure 134 shows the garnet witness sample test stand at different stages of assembly. The witness sample sits in a box made of MN-60 ferrite as a flux return. MN-60 has a high permeability of 6000. The high permeability of the box ensures that the H-fields are concentrated in the sample. Fig. ?? shows the distribution of B-fields. Figure 134 shows how the witness piece and ferrite box are assembled.

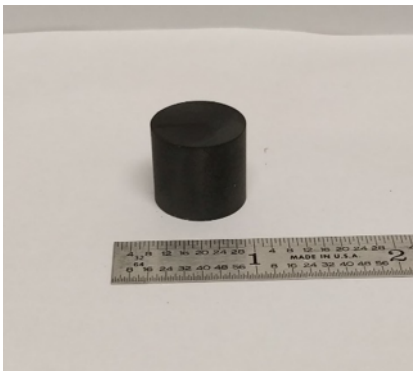

Figure 133: An example of an witness sample. The sample is a cylinder with a circular cross section that is 16 mm long, and 17.8 mm in diameter.

An excitation coil and a measurement coil were wound to fit inside the measurement box with the excitation coil surrounding the measurement coil, which fits as closely around the sample as possible. The excitation coil is wound with 183 turns of #14 (0.62 mm) insulated copper wire, and the measurement coil with 80 turns of #34 (0.16 mm) insulated copper wire. The measurement coil has been wound to match closely the diameter of the samples while still allowing the samples to be easily placed inside. Both windings were done on a device with a turn counter to ensure an accurate turn count, as shown in Figure 135(b).

The coils were wound around spools printed with an Ultimaker 2 Extended+ 3D printer. The printed spools measured 20.3 mm in diameter for the excitation coil and 17.8 mm in diameter for the measurement coil. The excitation coil was wound around the larger spool (Fig…) and a layer of Kapton® tape (0.12 mm thick), which functioned as a spacer. After each layer of wire, quick cure epoxy was added to keep the wire bound together. Prior to the winding, the surface of the spool and end washers were coated in petroleum jelly to prevent the epoxy from adhering to the spool pieces. When the winding was completed, and the epoxy cured, the Kapton® tape was removed from the inner radius. The measurement coil was prepared using the same method as the excitation coil, but with an additional layer of Kapton® tape which was not removed. It was found that when the coil was wound

using only one layer of tape, the finished coil was too small to easily fit around the witness samples. The extra space created a small air gap that had to be accounted for in the calculations.

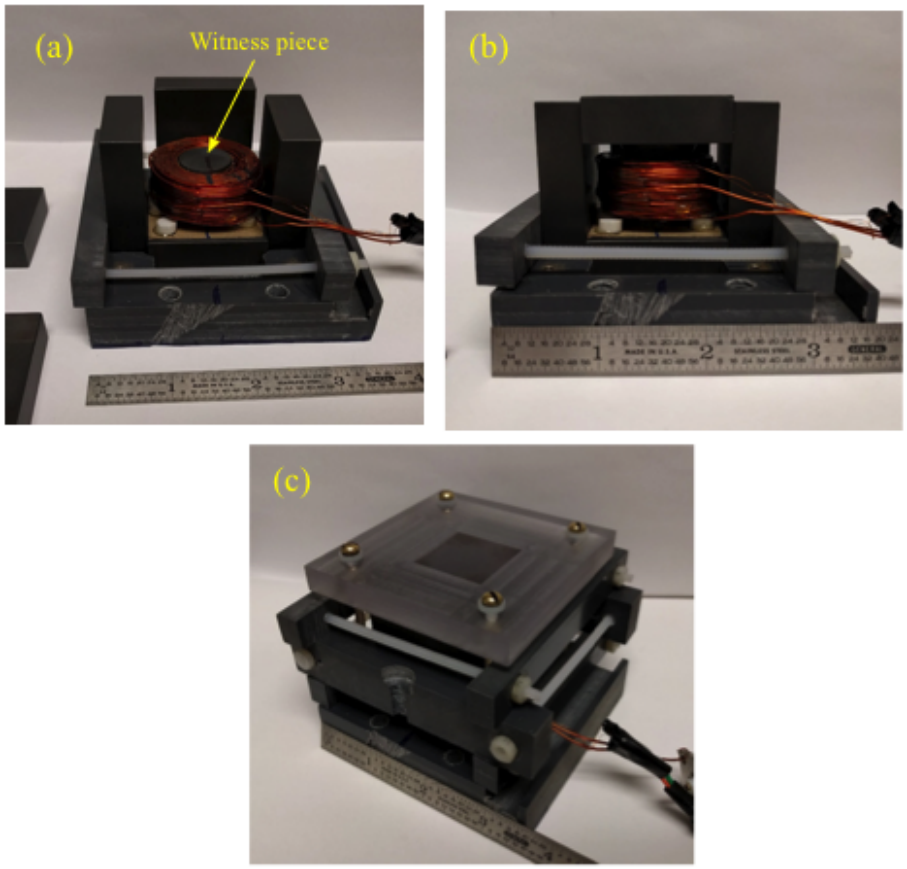

Figure 134: The garnet witness sample test stand at different stages of assembly. (a) The sample sitting in the partially assembled ferrite box. (b) The top cover is on. (c) The test stand fully assembled.

In order to ensure repeatability of the measurements, non-magnetic supports were used to ensure that the position of the excitation coil relative to the samples was centered and repeatable. Furthermore, the coils, flux pieces, and measurement samples have been marked to ensure repeatability during assembly and alignment of the apparatus. The apparatus is held together with clamps made from PVC and acrylic to minimize movement and to improve contact between the ferrite flux return. The clamps had to be tightened carefully for each measurement. If the clamps were too loose, vibration during the measurement pulse can affect the measurement and damage the sample. If the vertical clamp was too tight, the downward compression would damage the samples.

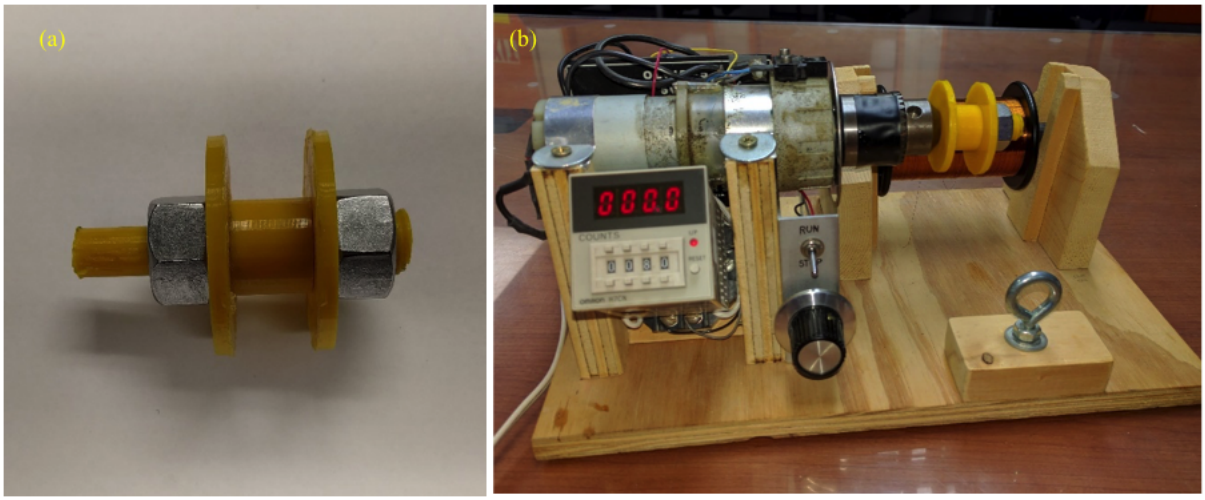

Figure 135: (a) is an example of a 3D printed spool piece and (b) is the winding device with its integrated counter.

16.1.3 Circuit and measurement technique

The sample measurement circuit is shown in Figure 136. The bias AC field is generated by an Agilent 33250A signal generator and amplified by the Behringer iNuke 6000 amplifier, which can generate currents up to ~20 A in the excitation coil. This current is measured using a precisely known shunt resistance (R = 3.92 Ω). A 1000 μF blocking capacitor prevents the DC component of the current from biasing the magnetic circuit. It has been found that this DC bias, if not removed, can result in substantial distortion of the measurement results.

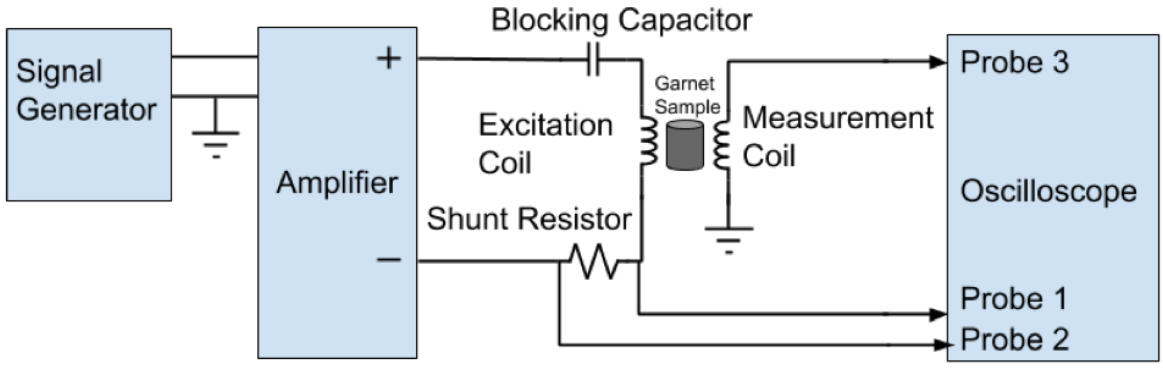

Figure 136: The sample measurement circuit. The probes connections discussed in the text are shown here.

The excitation current and the voltage generated in the measurement coil are recorded using a Tektronix TDS5054B-NV digital oscilloscope. Before each measurement, the sample was demagnetized using a decaying 180 Hz sine wave with the initial amplitude of the current 25% greater than the maximum current used in the previous measurement cycle. Figure 137 shows a typical measurement and demagnetization cycle. After each cycle, the apparatus is taken apart and the sample inverted for the next measurement to check whether there is any remnant magnetization or other systematic errors.

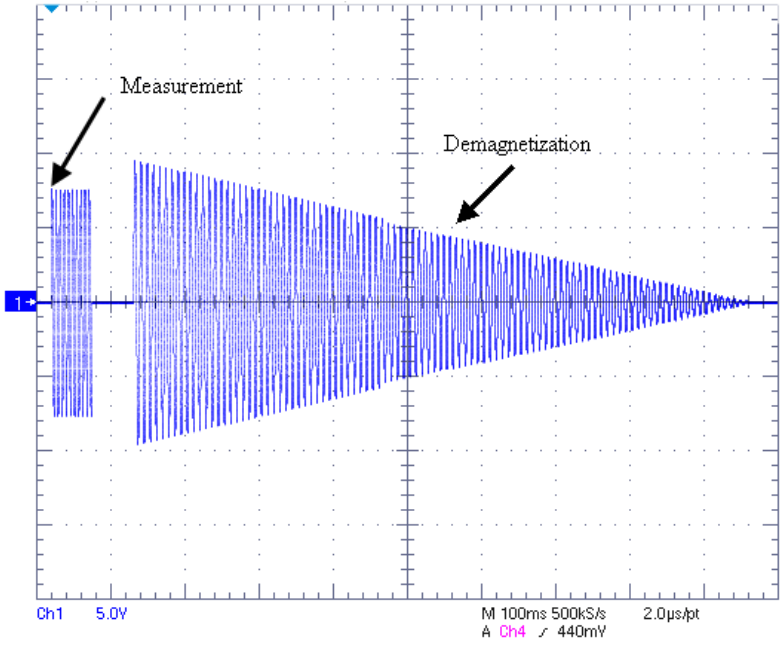

Figure 137: This is a typical measurement and demagnetization cycle. The demagnetization current is a decaying sine wave that starts with a current that is 25% higher than the measurement current.

The excitation current during the measurement is a 180 Hz sine wave with a peak current of 19.1 A. The measurement is taken during the first quarter of the sine wave from zero amps to peak current. During the measurements, the voltage to ground is measured at either side of the shunt resistor (probes 1 and 2 in Figure 136) and across the measurement coil (probe 3). The difference between the voltages on probes 1 and 2 is used to calculate the current and magnetic field in the sample (as the magnetic properties of the flux return in the sample holder are known). It is necessary to do a differential measurement as neither side of the amplifier is grounded. The measured voltage across the measurement coil allows the calculation of the magnetic flux through the sample by numerical integration. Two additional corrections have been made to achieve acceptable reproducibility and accuracy of the magnetization curve measurement. First, the internal DC offset of the scope must be

taken into consideration because this offset introduces noticeable systematic error in the results of numerical integration. Second, a very small (~0.20 mm) air gap between the witness sample and the measurement coil must be taken into accounted in the calculations. This air gap contains additional magnetic flux that contributes to the measured voltage and must be excluded when the magnetic flux in the sample is calculated.

16.1.4 Analysis

Each measurement results in two sets of data. The first is the difference between the voltage on the probes on either side of the shunt resistor, V_{rp}, and the second is the voltage across the measurement coil, V_s. Both data sets have a small DC offset that must be subtracted. The correction is made by taking the average of the pre-pulse offset and subtracting it from the entire set.

The magnetic field strength is calculated from Eq. (63) above, which becomes

$$H = \frac{N_e V_{rp}}{LR} \tag{71}$$

where $N_e = 183$ is the number of turns in the excitation coil, $L = \sim 0.0184$ m is the length of the coil, and $R = 3.92\ \Omega$ is the shunt resistance.

In the calculation of B, we start with Eq. (68) above

$$V_s = -N_m A \frac{dB}{dt} \tag{72}$$

where $N_m = 80$ is the number of turns in the measurement coil and $A = 264$ mm^2 is the area of the coil. The diameter of the measurement coil is larger than the diameter of the witness samples which creates an air gap between them. We account for the air gap by separating the air gap terms and garnet terms, i.e.

$$V_s = -N_m \left(A_{\text{air}} \frac{dB_{\text{air}}}{dt} + A_{\text{garnet}} \frac{dB_{\text{garnet}}}{dt} \right) \tag{73}$$

Integrating both sides we have

$$\begin{aligned} \int_0^t V_s\, dt &= -N_m \left(A_{\text{air}} B_{\text{air}} + A_{\text{garnet}} B_{\text{garnet}} \right) \\ B_{\text{garnet}} &= -\frac{1}{N_m A_{\text{garnet}}} \int_0^t V_s\, dt - \frac{A_{\text{air}} B_{\text{air}}}{A_{\text{garnet}}} \end{aligned} \tag{74}$$

In the air gap,

$$B_{\text{air}} = \mu_0 H \tag{75}$$

The equation, then, becomes

$$B_{\text{garnet}} = -\frac{1}{N_m A_{\text{garnet}}} \int_0^t V_s \, dt - \frac{A_{\text{air}} \mu_0 H}{A_{\text{garnet}}} \tag{76}$$

The integration of V_s is done numerically using a mid-point Riemann sum,

$$B_{\text{garnet}} = -\frac{1}{N_m A_{\text{garnet}}} \left[\sum_{i=0}^{N-1} \frac{V_{s,i} + V_{s,(i+1)}}{2} \Delta t \right] - \frac{A_{\text{air}} \mu_0 H}{A_{\text{garnet}}} \tag{77}$$

where the integration time has been divided into N equal Δt intervals, and $V_{s,i} = V_s(i\Delta t)$.

With the above expression for B and having previously calculated H, the relative permeability of the garnet is then found using Eq. (62), i.e.

$$\begin{aligned} \mu_{\text{garnet}} &= \frac{B_{\text{garnet}}}{\mu_0 H} \\ \mu_{\text{garnet}} &= -\frac{1}{N_m A_{\text{garnet}} \mu_0 H} \left[\sum_{i=0}^{N-1} \frac{V_{s,i} + V_{s,(i+1)}}{2} \Delta t \right] - \frac{A_{\text{air}}}{A_{\text{garnet}}} \\ \mu_{\text{garnet}} &= -\frac{LR}{N_e N_m A_{\text{garnet}} \mu_0 V_{rp}} \left[\sum_{i=0}^{N-1} \frac{V_{s,i} + V_{s,(i+1)}}{2} \Delta t \right] - \frac{A_{\text{air}}}{A_{\text{garnet}}} \end{aligned} \tag{78}$$

16.1.5 Results

The results of the measurement of 83 witness samples is shown in Figure 138 and Figure 139. Figure 140 shows an example of the reproducibility of the measurements using sample #162. This plot clearly shows that the deviation from the mean at low field (< 800 G) is due to the difficulty in getting a consistent result. Also, these results show that at high bias field, over 800 G, the permeability of the set of witness samples is acceptably uniform. A fit of the data to the theoretical model with an added offset, $\Delta\mu$,

$$\mu(B) = \frac{1}{1 - \frac{4\pi M_s}{B}} + \Delta\mu \tag{79}$$

gives $4\pi M_s = (743 \pm 2)$ G and $\Delta\mu = (0.076 \pm 0.001)$. This result can be compared with the vendor data shown in Table 11 which has a mean $4\pi M_s = (775 \pm 7)$ G. Our fitted value of $4\pi M_s$ is about 4% smaller than the vendor's value.

Although the fit shows that the measured $4\pi M_s$ is smaller than the vendor's data., the more important consideration is the consistency of the permeability between batches. This consistency gives confidence that the sectors of the fully assembled garnet rings will not have significant variations between them. This is important to avoid hotspots and possible damage to the rings during operation of the cavity.

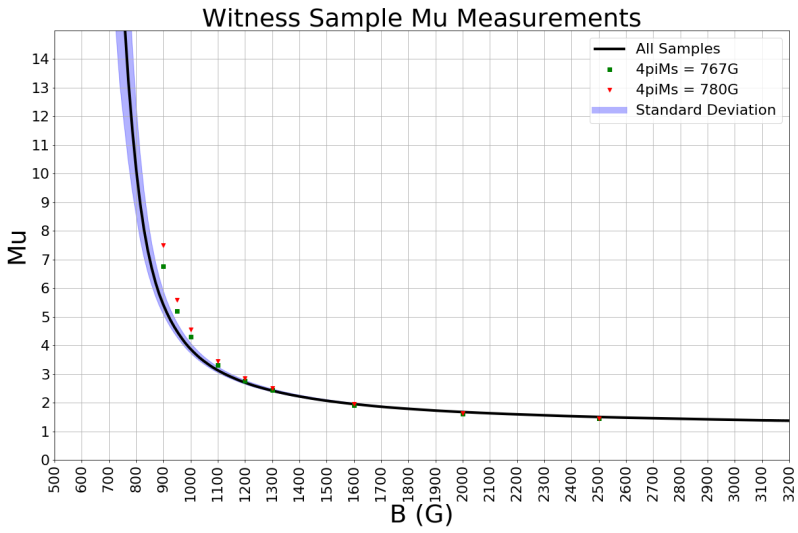

Figure 138: The average permeability as a function of the bias magnetic field for the entire sample set of 83 witness pieces.

The low field results, when the bias field is less than 500 G, of these measurements have too much variation to be significant. This is due to the low signal to noise ratio of the measurements in this region that allows small variations to have substantial effects on the calculations (and also the behavior of permeability below saturation which in theory, has a pole at exactly when $B = 4\pi M_s$). One source of the noise at low field is an 88 kHz signal that originates from the iNuke amplifier. This noise signal has little impact on the measurements in our primary region of interest which is above 800 G.

One effort to reduce the overall variability in the measurements was to flatten and polish smooth the pole pieces of the flux return box. The manufacturing process of the pole pieces left small ridges on the surface which causes imperfect contact with the witness samples. Unfortunately, after the edges were ground flat, it allowed the witness samples and pole pieces to move out of position during the

assembly between measurements. The improper positioning of the samples negated any potential benefit of the flatter surface.

In summary, the parameters used in the analysis are:

1. Length of the excitation coil $L = 18.4$ mm. Note: the length of the coil has to be used here because N_e/L in Eq. (70) is the number of turns per unit length of the excitation coil.
2. Number of turns in excitation coil $N_e = 183$.
3. Number of turns in measurement coil $N_m = 80$.
4. Cross sectional area of the coil $A = 264$ mm^2.
5. Cross sectional area of sample $A_{\text{garnet}} = 249$ mm^2.

Table 11: The vendor supplied data for the witness samples. Each witness sample is mapped to each sector of the garnet ring.

Lot #	Segment #	ε'	$\tan \delta_\varepsilon$	$4\pi M_s$ (G)	Line width (Oe)
66747	1 to 17	13.76	0.0001	765	28.6
66962	18 to 43	13.78	0.0001	780	29.0
67232	44 to 67	13.93	0.0001	776	21.3
67366	68 to 72	13.81	0.0001	778	19.98

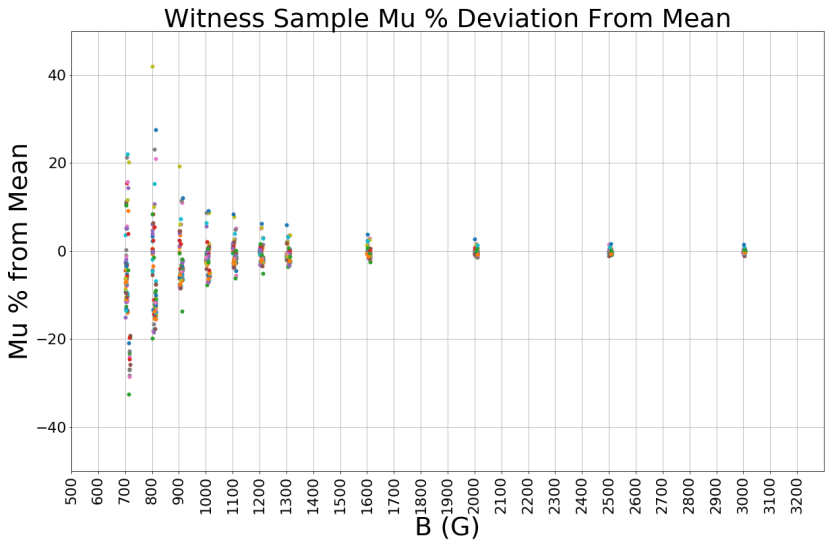

Figure 139: The fractional deviation of each sample from the mean of all the samples .

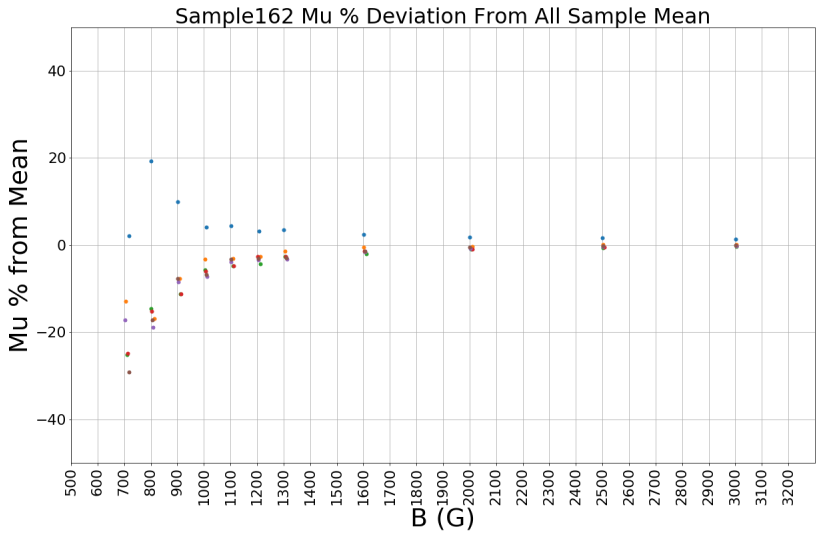

Figure 140: The fractional deviation of sample #162 from the mean of all samples.

16.2 Garnet ring measurements(J. Kuharik, R. Madrak, A. Makarov, G. Romanov, I. Terechkine, C.Y. Tan)

A garnet ring test stand has been built to measure the RF properties of each garnet ring. The test stand consists of a cavity and a bias solenoid, plus power supply, multimeter and network analyzer. A photograph of the test stand is shown in Figure 141. The cavity is a quarter wave resonator with large gap capacitance. The unloaded cavity resonant frequency is ~138 MHz. The bias solenoid consists of 224 turns of 10-gauge square copper wire and a flux return made of 1010 low carbon steel. A drawing of the test cavity and its photographs are shown in Figure 143.

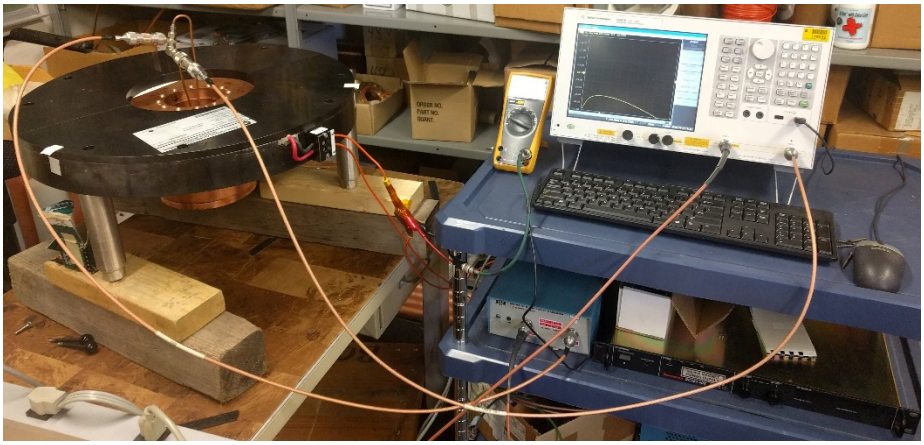

Figure 141: The garnet ring test stand. The block diagram of the setup is shown in Figure 142.

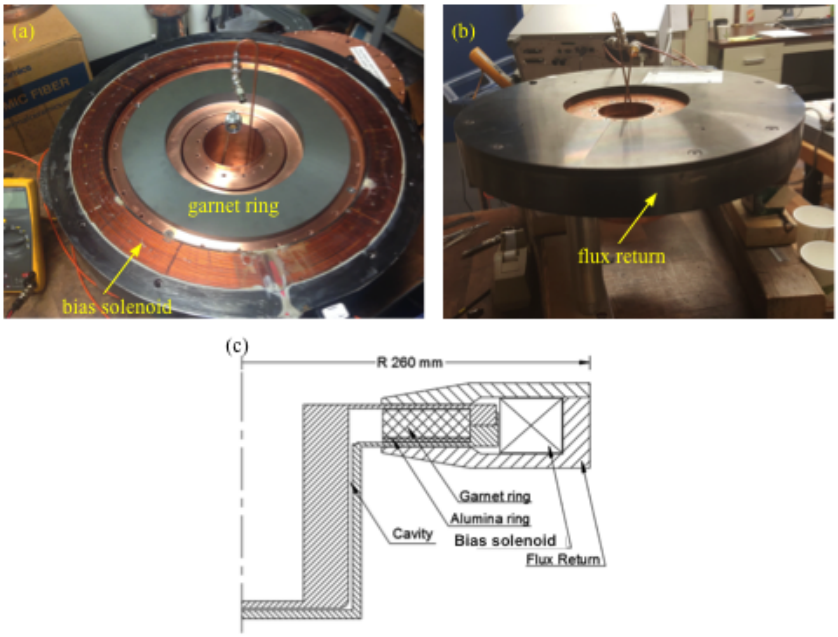

Figure 143: (a) The cavity with its lid open showing the garnet ring and bias solenoid. (b) The cavity closed with the solenoid flux return installed. (c) A cross sectional view of the cavity and the bias solenoid with the garnet ring.

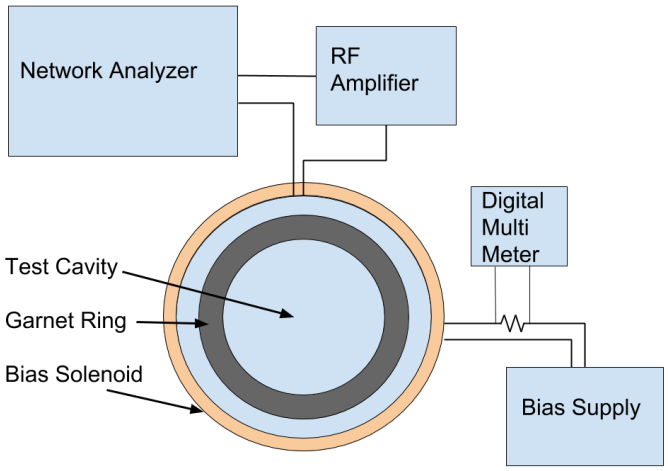

Figure 142: The block diagram of the garnet ring test stand.

16.2.1 Setup

Figure 142 shows the block diagram of the setup for our measurements. RF is supplied to the cavity via an Agilent Technologies E5061B Network Analyzer and an ENI 601L 1.2 Watts linear RF

amplifier. The biasing solenoid is powered with a Sorensen DCS60-20E power supply. The current is monitored with a FLUKE 26III True RMS Multimeter measuring voltage across a 0.01Ω resistor.

16.2.2 Initial testing and modifications

The Q and resonant frequency of the unloaded and loaded cavity was measured with the setup described above. Initial testing showed both the loaded and unloaded Q to be lower than expected indicating a problem with the contact between the cavity and cavity lid. The initial measured Q of the loaded cavity was measured between 1750 and 1850. The expected value of Q from simulation was 2400.

The addition of copper gaskets between the lid and both the inner and outer conductor showed improvement in Q, but the results were greatly dependent on the quality of the gaskets and the gaskets were not reusable after a measurement.

It was necessary to find a method that would improve the electrical contact between the lid and the cavity that was reusable for multiple measurements. A pair of grooves was machined into the lid that allowed for the addition of Spira [53] shield gaskets to improve the electrical contact. The addition of the Spira shield gasket improved the measured Q by 20%, but it is still 10% less than the simulated results at high bias. The comparison is shown in Figure 144. Figure 145 shows the cavity lid with the Spira shield gaskets added.

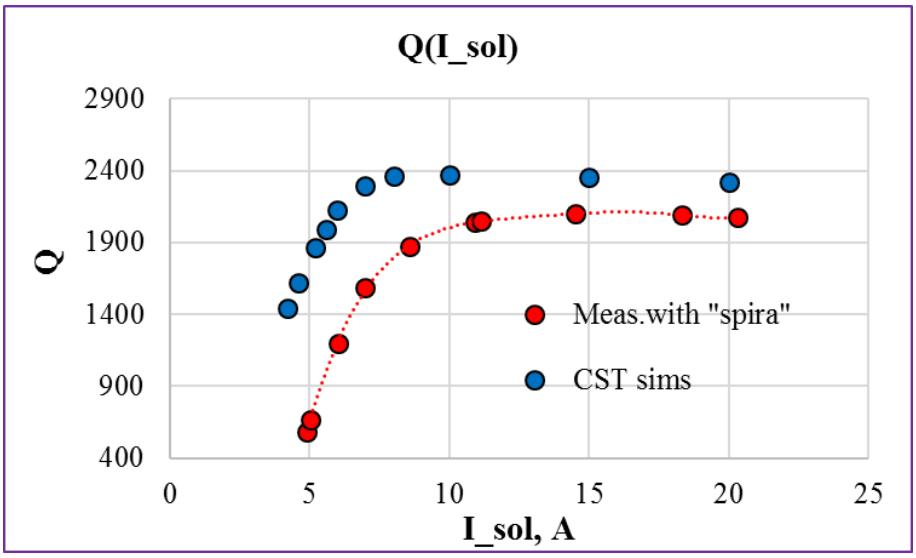

Figure 144: This is a comparison of the Q for the loaded cavity found from simulation and measurement.

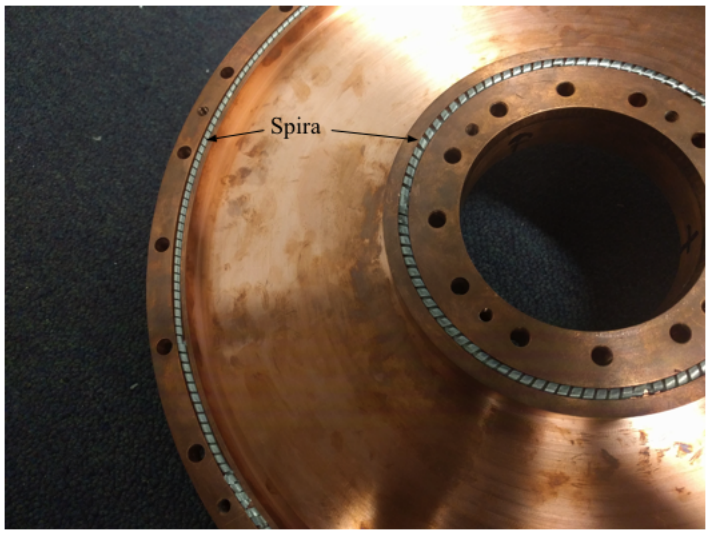

Figure 145: The Spira spring fingers are sued to improve the RF seal between the lid (shown here) and the cavity.

16.2.3 Results

We have 5 garnet rings shown in Figure 53. The Q and resonant frequency as a function of bias current (4 – 20 A) has been measured for the 5 garnet rings. Figure 146 shows the Q of each of the 5 rings. Figure 147 shows the averaged Q and difference from the mean for each ring. These measurements show that the RF properties are consistent and there are no outliers. Variability in the low bias region is a result of measurement uncertainty. Although the Q is lower than simulation results, the frequency data matches closely to CST Microwave Studio modeling, as shown in Figure 148.

Editor's note: The difference between the measured Q and the simulated Q of the loaded cavity shown here presented a major problem: we assumed that α is constant based on measurements discussed in section 3.2. However, there is an indication that α is not constant at low field from Figure 15. Using a constant α in the simulations could not match the loaded cavity measurements. The CST MWS simulations [54] **showed that for $\mu' < 3.5$, α can be treated as a constant with value 0.0036 (The value of α used here comes from the vendor. Our measurement gave $\alpha = 0.0033$. See section 3.2). However, without the actual 2nd harmonic cavity it is difficult to know whether the modeling of the RF losses is close to reality. This was the compelling reason to monitor the temperature of the garnet with IR sensors during high power tests. See 22.5.1.**

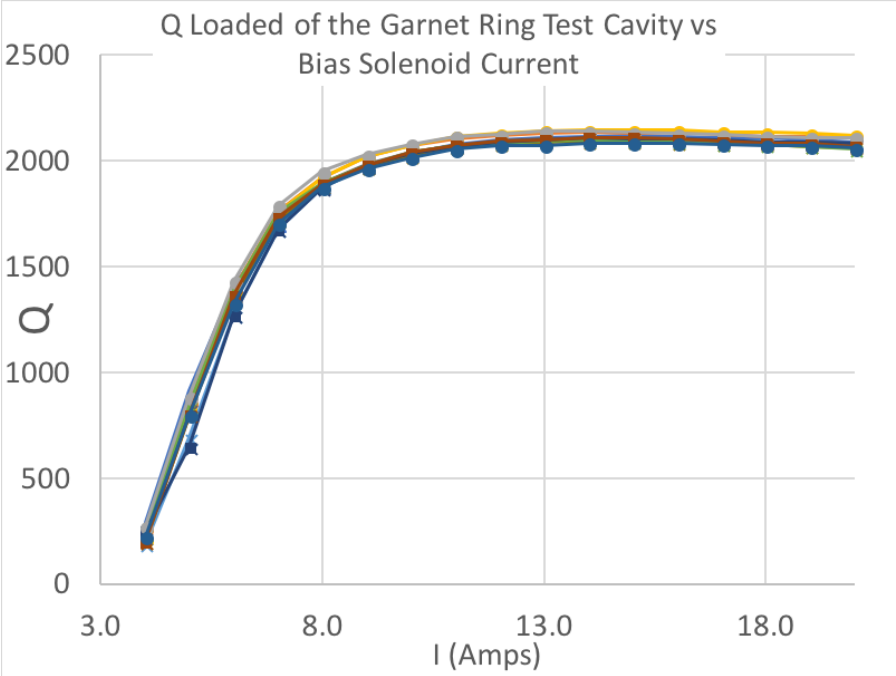

Figure 146: The Q of the 5 garnet rings as a function of the bias current.

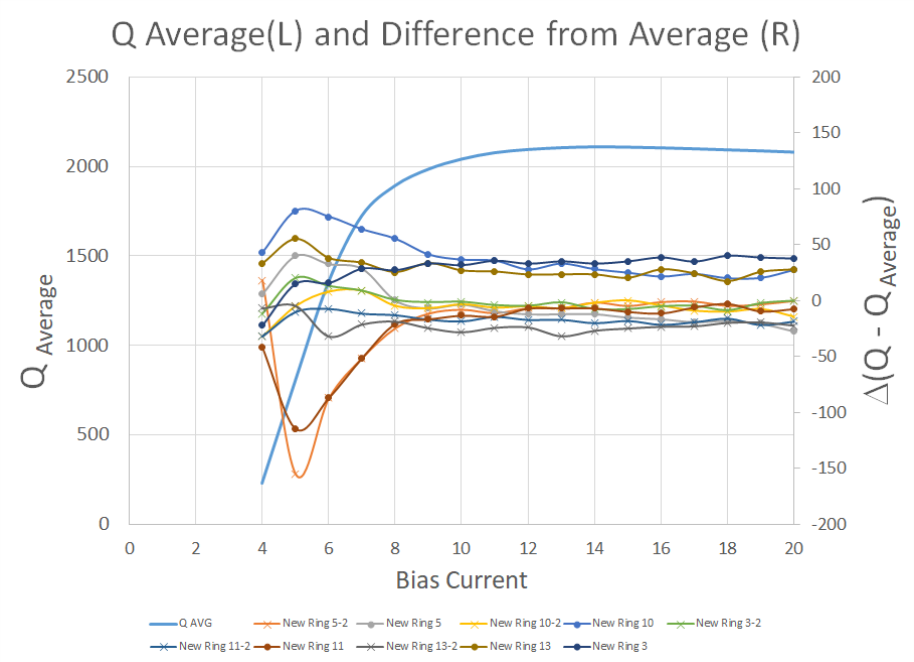

Figure 147: The averaged Q of the 5 rings and the difference from the averaged Q for each ring.

We did not measure the RF properties of the 2 shim rings (shown in Figure 54) because, due to an oversight, the depth of the cavity is too shallow to hold the shim rings. For the 2 shim rings, the tests of the witness pieces show that they are within the normal spread of permeability.

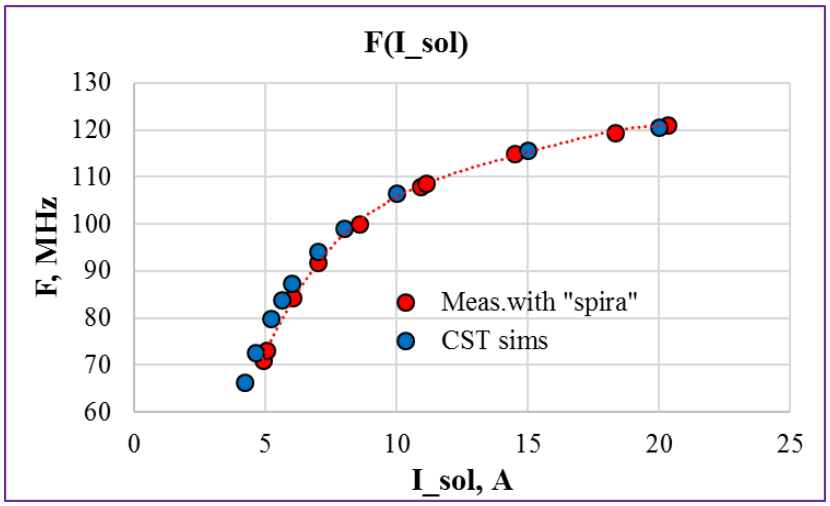

Figure 148: This figure shows that the measured and simulated frequency matches for the garnet loaded cavity.

17 Mechanical design (K. Duel & M. Slabaugh)

We will highlight the important considerations and problems that we have found during the manufacture and the assembly of the cavity. The drawing numbers are shown in section 17.11.1.

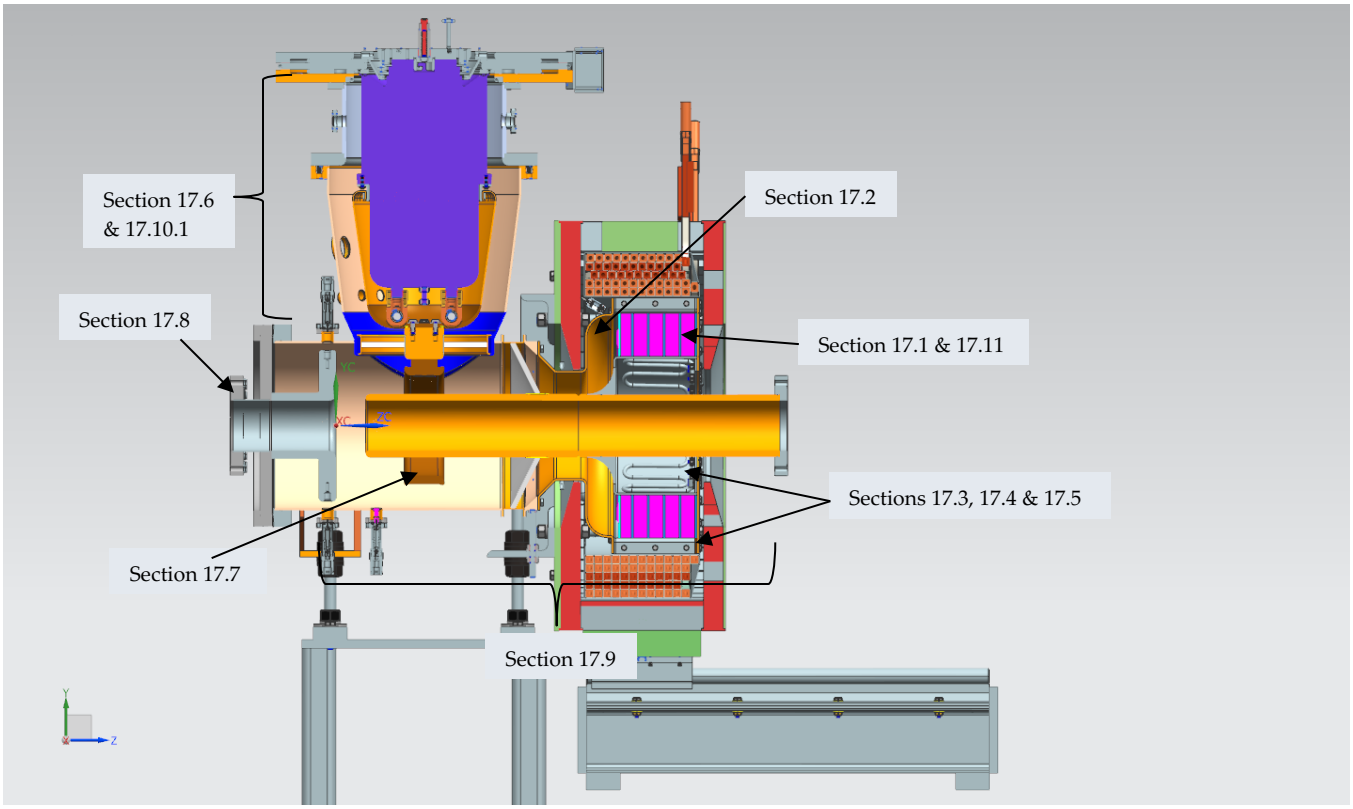

Figure 149: The 3D model of the cavity sitting on its stands. The parts of the assembly that are discussed in this section are indicated in this figure.

17.1 Garnet sectors and alumina

The garnet sectors are made from rectangular pieces of garnet that are cut into polygons and then glued together with the alumina ring using the procedure discussed below. It is necessary to do it this way because National Magnetics can only make garnet pieces that have the maximum size shown in Figure 150. The polygonal garnet pieces are glued together and then the excess removed by turning to form the final ring.

The alumina ring is made from 99.5% pure alumina (Al2O3, Coorstek material id: AD995 [55]).

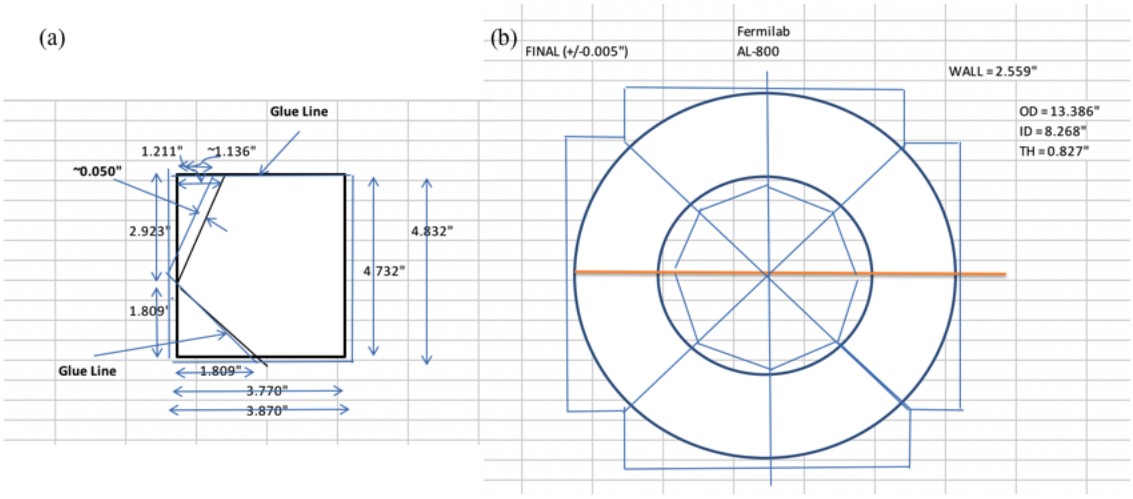

Figure 150: Each sector of the garnet ring first starts out as a rectangular piece of garnet shown in (a) and then cut into a polygon. The polygons are then glued together onto the alumina substrate and then turned to produce the final ring.

17.1.1 Procedure for gluing garnet sectors and alumina

This was the procedure given to the vendor (National Magnetics) on 12 Sep 2016 for gluing the garnet sectors together and also to the alumina.

Materials

1. STYCAST 2850 FT [22]
2. Catalyst 9

Equipment

1. Vacuum Chamber
2. Vacuum pump capable of achieving less than 10 Torr (29 inHg) of vacuum
3. Vacuum gauge
4. Clamps or weights to apply even pressure
5. Scale

Procedure steps

1. Measure the correct ratio of epoxy to catalyst by weight per the technical data sheet specification. Put contents into a container and mix thoroughly.
2. Put container of mixture in vacuum chamber and pump down until vacuum level is greater than 28 inch-Hg and is maintained for 3 minutes.
3. Let up vacuum chamber and inspect surface of epoxy. If slight ripples or evidence of bubbles surfacing are visible, then put under vacuum again to the same vacuum level and time. If surface

appears smooth, then proceed to next step. We repeated step 2 once. Alternatively if a clear vacuum chamber is available, then the mixture can be put under vacuum and observed until the bubbling has ceased.

4. Apply thin layer of epoxy to cover entire mating surface of both pieces.
5. Bring pieces together and apply pressure so that interface is only around 5 mils or less thick. We used a 6 kg weight during our test on 3" square pieces of glass, so ~1.5 psi.
6. Allow epoxy to cure according to the technical data sheet specification.
7. Add the next pie piece and perform procedure again unless there exists the capability to glue all pieces at once with sufficient pressure to reduce interfaces to less than 5 mils thickness.

Note: Use the same procedure for gluing the alumina to the garnet.

17.2 Tuner neck assembly

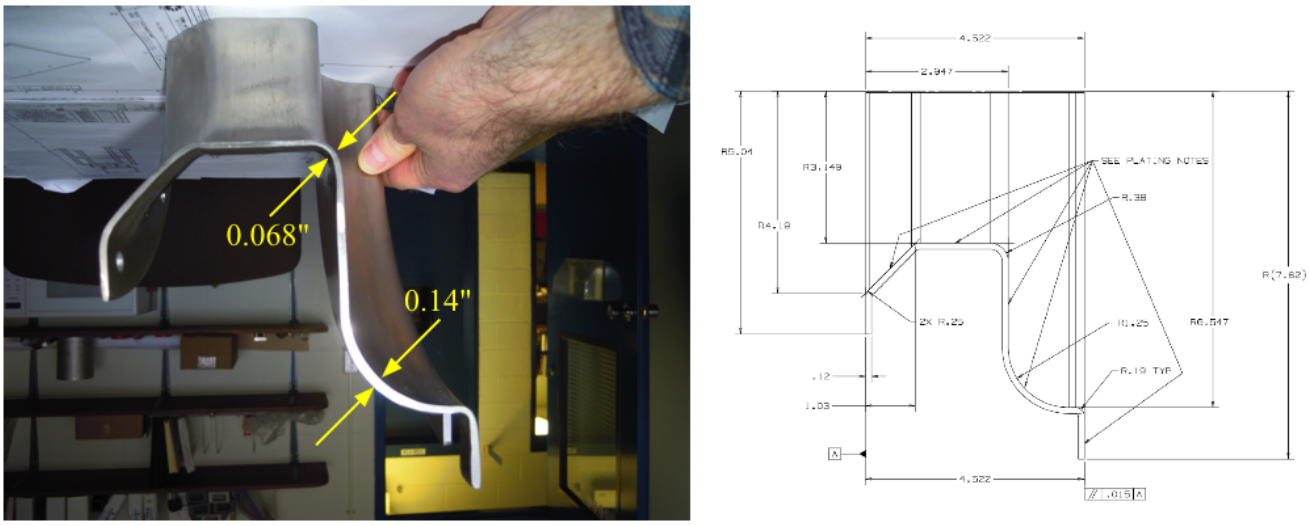

Figure 151: The manufactured tuner shell has thickness that do not meet specifications. The specified thickness is (0.12 ± 0.02) inches.

The tuner neck shell made from stainless steel and spun into the required shape shown in Figure 151. However, the result did not meet the drawing specifications of (0.12 ± 0.2)". A quick back of the envelope calculation showed that the Eddy power losses on the 0.14" thickness area would increase by 33%. However, from the MWS simulations shown in Figure 70, this is the coolest part of the tuner neck and so should not pose any heating problems. The frequency shift from the change in volume of the transmission line should be minimal as well.

Furthermore, the tuner neck shell did not meet the length specification as well. It is 90 mils too long. From our inspection of the shell, we suspect that the shell was made from two separate spinnings

because the quadrants do not match. In hindsight, instead of making this part from spinning, we would have either milled it from a solid pieces of steel or cast it and then finished it by milling. We encountered many problems during the initial installation of this assembly. All these problems can be traced back to the fact that this assembly did not meet dimensional specifications. See section 17.2.1. Figure 152 shows two views of the shell.

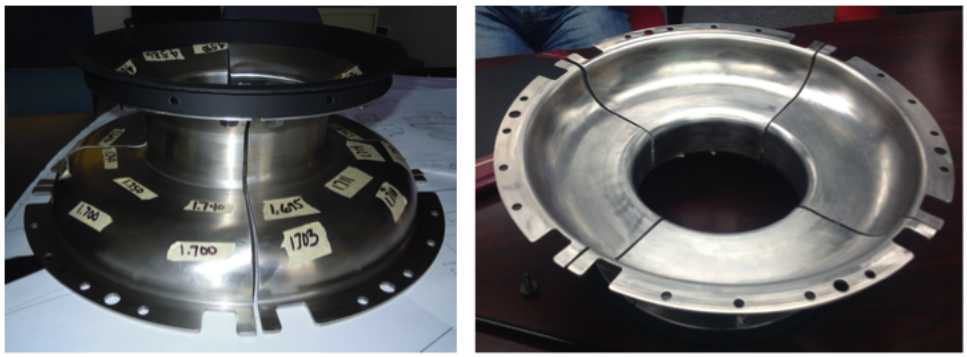

Figure 152: Two views of the tuner shell before copper plating. Close examination of the quadrants show that they had to be made from two separate spinnings.

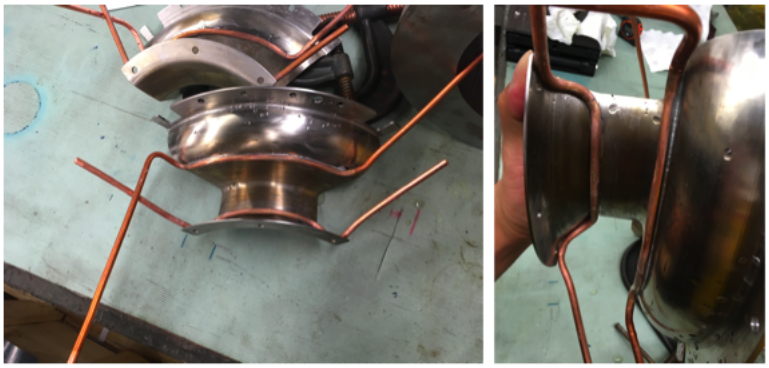

Figure 153: The ¼" cooling pipes are hand soldered onto the shell.

Water cooling pipes are hand soldered onto each quarter of the shell. Figure 153 shows two views of the ¼" water cooling pipes after the soldering process. Note: In hindsight, it is better to solder these pipes after the neck assembly is dry fitted with the solenoid end plate installed. This allows for the correct bending of the pipes to fit into the slots of the end plate. See section 17.2.1.

Although not shown here, two of the shells will have ¼" holes after copper plating for the IR sensor that will be discussed in section 22.5. The surface that sees RF is plated with 1 mil of copper while the outer surface is left as is. See Figure 154.

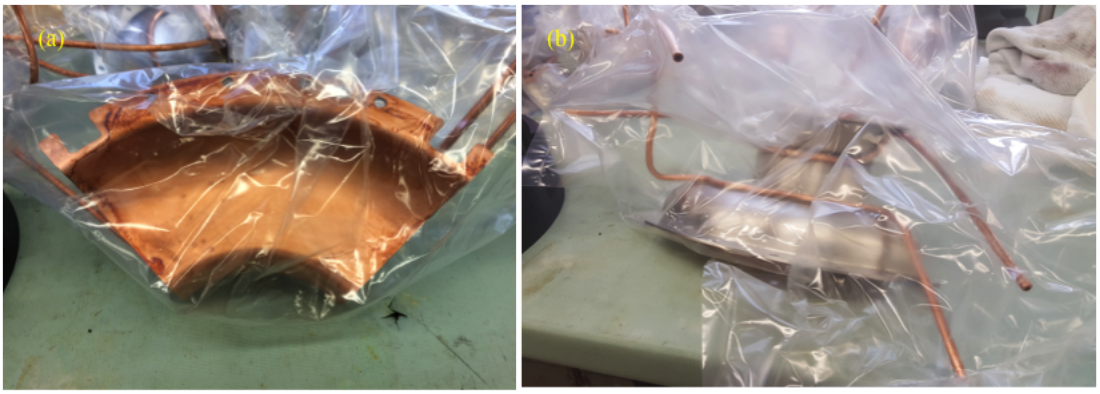

Figure 154: The neck assembly after (a) the RF surface is copper plated and (b) leaving the outer surface un-plated.

From the experiments that we did with the unloaded cavity (to be discussed in section 21), we have modified this assembly. The modifications are:

1. Pairs of wires (22 AWG, 0.025″ diameter annealed copper wire) have been tacked with solder to each contact surface so as to form an RF lip. The wires also serve to fix the problem with the slot for the wire that was EDM'd away in the outer shell assembly. See section 17.4.
2. Added two holes so that screws can be used to better RF seal the neck assembly to the tuner outer shell assembly. See section 17.4 for the extra hole and contact surface that this assembly will be bolted to. 4-40 screws with nuts and lock washers are used to close the ends.
3. Tin plated the contact surface to mitigate corrosion.

These modifications are shown in Figure 155.

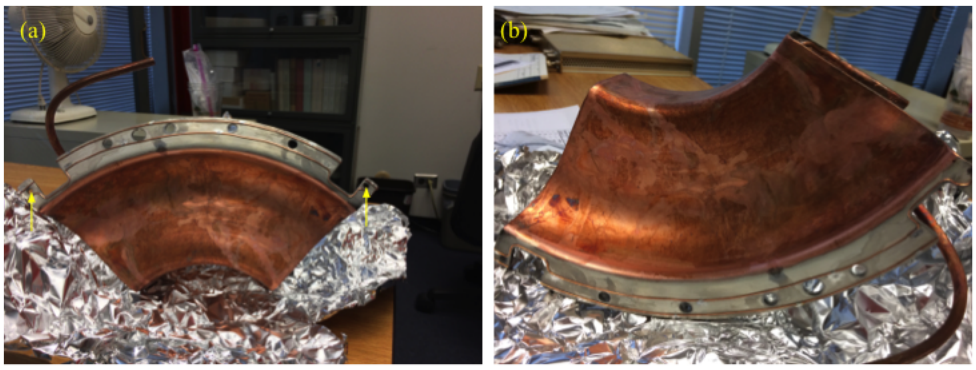

Figure 155: The contact surfaces have been tinned and wires tack soldered to form an RF lip. On the contact surface shown in (a), extra holes (indicated by arrows) have been drilled so that these surfaces a screw can be used to clamp this surface to the tuner outer assembly so as to form a better RF seal.

17.2.1 Modifications

The neck assembly had to be modified for attachment to the cavity body with the solenoid end plates attached because it was discovered that

1. The support rod indicated in Figure 156(a) cannot go through its hole in the neck assembly. This hole has been made into a slot. Note: spinning stainless actually hardens the steel which makes it a lot more difficult to cut.
2. The water pipe as mounted in the position as drawn, prevented the neck assembly from being bolted to the cavity body. See Figure 156(b). The solution is to move the pipe. The source of the problem can be traced back to the neck assembly not meeting the length specifications.
3. After this water pipe was removed, it was found that it was much easier to correctly bend the new pipe into the slot on the solenoid end plate during the dry fit. The pre-bent pipe was then soldered onto the neck assembly.

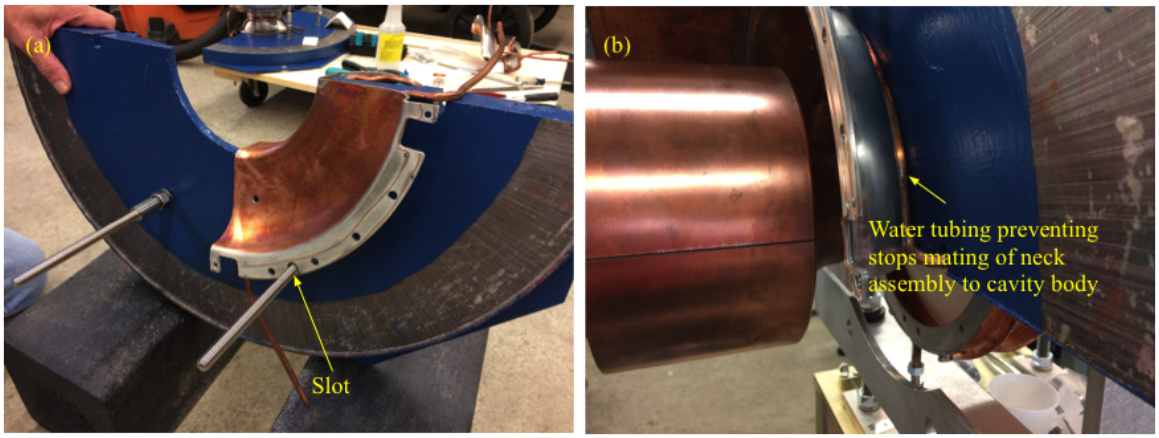

Figure 156: (a) The hole in the neck assembly for the support rod has been modified into a slot and (b) the water pipe will need to be moved because it stops the neck assembly from being attached to the cavity body.

Lessons learned: in the postmortem analysis of the problems that we have had with the neck assembly can be traced back to the decision to manufacture it with a spinning process. In hindsight, most of the problems would have been eliminated if we had CNC'd it.

After modifying the neck assembly, they have been successfully installed onto the cavity. See section 17.11.

17.3Tuner inner shell assembly

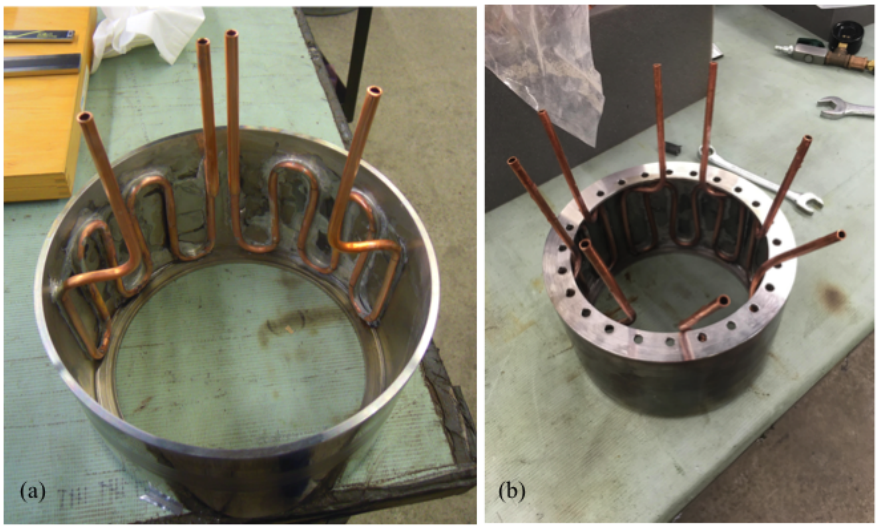

Figure 157: The inner shell of the tuner. (a) Half the required water pipes have been soldered to its inner surface. (b) All the water pipes have been soldered, outer surface machined and the required flange welded on.

The inner shell assembly is shown in Figure 157(a) with only half the required water cooling pipes soldered on it. We noticed that after completing the soldering of the pipes to the inner surface, there was some unevenness on the outer surface. We had anticipated this soldering effect and had left enough material so that this unevenness can be removed with a lathe. After correcting the unevenness, Figure 157(b) shows the required flange that was welded on.

After all the cooling pipes have been soldered on. A stainless steel neck piece that has been brazed to a copper beam pipe is then welded to the inner shell. Then 4 cuts are made, 90° apart with a wire, into the shell. Finally, the entire outside surface is plated with 1 mil thick copper while the inner surface is not. See Figure 158.

The conical window is then welded to the inner shell. See Figure 159. We have had some difficulties getting a good vacuum weld joint. We suspect that either (a) the single V-groove weld prep that is 1/8" thick is too thick or (b) excessive cooling was used so that the copper did not flow properly during the weld.

After the weld joint is completed, it is smoothed and polished by hand. The weld joint after hand smoothing and polishing is shown in Figure 160. This assembly has been leak checked and its steady state leak rate is 1.8×10^{-10} Torr·L/s. The tuner inner shell assembly is then welded to the outer cavity body assembly discussed in section 17.9.

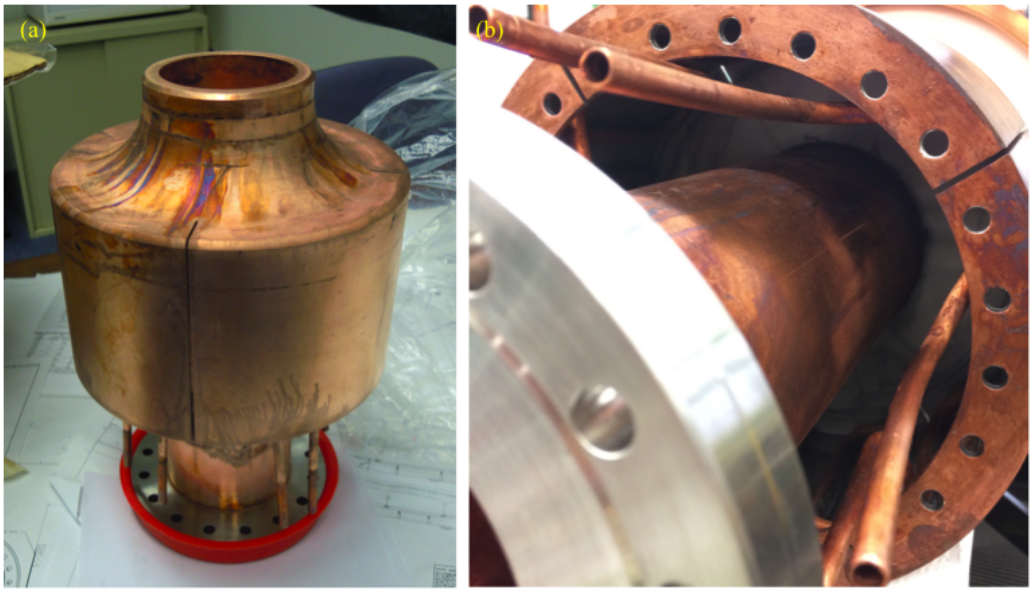

Figure 158: The inner shell after copper plating. (a) The outer surface sees RF and so has to be copper plated. The shell has 4 cuts made in it. (b) The inner surface is left un-plated.

Figure 159: The setup for welding the conical window to the inner shell. (a) Cooling and fixture. (b) The weld joint.

Figure 160: The weld joint after hand smoothing and polishing.

17.4 Tuner outer shell assembly

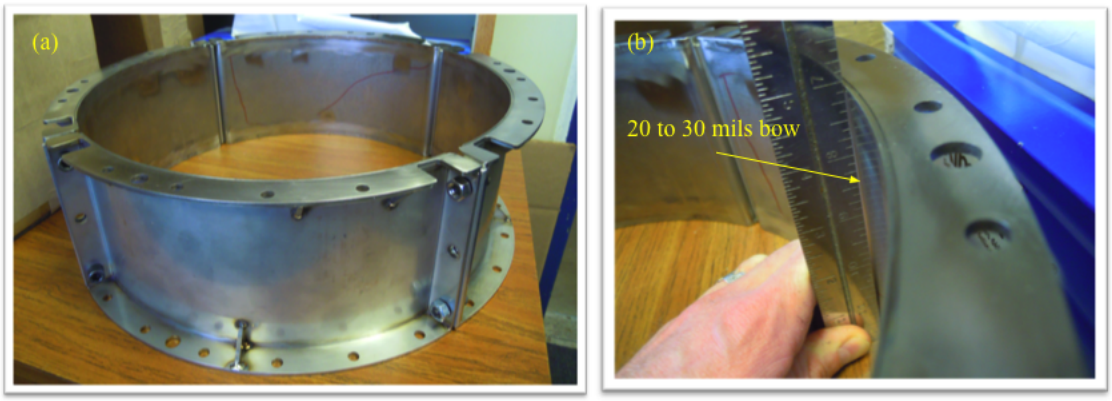

Figure 161: The tuner outer shell assembly exhibited a 20 to 30 mils bow after welding. This bow has to be removed because good contact between the shell and the garnet tuner stack is essential for heat removal.

The outer shell assembly before the water pipes were soldered on is shown in Figure 161. The welding that joined the lips to the cylinder caused some bowing. It is essential that there is good

contact between the shell and the garnet tuner stack and so this bow must be machined out. The bow has been corrected by EDM cutting the affected area after the water pipes have been soldered onto it. This sequence is used because soldering causes further unevenness to the shell. Once the machining is complete, the side that has the water pipes will be masked before copper plating. Figure 162 shows the outer shell assembly after successfully removing the bow by EDM'ing. Unfortunately, after EDM'ing, the grooves for the wires for sealing the RF were removed as well. In order to fix this problem, wires were tack soldered to the neck assembly to form an RF seal. See section 17.2.

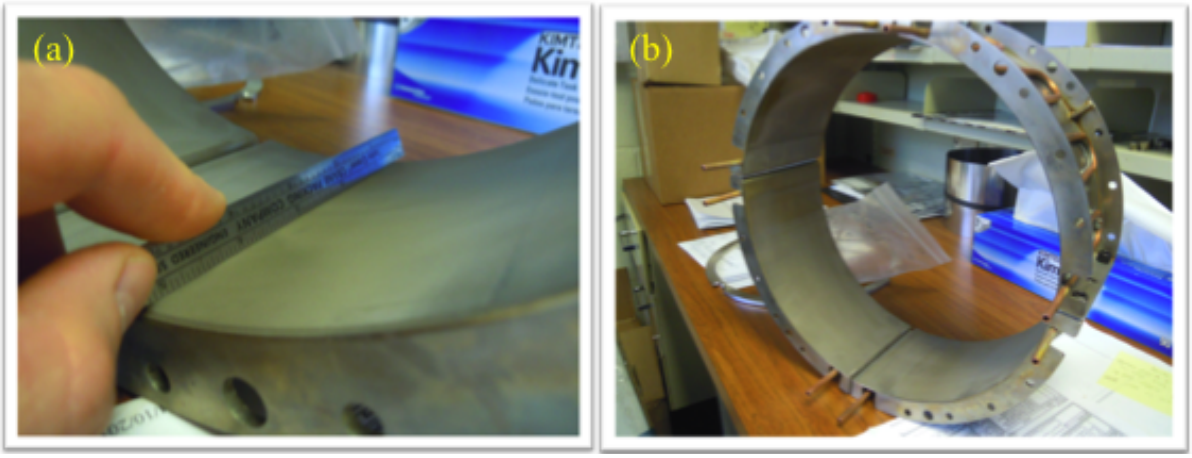

Figure 162: (a) The bow is gone after the surface was cut with an EDM. (b) The outer shell copper before plating. Unfortunately, after removing the bow, the groove for the wire used as an RF seal was removed as well.

Editor's note: Although EDM'ing was successful in removing the bow, it introduced another problem. See section 17.4.1

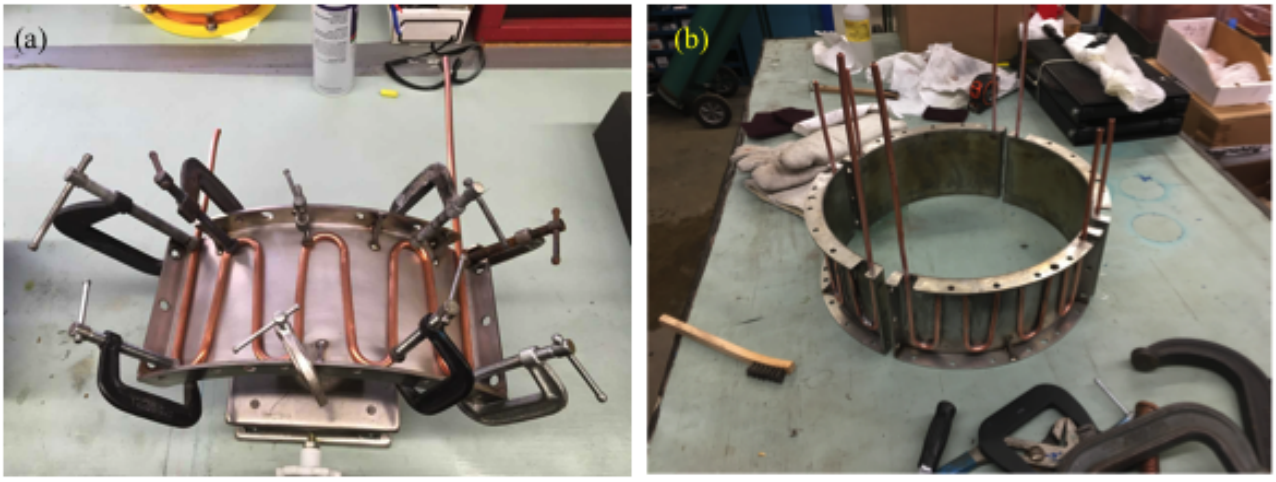

Figure 163: (a) The water pipes are clamped to the outer shell before soldering. (b) All the water pipes soldered to the outer shell.

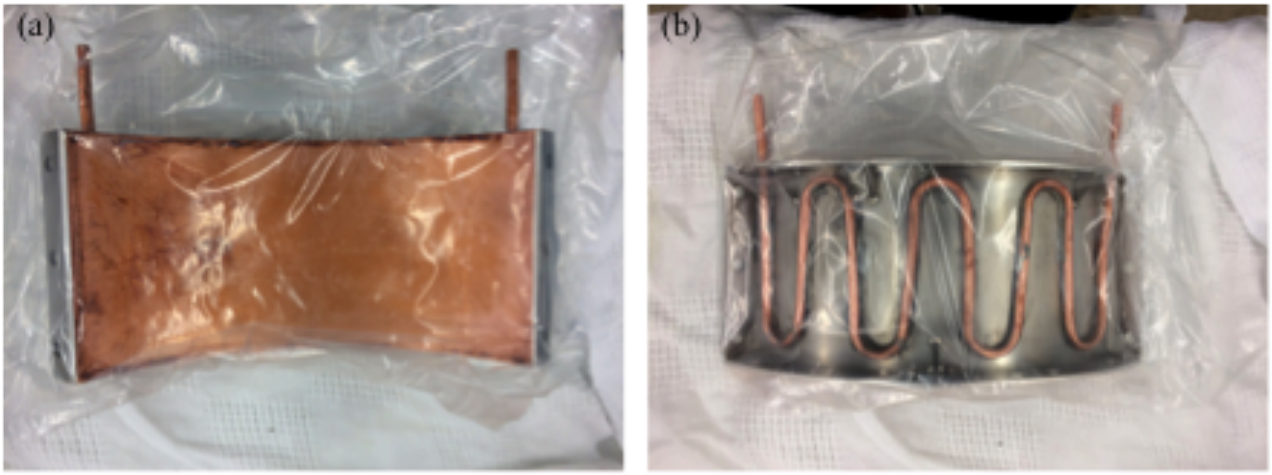

Figure 164: (a) The copper plated side and (b) the un-plated side of the outer shell.

Figure 163 shows the water pipes soldered to the outer shell assembly.

The results after plating the surface that sees RF with 1 mil of copper while leaving the other surface un-plated is shown in Figure 164.

Figure 165: The contact surfaces have been tin plated and 8-32 threaded holes added (arrowed). Editor's note: 4-40 (and even one 2-56) screw was used and the threaded hole bypassed because these holes could not be aligned to those on the neck assembly.

The contact surfaces have been tin plated to protect them from corrosion. Two holes have been made on the contact surface so that a screw can be used to clamp the edge formed by this assembly and

the neck assembly (see section 17.2). This addition is used to improve the RF seal between these two surfaces. See Figure 165.

17.4.1 Problems introduced by EDM corrections

Although EDM'ing corrected the bow, it also introduced another problem that we did not discover until assembly: there are cracks at the weld joints in three of the four outer shells. See Figure 166. An example of the crack on one of the shells after cleaning can be seen in Figure 167. The size of this crack is between 3 mils to 5 mils depending on how the feeler gauge is inserted. We believe that the EDM correction not only removed the bow, it also removed enough of the weld material to cause cracks between the lip and the body. Remaking the outer shells is not an option due to funding and time constraints. Therefore, we have to repair them.

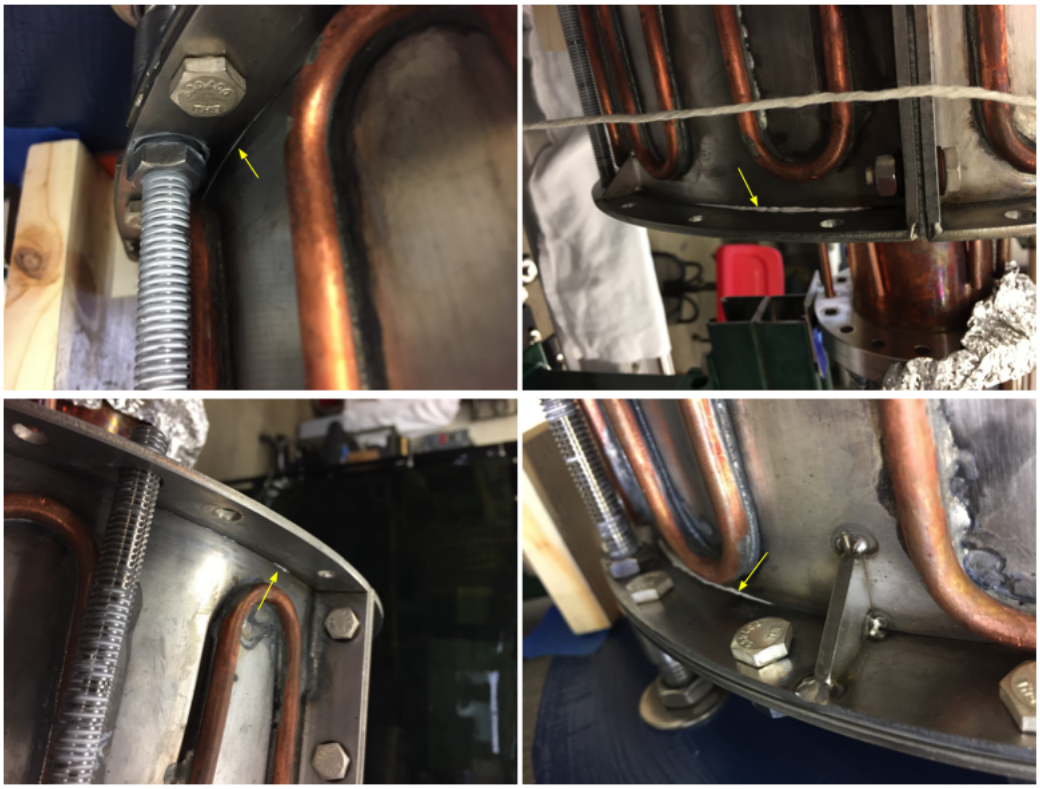

Figure 166: Three of the four outer shells exhibited cracks. The cracks allowed the grease to ooze out as indicated by the arrows.

We have two options for repair:

1. Weld on the outer surface joint, i.e. not on the joints on the copper plated surface. The dangers are that welding will warp the cover again and also peel off the plated copper.

2. Fill the cracks with braze material. Brazing can only work if the cracks are not too wide. Initial measurements show that the cracks < 5 mils which we think should allow the brazing method to work.

We have decided to go with option 2 because we believe that is the lesser of the two evils. The repair with the associated RF tests before and after the repair is described in section 18.

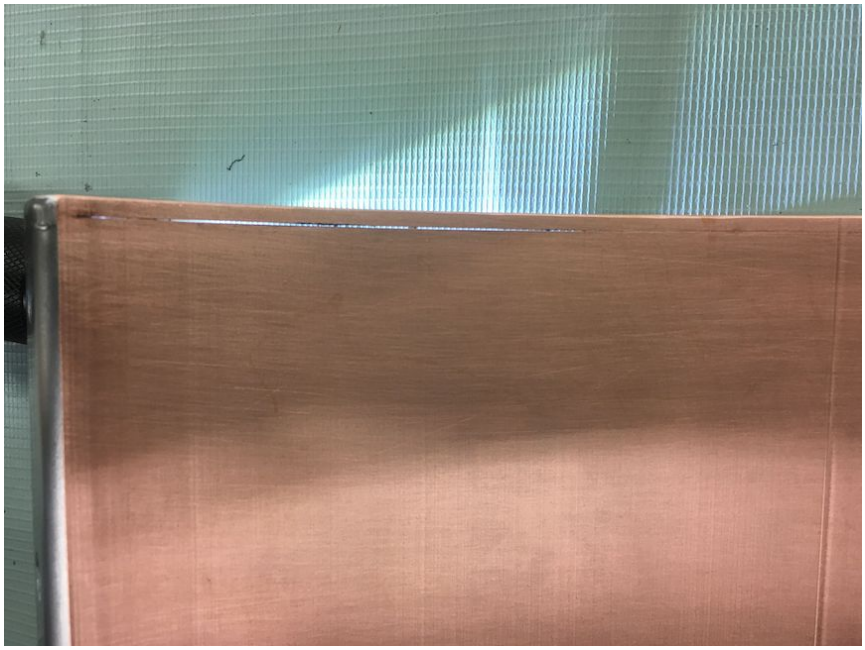

Figure 167: This photo shows the crack in the shell. A 3 mils feeler gauge can be easily inserted into it, and a 5 mils feeler gauge can be lightly forced into it.

17.5 End plates

The end plates have two grooves on the RF side so that copper wires (19 AWG, 0.036″ annealed copper wire) can be inserted into them. These wires act as RF seals when they are compressed onto the lips of the outer shell. Figure 168 shows one of the four end plates sections. Figure 169(a) shows a close up of the groove and the copper wire after it is inserted into it. Figure 169(b) shows the end plate after its contact surfaces have been tin plated. The tin plating is to prevent corrosion.

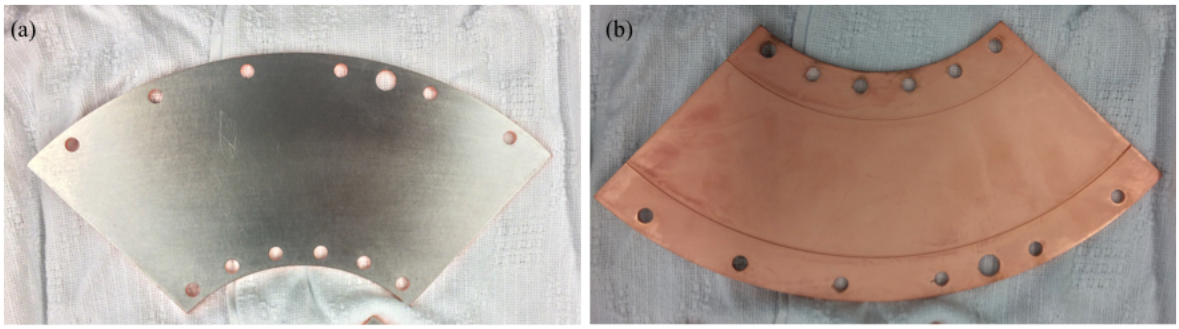

Figure 168: These are photos of one of four end plate sections. (a) is the outer side that is un-plated. (b) is the plated side that sees RF. There are two grooves for inserting wires that act as RF seals.

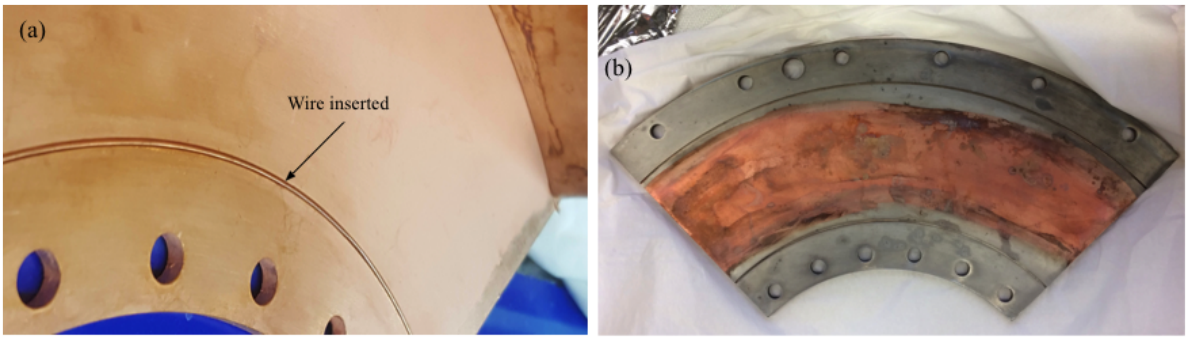

Figure 169: (a) shows a piece of copper wire inserted into the groove to form an RF seal when it is compressed onto the lips of the outer shell. (b) shows the contact surfaces have been tin plated.

Editor's note: The wires shown in Figure 169(a) had to be relocated because it was discovered during installation that they would miss the surface of either the outer conductor or the inner conductor. The modification is shown in Figure 190.

17.6 Power module assembly

Figure 170: Parts of the power module without the RF window are shown here: (a) PA shell upper assembly, (b) PA shell and (c) PA cone.

The parts of the power module assembly without the RF window is shown in Figure 170. Although shown in the final drawing, the upper PA shell assembly has not been plated with 0.5 mils of tin because of an oversight. The tin is used for anti-corrosion purposes and has no effect on its RF performance. The installation of the power module into the cavity body assembly is discussed in section 17.10.1

17.7 Coupling ring

The coupling ring was TIG welded to the coupling stem shown in Figure 171. Although, the welding process left some pits which should not cause sparking problems, the joint was further polished to successfully remove most of the pitting. The coupling ring was also tested for virtual leaks before installation and none was found. In version 2 of this cavity, we will use a braze joint instead.

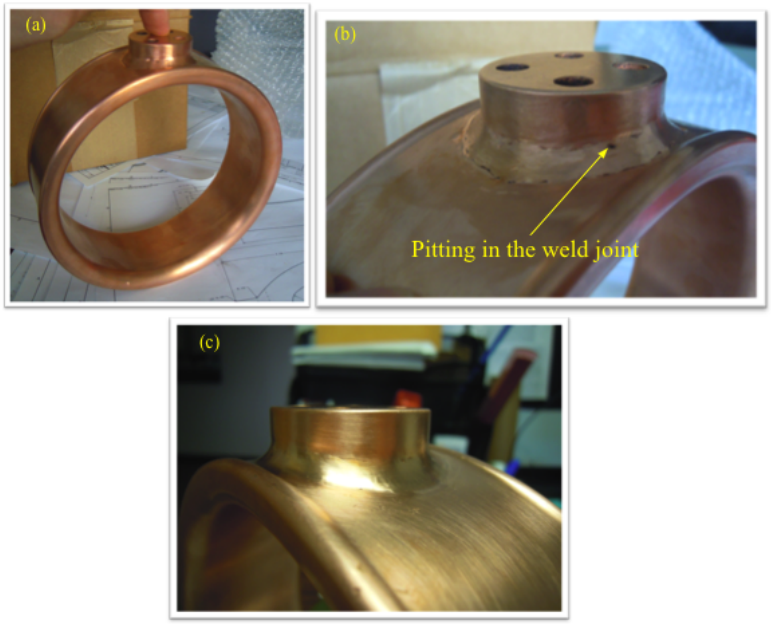

Figure 171: (a) The coupling ring welded to its stem. (b) There are pits left by the welding process. (c) Most of the pitting removed after polishing.

17.8 HOM damper

Figure 172 shows the HOM damper after copper plating. The un-plated parts labelled in the figure form the inner surfaces of the HOM cavity. The high resistivity of stainless steel will help damp the HOM modes.

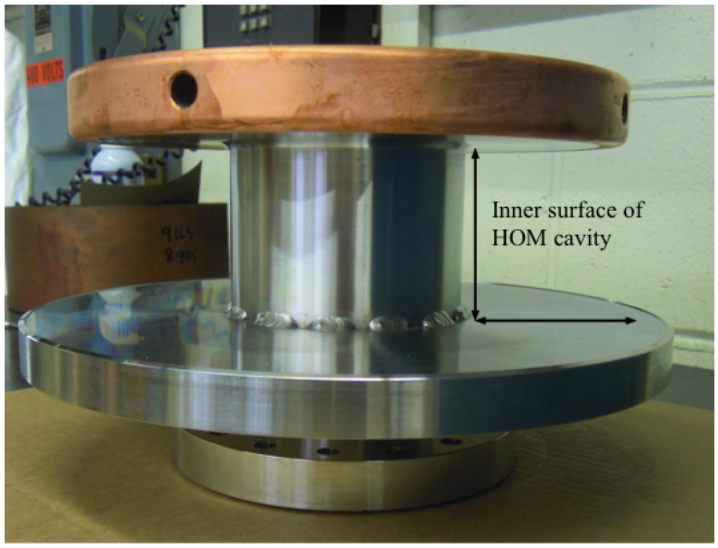

Figure 172: The HOM cavity. Only the necessary surfaces are copper plated. The rest are left bare to help damp the HOM modes.

17.9 Outer body assembly

The assembly of the outer body of the accelerating cavity is shown in the figures below. During welding, He gas is flowed across the weld surfaces to prevent oxidation and to provide convective cooling as well. Even with these precautions, the surface is contaminated, probably with carbon, which has to be carefully polished away.

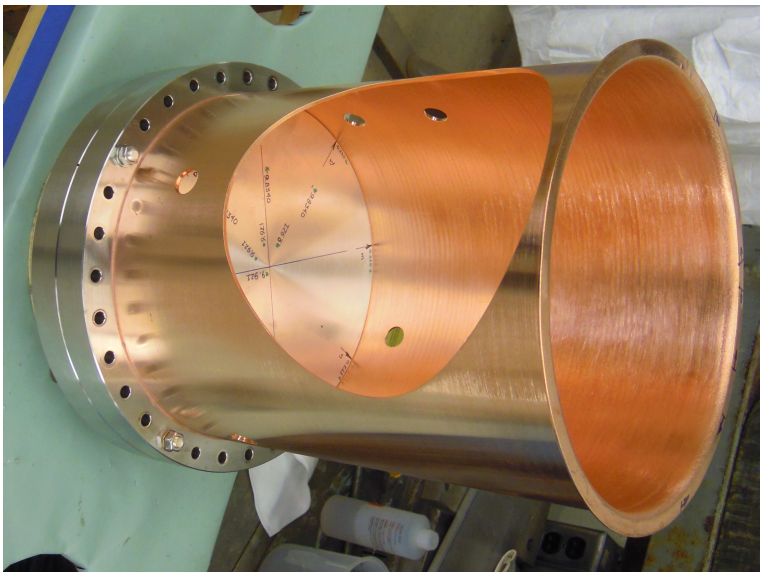

Figure 173: The accelerating cavity without the RF window.

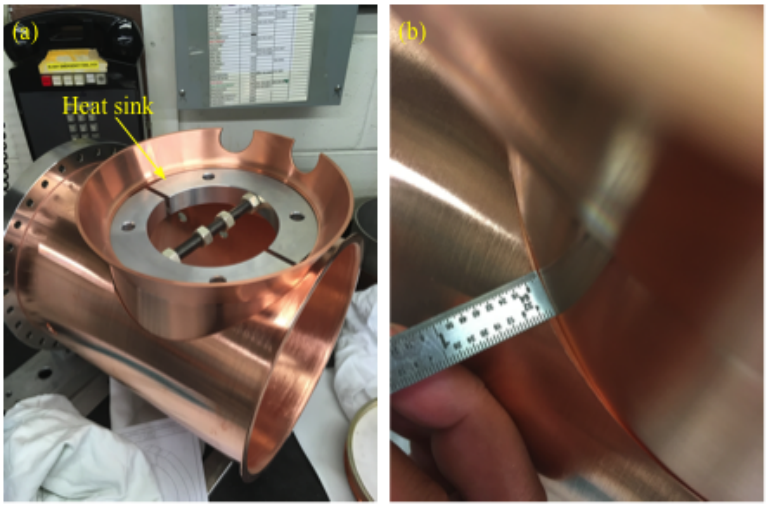

Figure 174: (a)The PA neck shell sitting on the accelerating cavity with a heat sink fixture before welding. (b) There is a 1/8″ gap between the neck shell and the accelerating cavity which will be filled in during the weld.

The cooling tubes used for welding the neck shell to the cavity body is shown in Figure 175(a). This is to prevent the neck from deforming. The successful weld is shown in in Figure 175(b).

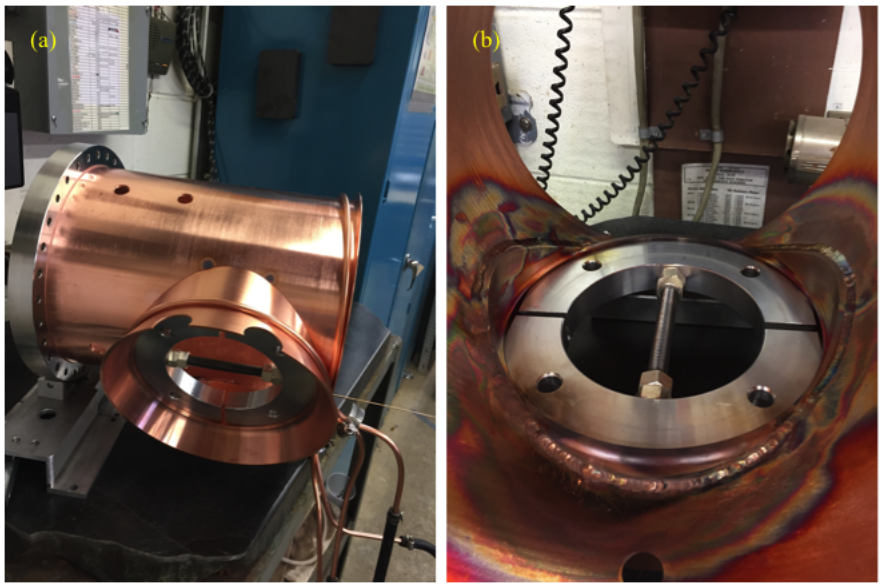

Figure 175: (a) The neck shell is cooled both by convection via the aluminum heatsink and by conduction with ice water flowing in the cooling pipes wrapped around the neck. (b) The completed weld.

After the neck has been welded to the accelerating body, the feet and the probe ports are welded next. The assembly after this step is shown in Figure 176. This assembly has been leak checked to 5×10^{-10} Torr·L/s. The next step is for the flat window to be welded to it.

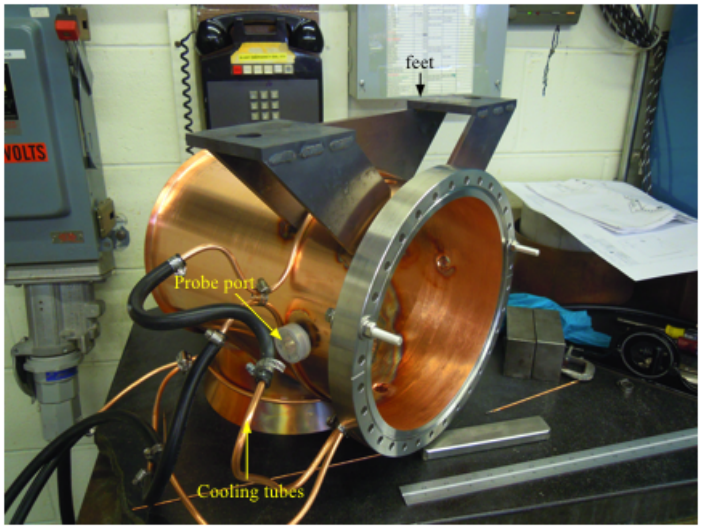

Figure 176: The feet and probe ports are welded to the accelerating cavity.

The flat window has been oriented to the correct direction with the coupler ring attached by the use of a fixture shown in Figure 177(a). Cooling was applied to prevent the window from cracking or melting of the braze joint during the weld. During the weld, a shield made from copper foil was used to protect the window surface from carbon specks. See Figure 177(b). The completed welds are shown in Figure 177(c) and (d). This subassembly has been leak checked to 2×10^{-10} mbar-L/s.

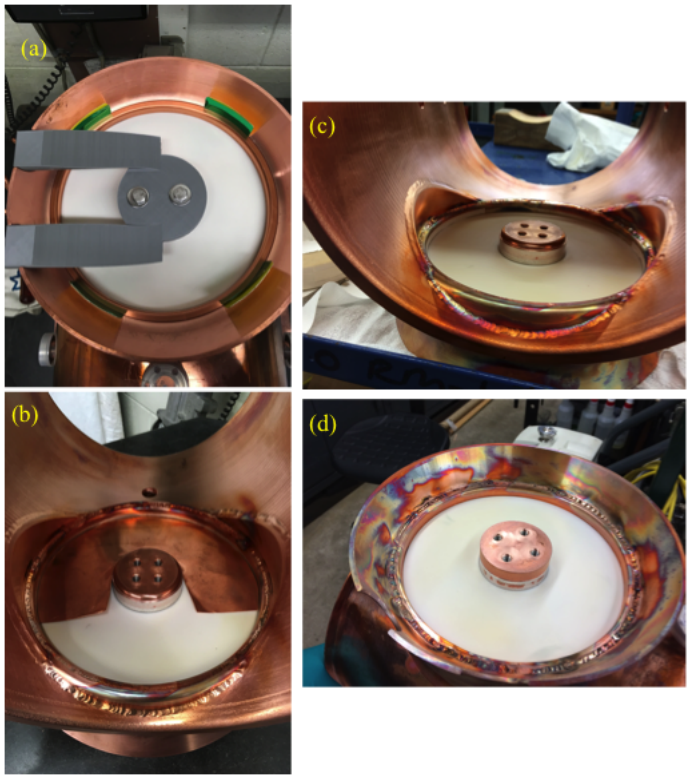

Figure 177: (a) The fixture used to center and orientate the flat window so that when the coupler ring is attached, it faces the correct direction. (b) A shield made from copper foil is used to protect the window surface from carbon specks during welding. (c) The completed weld on the vacuum side and (d) the air side.

Following the successful weld of the flat window, the next item to be welded is the PA shell that is shown in Figure 170(b). Again, ice water has been used to cool the area near the ceramic window. Figure 178 shows the PA shell welded onto the cavity body.

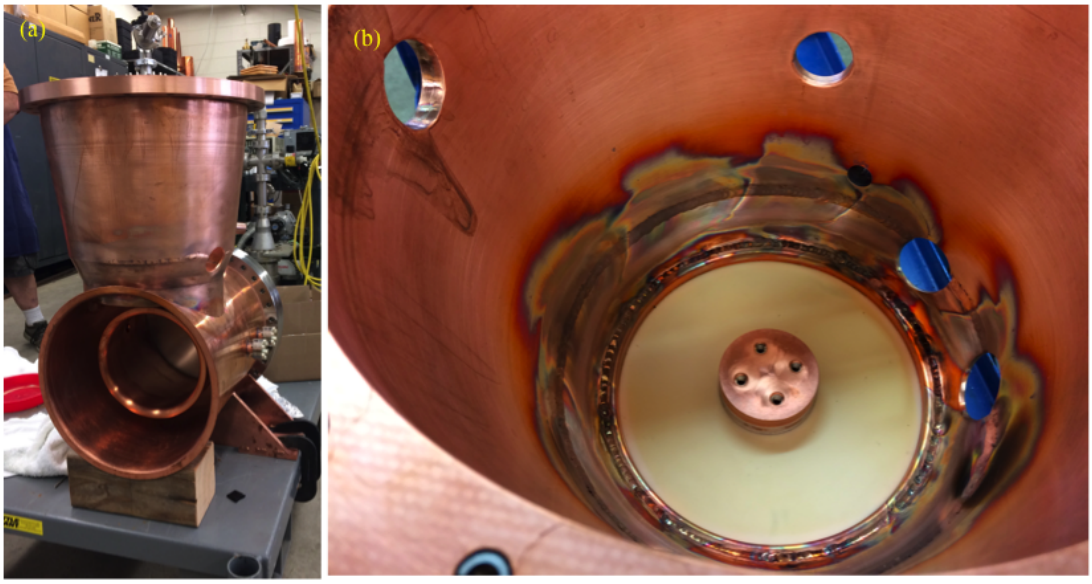

Figure 178: The PA shell welded onto the cavity body. (a) The external view. (b) The view of the weld joint.

17.10 Assembling the cavity

The tuner inner shell assembly (discussed in section 17.3) is aligned and welded to the outer body (discussed in section 17.9). See Figure 179(a) and (b). An alignment fixture that is used to center the beam pipe in the body of the cavity is shown in Figure 179(c).

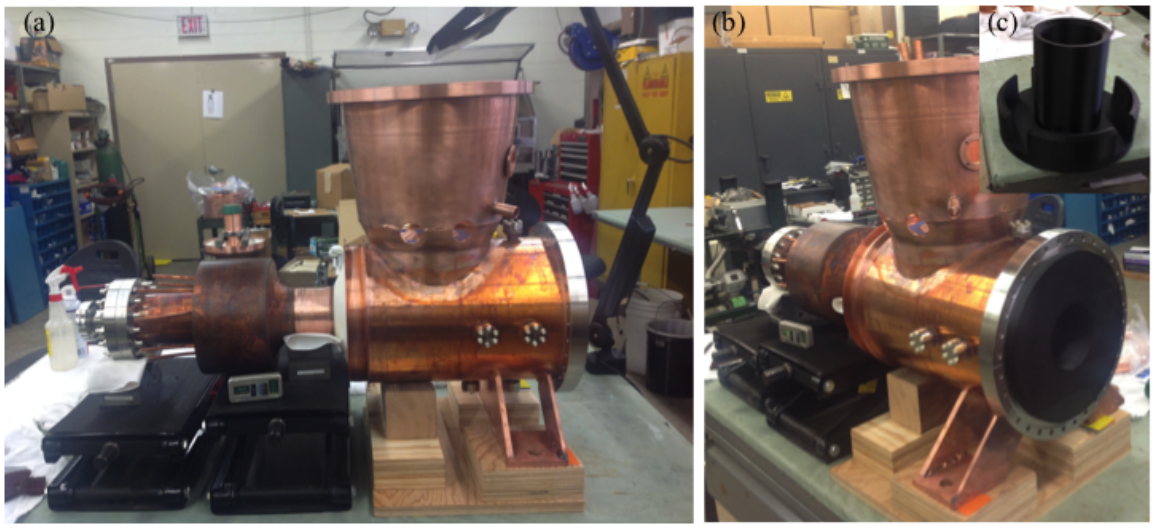

Figure 179: (a) and (b) are two views of the cavity with the tuner inner shell aligned to the outer body before welding. (c) shows the alignment fixture that is used to center the beam pipe in the body of the cavity.

Figure 180: When aligned, the weld lips do not line up and have to ground to match

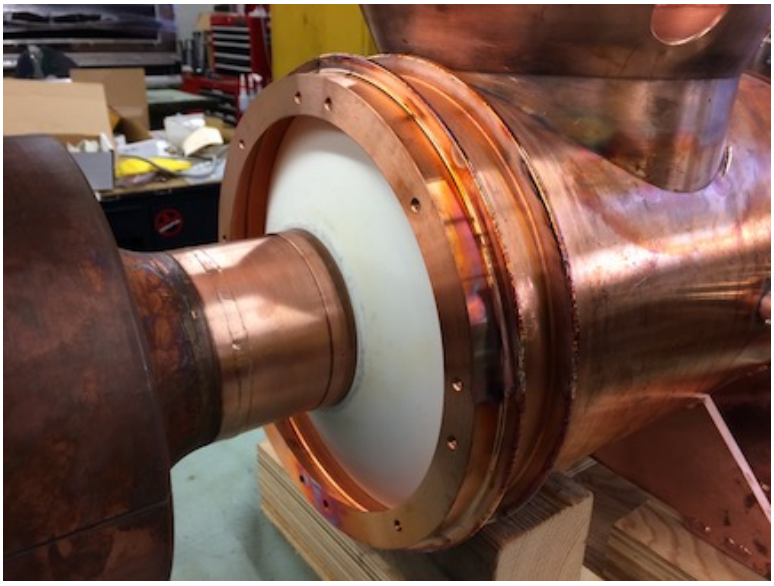

Figure 181: The completed welds between the inner shell assembly and the cavity body and the copper flange to the inner shell assembly.

However, when they are pressed together as shown in Figure 180, the weld lips do not match up because the cross section of the outer body is an oval and not a circle. The difference in radii is about 1/8″ at the location of greatest mismatch. The extra material has to be ground off before welding can take place. Figure 181 shows the completed welds between the inner shell assembly and the cavity body and the copper flange to the inner shell.

17.10.1 Installing the power module and power amplifier

The next step is to install the power module together with the power amplifier and its cathode resonator plus other assemblies associated with the amplifier. Figure 182 shows photos of the various steps.

Figure 182: (a) shows the PA shell, window and stem where the PA cone will be connected; (b) shows the bottom of the PA cone with the spring fingers; (c) cone has been installed; (d) installation of the PA and its associated parts; (e) after installation.

17.11 Tuner stack assembly

Editor's note 1: Before the garnet rings were installed onto the cavity, the RF properties of the first two modes of the empty cavity with and without the PA were measured. See section 20.

Editor's note 2: There were many modifications made to the tuner neck assembly in order to mate it to the cavity body with the solenoid end plate attached. These modifications are documented in section 17.2.1.

Editor's note 3: The outer shell had bad weld joints. Its discovery and future repair was discussed in section 17.4.1.

There is a lot of preparation work before the garnet rings can be installed onto the cavity. Some of the steps are outlined below:

1. Attachment of the solenoid end plate and support structure. See Figure 183(a).
2. Installation of the neck assembly. The neck assembly has been modified (see section 17.2.1) so that it can fit properly with the solenoid end plate installed. See Figure 183(b).
3. Support system for the garnet rings. See Figure 185(f). The support was printed on a 3D printer and bolted on a unistrut.

After the support structures and the neck assembly are installed, only then can the garnet rings be installed.

Figure 183: (a) A turn buckle is used to ensure that the frame holding the solenoid end plate is square. (b) The neck assembly is installed onto the cavity together with the end plate.

17.11.1 Installing the garnet rings

Before the garnet rings are installed, we used a hose clamp to compress the 4 sectors of the inner conductor. This reduced the radius of the inner conductor makes it easier for the garnet rings to slip onto the inner conductor. When all the rings are installed, we release the hose clamp and friction will then partially hold the rings in place. See Figure 184.

In order to make sure that we do not damage the garnet rings during the installation process, we have made aluminum rings for practice. See Figure 185(a). Once we were satisfied, we started the garnet ring installation process.

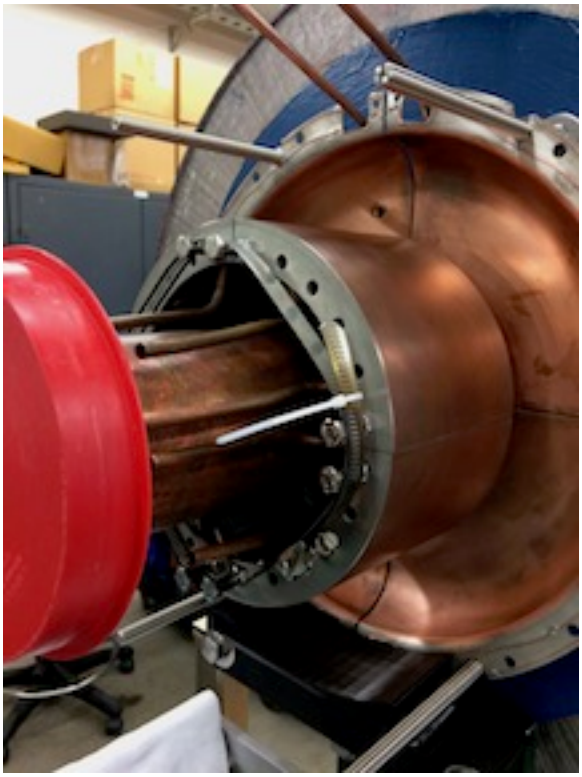

Figure 184: Hose clamps are used to squeeze the four sectors of the inner conductor together to reduce its radius.

We have pre-selected the garnet rings for the installation: the best shim ring that we have, goes on first. Then the best regular garnet rings go on next in sequence until the worst ring. This sequence was picked because the MWS simulations, see Figure 216, showed that the magnetic field is weakest at the shim end and strongest at the shorted end. This means that the highest RF losses will be at the shim end and the smallest at the shorted end. This is the reason for our chosen sequence. For the record, the ring sequence as installed is: best shim ring, ring #3, #11, #5, and #1. (The number that identifies each ring is the smallest number marked on each ring. These numbers identify the garnet sector/witness

piece pair). **Editor's note: The method below describes the second installation attempt. In the first attempt, there was insufficient grease between the ID and the inner conductor which required complete disassembly of the rings. See section 17.11.5 for lessons learned from the first attempt.**

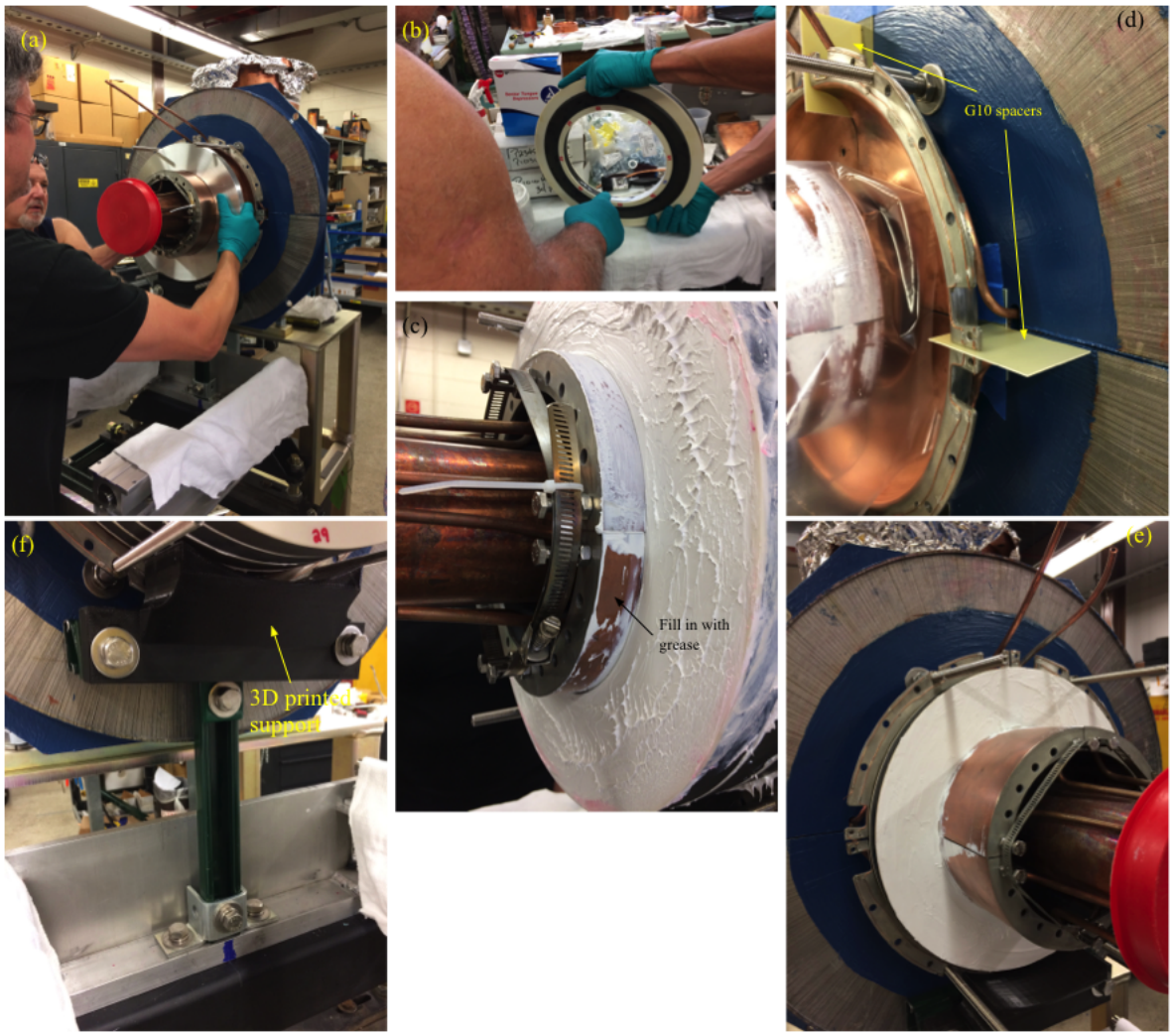

Figure 185: (a) An aluminum ring that has the same dimensions as a garnet ring is used for practice. (b) Grease is applied liberally to the ID of the garnet ring. (c) Grease is applied to the inner conductor before each ring is inserted. There is already grease on the face of the ring because this is the second installation attempt. And the arrow indicates where there was insufficient grease from the first install. (d) G10 spacers are sued to set the position of the stack. (e) A thin layer of grease is applied to the face of the garnet ring. (f) A support is used after the 1 shim + 2 regular rings have been installed.

We grease (for information about the grease, see section 5) the ID of each ring before installation. See Figure 185(b). It is necessary to apply a thick layer here because any air gap between the ring and the inner conductor can cause sparking or even "melting" of the garnet [5, 15] when high power RF is applied. We also apply grease to the inner conductor to ensure that grease fills the gap.

We install the shim ring (see section 8.2) first. We tighten the hose clamp shown in Figure 184 to allow the shim ring to go onto the inner conductor. Once it gets into its approximate position, we loosen the clamp and then visually check for grease at the gap. If we can see oozing of the grease beading out of the gap, then we know there is sufficient grease that fills the gap. If not, we pull the shim ring off, apply more grease to its ID and to places there is insufficient grease on the inner conductor. See Figure 185(c). The shim ring is pressed onto G10 spacers which are set to approximately its final position. See Figure 185(d).

The regular rings are installed next. We repeat the application of grease to the ID and the inner conductor. We push a ring to about 1/8" from its predecessor. We visually inspect the gap to check that grease does fill it using the same methodology described from the shim ring. Once we are satisfied, we then push the ring onto its predecessor. Once the ring is pushed onto its predecessor, it is very difficult to remove because of suction from the grease. Flaking of the rings can result during separation. See Figure 192.

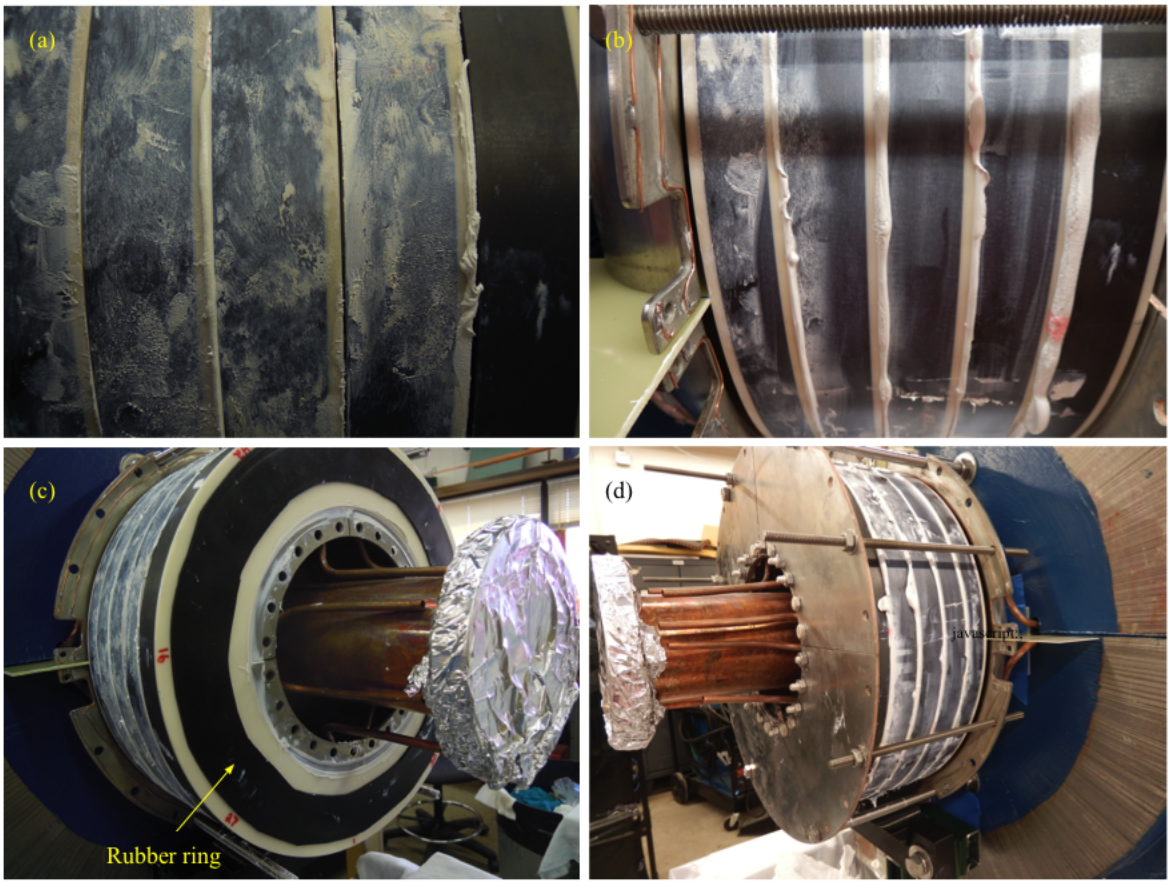

Figure 186: (a) shows gaps between rings. (b) The gaps are filled with grease after compression with the fixture shown in (d). A rubber ring shown in (c) is used to protect the rings.

Unlike the thick grease that is applied between the ID and the inner conductor, we only apply a thin layer of grease between rings. In this case, we just want to improve thermal contact by filling in any imperfections between the garnet and the alumina. See Figure 185(e).

The above sequence is repeated until all the four regular rings are installed. The installation is paused after the third ring (one shim + two regular rings) is installed. This is where we install a support to relieve stress on the conical window. See Figure 185(f).

After the final two rings are installed, we visually examine the stack to look for gaps. The seam between the garnet rings and the inner conductor is filled with grease. However, there are gaps between rings. See Figure 186(a). We believe the gaps are caused by the uneven fill of grease. The uneven fill happens when some grease is pushed between the rings due to the extra grease between the rings and the inner conductor. We made a compression fixture to fix this problem. The compression fixture is shown in Figure 186(d). A rubber ring, shown in Figure 186(c) is used to protect the garnet during compression.

The entire stack is pushed against the spacers with the fixture shown in Figure 185(d). Light, continuous pressure is used to squeeze out excess grease. The process takes about one day. The tension on the hose clamp is released during this compression phase. The gaps eventually fill with grease, shown in Figure 186(b). The final average thickness of the grease is 9 mils after we finished this process.

17.11.2 Installing the outer shells

We have to be very careful not to scrape away the grease while installing the outer shells. One obstacle to the installation are the long threaded rods that will be used to bear the weight of the tuner assembly. See Figure 187(a). These get in the way of the installation. This rod (drawing: F10078327) is a solid piece that has ½" threaded rod on the end plate side and 3/8" threaded rod that is visible in the photo. Our backup plan, if it is not possible to slide in the outer shells without disturbing the grease, is to replace the solid rod with one ½" threaded rod, a female hex thread adapter (McMaster-Carr catalog part number: 98434A410), and a 1/8" threaded rod. However, by breaking up the solid rod into three pieces, the strength of this assembly is weaker than the original solid rod.

The outer shell is slid onto the rod via a hole made for it. A nut on the rod is turned in order to advance the shell to its final position. All the while, the shell has to be held up so that it does not scrape the grease. See Figure 187(b) and (c). After careful maneuvering, all four outer shells made it to their final positions. See Figure 187(d). **Editor's note: In the first installation attempt, we discovered that there were cracks in the joint between the lips and the cylindrical body of the outer shell. We have left the cracks as is. We will repair the cracks in the future. See section 17.4.1.**

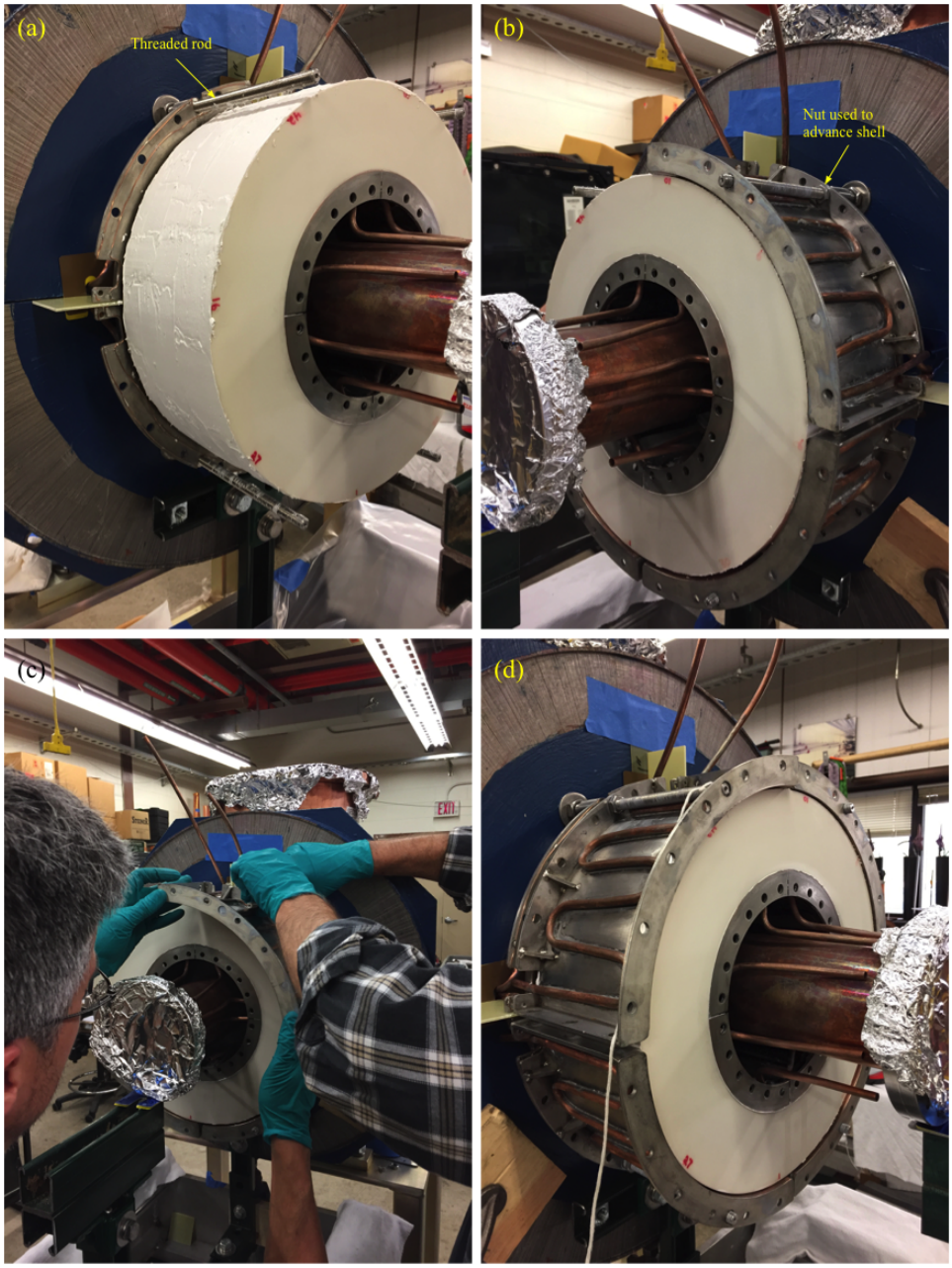

Figure 187: (a) A thin layer of grease is applied to the outer surface of the tuner stack. The threaded rod makes the installation of the outer shell more difficult. (b) A nut is used to advance the shell into its final position. (c) One technician holds up the outer shell, while another advances the shell by turning the nut. (d) Almost there!

Next, the spacers are inserted into the slots and the shells are then bolted together. At this point the shells are not tightly bolted to the neck assembly yet. Once the nuts along the slots with the spacers are tightened, we have to visually ensure that grease flows out of the seams. This is to make sure that

grease fills the space between the outer shell and the tuner stack. See Figure 188(a). Insulating washers are used to prevent the bolts from electrically shorting the outer shells. See Figure 188(b).

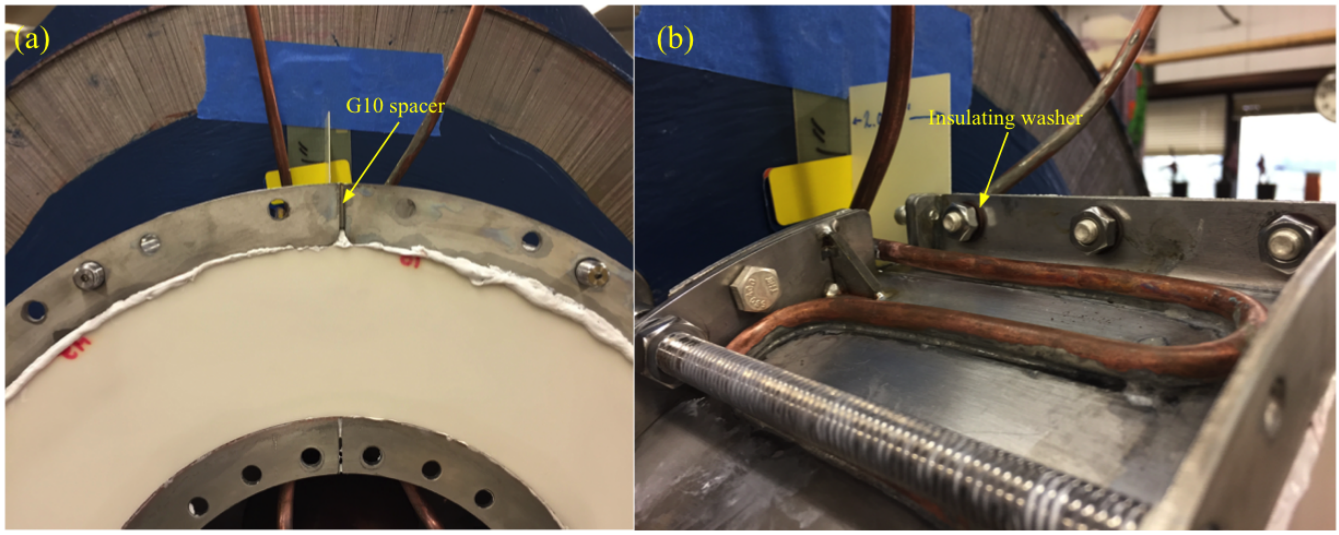

Figure 188: (a) A G10 spacer that is between the outer shells defines the spacing between them. Grease flows out from the seams which tells us that there are no air gaps between the outer shell and tuner stack. (b) Insulating washers are used to electrically isolate the bolts from shorting out the outer shells.

17.11.3 Preparing for end plate installation

Before the end plates can be installed, the position of the tuner stack w.r.t. the inner conductor and the outer shell has to be established. The goal is to try to position the tuner stack so that it is about 10 mils below both the inner conductor the outer shell. However, we found that the dimensional errors of the neck assembly prevented us from achieving this number at the OD of the tuner stack. Thus, we were only able to have the ~10 miles requirement at the ID and we did the best we could for the OD. The procedure is as follows:

First, the three nuts along the shell shown in Figure 188(b) and its sister nuts on the other three quadrants are loosened so that the tuner stack is free to move. The nuts that connect the outer shell to the neck assembly are tightened to 45 inch-pounds (1/2 of the final torque). The tuner stack is set into position, about 10 mils w.r.t. the inner conductor , by pushing using the fixture shown in Figure 189(a) and inserting shims behind the space shown in the inset of Figure 189(b). The outer shell is set to its final position w.r.t. the tuner stack by turning the adjustment nut shown in Figure 189(b) and nut 2 shown in Figure 189(c). The shim shown Figure 189(b) is supposed to stop the tuner stack from moving inwards. But in practice they do not seem to be stiff enough to hold the stack. While turning the adjustment nut to draw in the outer shell, the relative position of the tuner stack moves outward w.r.t.

the inner conductor. **Editor's note: We really do not know how much grease is dripping on the front of the tuner stack because it is hidden from view. How the excess grease will affect performance of the cavity is unknown at this time.**

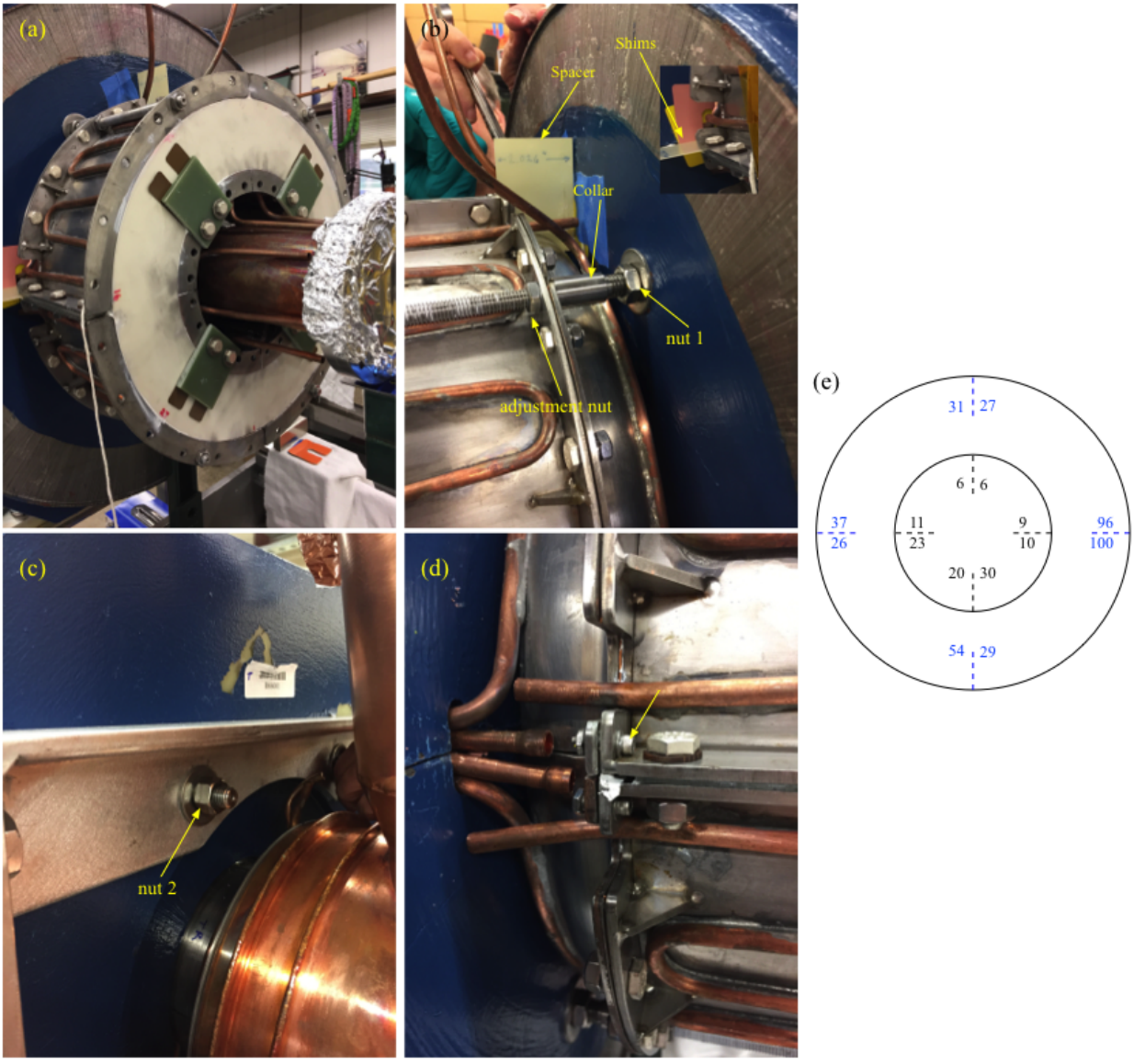

Figure 189: (a) shows the fixture that pushes the tuner stack inward. They are made from ¼" thick G10 and a 10 mil shim is inserted beneath the G10 rectangle. (b) The adjustment nut and nut 1 that are used to pull outer shell into position. Shims are inserted behind the spacer to push the stack and to set its longitudinal position. (c) Nut 2 that is behind the solenoid end plate is also used to pull in the outer shell. (d) The gaps are closed with bolts. The 4-40 screw, as indicated, closes the edge. (e) The final position of the tuner stack measured w.r.t. the outer shell (blue) and the inner conductor (black) in mils. This measurement was done after all the nuts are tightened and the fixture shown in (a) is removed.

Finally, once the tuner stack and the inner and outer shells are in position, the nuts that connect the outer shell to the neck assembly, and the adjustment nuts are loosened. This is to allow the nuts shown in Figure 188(b) to be tightened to 30 inch-pounds. The loosening also means that the outer shell springs away from the collar. Unfortunately, loosening is necessary allow for compression of the outer shell onto the tuner stack. Once the nuts that are indicated in Figure 188(b) are tightened to 30 inch-pounds, the nuts that connect the outer shell to the neck assembly are tightened to 90 inch-pounds. Finally, the adjustment nut is used to pull the outer shell back to the collar and it is tightened to 130 inch-pounds. The last screws to be installed are the 4-40 screws (**Editor's note: originally 8-32 screws were supposed to be used but the holes did not line up, so smaller screws were used.**) that squeeze the end of the outer shell to the neck assembly. The final positions of the tuner stack w.r.t. the inner conductor and outer shells are shown in Figure 189(d).

17.11.4 Installing end plates

We found problems with the wires on the end plates that are shown in Figure 169(a) that act as RF lips. The wires inserted into the slots on the end plates can miss contacting either the outer shell or the inner conductor. This is not a good situation because from the simulations (see Figure 216), the highest surface current density will be close to the end plates. Therefore, we had to change the location of the wires by soldering on new wires that will definitely make contact with the required surfaces. The relocated wires are shown in Figure 190.

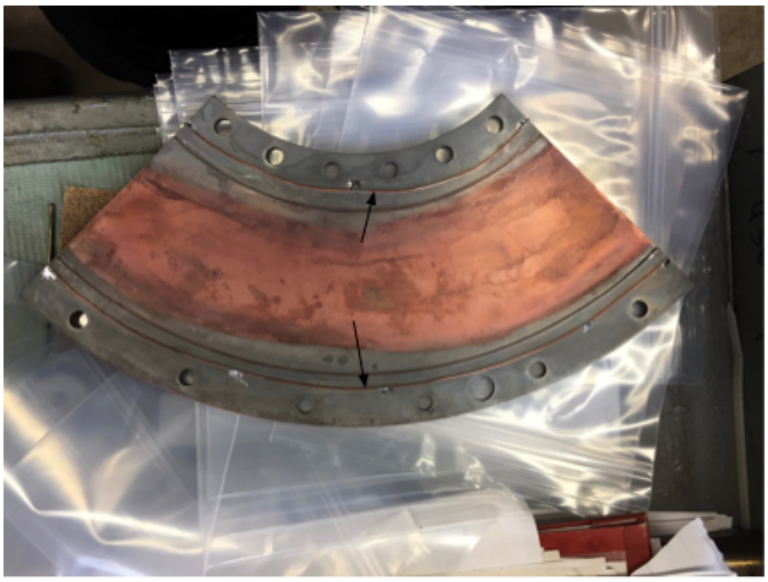

Figure 190: The wires that form the RF lips have been moved to guarantee contact with both the outer shell and inner conductor.

Grease is then applied, one quadrant at a time, to the face of the tuner stack and to the end plates. An application tool is used to ensure that the depth of the grease is consistent between for each application. The goal is to achieve 80% grease fill without contaminating the contact surfaces with grease. Figure 191 shows the some of the steps that we have used to achieve the requirements. The bolts have been tightened to 90 inch-pounds. And after the bolts are tightened, we examine the edges to make sure that there is no grease contamination of the electrical contacts.

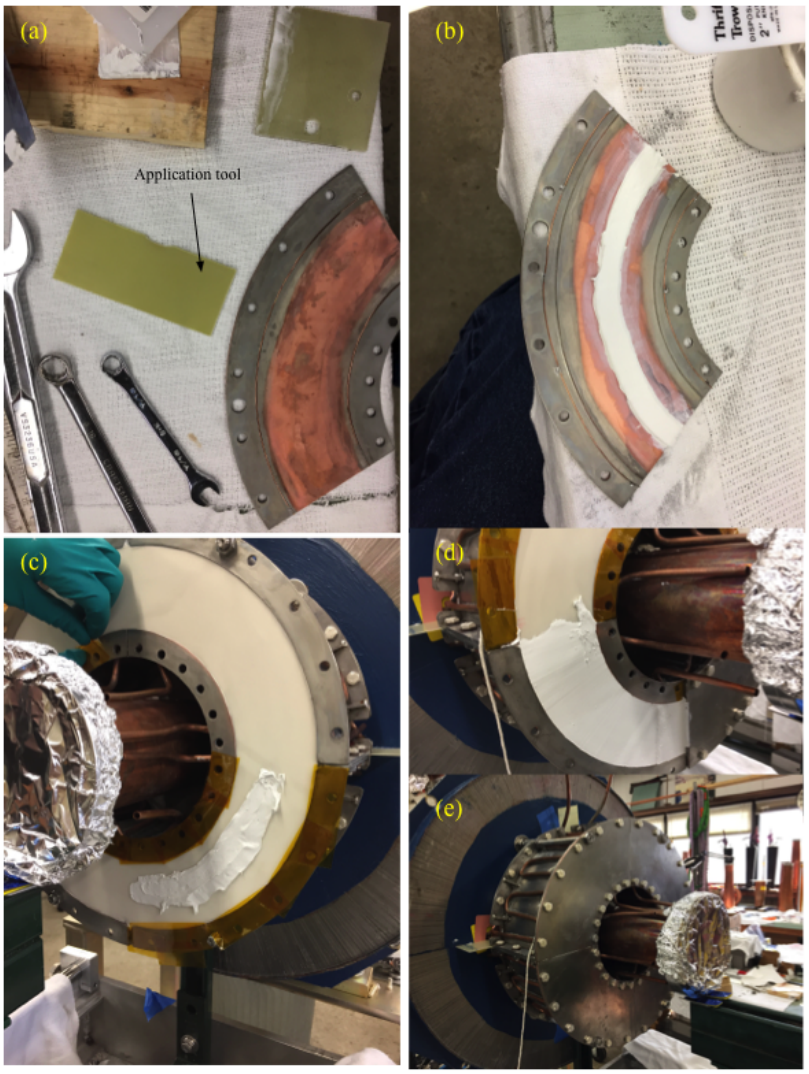

Figure 191: (a) The application tool has a groove that is ¾″ long and 1/8″ deep. (b) The tool allows a consistent application of the grease on the end plate. (c) Grease is applied to the face of the end plate one quadrant at a time. Kapton tape is used to protect the contact surfaces. (d) shows the grease filling the quadrant. Also shown is an end plate bolted onto the outer shell and inner conductor. (e) All buttoned up!

This completes the assembly of the cavity. The next step is to install the bias solenoid. The write up for this installation can be found in section 20 after our discussion on the construction of the solenoid that is presented in the next section.

17.11.5 Lessons learnt

Our first attempt at installing the garnet rings did not go well. We had to unstack the garnet rings to correct. On close examination of the seam between the garnet ring and inner conductor we found a gap that was devoid of grease. After this discovery, we decided to remove the final ring and saw that, indeed, there was not enough grease. See Figure 185(c). After this, we made the decision to remove all the rings and we found that there were voids. In the second go-around, we applied more grease to the garnet ID as well as to the inner conductor. We outlined the new installation method in section 17.11.1.

However, we have to be very cautious if we want to ever remove garnet rings from the stack again. The reasons are:

1. The suction between rings from the grease between rings is very strong. It is very difficult to separate the rings.
2. Separating the rings can cause flaking of the garnet. See Figure 192. The original ring #13 that was used in the first install was replaced with our spare ring #1.
3. Just handling a ring can cause a flake to fall off the alumina. For example, ring #1 has flaked from handling during installation. See Figure 197(d).

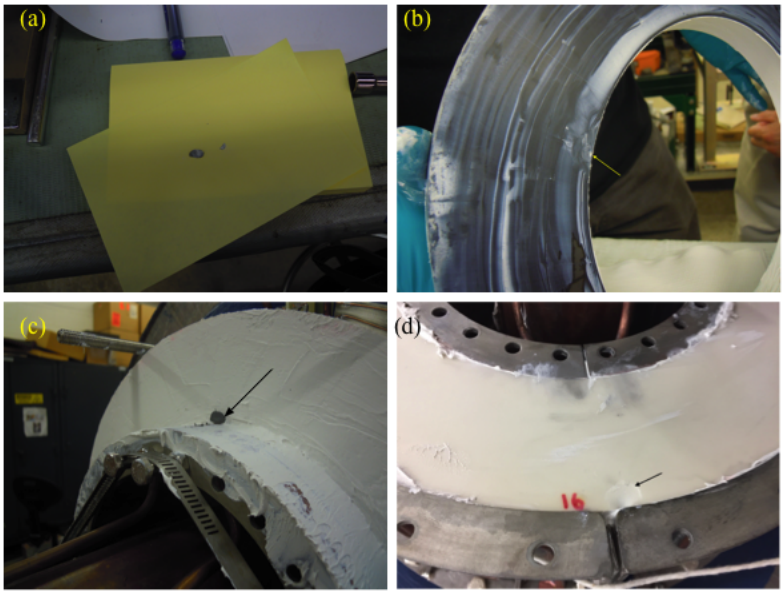

Figure 192: Ring #13 flaked during removal and reinstallation. (a) shows the flake during removal and its location where it fell off indicated with the arrow in (b). (c) shows a large flake that fell off during the second installation when we were pulling it off to add more grease. (d) Handling caused an alumina flake to fall off.

17.12 Drawing numbers

Assembly name	Drawing numbers
Cavity parts	F1007285, F10078211, F10078327, F10084457
Cavity support plates	F10085366, F10085380, F10085403
Coupling capacitor stem	F10049215
Inner shell and beam pipe assembly	F10045157, F10071896, F10071900, F10071903, F10071904, F10072881, F10073008, F10086213
PA base (power module base)	F10049183, F10049230, F10074277, F10078196, F10084373, F10084526, F10084563
PA base assembly (power module base assembly)	F10049209, F10058169
PA outer shell upper assembly (power module outer shell upper assembly)	F10074295, F10074300, F10074301, F10074311, F10084234, F10084238
Support stand	F10078399, F10083770, F10083772, F10086275, F10086868
Tuner outer conductor parts	F10045210, F10057399, F10058135, F10073336, F10078528, F10085151, F10086381
Y567 tube parts	F10056022, F10072884, F10073542, F10075073, F10075318, F10076332, F10076874, F1007746

18 Tuner outer shell crack repair and RF measurements (R. Madrak, C.Y. Tan, K. Duel & M. Slabaugh)

We decided that the best way to repair the cracks (see section 17.4.1) is to fill the cracks with braze material. Before we made the repair, we made RF measurements of a pillbox cavity made from the tuner shells. The measurements are described in section 18.1. The entire brazing process is described in section 18.2. And finally, the RF measurements after the repair are described in section 18.3.

18.1 RF measurements before repair

We made a pillbox cavity out of the tuner shells after they were cleaned. We bolted the 4 shells to form the walls of the pillbox and copper sheets to form the end walls. See Figure 193. Two short wire antennas serve as the pickup and excitation ports for the network analyzer.

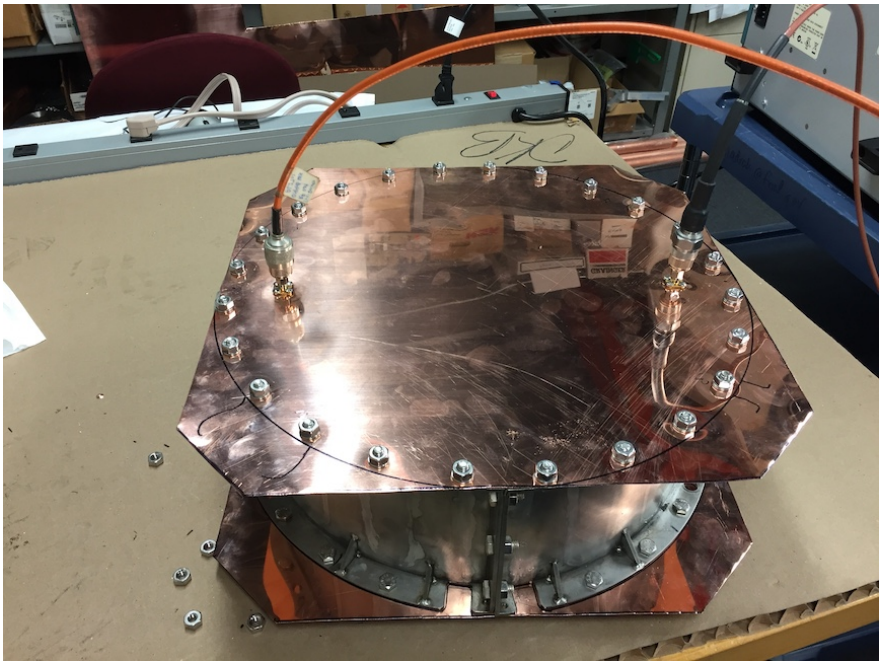

Figure 193: The pillbox cavity made from the cracked tuner shell and copper plates.

Note: the tuner shells were not ultrasonically cleaned when these RF measurements were made. There was still grease trapped in the cracks.

The wide span view of the resonances of the cavity is shown in Figure 194. The zoomed in view of the fundamental is shown in Figure 195. The s21 measurements are summarized in Table 12. We also measured s11 and s22. Since the magnitude of the inverse peak is only ~25 mdB, there is no need to correct the measured Q for loading (weakly coupled). A simple calculation indicates that the Q of a perfect copper pillbox cavity with these dimensions should be ~28,000.

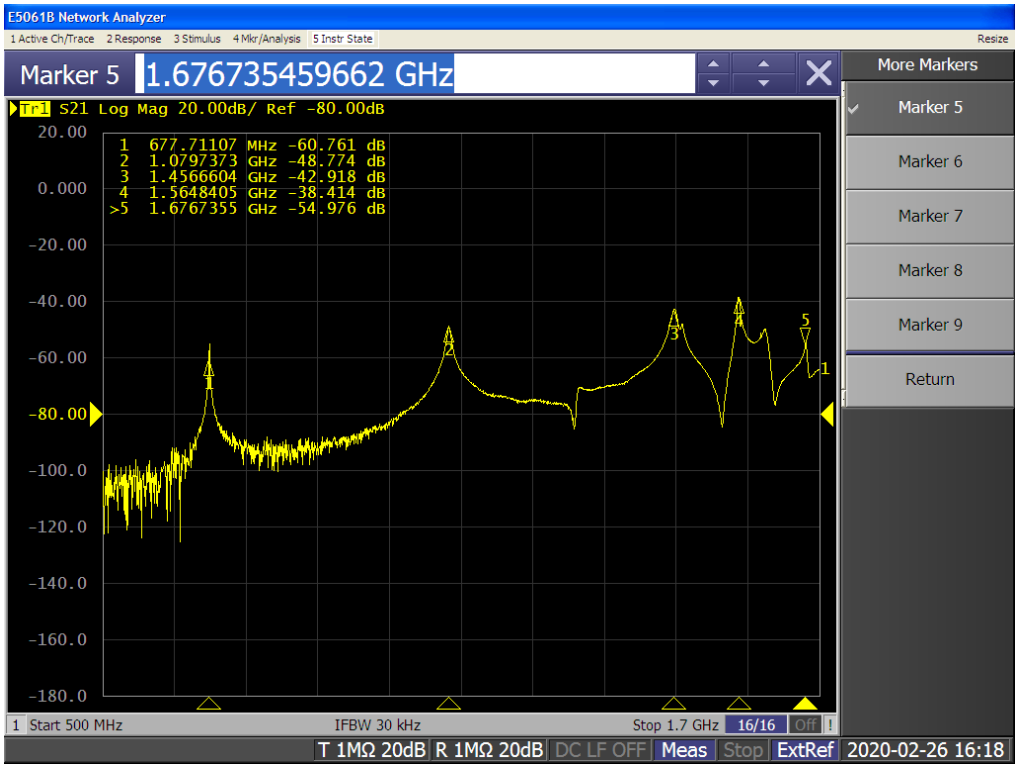

Figure 194: A wide span view of the pillbox resonances before repair.

Mode	Frequency (MHz)	Q
fundamental	678.2 – 678.6	660 – 805
1	1079.75	190

Table 12: The modes of the pillbox cavity before repair.

A CST simulation shown in Figure 196 shows the distribution of the currents in the cavity. Since the currents run directly across where the cracks are, a pillbox cavity measurement of the Q should be sensitive to any improvements.

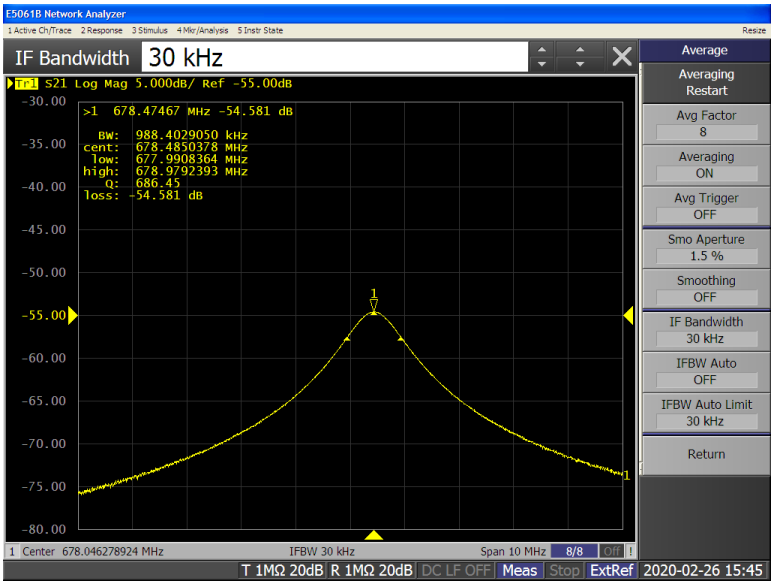

Figure 195: The s21 measurement of the Q and frequency of the fundamental mode.

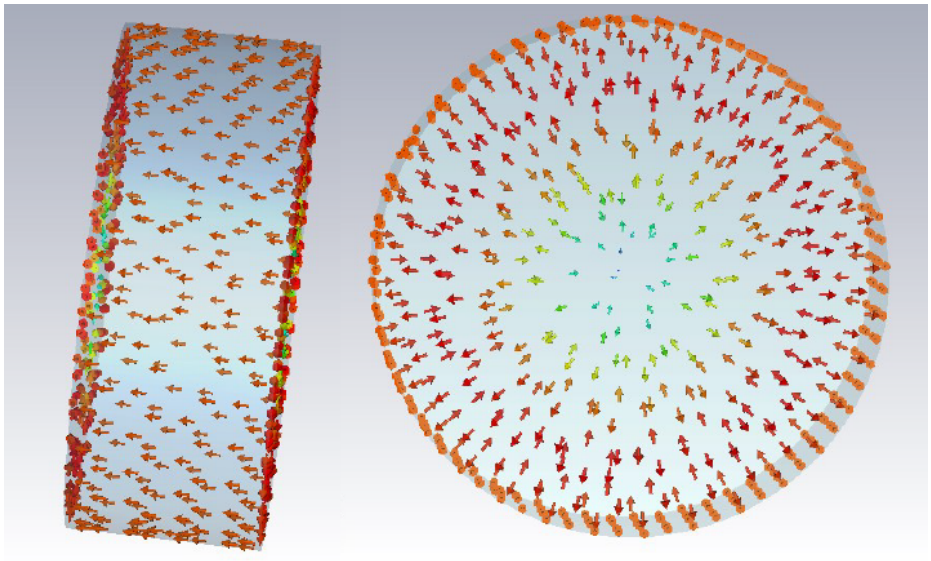

Figure 196: CST simulation showing the current distribution in the cavity for the fundamental mode.

18.2 The brazing process

Hello world

18.3 RF measurements after repair

Hello world.

19 Solenoid construction (A. Makarov)

This type of laminated solenoid has never been built at Fermilab. The construction of the solenoid is extremely labor intensive because of the large number of laminations that need to be stacked to form the end plates (about 3000 laminations) and the core blocks (about 4500 laminations). Figure 197 shows the assembly drawing of the solenoid.

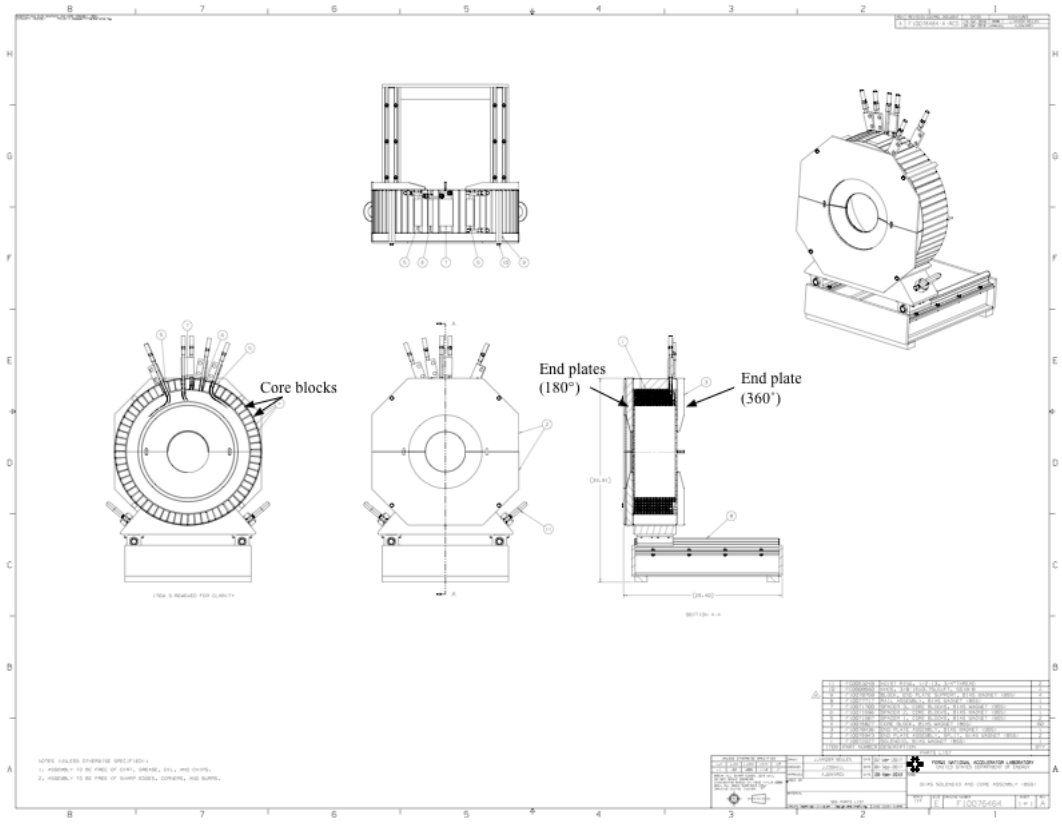

Figure 197: The solenoid assembly drawing (F10076464). The core and the end plates are made by stacking thin sheets of steel laminations.

The travelers for the assembly process can be found in Ref. [56]. The following sections highlight some of the procedures.

19.1 End plate assembly

An example of the process for making the end plate is shown in Figure 199. There are 4 different lamination shapes that have to be stacked in order. The different types of laser cut laminations are shown in Figure 198. The laminations are made from C3 coated, M15 silicon steel sheets that are 0.014" thick. Each lamination is individually epoxied and then stacked in order in a stacking fixture. For the end plate (180°) (see Figure 197), it is made up of two 180° halves. For the end plate (360°), it is one circular piece. After the epoxy has cured, the curing fixture is removed and the end plate is revealed. More photographs of the construction process can be found in Ref. [57].

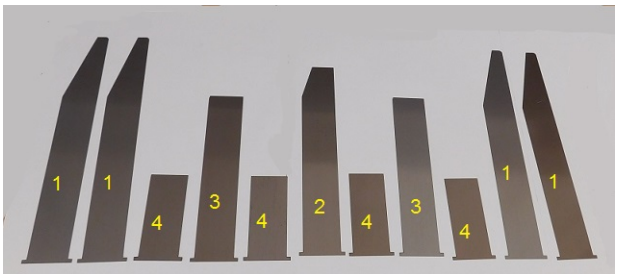

Figure 198: The 4 different types of laminations that have to be stacked in order.

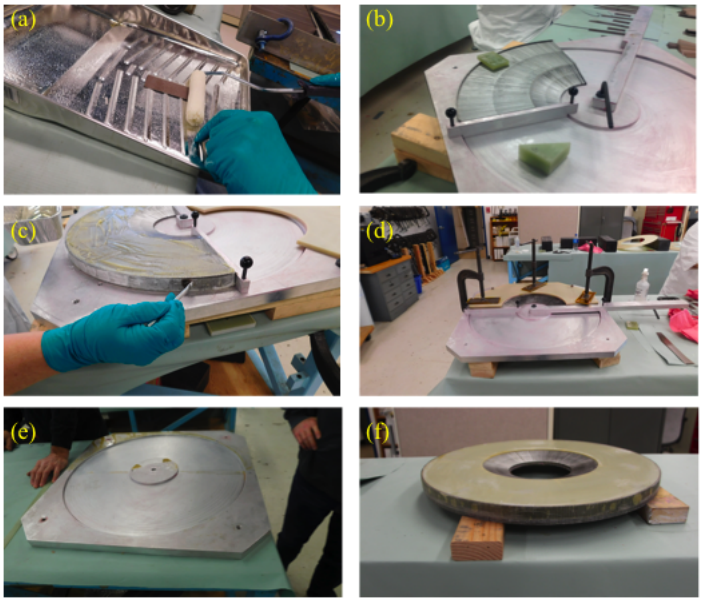

Figure 199: The construction of the end plate of the solenoid. (a) Each individual lamination is epoxied. (b) The laminations are stacked in order. (c) Epoxy is brushed on before applying a layer of fiber glass tape to the edge. (d) Example of 180° of the end plate is clamped in a curing fixture. (e) The 360° end plate in the fixture. (f) The end plate (360°).

19.2 Core assembly

There are sixty core blocks that have to be made. Each core block is made from more than 66 laminations. The laminations are made from C3 coated, M15 silicon steel sheets that are 0.014" thick. Each lamination is individually stacked in a potting fixture which makes one core block.

Thirty of the above described core blocks are then installed into a stacking fixture where the laminations are compressed. The laminations are bonded by baking the fusion coating that is on adjacent laminations. The second set of thirty core blocks are made with the same procedure so that sixty core blocks are produced. Figure 200 shows thirty core blocks installed in the stacking fixture.

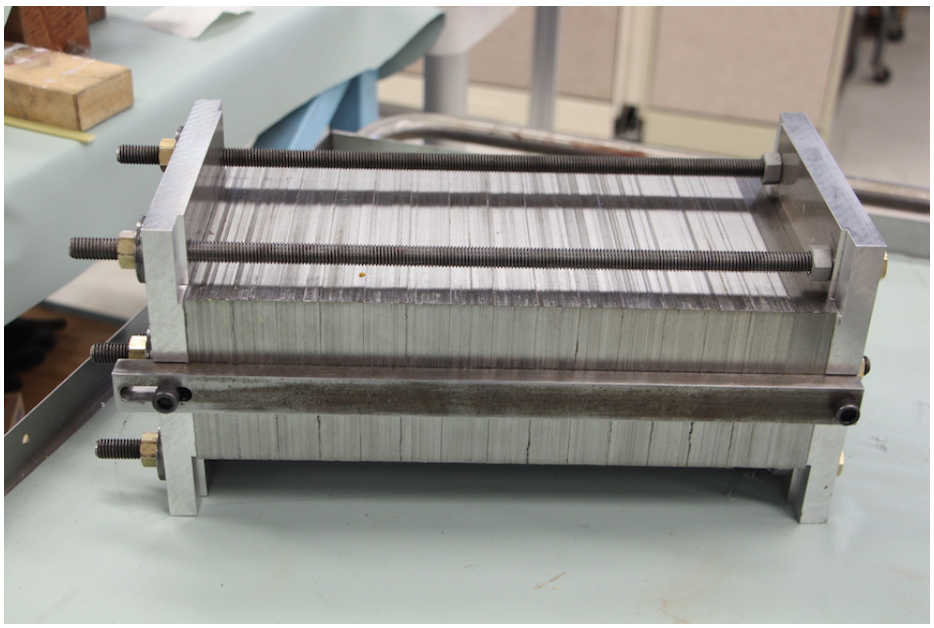

Figure 200: Thirty core blocks are installed in the stacking fixture so that the laminations can be compressed and baked.

19.3 Solenoid coil assembly

The solenoid coil assembly is made of 3 sets of coils. Electrically there are only 2 coils in the solenoid which can be powered independently. The main coil consists of two pancake type sections wound in 4 layers. These sections are connected in series with a jumper brazed to the leads to give 48 turns. An outer 5th layer coil has 12-turns. The total number of turns is 60.

Since there are 3 coils, there are 3 independent water cooling passages in the solenoid (two for the main coil, and one for the second coil). The assembly drawing is shown in Figure 201. All the coils are made from 0.46" square, 0.25" ID copper conductor. To prevent shorts between the conductors, fiberglass tape is applied as electrical insulation. The coils are then installed into a potting fixture and vacuum impregnated with epoxy. Figure 202 shows a few of the steps in the procedure for making the solenoid coil assembly.

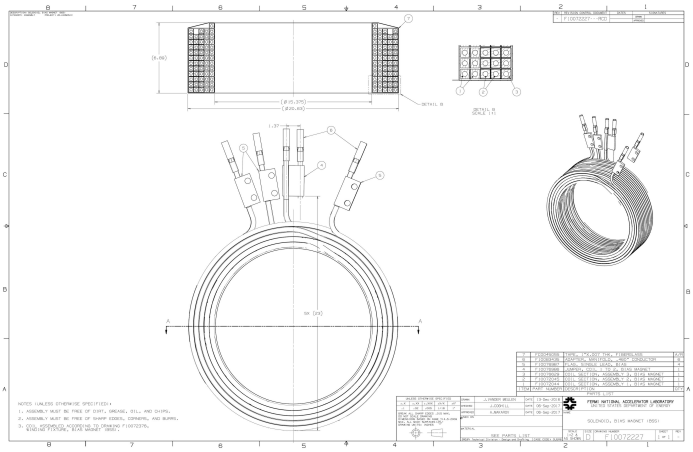

Figure 201: The assembly drawing of the solenoid coils (F10072227).

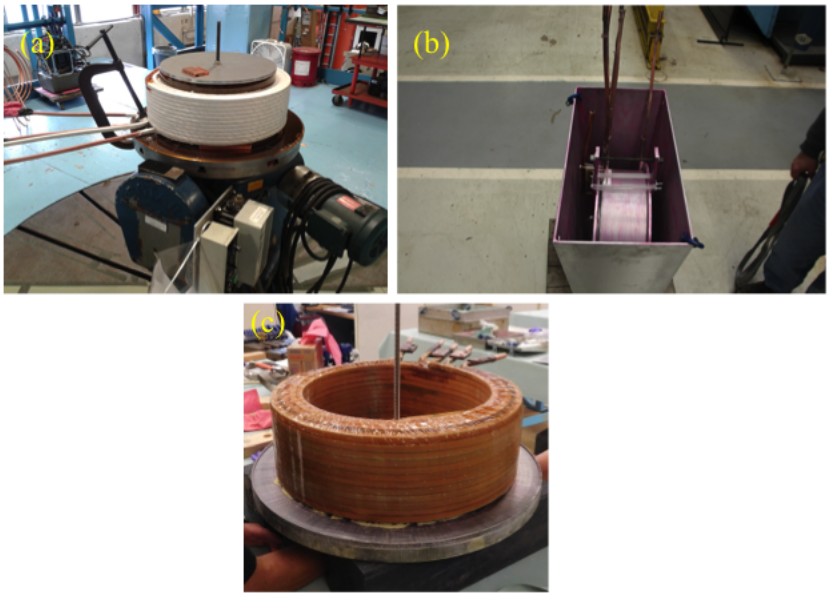

Figure 202: (a) The copper conductor being wound on the winding table. (b) All three coils in the in the potting fixture ready for vacuum impregnation of epoxy. (c) The completed coil assembly glued to the 360° end plate.

19.4 Final assembly

In the final assembly, the coils are glued to the 360° endplate with room cure Cab-O-Sil filled epoxy. See Figure 202(c). The coil-end plate and coil alignment was achieved with a simple tooling shown in Figure 203(a) and (b). Then the core blocks are installed around the coils by gluing them with room temperature cure Cab-O-Sil filled epoxy. See Figure 203(c).

The completed solenoid painted in blue and sitting on its slide is shown in Figure 204. The final weight of the solenoid is 750 lbs. The solenoid was delivered from Technical Division to Accelerator Division on 31 May 2018.

Figure 203: (a) and (b) show the simple tooling used to align the end plate and the coils. (c) Core blocks partially glued to the coils.

The as-found inductances of the coils at "zero" current and resistance are shown in Table 13. The series inductance of coils 1&2&3 is smaller than those shown in Figure 75 because the garnet tuner is

not in the solenoid. Note that the measured inductances of the coils connected in series are not the sum of the inductance of the individual coils. We do not offer an explanation why this is so at this time.

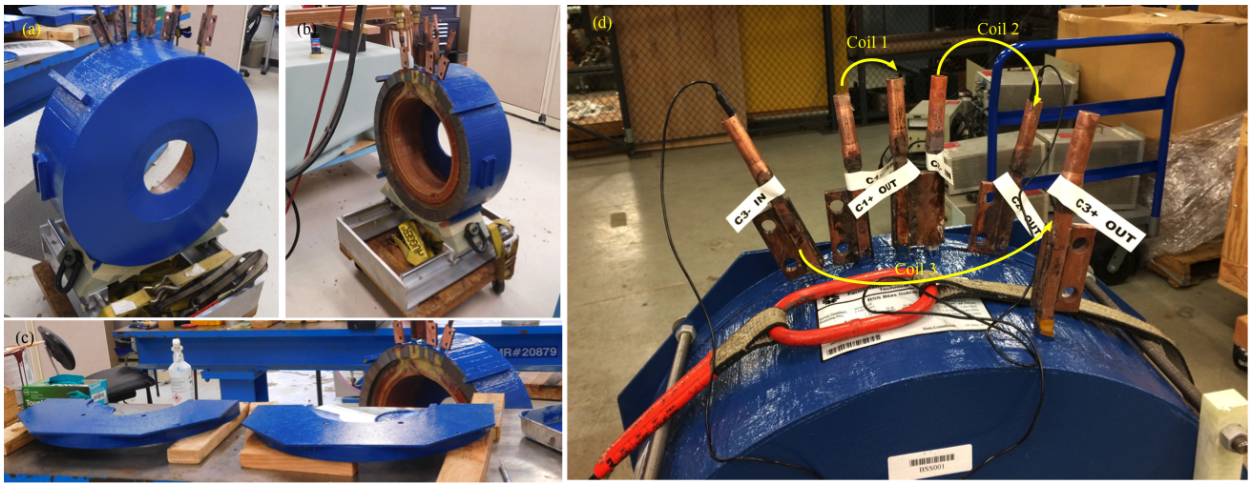

Figure 204: The completed solenoid on its slide. (a) The end of the solenoid farthest from the cavity gap. (b) The end of the solenoid without its plates which allow the tuner to slide in and out. (c) The 180° end plates are in the foreground. (d) The leads of each coil is labeled here. Notice that (i) the direction of the arrows indicate the direction of the current flow and (ii) that coil 1 out is already electrically connected to coil 2 in.

Coil[6]	Inductance @0.1 kHz (mH)	Inductance @ 1kHz (mH)	Inductance @10 kHz (mH)	Resistance (mΩ)
1	0.55 [0.5241]	0.459 [0.5005]	0.455	[5.7]
2	[0.5549]	0.497 [0.46213]	0.509	[5.56]
3	0.176 [0.1771]	0.134 [0.13622]	0.129	[3.2]
1&2 in series	2.06	2.05	1.87	
1&2&3 in series		2.97	3.08	

Table 13: Inductance and resistance of the solenoid coils at "zero" current. Values in [.] were measured at Technical Division.

[6] Inductances were measured by R. Madrak and C.Y. Tan with a HP4263A LCR meter after delivery. We have not chosen to truncate the inductance values from Technical Division. These numbers are as reported.

19.5 Drawing numbers

Assembly name	Drawing numbers
Bias solenoid and core assembly	F10076464
Core block, bias magnet	F10076827
Lamination, core block, bias magnet	F10076825
Potting assembly, core blocks, bias magnet	F10087617
End plate assembly, bias magnet	F10078436
End plate assembly, split, bias magnet	F10076943
Potting fixture, end plate assembly, bias magnet	F10078214
End plate lamination assembly, bias magnet	F10071718
Laminations, end plate	F10071658, F10071717, F10071751, F10071752
Bias solenoid	F10072227
Potting tooling, bias coil	F10081880
Coil section, assembly 1	F10072044
Coil section, assembly 2	F10072045
Coil section, assembly 3	F10076629

20 Mating the solenoid to the cavity and final assembly

The solenoid without the end plates is unbalanced. The location of the channels that guide the sling is not at the center of gravity of the solenoid in this configuration. Therefore, the sling has to be positioned in the manner shown in Figure 205 for lifting.

Figure 205: Asymmetric slinging of the solenoid is necessary because the center of gravity of the solenoid is shifted to the side with the end plate because one set of end plates have been removed.

Figure 206: (a) shows the solenoid on the slide. Once it is on the sliders, the solenoid is secured to them with screws. (b) The solenoid is pushed approximately into place.

Once the solenoid is properly and safely slung for lifting with a crane, it is lifted an placed on the rails of the slide. See Figure 206(a). Screws are used to hold the solenoid to the sliders. The solenoid is pushed approximately into place. See Figure 206(b).

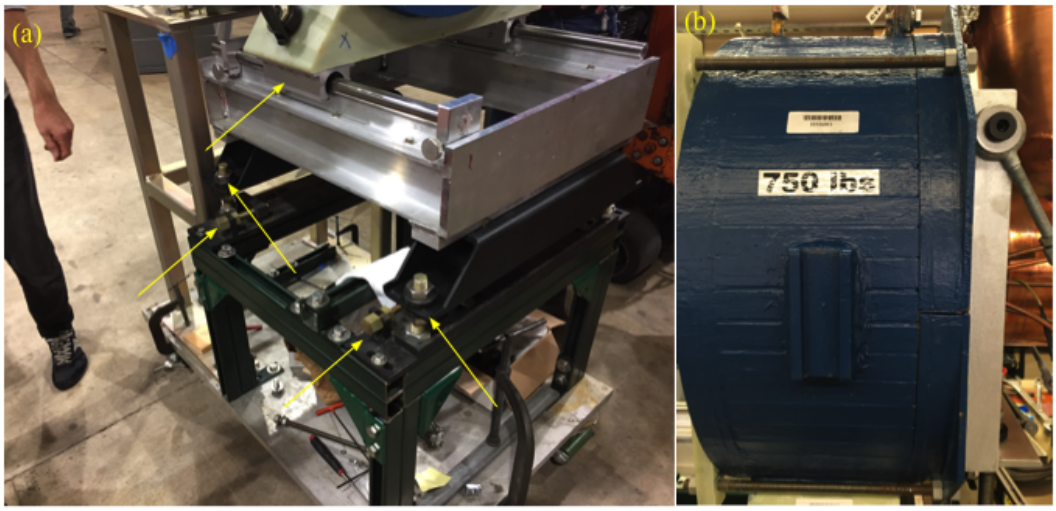

Figure 207: (a)The solenoid stand has x,y,z adjustors indicated by the arrows. (b) The solenoid clamped to the end plate and sealed.

To adjust the position of the solenoid w.r.t. the cavity, there are adjustments in all three directions to allow the solenoid to clear the tuner. The adjustors shown in Figure 207(a). Finally, after carefully adjusting the position of the solenoid, it is closed with its end plate and we have a nearly fully assembled cavity! See Figure 207(b) and Figure 208.

Figure 208: The nearly complete cavity.

20.1 Connecting water tubes

Once the solenoid has been installed, the water tubes on the tuner are connected together. Figure 209 shows a sketch of the water connections and some of the soldered connections.

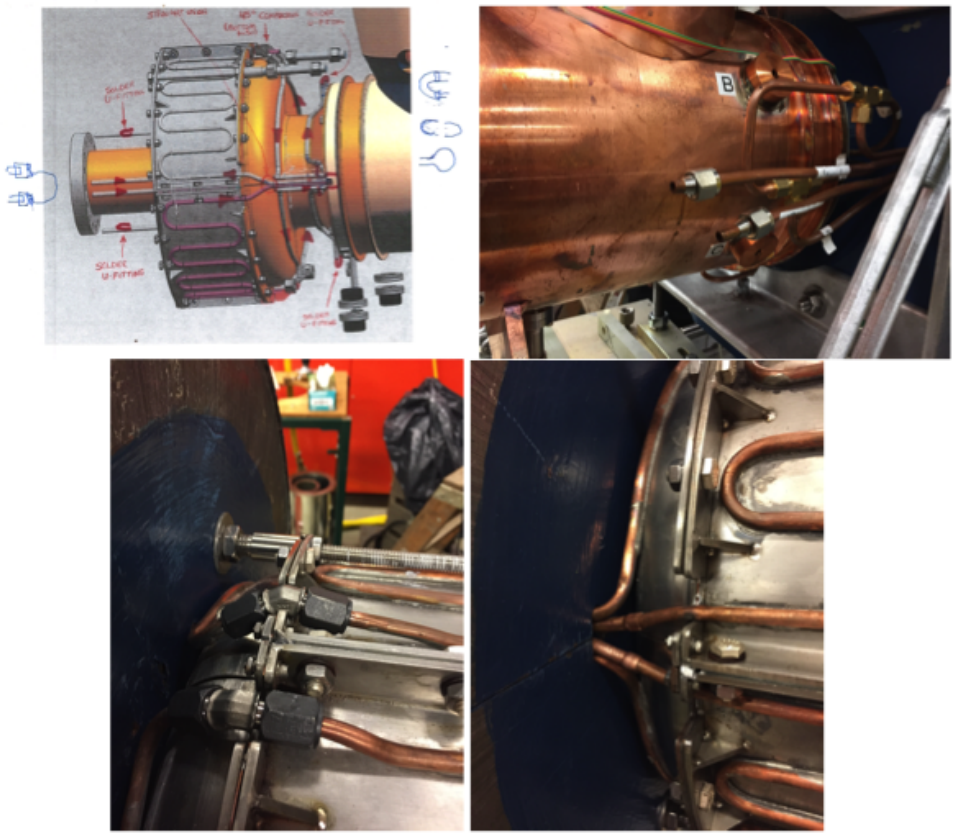

Figure 209: The water connections on the tuner assembly. Due to the restricted space that is available, it was very challenging to install the elbow compression fittings. Heat shields (made from aluminum foil) were also used during the soldering process to prevent scorching or burning of the epoxy filled laminations of the solenoid end plates.

21 Low power tests (R. Madrak, D. Sun, G. Romanov, & C.Y. Tan)

The lower power tests are divided into two parts below. This first is for the cavity without the garnet rings, i.e. an unloaded cavity and the second is with the garnet rings, i.e. a loaded cavity. The goals of the low power tests are to obtain RF parameters of the cavity before high power is applied. An added goal for the unloaded cavity test is to check its overall dimensions are correct by verifying that its resonant frequencies match simulations.

21.1 Unloaded cavity

The simulated H-field distribution for the fundamental and mode 1 of the unloaded cavity with open pickup and damper ports (no damping resistors) for the fundamental and shorted ports for mode 1 are shown in Figure 210. It is interesting that the magnetic field for the fundamental is not the strongest at the shorted end of the cavity but at the coupler stem and the neck region of the cavity. This is in contrast with mode 1 (Figure 210(b)) and the loaded cavity, shown in Figure 216, where the strongest magnetic field is at the shorted end. **Editor's note: All these simulations assume that the mode has 1 J in the cavity. Therefore, these plots are only useful for seeing the distribution of the magnetic field for that mode and should not be used to compare strengths between modes.**

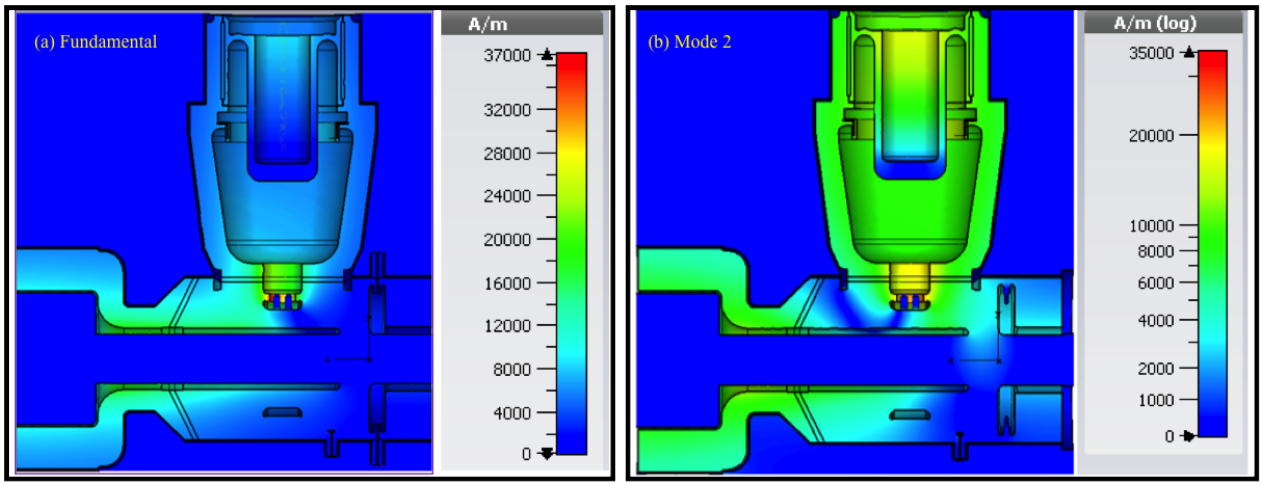

Figure 210: The magnetic field distribution for fundamental and mode 2 of the unloaded cavity. For the fundamental, the ports are open in the MWS simulation. Interestingly, the magnetic field is not highest at the shorted end. The highest fields are at the coupler stem and in the neck area. For mode 2, the ports are shorted out. Unlike the fundamental, there are fields in the PA shell and at the shorted end of the cavity.

The frequencies and Q of the frequency of the fundamental and the next higher mode are shown in Table 14. In this MWS model, all parts are made of copper except for the windows which are made of Al_2O_3. The MWS results for other unloaded cavity configurations can be downloaded from [58].

The frequency and Q measurements of the cavity used a network analyzer connected to the two probe ports. The probes are made of straight pieces of wire connected to type N connectors. Figure 211 shows the installed probes. At the beginning, the probes were 1.25" long but as the measurements proceeded, they were eventually trimmed down to 0.5". The goal has been to keep the probes weakly coupled to the cavity RF fields.

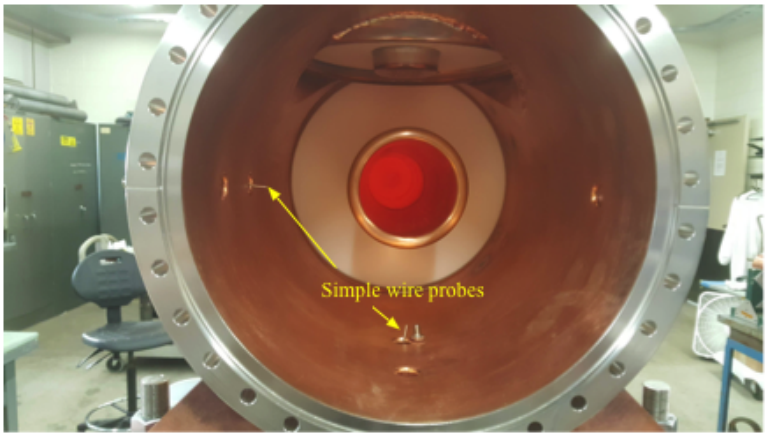

Figure 211: Simple wire probes that are used for the measurements. In this photo, the probes are 0.5" long. Their length is compared to a screw placed besides next to one of the probes.

The completely assembled unloaded cavity with the HOM cavity and PA installed used for these experiments is shown in Figure 212.

Table 14: Comparison between MWS and measured results for the unloaded cavity with open ports.

	MWS results		Measured results	
Mode	**Frequency (MHz)**	**Q**	**Frequency (MHz)**	**Q**
Fundamental	120.4	6079	120.68	2000
1	170.7	5225	173.72	472

It is clear from Table 14 that the mode frequencies match up quite well, especially the fundamental, between the MWS and measured results. The frequency results mean that the as built dimensions of the cavity are essentially the same as that used in the simulation model.

However, the Q of the unloaded cavity is clearly problematic: The Q of the fundamental is 3 times smaller than the expected value. The lowered Q for mode 1 is explained by noting that its H field is strong in the PA shell and the cathode resonator is made of aluminum rather than copper: these two conditions give extra damping. See Figure 210(b).

Figure 212: The unloaded cavity with both the HOM cavity and PA installed.

21.1.1 Low Q investigation

The Q of the fundamental that is 3 times smaller than expected is somewhat problematic but it has to be put in perspective: the magnetic fields are fundamentally different when the garnet is installed into the cavity. This can be seen by comparing the magnetic fields of the fundamental shown in Figure

210 and Figure 216. However, we still need to understand why. The way we chose to understand the source of the problem is to disconnect both the HOM cavity, the PA, the PA cone (see Figure 170(c)) and the coupling ring from the main body of the cavity. This means the problem of the low Q can be isolated to the main cavity body. The MWS simulation of the "empty" cavity is shown in Figure 213.

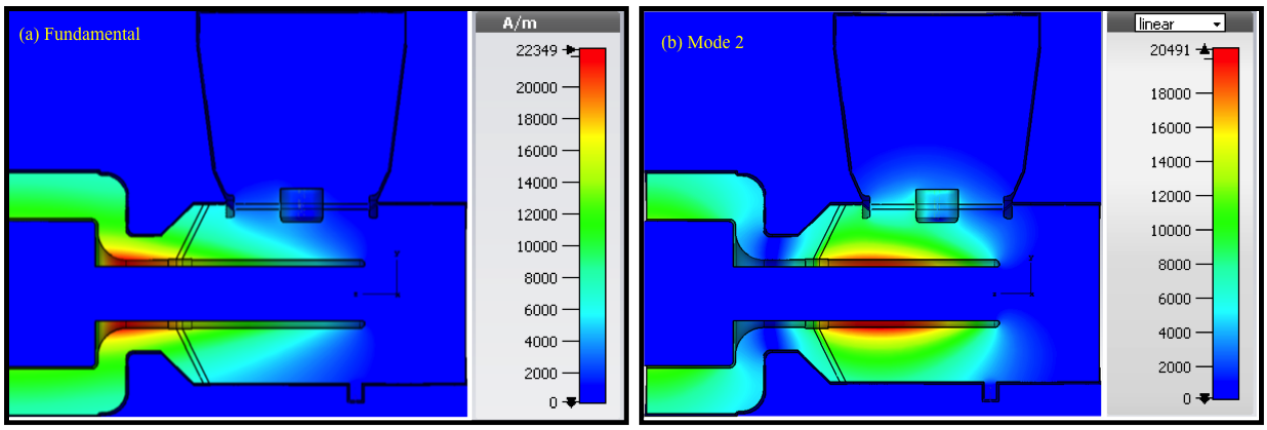

Figure 213: The magnetic field distribution for the fundamental and mode 1 for an "empty" cavity. For the fundamental, the magnetic fields are concentrated in the neck region of the cavity.

Photos of the "empty" cavity are shown in Figure 214.

The MWS and measured results are summarized in Table 15. These results show that although the Q is improved by about 30% for the fundamental Q shown in Table 14, the low Q problem remains.

Table 15: Comparison between MWS and measured results for the unloaded cavity. MWS uses shorted ports while the measurements had open ports.

	MWS results		Measured results	
Mode	**Frequency (MHz)**	**Q**	**Frequency (MHz)**	**Q**
Fundamental	148.04	8000	147.5	2900
1	345.0	14600	342.6	~1000

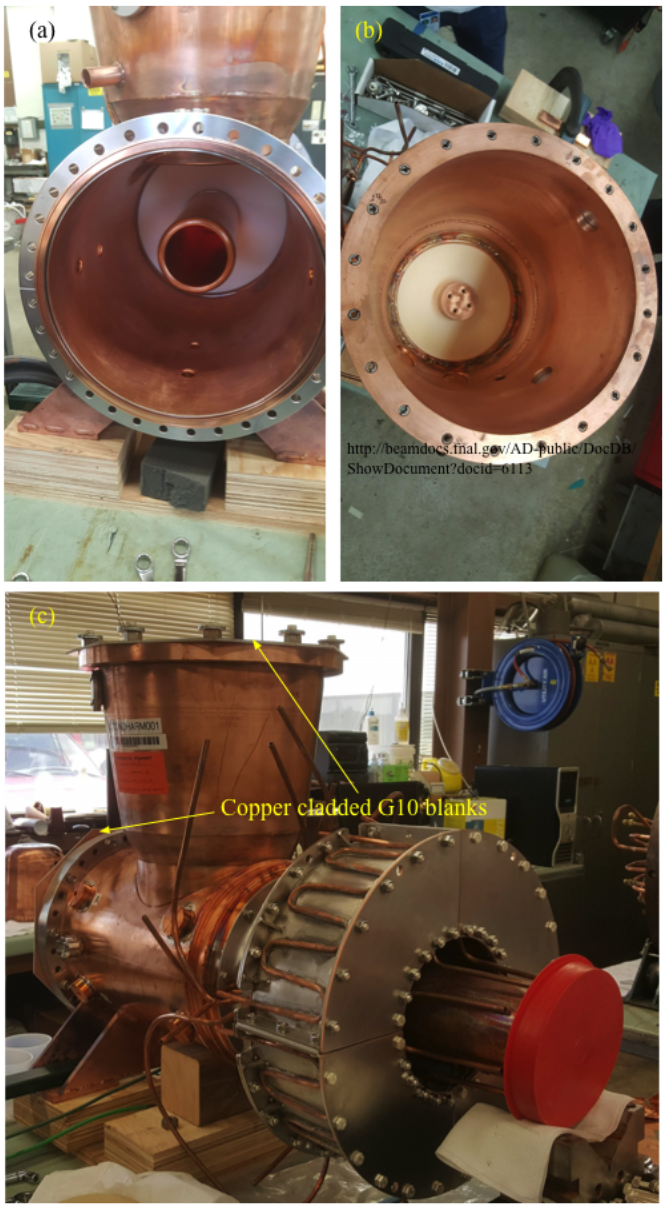

Figure 214: (a) The coupling ring and the HOM cavity has been removed. (b) The PA and cone has been removed. (c) The open ends of the cavity have been blanked off by bolting on copper cladded G10 sheets.

21.1.1.1 Joints

When we look at the theoretical magnetic field map for the fundamental shown in Figure 213(a), the strongest magnetic field is in the neck region. Therefore, it behooves us to concentrate our investigation in this region. There are three joints in this area shown in Figure 215.

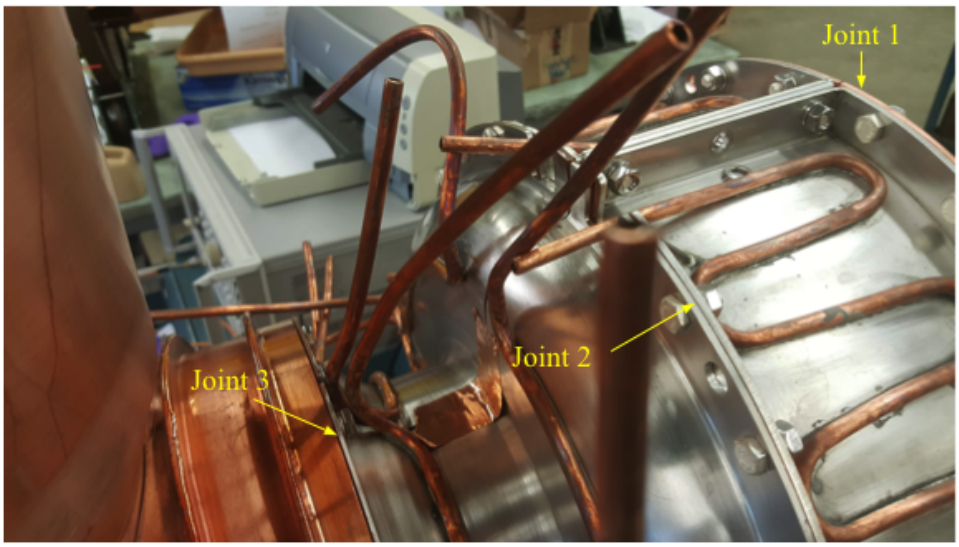

Figure 215: There are three joints in this region. Joint 1 is at the shorted end of the cavity. Joint 2 is joint between the neck assembly and the outer shell. And Joint 3 connects the neck assembly to the cavity body. Copper tape is used to cover up the slots.

Here is the summary of our investigation of the Q of the fundamental:

1. Removing the wires (see Figure 169(a)) in one quadrant of the shorting plate and tightening the bolts to only finger tight does not change the Q.
2. Loosening the bolts in Joint 2 in one quadrant drops the Q by 200.
3. Loosening the bolts in Joint 3 does not change the Q.
4. Covering the slots with copper tape does not change the Q.

From the magnetic field distribution of the fundamental shown in Figure 213(a), it is possibly not surprising that our actions stated in item 1 and 3 above does not change the Q. We see a change in Q when we loosen Joint 2 is consistent with the magnetic field distribution. Therefore, we conclude that we need to improve the joints for RF.

The way we plan to improve the joints is to add annealed copper wires to the neck assembly and add addition screw holes to reduce gaps in the Joint 2. See Figure 155. The wires will act as RF lips when compressed.

More details of the above and other measurements can be downloaded from [58].

Note: No other measurements had been made with the "improved" joints because we were running out time for installation. We will assume, from this point forward, that the problem of the low Q for the "empty" cavity has been fixed with the improved RF joints.

Editor's note: It was discovered during the assembly of the outer shell with the tuner installed that there are cracks in the weld joints on the outer shell. The cracks could be one contributor to the low Q. The other contributors are the contacts between the joints. See log entry https://www-bd.fnal.gov/Elog/?orEntryId=138637 where the outer shell was replaced with a shell made from copper sheets. The Q increased by about 30% from 3000 to 4000. Also see section 17.4.1.

21.2Loaded cavity

The simulated H-field distribution of the loaded cavity is shown in Figure 216. Notice that the magnetic field distribution for the fundamental is quite different from that of an unloaded cavity. Our over-riding concern is the RF joint at the shorted end.

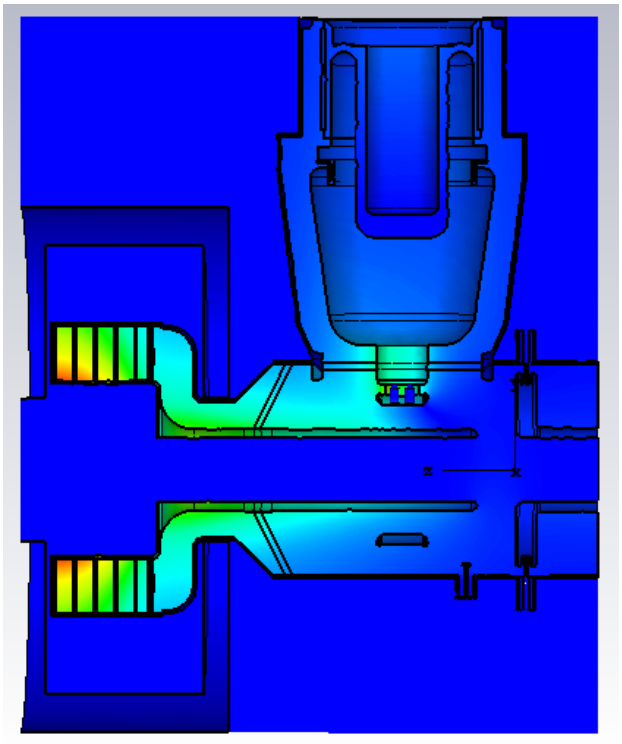

Figure 216: The fundamental magnetic field distribution for a loaded cavity with open ports.

The basic setups for measuring the resonant modes, Q and the shunt impedance of the cavity are shown in Figure 217.

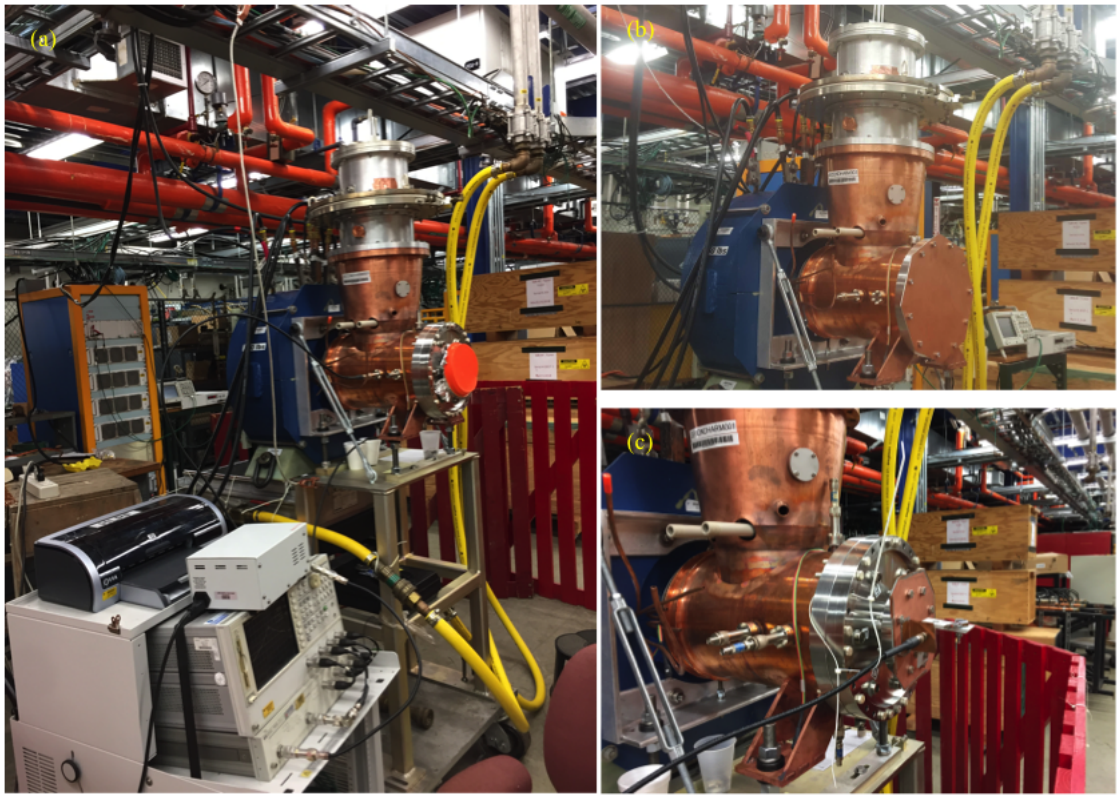

Figure 217: The basic setup for measuring the RF properties of the cavity. (a) Shows the setup for measuring the resonant modes and Q with the HOM cavity installed. A Mini-Circuits 35 dB RF amplifier (TIA-1000-1R8) is in series with the excitation leg of the network analyzer because of the weak coupling of the excitation probe to the cavity. (b) shows the cavity without the HOM cavity. and (c) shows one of the beam pipe ends of the cavity with the stretched wire fixture installed for shunt impedance measurements.

21.2.1 Resonant modes and Q measurements

The resonant modes and Q of the cavity are measured with a network analyzer. Due to the weak coupling of the excitation probes (Figure 211) to the cavity, an RF amplifier (Mini-circuits 35 dB RF amplifier, TIA-1000-1R8) is connected in series with the excitation leg of the network analyzer. The measured resonances and Q's when the fundamental frequency is at 75.7 MHz is summarized in Table 16 for the cases when the HOM cavity is not installed (Figure 217(b)), with the HOM cavity installed connected to 50 Ω loads (Figure 217(a)) . Again, we have found that the fundamental Q is smaller by a factor of 3 when compared to simulations (Table 5). This reduction factor is the same as what we saw for the empty cavity. See Table 14 and Table 15.

21.2.2 Shunt impedance measurements

We have measured the shunt impedance of the lowest 5 modes with the stretched wire. Our analysis is a lot more intuitive than the usual method discussed in the literature, for example see Ref. [59]. In the limit of infinite shunt impedance, both methods yield the same shunt impedance. See Ref. [60].

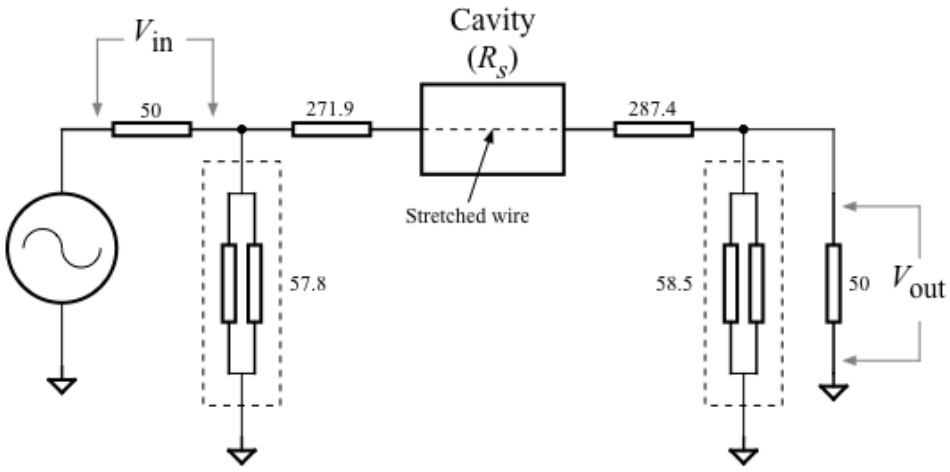

Figure 218: The circuit used for measuring the shunt impedance. The two 50 Ω resistors represent the input and output impedances of the network analyzer. The voltage source has zero impedance because it is an ideal voltage source.

The measurement circuit is shown in Figure 218. The choice of the resistor values will be discussed in section 21.2.2.1 below. Unlike the previous measurement, no RF amplifier is used in the circuit. A network analyzer is used to measure $s21\text{dB}$ which is related to the input voltage, V_{in}, and the output voltage, V_{out}, by the following equation in units of dB

$$s21\text{dB} = 20 \log \frac{V_{\text{out}}}{V_{\text{in}}} \text{ [dB]} \tag{80}$$

Our simple application of Ohm's Law to the circuit, gives us the required formula for calculating the shunt impedance, R_s, at resonance

$$R_s = \left(\frac{27}{10^{s21\text{dB}/20}} - 586.3 \right) \text{ [Ω]} \tag{81}$$

There is no correction from strong coupling of the wire to the cavity because the measured Q from this experiment matches that of the weakly coupled s21 measurement, i.e. R/Q is the same in both types of measurements.

21.2.2.1 Choosing resistor values

The resistor values that are shown in Figure 218 have been chosen to minimize the reflections at the boundary of a transmission line that is formed by the 0.028″ wire inside a 3″ OD beampipe. In this configuration, the characteristic impedance is 280 Ω. Our s21 results for this configuration is shown in Figure 219.

Figure 219: The s21 measurement of the stretched wire in a 3" OD beampipe.

From this measurement, we can calculate the shunt impedance of the beampipe: for $s21\text{dB} \approx -26.6$ dB and Eq. (81), we find that the shunt impedance of the beampipe is 18 Ω. Thus, we can see from Table 16 and Table 17 that this contribution to the measurement of the shunt impedance of the cavity modes is small. Therefore, we will not apply any additional corrections to the stretched wire results when calculating the shunt impedances.

21.2.3 Results

All the results from the s21 measurements and the stretched wire measurements are summarized here in Table 16 and Table 17. We did not perform a stretched wire measurement for the "No HOM cavity" configuration.

	No HOM cavity (Figure 217(b))		HOM cavity with 50 ohm terminations on HOM cavity (Figure 217(a) & (c))		
Mode	**Frequency (MHz)**	**Q**	**Frequency (MHz)**	**Shunt impedance (kΩ)**	**Q**
Fundamental	75.73	780	75.7	26.8	720
1	142.0	958	142.1	4.0	665
2	189.96	515	188.9	7.1	220

Table 16: The comparison between the RF parameters of the cavity without and with the HOM cavity.

	HOM cavity with open loads			HOM cavity with 6 dB attenuators		
Mode	**Frequency (MHz)**	**Shunt impedance (kΩ)**	**Q**	**Frequency (MHz)**	**Shunt impedance (kΩ)**	**Q**
Fundamental	75.7	29	800	75.7	26.7	730
1	142	6.2	933	142.1	3.7	616
2	189.6	13.3	516	189.1	6.7	211
3	264.1	-	656*	264.8	-	402*†
4	293.6	8.7	520	293.6	6.3	172

Table 17: The comparison between open and 6 dB loads. The stretched wire did not excite mode 3 and so no shunt impedance was measured. *For mode 3, the Q came from the s21 measurement between the button pickups. † With the buttons shown in Figure 33 and under vacuum, the measured Q for this mode is 298. The measured Q's of the other modes are, within the error of the measurements, unchanged.

For the configuration with the HOM cavity installed, we made measurements with open (i.e. no loads), 50 Ω loads, 6 dB attenuators (equivalent to 83.5 Ω loads) and 3 dB attenuators (equivalent to 150.5 Ω loads) attached to each of the four HOM cavity ports. Table 17 compares the measured RF

parameters for open and 6 dB loads for the first 5 modes. Note that for mode 3 (~260 MHz), the stretched wire excitation did not couple to it and so there is no measured shunt impedance. The 6 dB loads on the HOM cavity is the configuration which will be used in operations because of the results from the MWS simulations. See section 7.1.2 and Figure 45.

We have also measured the RF parameters of the cavity at the maximum current of 200 A that the bias supply is able to provide at this time. (see section 10).

The following subsections show all the collected data represented with plots.

21.2.3.1 Static properties at injection and maximum bias current

The Q's and shunt impedances of the cavity of the first 5 modes are shown in Figure 220 and Table 18 for the maximum bias current of 200 A. The addition of load resistors clearly reduces both the Q's and shunt impedances of the higher order modes with a smaller effect on the fundamental.

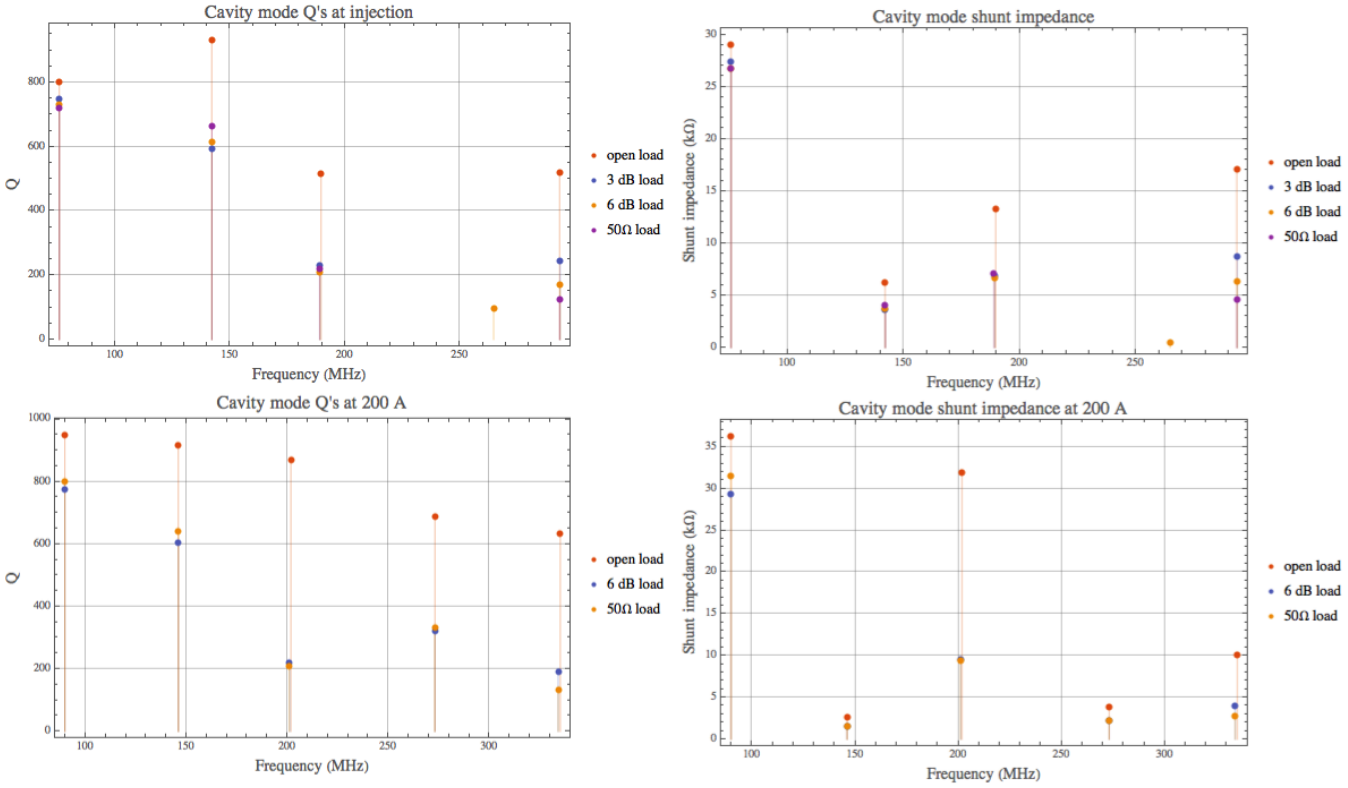

Figure 220: The Q's and shunt impedances of the cavity with the fundamental mode at the injection frequency and when the bias solenoid is at 200 A.

21.2.3.2 Dynamic mode properties

The evolution of the modes as a function of the bias current is shown here. For the fundamental, when the biased current is at 127.6 A, the injection frequency, 75.7 MHz, is achieved for the case when the HOM cavity has 6 dB loads. This value is lower than the theoretical value of 139 A from section 9.

The evolution of the frequency of the modes are shown in Figure 221 and the Q's are shown in Figure 222. Although not shown, the error bars for Q is ±10 with 16 trace averaging on the network analyzer.

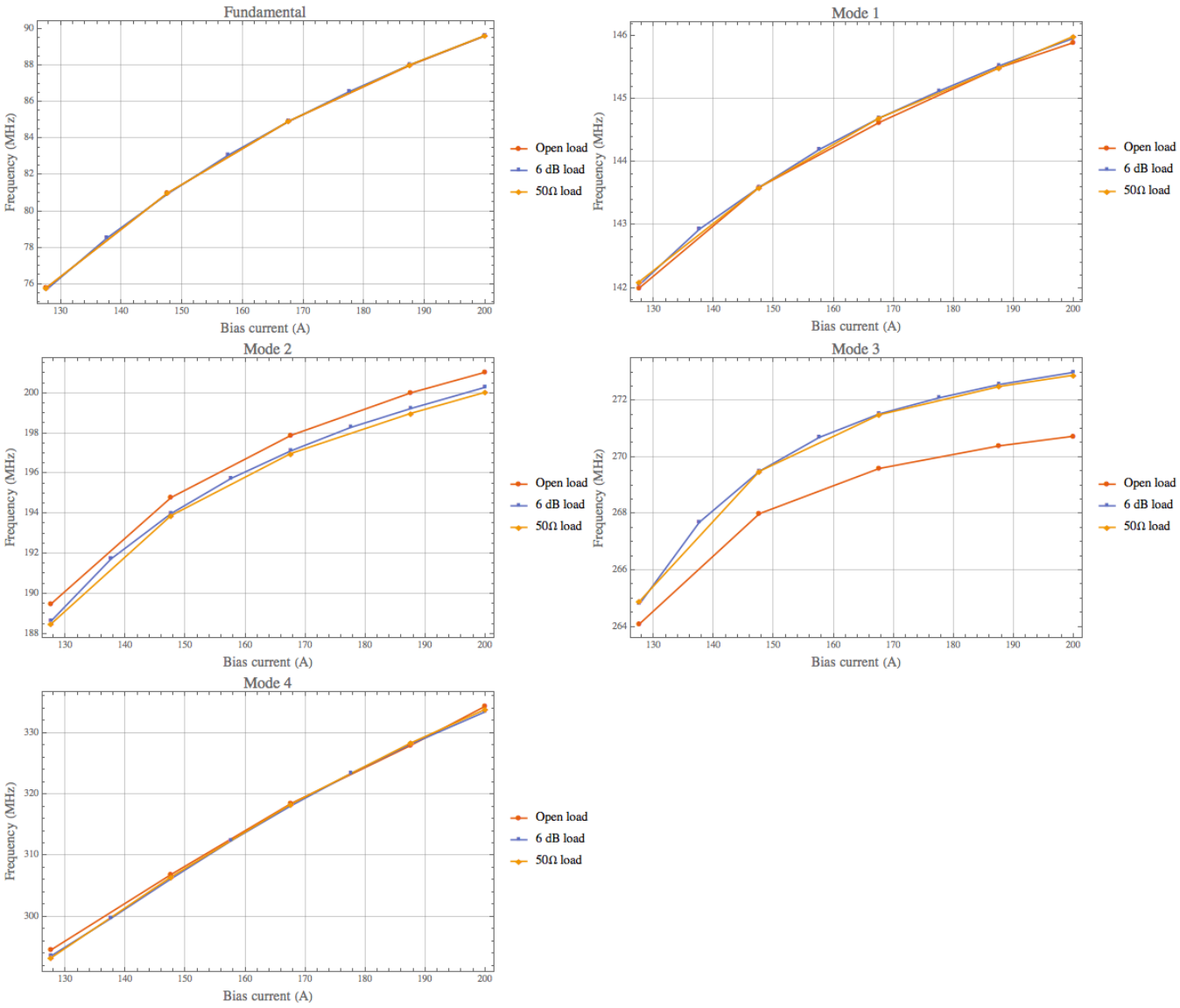

Figure 221: Mode frequency evolution as a function of bias current.

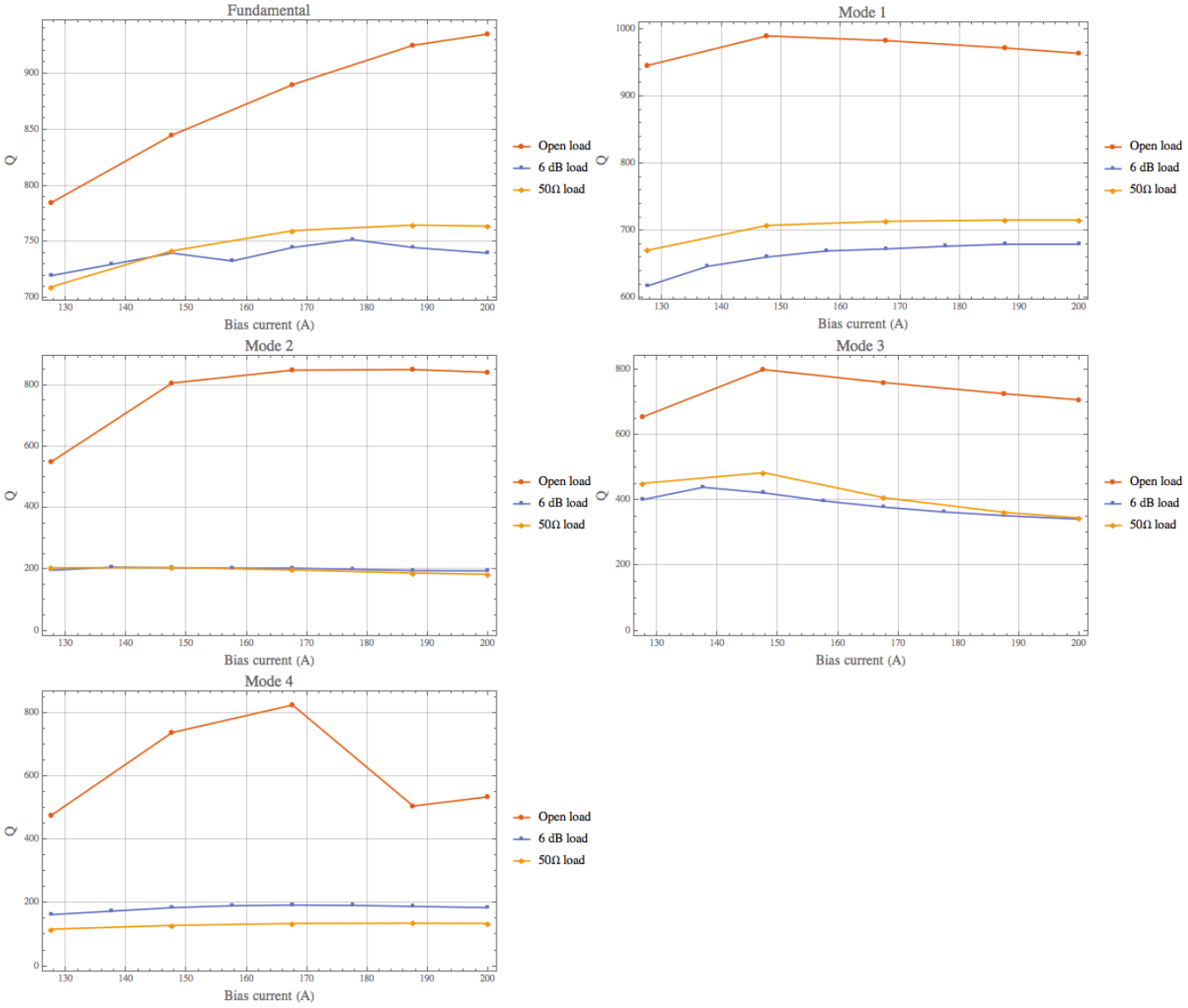

Figure 222: Mode Q evolution as a function of bias current.

Editor's note: The numbering of the modes starts from "1" after the fundamental to keep it consistent with the numbering scheme used in the MWS simulations shown in section 7.1.2. However, the mapping of the mode numbers to the mode frequencies between measurement and simulations do not match up after mode 2. Therefore, it is better to rely on the mode frequency rather than the mode number for discussions.

	HOM cavity with open loads			HOM cavity with 6 dB attenuators			HOM cavity with 50Ω attenuators		
Mode	**Freq. (MHz)**	**Shunt imped. (kΩ)**	**Q**	**Freq. (MHz)**	**Shunt imped. (kΩ)**	**Q**	**Freq. (MHz)**	**Shunt imped. (kΩ)**	**Q**
Fund.	89.76	36.3	950	89.77	29.4	775	89.78	31.5	800
1	145.95	2.7	916	145.98	1.5	606	146.00	1.6	640
2	201.67	31.9	868	201.05	9.6	220	200.87	9.4	208
3	273.00	3.9	688	273.00	2.2	320	272.91	2.3	333
4	335.08	10.1	633	334.02	4.0	190	334.04	2.8	132

Table 18: The comparison between open 6 dB and 50Ω loads for 200 A bias.

21.2.4 Button calibration

The wire antennae used for the preceding s21 measurements (Figure 211) are replaced with buttons (Figure 33) for operations. These buttons will be used to monitor the accelerating voltage and thus need to be calibrated. The setup for the calibration is shown in Figure 223. We used a 4 port network analyzer (Agilent Technologies, E5071C) to simultaneously measure both s21 and s31. The network analyzer's port 1 is the excitation port and is connected to a 35 dB RF amplifier ((Mini-circuits 35 dB RF amplifier, TIA-1000-1R8) which in turn is connected to a magnetic loop in the PA shell. This is so that we have enough signal to noise to get a good strong signal on the ports 1 and 2 of the network analyzer. Port 2 is connected to one of the buttons. Port 3 is connected to a high frequency RF 10× probe (Hewlett Packard 85024A). Its measured gain is (21.15 ± 0.05) dB. The probe end of the RF probe touches one side of the gap, while the ground of the RF probe touches the opposite side of the gap.

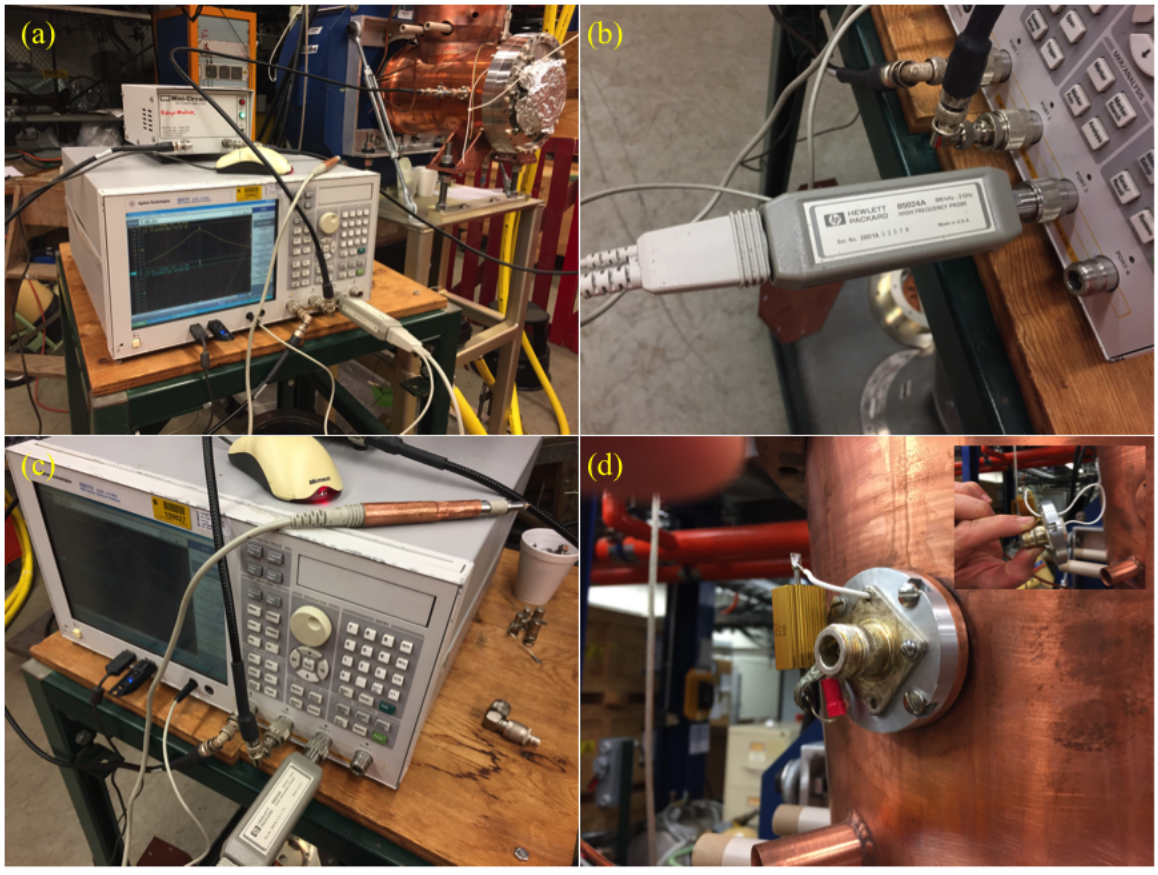

Figure 223: (a) Shows the 4 port network analyzer with port 1 connected to the RF amplifier, port 2 connected to the button and (b) port 3 connected to the RF probe. (c) The business end of the RF probe. The body of the probe is wrapped with copper tape which is at ground. (d) shows the magnetic probe port that is used to excite the cavity. The inset shows the loop which is rotated to maximize coupling to the cavity. The output of the RF amplifier is connected to this port.

The modes of interest are the fundamental and mode 1. The calibration factor between the gap voltage to the button voltage are shown in Figure 224 for the two buttons as a function of mode frequency.

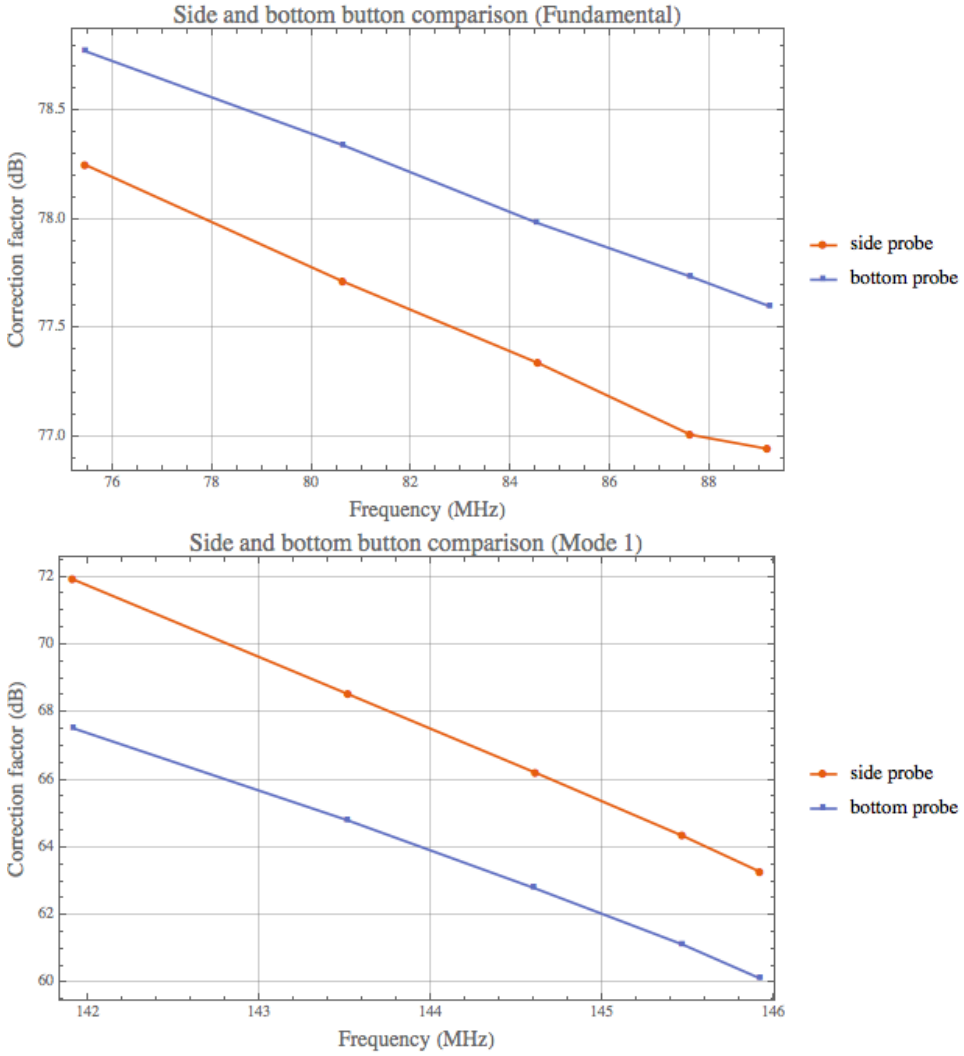

Figure 224: The calibration factor for the two buttons for the fundamental and mode 1 as a function of mode frequency.

For the fundamental, the difference in the calibration factor between the two buttons is less than 2 dB. As a comparison with simulations, the measurements show that the calibration at injection is between 77 dB (side) to 78.5 dB (bottom) while MWS predicts a calibration factor of 80 dB from section 6.2.3. However for mode 1, the calibration difference between the two buttons is ~3 dB.

21.2.5 No bias current

We want to see whether there are any modes that can cause problems when both the cavity bias and RF power are off. This will be the mode of operation when there is a problem with the cavity. The spectrum of modes excited by the stretched wire from 10 MHz to 1 GHz is shown in Figure 225. Most of the dips do not have 3 dB points and are very wide and so are really not considered to be resonances. The "strongest" modes are summarized in Table 19. Only the 716 MHz mode may be problematical.

Mode frequency	Q	Shunt impedance (kohms)
278.8	20	0.87
628.1	19	2.1
716.7	205	2.5

Table 19: The "strongest" modes with no bias current.

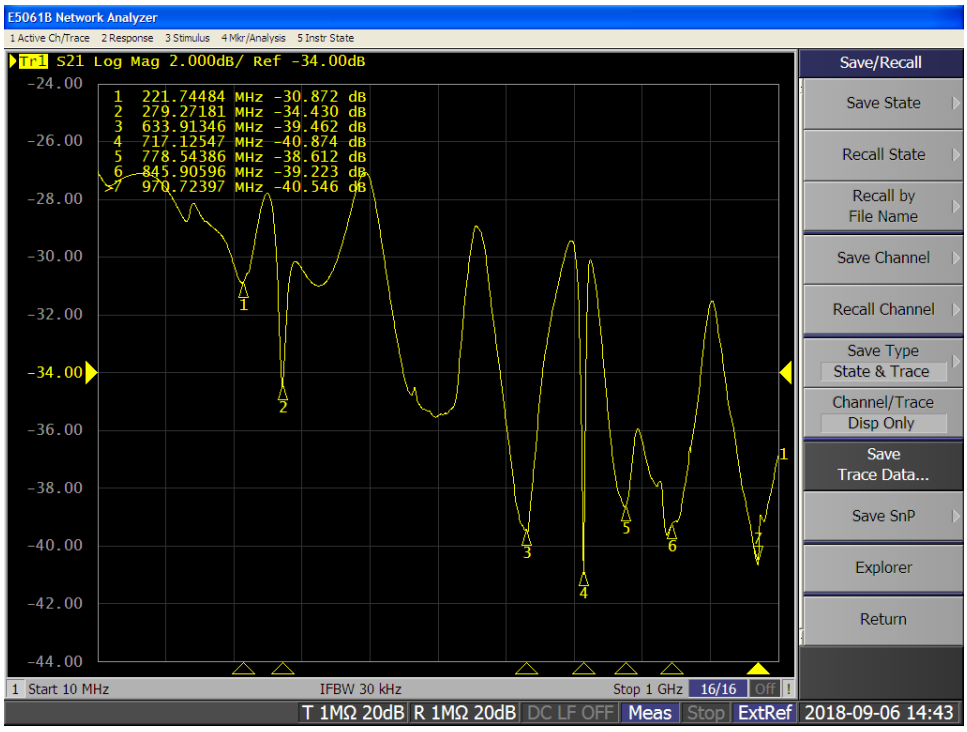

Figure 225: The mode spectrum excited by the stretched wire. Note that it is the dips that are the modes in the cavity because in this configuration, energy is "lost" into the cavity. Not all the modes are real. The modes that give an actual Q are summarized in Table 19.

22 High power tests (J. Reid, R. Madrak & C.Y. Tan)

The first attempt to drive the cavity with a PA was on 2 Jul 2019. The tuner was biased near to the supply's maximum output current. At this current, the cavity frequency was 89.6 MHz. The RF pulse width and repetition rate were 100 μs every 127 ms. The anode voltage was set to 12 kV and the drive power was raised until it was close to the maximum output power of the TOMCO amplifier. At this drive power level, there was about 6 kW of forward power and 700 W of reflected power. The anode DC voltage and current were 12 kV and 8.9 A respectively. Assuming a PA efficiency of approximately 60%, this implies that the power dissipated in the cavity is 12 kV × 8.9 A × 0.6 = 65 kW. The measured gap voltage, however, was only 22 kV, which corresponds to a shunt impedance (Rshunt) of only 3.7 kΩ. At this time, we knew from low power measurements in the summer and fall of 2018 that both the Q and shunt impedance were much lower than the design values by a factor of four to five. The first high power results indicated that the shunt impedance is only about 3% of the design value.

We did notice a substantial amount of stray RF detected by an antenna mounted inside the cave near the cavity. The antenna pickup signal increased as the drive was increased. With 8.9 A on the anode, the pickup on the antenna was 17 V. See section 22.3.

Condition	Frequency (MHz)	Q
Filaments ON, using amplifier	89.595	520
Filaments ON, using amplifier	76.196	650
Filaments OFF, using amplifier	76.191	620
Filaments OFF, NO amplifier	76.184	627
Filaments OFF, NO amplifier	89.595	517

Table 20: Measured Q values of the cavity. It is very peculiar that the Q of the cavity is lower at high bias (highlighted in red).

Next, network analyzer measurements of the cavity Q were performed with the filaments on/off and with/without an amplifier on the network analyzer drive. This was done for two bias settings. The cavity was driven (Port 1) by a loop connected to the anode monitor port with the anode monitor removed. Port 2 was connected to the cavity gap monitor. The Q was determined by measuring the width of the s21 resonance. Results are shown in Table 20. The Q does not appear to be affected by the state of the filaments or presence of the amplifier. Note: in Sep 2018, the Q at high and low bias was measured to be 925 and 800. Not only has the Q dropped substantially, but the Q at high bias is lower

than at low bias. This observation is unexpected because the losses in the garnet should increase as the bias is decreased. It was suggested that the Q could be lower due to RF leakage; the measurement was redone with copper tape covering the hole for the PA fan exhaust, which could be a source of leakage. There was no difference in Q.

An independent measurement of Q was also performed with the PA drive by adjusting the frequency of the drive until the gap probe voltage dropped by a factor of $1/\sqrt{2}$. This was done at high bias (resonant frequency was about 89 MHz). In this case the Q was 530, which is consistent with the low power measurements shown in Table 20.

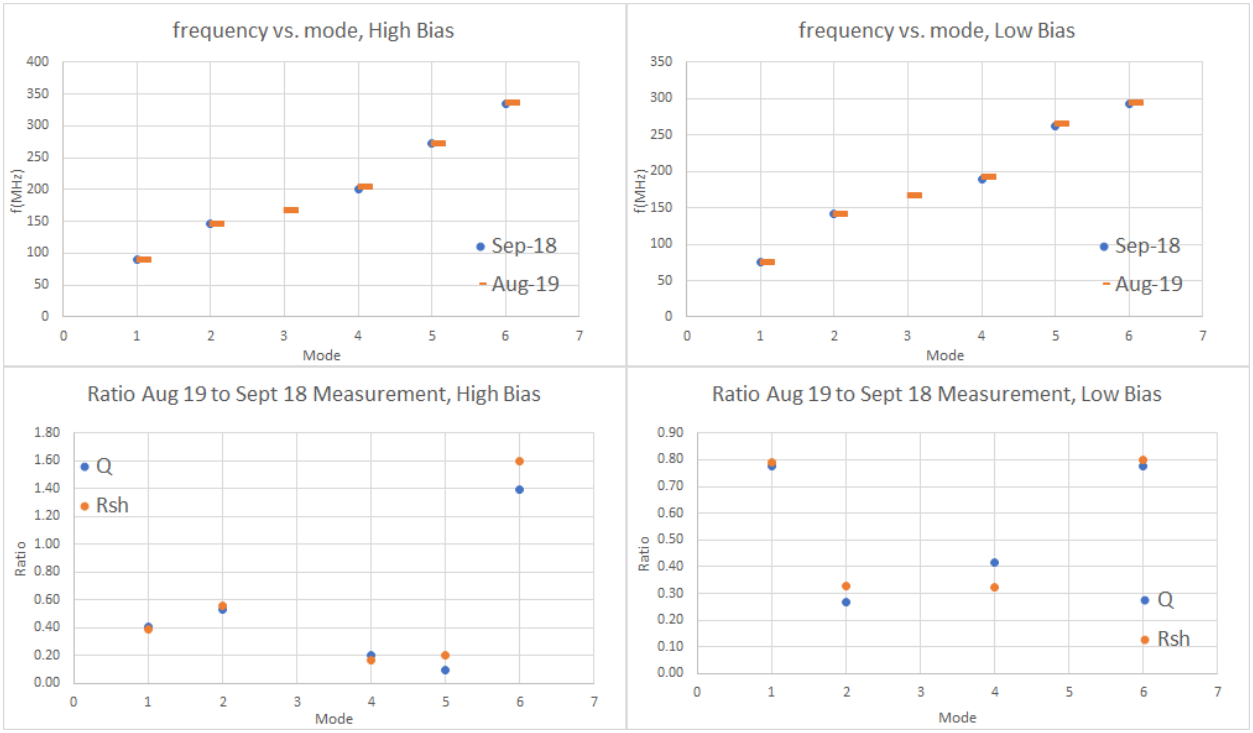

Figure 226: For both high and low bias, the frequencies of the various modes in Aug 2019 were compared to those measured in Sep 2018. The frequencies of the modes did not change over the period of one year. Bottom: The ratios Q (Aug 2019)/ Q (Sep 2018) and shunt impedances, Rshunt (Aug 2019)/ Rshunt (Sept 2018) for the various modes are shown here. The change in the shunt impedance from Sep 2018 to Aug 2019 tracks the change in Q. The changes are different for each mode.

The cavity was also powered at low bias (resonant frequency was 76.8 MHz) to 15 kW. The peak gap voltage was 7 kV, and thus the shunt impedance was 1.7 kΩ. The bias (tube?) was then increased at which point the drive was turned all the way up, and the grid voltage was adjusted. With the anode voltage and current of 12 kV and 9.7 A respectively, the peak gap voltage was 31.9 kV. This

corresponds to a shunt impedance of 6.1 kΩ. An attempt was made to adjust the grid voltage, but this had no effect on the shunt impedance.

After these high power tests, the cavity was opened and the probe calibration (discussed in section 21.2.4 and in the next section) was repeated. Results were consisted with what was measured previously. The stretched wire measurement was also repeated. Results are shown in Figure 226. While the frequency did not change much after one year, the Q and shunt impedance changed substantially, and the change in Q tracks the change in shunt impedance, as can be seen by comparing the ratios of each. The fractional change varies depending upon the mode.

22.1 Probe recalibration

The probe calibration was redone as described in section 21.2.4. Those measurements (performed in Sep 2018 and was done again in Aug 2019) compared the measured power from the permanent gap probes to an Agilent high frequency probe that was simultaneously placed across the gap. The cavity was driven by the network analyzer and the response of both the gap probe and the high frequency probe were measured simultaneously by the network analyzer.

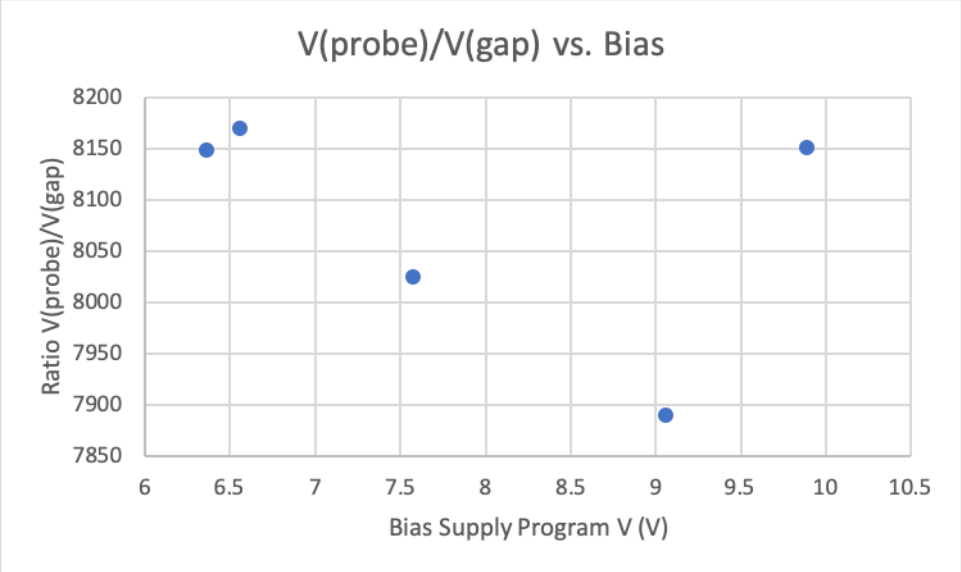

Figure 227: Gap probe ratios for the fundamental mode measured using a vector voltmeter and spectrum analyzer.

Another method was performed in Aug 2019 to check the above described method. A synthesizer, spectrum analyzer, and vector voltmeter were used. The vector voltmeter was an HP8508A with an Agilent 85081B input module for probes. The cavity was driven by the synthesizer. The vector voltmeter and probe were used to measure the voltage on the gap. The spectrum analyzer was used to

measure the voltage on the gap probe. Results for the fundamental mode are shown in Figure 227. The original (network analyzer) method yielded probe ratios of 8128 and 6993 for the side probe at low and high bias. This is consistent with results from the new (vector voltmeter) method at low bias. The results at high bias differ by about 15%.

22.2 More high power measurements

After performing the low power measurements discussed above which required access to the area under vacuum, the cavity was again pumped down and we proceeded with high power measurements. Again, at high bias, with an anode voltage and current of 12 kV and 11.6 A respectively, we measured 30.6 kV on the gap. Assuming a tube efficiency of 60%, this gives a shunt impedance of 5.6 kΩ.

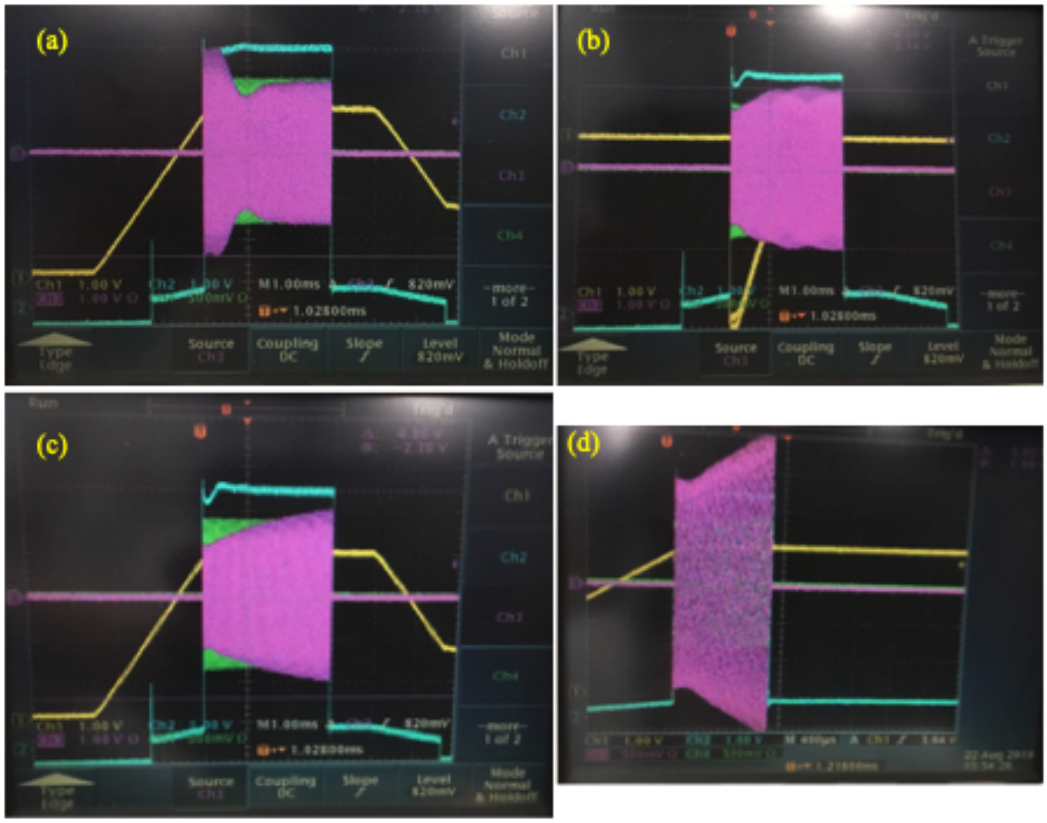

Figure 228: The gap voltage during long pulse widths (magenta trace). (a) The gap monitor shows a vase like shape when the drive frequency does not quite match the cavity resonance. (b) and (c) By tuning the RF frequency, we can change the shape of the gap voltage. (d) Shorter pulses have a larger gap voltage.

Until this point the pulse width had not been increased beyond 100 μs. When the pulse width was increased to 3 ms, the gap voltage exhibited much variation. The shape varied between being linearly increasing throughout the pulse and a vase shape. It appeared that the cavity could have been detuning

during the pulse. Varying the drive frequency caused large changes in the shape of the gap voltage pulse. Decreasing the pulse width resulted in a higher gap voltage. Some examples are shown in Figure 228.

Since the cavity and PA water cooling were instrumented with flowmeters and temperature sensors, an attempt was made to measure the cavity dissipated power calorimetrically. It was not possible to make an accurate enough temperature measurement for our calculation because the temperature probe readout modules would not function while the cavity was powered. This was presumably due to the large amount of RF leakage that caused the readout modules to malfunction.

Regardless of the fact that the power calculation required an assumption about the efficiency of the tetrode, the high power tests made it clear that it is not possible to get to higher than 30 kV on the gap with the current state of the cavity (end of 2019. See section 17.4.1). In addition, pulses with widths on the millisecond time scale show large variation in the gap envelope. It was decided that the cavity could not be usefully installed in this condition, and that we should repair the cracked weld joints in the tuner shell.

22.3 RF leakage

A dipole antenna was used to detect any RF leaks. The dipole antenna when placed on the side opposite to where the cooling water comes into the PA had a much lower value than when placed on the same side as the cooling water. On this side, the detected RF voltage is about 1 V! See Figure 229. We will have to mitigate this leak with a tapered shell that covers up the hole before installation in the tunnel.

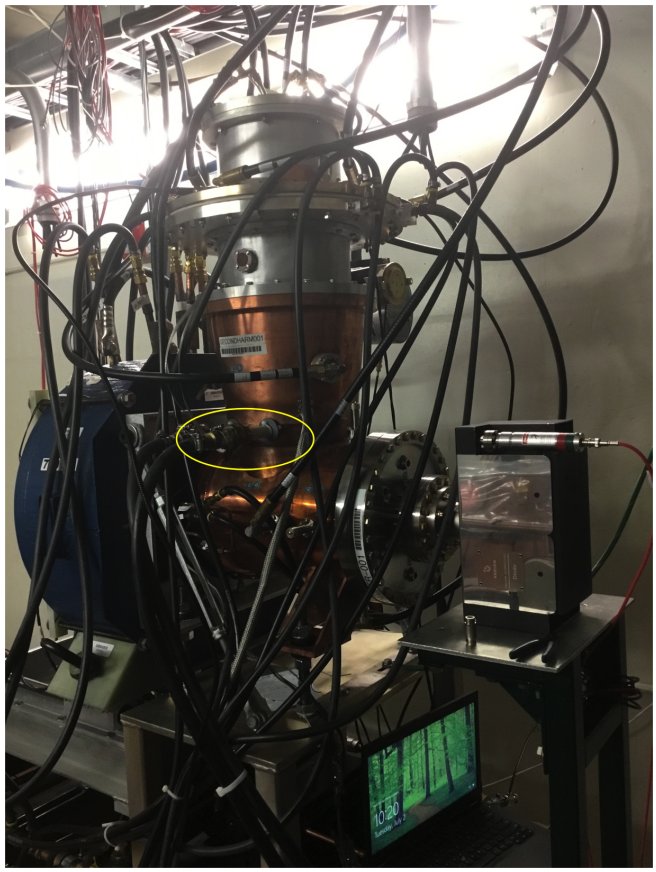

Figure 229: The source of the major RF leak is where the cooling water enters the PA (enclosed by a yellow ellipse in the photograph).

22.4 Heating of beam pipe from Eddy currents

We measured the heating of the copper beampipe from the bias ramp.[7] In this experiment a 15 Hz triangle signal shown in Figure 230 was used to pulse the solenoid. The triangle wave mimics the expected bias ramp discussed in section 10.1. The triangle pulse used in this experiment has faster drop after 3 ms to maximize dI/dt, i.e. we wanted to create more heating than in practice. The triangle pulse has a DC offset of 6.4 V (solenoid current is 128 A) which corresponds to the DC bias necessary for 76 MHz cavity resonance. The peak value is 9.9V (solenoid current is 200 A) which is the maximum allowed in the present bias supply. This value corresponds to about 89 MHz cavity resonance. The bulk supply on the bias supply was set to 200 V in this experiment.

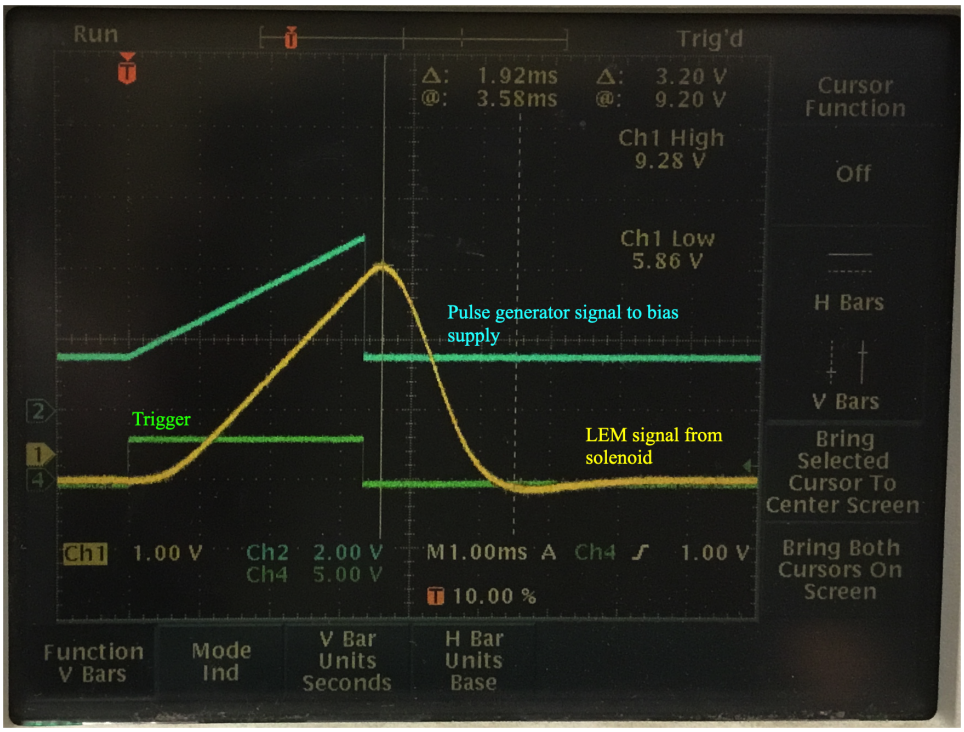

Figure 230: The triangle wave from the signal generator (cyan trace) is connected to the bias supply. The bias supply excites the solenoid and the current in the solenoid is monitored by the LEM (yellow trace). The current measured by the LEM clearly shows the step response of the solenoid, which is about 1.9 ms.

[7] In hindsight, the beampipe should have been made of stainless steel that is coated with copper in its inner surface to reduce heating from Eddy currents.

The temperature probe on the beampipe shows a very small temperature rise. See Figure 231. The duration of the experiment is from 12 noon to 12:30 pm. We used the following fit to determine the asymptotic temperature and the $1/e$ time

$$T = a\left(1 - e^{-t/T0}\right) + b \tag{82}$$

where T is the temperature in celsius of the beampipe. a, b are free parameters, together with $T0$ (the $1/e$ time) which will be determined by the least squares fit from the measured temperature data.

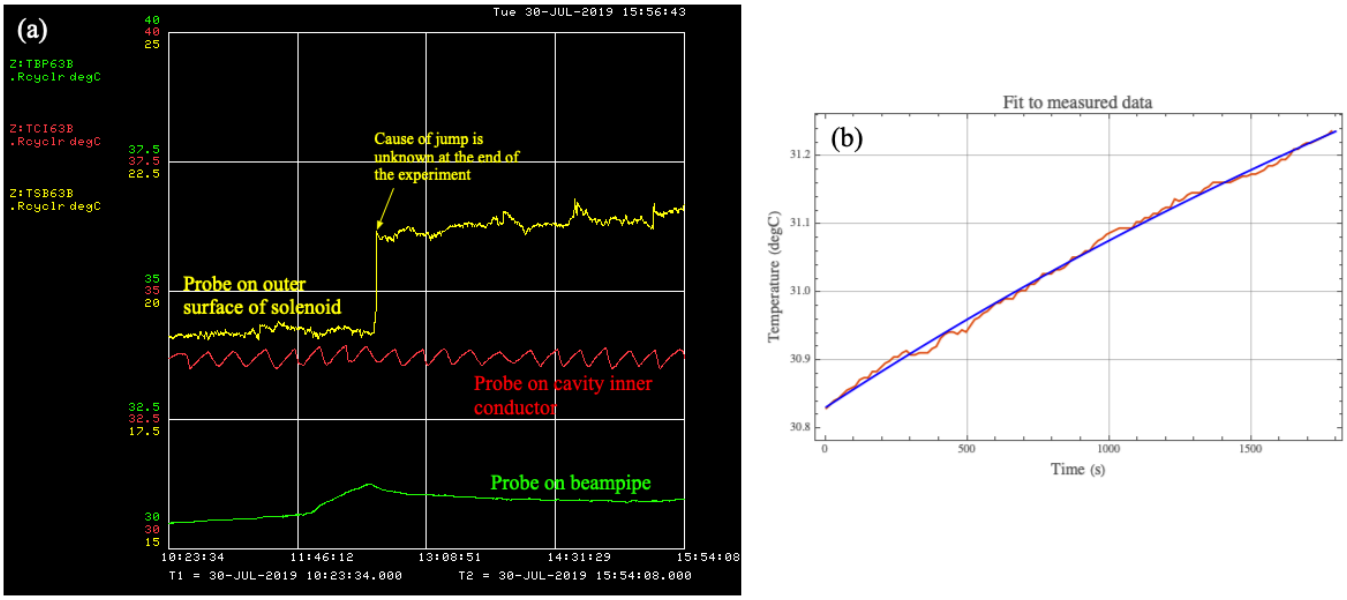

Figure 231: (a) The behavior of the three temperature probes on the cavity. There is a clear temperature rise on the beampipe during the experiment. The cause for the jump in temperature on the outer surface of the solenoid is unknown at this time. (b) The fit to the temperature on the beampipe with Eq. (82) is shown here.

The results from the least squares fit of Eq. (82) to the beampipe temperature data are as follows:

$$a = 1.2 \pm 0.1\ [\text{°C}] \quad b = 30.831 \pm 0.002\ [\text{°C}] \quad T0 = (4.5 \pm 0.4) \times 10^3\ [\text{s}] \tag{83}$$

or $T0 = (1.3 \pm 0.1)$ hours.

The asymptotic temperature from the fit is $T_\infty = 32$°C. Therefore, the temperature rise is $\Delta T = b - T_\infty \sim 1$°C. Thus, the temperature rise on the beampipe is negligible when operating in this mode.

22.5IR sensor interlock (C.Y. Tan & R. Madrak)

As part of the safety system during the high power tests, we have installed an IR sensor between the solenoid and the tuner. See Figure 232. The IR sensor will monitor the temperature at the front of the tuner stack. The reasons for monitoring the temperature at this location are twofold:

1. Our computer simulations have shown that the highest temperatures are found on this surface. See Figure 57, Figure 58 and Figure 70.
2. There is still some uncertainty in the behavior of the loss coefficient α at low field despite our best efforts in measuring it. Figure 15 shows the reason for our caution: the rapid rise of α at low field makes it very difficult to measure accurately.

Thus, the IR sensor will allow us to trip off the PA during high power testing and prevent damage to the garnet. Note: we do not expect the IR sensor to survive in the tunnel during operations because of damage from radiation and the effects from Eddy currents. This sensor will only be used during high power testing.

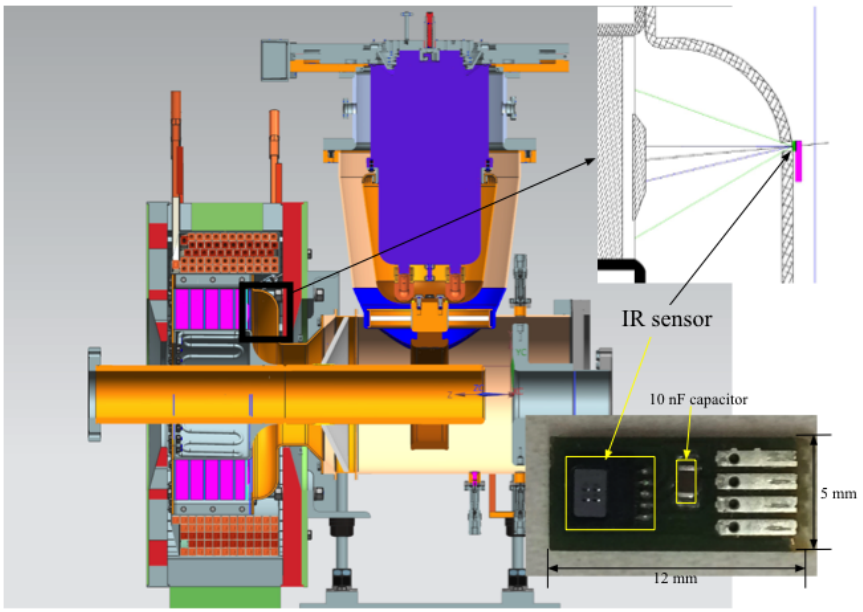

Figure 232: The IR sensor is mounted between the tuner and the solenoid. It peers at the front face of the tuner through a hole drilled through the tuner shell. The 10 nF chip capacitor (0602 surface mount capacitor) on the printed circuit board (bottom right photo) is magnetic and has been replaced.

The IR sensor is made by Melexis, model MLX90632 FIR sensor [61]. Note that the 10 nF capacitor (0602 surface mount chip capacitor) that was on the printed circuit board sent to us by Melexis is magnetic. We replaced it with a non-magnetic chip capacitor.

22.5.1 IR sensor test

We used a hotplate to heat a spare garnet sample (AL400) for the IR sensor test. We used PTC temperature sensors (Model 311C and 309FCOMP [62, 63]) that have large surface areas for the comparison measurements. Since the PTC sensors require 2 minutes to equilibrate, we did not generate a plot of the IR sensor temperature versus PTC sensor temperature. Instead, we had the hot plate heat the garnet sample to about 100°C to check whether the IR sensor gave the same temperature. Since the IR sensor averages over an area that subtends ±25° it would not see small, single point hotspots. Our calculations had shown that when there is a strip that subtends an angle of 13° at 200°C, with the rest of the area at 100°C, the average temperature measured by the IR sensor is 120°C. This calculation took into account the response of the IR sensor. Note: the Curie point of the AL800 garnet is 200°C. Figure 233 shows the measurement setup.

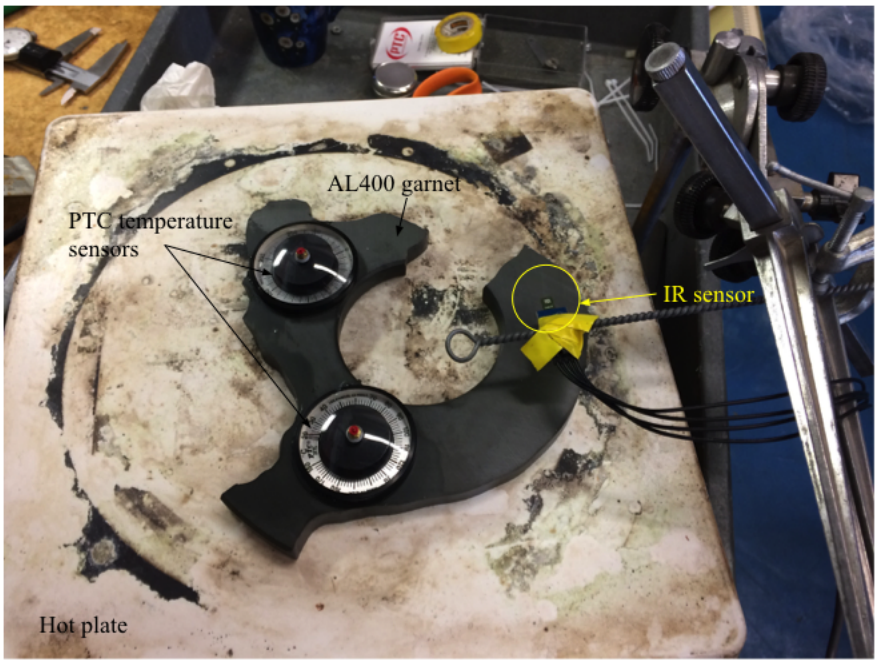

Figure 233: The IR test setup.

From the above setup, when both the PTC temperature sensors read 100°C, the IR sensor read 90°C. This means that we will have to correct for this discrepancy in our safety system.

23 High level RF (R. Padilla, R. Madrak, R. Scala, B. Schupbach)

The block diagram of the HLRF (high level RF) system is shown in Figure 234.

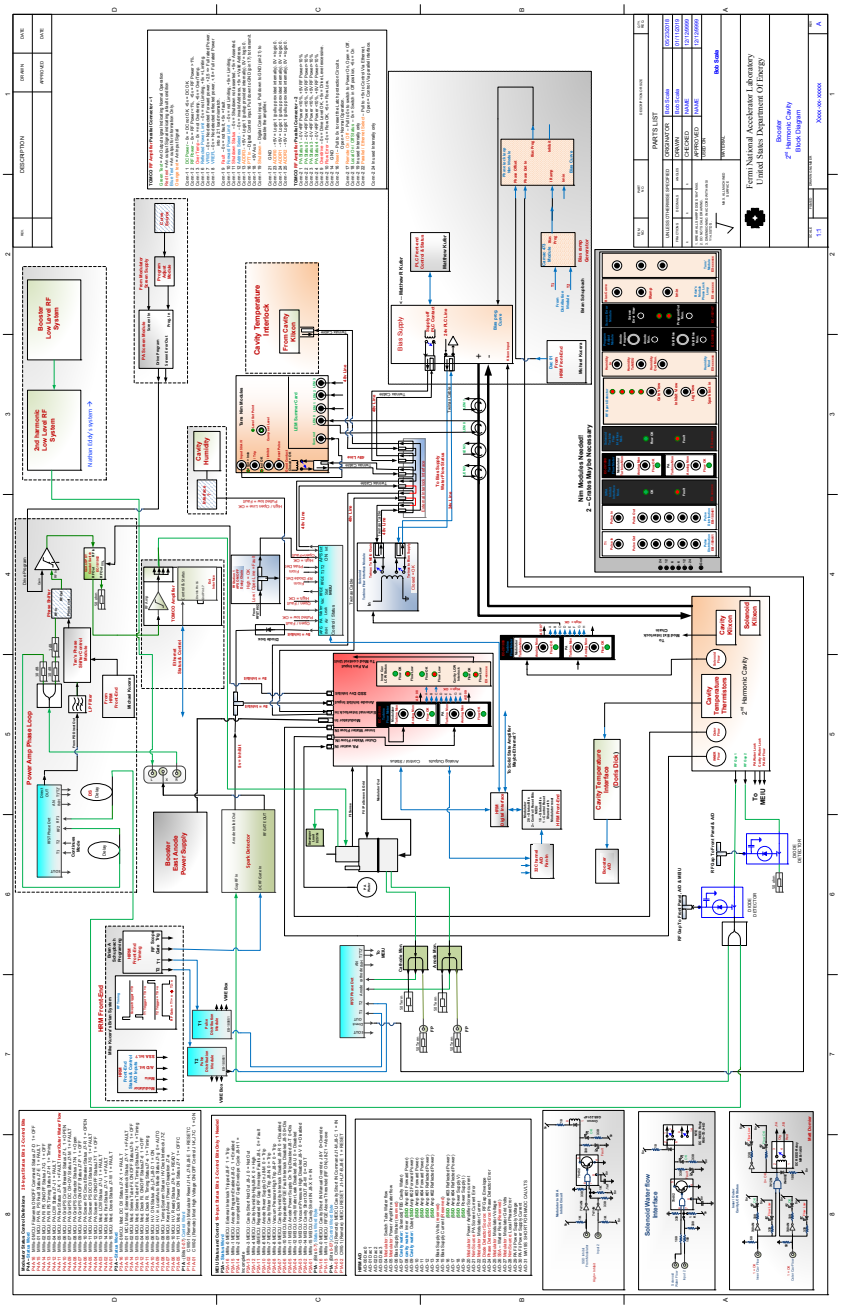

Figure 234: Block diagram of the high level RF. (Preliminary 15 Jan 2019)

24 Cavity installation

The cavity will be installed at L11. Figure 235 shows the before and after photos of the location. The main change at L11 is the relocation of the vacuum roughing line. Bellows have been added as well. A spool piece is temporarily fills up the spot where the cavity will be eventually installed.

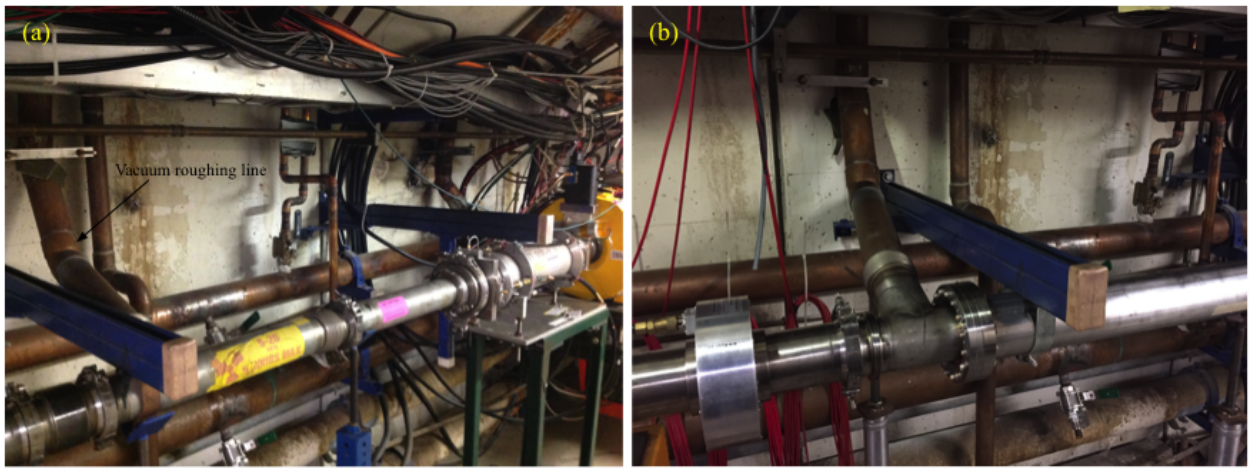

Figure 235: The before (a) and after (b) photos of the installation location at L11. The vacuum roughing line has been moved upstream w.r.t. beam. The blue unitstruts will be removed during the cavity installation. In the meantime, a spool piece takes the place of the cavity.

Figure 236: The water manifold.

24.1 Cooling water

The water manifold that will be distributing cooling 90 degF water to the cavity is shown in Figure 236. The required water connections and minimum flow rates are shown in Figure 237.

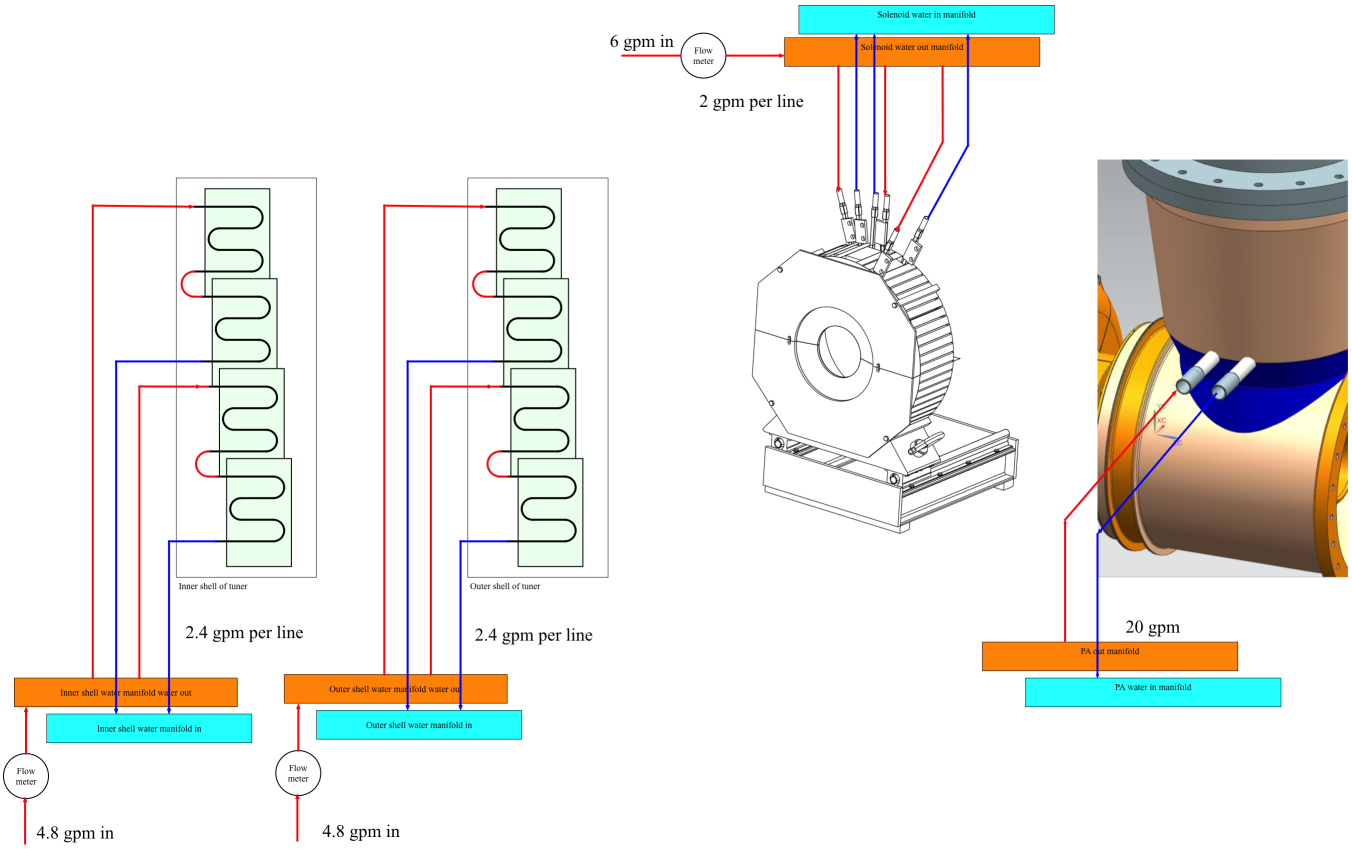

Figure 237: The required water connections and minimum flow rates for cooling the tuner, solenoid and the PA.

24.2 Water leak detection (R. Madrak & C.Y. Tan)

Due to the confined space where the cooling water enters and exits the PA of the cavity, it is not possible to use a standard "dissolved aspirin" based leak detector that is used for all the Booster RF cavities. Therefore, another method will be used for leak detection.

The leak detection method that has been chosen is based on differential humidity. If there is a leak in the PA cooling system, and if the PA is operating, any water that leaks into the cavity PA shell is instantaneously vaporized. This means that the humidity level near the cavity will increase w.r.t. the humidity elsewhere in the tunnel. A differential measurement between these two humidity levels will alert the control system that there is a potential leak.

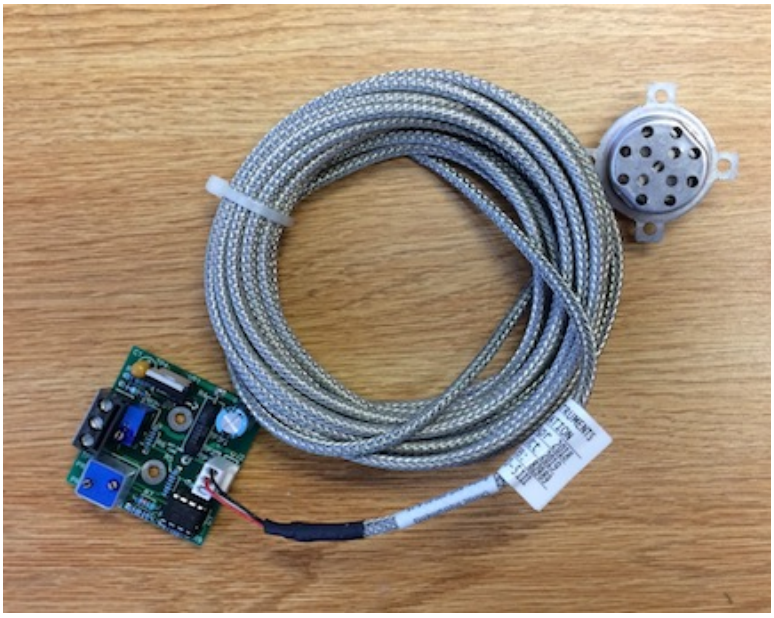

Figure 238: The AHT-200-01 humidity sensor is connected to its amplifier via 15 ft of shielded cable.

The humidity sensor that has been chosen for leak detection is the AHT-200-01 absolute humidity sensor made by Ohmic Instruments [64]. The sensor is based on a differential measurement of the thermal resistance between a thermistor that is encapsulated in dry nitrogen and another thermistor exposed to air. This sensor was chosen over other types of sensors because it does not contain plastic because plastic can deteriorate in a high radiation environment. However, the detection signal right out of the AHT sensor is very low and so it has to be amplified in the tunnel before it can be sent upstairs to the control system. In order to keep the amplifier as far away from the beam pipe as possible, the 15 ft cable version of the sensor/amplifier combo is used. This sensor has been installed in the tunnel at the

location where the cavity will be installed and has survived high energy physics operations for a month (08 June to 8 July 2018). Figure 238 shows a photo of the sensor, amplifier and the 15 ft of shielded cable that connects them together.

Fig ?? shows the sensor mounted on the cavity. The reference sensor for measuring the regular tunnel humidity is located at ??.

25 Operating the cavity

26 Acknowledgements

We would like to thank the following people:

1. G. Das and P. Oberbeck (National Magnetics Group/TCI Ceramics) for accommodating many of our requests during the manufacture of the garnet rings. And the following NMG personnel for their enthusiastic contributions to the manufacture of the garnet rings:
    a. A. Samanta (Material Development, Production & Testing).
    b. B. Troxell (Machining and Assembling).
2. J. Reid (TOMCO) for quickly fixing the problems with the solid-state amplifier.
3. T. Berenc (ANL) for helpful discussions about the cathode resonator model.
4. F. Caspers (CERN) and C. Vollinger (CERN) for giving us information about their perpendicular cavity design.
5. S. Clement (CERN) for sending us their procedure for gluing their garnet sectors together and to the alumina.
6. S. Kurennoy (LANL) for sending us drawings of the LAMPF cavity.
7. V. Yakovlev (FNAL) for presenting his experiences with the SSC low energy booster perpendicular biased cavities at a special seminar for us.
8. P. Seifried (FNAL) and W. Mueller (FNAL) for multiple installations and de-installations of the solid-state amplifier during testing.
9. FNAL Technical Division technicians: W. Ostrom, T. McKenna, J. McQueary, P. Sanchez, J. Szal, S. Sanchez, N. Unold, C. Pribyl and D. Howard for assembling the solenoid.
10. D. Plant (FNAL) and J. Holm (FNAL) RF work.
11. R. Montiel (FNAL), M. Rauchmiller (FNAL) and K. Klotz (FNAL) for assembling the cavity.
12. D. Watkins (FNAL) for excellent welding work.
13. M. Henry (FNAL) for assembling the bias magnet power supply and its associated controls.
14. K. Koch (FNAL) for building the PLL module.
15. C. Olsen (FNAL) for building many iterations of the holders for the garnet witness pieces test stand.
16. T. Johnson (FNAL) for loaning us his coil winding machine.
17. G. Bulat (FNAL) for getting our mechanical requisitions through the system in record time.
18. T.J. Gardner (FNAL) as liaison between us and Technical Division.
19. J. van Bogaert (FNAL), B. Fellenz (FNAL) and C. Lundberg (FNAL) for relocating electronics at L11.
20. J. Ranson (FNAL) and the electricians.
21. B. Oshinowo (FNAL), C.J. Wilson (FNAL) and the survey group.
22. D. Hixson (FNAL) and D. Wallace (FNAL) for water work.
23. J. Kubinski (FNAL), J. Briney (FNAL) and B. Ogert (FNAL) for vacuum work.
24. K. Triplett (FNAL) and S. Chaurize (FNAL) for coordinating the cavity installation at L11.

And to all persons who have worked on this project and were inadvertently not listed here, we give our sincerest thanks!

26.1 People

Photo 1: The principal designers of the cavity: I. Terechkine (left) and G. Romanov (right).

Photo 2: From left to right: D. Plant, R. Madrak and R. Padilla.

Photo 3: National Magnetics Group: From left to right: A. Samanta, G. Das, P. Oberbeck, and B. Troxell.

Photo 4: K. Duel.

Photo 5: R. Montiel and M. Rauchmiller.

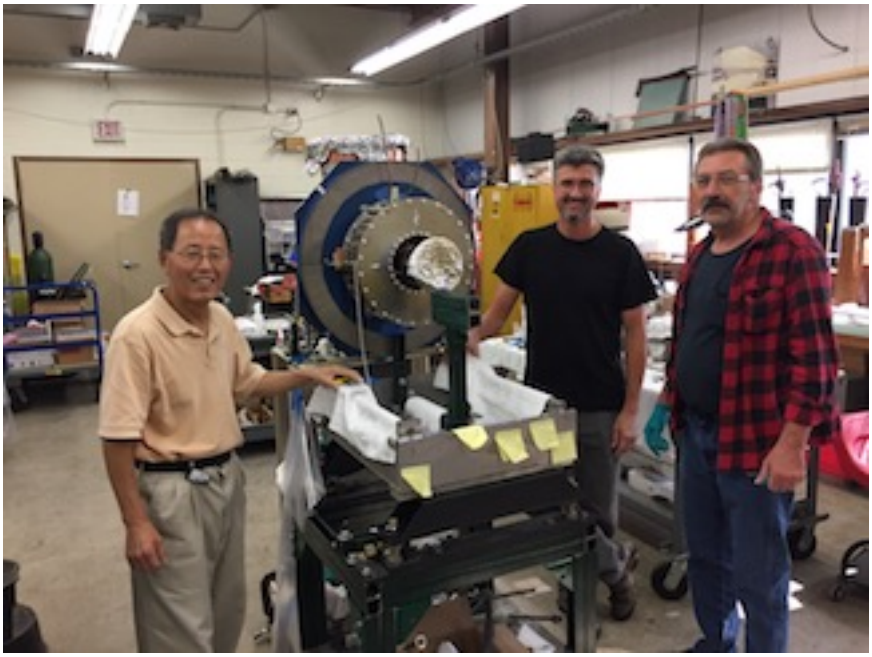

Photo 6: D. Sun, R. Montiel and K. Klotz.

Photo 7: A. Makarov.

Photo 8: Technical Division technicians. Front row from left to right: W. Ostrom, and T. McKenna. Middle row: J. McQueary, P. Sanchez, J. Szal, S. Sanchez, and N. Unold. Back row: C. Pribyl and D. Howard.

Photo 9: B. Oshinowo and C.J. Wilson.

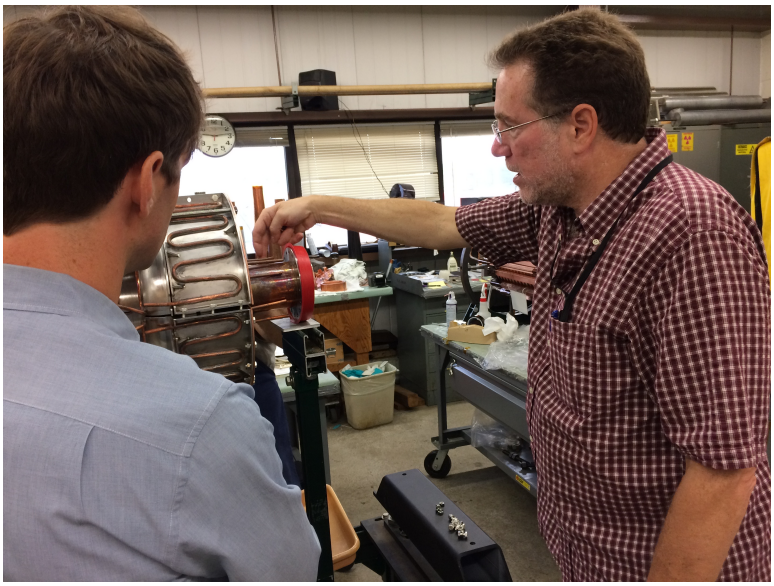

Photo 10: Left to right: K. Duel and D. Hixson.

Photo 11: B. Fellenz and J. van Bogaert.

Photo 12: J. Reid, D. Plant (hidden) and R. Madrak.

• • •

A Definition of shunt impedance

During the design of our cavity, there has been great angst about the definition of shunt impedance. It turns out that the source of the "confusion" is because there are two different definitions for shunt impedance. Accelerator physicists use one definition while RF engineers use another. The accelerator physicist's definition of shunt impedance, R_s', comes from how a charged particle gains energy after it travels through a cavity and the power loss, P_{rms}, of the cavity, (see for example, Edwards & Syphers [65], page 27, Eq. 2.22, and T.P. Wangler [66], page 42, Eq. 2.54) i.e.

$$R_s' = \frac{(eV_0/q)^2}{P_{\text{rms}}} \tag{84}$$

where eV_0 is the maximum energy gained by a particle of charge q after it goes through the cavity in units of eV. When we set $V_p = eV_0/q$ where we have defined V_p to be the equivalent peak voltage of a sine wave[8], we have

$$R_s' = \frac{V_p^2}{P_{\text{rms}}} \tag{85}$$

From the above, we can see that when we write down the physicist's definition of shunt impedance in this way, it becomes obvious why there is a factor of "2" between it and the engineer's definition. This is because the engineer's definition comes from the RLC circuit for a resonator and it is well known that the shunt impedance, R_s, is

$$R_s = \frac{V_p^2}{2P_{\text{rms}}} \tag{86}$$

Thus, since both power losses in terms of rms must be the same, we must have

$$R_s = \frac{R_s'}{2} \tag{87}$$

[8] Technically, the transit time factor T should be included in the definition of V_p. We have set $T = 1$ here. A more mathematical argument that shows the factor of "2" between the physicist's definition and engineer's definition of shunt impedance can be found in a technical note ref ??.

Therefore, since MWS uses the physicist's definition of shunt impedance, we have to divide its result by 2 to convert it to the engineer's definition. We also have to be careful to do the same for R/Q because the shunt impedance is embedded in there as well.

For other cavity parameters, we have to be careful when translating between MWS and the RF engineer's practical definitions. We have made a cheat sheet, shown in Table 21, for converting between the MWS definitions to the engineer's definitions.

MWS definition	Engineer's definition	Comments
$\boldsymbol{R'_s}$	$R_s = \frac{R'_s}{2}$	Shunt impedance definitions.
$\boldsymbol{P}_{\text{rms}} = \frac{\boldsymbol{V^2_{p,g}}}{\boldsymbol{R'_s}}$	$P_{\text{rms}} = \frac{V^2_{p,g}}{2R_s}$	P_{rms} is the same rms power loss in both cases. $V_{p,g}$ is the peak voltage in the gap.
$\boldsymbol{P}_{\text{rms}} = \frac{\boldsymbol{V^2_{p,\text{an}}}}{\boldsymbol{R'_{\text{an}}}}$	$P_{\text{rms}} = \frac{V^2_{p,\text{an}}}{2R_{\text{an}}}$	$V_{p,\text{an}}$ is the peak anode voltage. Again, the anode impedance definitions between the physicist and engineer is related by $R_{\text{an}} = \frac{R'_{\text{an}}}{2}$.
$\frac{\boldsymbol{V_g}}{\boldsymbol{V}_{\text{an}}} = \boldsymbol{k}$	$\frac{V_{p,g}}{V_{p,\text{an}}} = k$	k is the step up ratio. V_g is the rms gap voltage and V_{an} is the rms anode voltage.
$\boldsymbol{R'_{\text{an}} = R'_s/k^2}$	$R_{\text{an}} = R_s/k^2$	After some manipulation, it can be shown that $R_{\text{an}} = \frac{R'_{\text{an}}}{2}$ as required.

Table 21: Cheat sheet for converting between the physicist's and engineer's definitions of cavity parameters.

B R/Q formula

The R/Q formula for an RLC circuit comes from Ref. [67], which we will derive here.

In a parallel RLC circuit, the admittance of the circuit is given by

$$Y(\omega) = \frac{1}{R} + \frac{1}{i\omega L} + i\omega C \equiv A + iB(\omega) \tag{88}$$

where R is the shunt resistance, L is the inductance and C is the capacitance of the RLC circuit.

When we look at the susceptance part of Y only, and differentiate it w.r.t. ω, we get

$$\frac{dB}{d\omega} = C + \frac{1}{\omega^2 L} \tag{89}$$

Since at resonance, $\omega_0 = 1/\sqrt{LC}$, this means that

$$\frac{dB}{d\omega} = \frac{1}{\omega_0^2 L} + \frac{1}{\omega^2 L} \tag{90}$$

Therefore, at resonance, we have

$$\left.\frac{dB}{d\omega}\right|_{\omega=\omega_0} = \frac{2}{\omega_0^2 L} \quad \Rightarrow \omega_0 L = 2\left(\omega_0 \left.\frac{dB}{d\omega}\right|_{\omega=\omega_0}\right)^{-1} \tag{91}$$

We recall that the quality factor Q of the parallel RLC circuit is given by $Q = R/\omega_0 L$, [20] and thus

$$R/Q = \omega_0 L = 2\left(\omega_0 \left.\frac{dB}{d\omega}\right|_{\omega=\omega_0}\right)^{-1} \tag{92}$$

C Edit history

Date	Submitter	Changes
1 June 2017	G. Romanov	Added edits to section 2.1.
10 Jan 2018	C.Y. Tan	Added PLL section. Section 11.
12 Jan 2018	C.Y. Tan	Added MWS HOM modeling results. Section 7.1.2.
22 Jan 2018	C.Y. Tan	Added Bias Solenoid. Section 9.
30 Jan 2018	C.Y. Tan	Added Tuner. Section 8.
01 Feb 2018	C.Y. Tan	Added MWS model. Section 6.2.
08 Feb 2018	R. Madrak	Updated Y567B measurements. Section 14.
14 Feb 2018	R. Madrak	Added Thermal grease measurements. Section 5.
22 Feb 2018	I. Terechkine	Made suggested changes to sections 1, 2, 3, 4, 6, 8, 9, 14 and 15.
23 Feb 2018	C.Y. Tan	Recalculated flow rate in section 9.2.1.1 for 3 coils rather than for 6 coils.
27 Feb 2018	C.Y. Tan	Added bias curve section. Section 10.1 and 10.1.1.
01 Mar 2018	C.Y. Tan	Added stub sections 24, 25 and 26.1.
05 Mar 2018	C.Y. Tan	Updated bias ramp in section 10.1. Removed incorrect $\sqrt{2}$ scaling of step up ratio in Figure 35.
06 Mar 2018	G. Romanov	Fixed incorrect statements in section 8.7 and Figure 72. Added more cavity specifications in Table 2. Replaced “magnetic field” with “bias magnetic field” appropriately in all sections. Fixed typos, reformatted and updated sections 1, 2, 3, 6.2, 8.3, 8.6.3, 9.3.
08 Mar 2018	G. Romanov	Updated Figure 32, Figure 45, Figure 46.
08 Mar 2018	C.Y. Tan	Added IR sensor, section 22.5. Updated Figure 54.
09 Mar 2018	C.Y. Tan	Added Garnet and alumina, section 17.1; HOM cavity, section 17.8.
13 Mar 2018	C.Y. Tan	Added table of HOM modes, Table 5.
20 Mar 2018	C.Y. Tan	Updated Figure 149. Filled in sections 17.6 and 17.9. Added drawing

		numbers section 17.11.1.
20 Mar 2018	C.Y. Tan	Added Tuner inner and outer shell assembly, section 17.3; Coupling ring, section 17.7; Accelerating cavity assembly, section 17.9. Added stub sections 17.11: Tuner stack assembly.
23 Mar 2018	C.Y. Tan	Added NMG personnel in acknowledgements.
26 Mar 2018	C.Y. Tan	Added more people to acknowledgements.
27 Mar 2018	C.Y. Tan	Updated section 2.
29 Mar 2018	C.Y. Tan	Added A. Makarov as contributor on title page. Added solenoid construction section 19.
06 Apr 2018	C.Y. Tan	Added tuner neck assembly photograph: Figure 153.
09 Apr 2018	C.Y. Tan	Updated section 22.5 because original IR sensor has been replaced with a different IR sensor. Added soldered water pipes in section 17.3.
11 Apr 2018	C.Y. Tan	Fixed typo in last paragraph of section 7.1.2: 9 kΩ $\rightarrow$ 93 kΩ.
12 Apr 2018	C.Y. Tan	Updated section 17.7 to include polishing of the neck.
16 Apr 2018	J. Kuharik	Filled in sections 16, 16.1: Garnet characterization and witness pieces measurement.
24 Apr 2018	C.Y. Tan	Updated section 16.1 and Figure 138 and Figure 139: witness pieces measurement.
25 Apr 2018	C.Y. Tan	Updated section 16.1.5 and added Table 11: witness pieces measurement. Updated section Figure 157 to show all pipes and flange have been welded.
30 Apr 2018	C.Y. Tan	Added Figure 162: Removal of bow in outer shell.
03 May 2018	A. Makarov	Filled in section 19: Solenoid construction.
03 May 2018	C.Y. Tan	Fixed errors in Table 6 and typos in editor's notes: "parallel" $\rightarrow$ "series". Added editor's note in section 9 that the size of the copper conductor and the thickness of the laminations are different than the final as-built solenoid.
04 May 2018	A. Makarov, C.Y. Tan	Corrected errors in section 19: Solenoid construction and filled in section 19.4: Final assembly.
09 May 2018	J. Kuharik	Improved section 16.2 and added section 16.2.2 for garnet ring initial measurements.

10 May 2018	C.Y. Tan	Updated section 17.9: welding parts to the accelerating cavity.
11 May 2018	C.Y. Tan	Added photos of people in section 26.1.
18 May 2018	C.Y. Tan	Fixed numbering of modes in Table 5 so that the text and and table numbering scheme is consistent.
21 May 2018	C.Y. Tan	Added more acknowledgements. Added window welding in section 17.9.
21 May 2018	J. Kuharik	Improved section 16.2.
22 May 2018	C.Y. Tan	Added sections 8.4.1 and 8.7.1 on power losses in the tuner from RF and Eddy currents.
29 May 2018	C.Y. Tan	Changed all relevant occurrences of 59 → 60 turns for final bias solenoid coil. Added turns information in section 19.3.
30 May 2018	C.Y. Tan	Added final solenoid final assembly photos in section 19.4. Updated flat window welding leak check numbers in section 17.9.
31 May 2018	C.Y. Tan	Updated acknowledgements and photos to include TD technicians.
01 Jun 2018	C.Y. Tan	Added R.G. Scala and B.A. Schupbach as contributors on title page. Clarified inductance values discussed in section 9. Added inductance and resistance of solenoid coils table: Table 13; and updated Figure 204 to include coil leads.
04 Jun 2018	C.Y. Tan	Added editor's note in section 3.2 (Loss tangent) to say that α is not a constant at low fields.
07 Jun 2018	C.Y. Tan	Found problems with the interpretation of Z11 in section 7.1.2. Z11 is not the shunt impedance. CST MWS results to follow and this section will be updated with these results. Section 0 that calculates the power that is dissipated in the HOM resistor is on hold until the shunt impedances are available.
08 Jun 2018	C.Y. Tan	Added more assembly photos (Figure 158 and Figure 158) in section 17.3: Tuner inner shell assembly.
25 Jun 2018	C.Y. Tan	Added photo of polished weld joint: Figure 160.
26 Jun 2018	C.Y. Tan	Added section 17.10: Assembling the cavity.
27 Jun 2018	C.Y. Tan	Added more photos and fixed photo numbering errors in section 26.1: People.
28 Jun 2018	C.Y. Tan	Clarified what Z11 is in section 7.1.2. Continued updates in section 17.10: Assembling the cavity.

29 Jun 2018	C.Y. Tan	Continued updates in section 17.10: Assembling the cavity, section 17.2: Tuner neck assembly; Added more photos to section 26.1: People; Updated section 26: Acknowledgements.
05 Jul 2018	C.Y. Tan	Updated section 17.4: Tuner outer shell assembly; section 17.10.1: Installing the power module. Added section 17.5: End plates.
06 Jul 2018	C.Y. Tan	Added section 20: Mating the solenoid to the cavity. Updated Figure 149: 3D model.
11 Jul 2018	C.Y. Tan	Updated acknowledgements. Added more photos to section 26.1: People.
24 Jul 2018	C.Y. Tan	Updated section 17.2 to include modifications to neck assembly; section 17.4 to include modifications to the outershell assembly. Started filling in section 21: Low power testing.
25 Jul 2018	C.Y. Tan	Added tin plated photo of endplate to Figure 169. Started filling in section 17.11: Tuner stack assembly.
26 Jul 2018	C.Y. Tan	Added section 17.2.1 to document modifications to the neck assembly.
27 Jul 2018	C.Y. Tan	Updated section 21.1: Unloaded cavity.
30 Jul 2018	C.Y. Tan	Added sections 21.1.1 and 21.1.1.1: Low Q investigations. Filled in section 21.1: Low power tests of the unloaded cavity.
31 Jul 2018	C.Y. Tan	Added HLRF block diagram to section 23. Added section 24.2: Leak detection. Added IR detector hole size information to section 17.2: neck assembly.
10 Aug 2018	C.Y. Tan	Added and filled in sections 17.11.1: installing the garnet rings; 17.11.1: installing the outer shell and end plates; 17.11.5: lessons learnt.
16 Aug 2018	C.Y. Tan	Filled in section 17.11.2: installing the outer shells.
17 Aug 2018	C.Y. Tan	Filled in section 17.11.3: preparation for installing end plates.
20 Aug 2018	C.Y. Tan	Added section 17.4.1: problems introduced by EDM'ing the outer shell.
23, 24 Aug 2018	C.Y. Tan	Filled in section 17.11.4: installing end plates. Added photo to section 26.1: people.
24 Aug 2018	C.Y. Tan	Filling in section 20: mating the cavity to the solenoid.
27 Aug 2018	C.Y. Tan	Added Editor's note that we do not know how much grease is dripping in front of the tuner stack in section 17.11.3. Updated Figure 189 to show 4-40 screw closing the gap.

28 Aug 2018	C.Y. Tan	Updated Figure 192 to include alumina flake.
31 Aug 2018	C.Y. Tan	Corrected Table 5. Added Figure 47 to clarify the models used in Table 5. Added reference [15] from Budker Institute. Updated acknowledgements list to include vacuum group.
04 Sep 2018	C.Y. Tan	Started filling in section 24: cavity installation.
06 Sep 2018	C.Y. Tan	Started filling in section 21.2: loaded cavity measurements.
10 Sep 2018	C.Y. Tan	Updated button pickup photo in Figure 33.
11 Sep 2018	C.Y. Tan	More filling in of section 21.2: loaded cavity.
12 Sep 2018	C.Y. Tan	Added water manifold photo: Figure 236. Start filing in section 7.1.3.1: power dissipated in RF harmonics into HOM loads. Updated mode numbering scheme in section 21: low power tests to match with the mode numbering scheme in section 7.1.2: HOM damper simulations.
14 Sep 2018	C.Y. Tan	Fixed error in gain of RF probe in section 21.2.4: button calibration. Filled in Table 5.
20 Sep 2018	C.Y. Tan	Updated section 21.2.4: button calibration to correct RF probe calibration. Filled in section 7.1.3: HOM power requirements.
21 Sep 2018	C.Y. Tan	Added Figure 49 photo of 6 dB attenuators. Added section 20.1: connecting water tubes.
24 Sep 2018	C.Y. Tan	Fixed wrong Q values in Table 17 for open loads. Added section 21.2.2.1 for how the resistor values in the stretched wire was chosen.
01 Oct 2018	C.Y. Tan	Updated Table 17 comments about mode 3 Q being lower when buttons are used in the Q measurement.
07 Dec 2018	D. Sun	Added section 12: RF windows.
15 Jan 2019	R. Scala	Updated Figure 234: HLRF block diagram.
15 Aug 2019	C.Y. Tan	Added Table 18 so that the properties of the modes at 200 A bias can be read directly. Added Photo 12.
16 Aug 2019	C.Y. Tan	Added section 22.3: RF leakage; section 22.4: Heating of beampipe from Eddy currents.
04 Dec 2019	R. Madrak	Filled in section 22: High power tests.
14 Apr 2020	C.Y. Tan	Updated section 17.4.1: Problems introduced by EDM corrections to include latest photo of cracks. Added new section 18 to describe the repair process.

15 Apr 2020	R. Madrak	Updated Table 12 and added Figure 195 and Figure 196. More notes to section 18.1.
09 Jul 2020	J. Kuharik	Improved the path chosen for the integral in section 16.1.1.
15 Sep 2020	R. Madrak	Corrected Eq. (81). Constant 559.3 replaced by 586.3.

Bibliography

[1] W. Weng and J. Kats, "Effects of the second harmonic cavity on RF capture and transition crossing," in *XVth International Conf. on High Energy Accelerators*, Hamburg, Germany, 1992.

[2] C. Bhat and C. Tan, "Fermilab Booster Transition Crossing Simulations And Beam Studies," in *57th ICFA Advanced Beam Dynamics Workshop on High-Intensity and High-Brightness Hadron Beams*, Malmö, Sweden, 2016.

[3] C. Bhat, "R&D on beam injection and bunching schemes in the Fermilab Booster," in *Proceedings of HB2016*, Malmö, Sweden, 2016.

[4] T. Enegren and R. Poirier, "Parallel bias vs perpendicular bias of a ferrite tuned cavity for the TRIUMF KAON factory Booster ring," in *EPAC 1998*, Rome, Italy, 1988.

[5] P. Coleman, F. Brandeberry, C. Friedrichs, Y. Goren, T. Grimm, G. Hulsey, S. Kwiatkowski, A. Propp, L. Taylor and L. Walling, "Status of the SSC LEB RF Cavity," in *PAC 1993*, Washington DC, USA, 1993.

[6] R. Poirier, T. Enegren and I. Enchevich, "AC bias operation of the perpendicular biased ferrite tuned cavity for the TRIUMF KAON factory Booster Synchrotron," San Francisco, CA, USA, 1991.

[7] R. Madrak, "A new slip stacking RF system for a twofold power upgrade of Fermilab's Accelerator Complex," *Nucl. Instrum. Meth.,* vol. A758, pp. 15-25, 11 September 2014.

[8] J. MacLachlan and J.-F. Ostiguy, "ESME," 12 September 2016. [Online]. Available: http://esme.fnal.gov/.

[9] C. Bhat, J. Griffin, J. MachLachlan, M. Martens, K. Meisner and K. Ng, "Transition crossing in proton synchrotrons using a flattened RF wave," *Phys. Rev. E,* vol. 55, no. 1, pp. 1028-1034, January 1997.

[10] X. Yang, A. Drozhdin and W. Pellico, "Transition crossing simulation at the Fermilab Booster," in *Particle Accelerator Conference*, Albuquerque, New Mexico, 2007.

[11] C. Bhat and C. Tan, "Fermilab Booster transition crossing simulations and beam studies," in *Proceedings of HB2016*, Malmö, Sweden, 2016.

[12] W. Merz, C. Ankenbrandt and K. Koepke, "Transition jump system for the Fermilab Booster," Batavia, IL, 1987.

[13] X. Yang, V. Lebedev and C. Ankenbrandt, "Reducing the Longitudinal Emittance of the 8-GeV Beam via the RF Manipulation in a Booster Cycle," Batavia, IL, 2005.

[14] C. Bhat, "2nd harmonic RF for the bunch rotation in the Fermilab Booster," 24 July 2017. [Online]. Available: http://beamdocs.fnal.gov/AD-public/DocDB/ShowDocument?docid=5717.

[15] J. Averboukh, M. Karliner, D. Soukhanov, N. Zinevtch, G. Hulsey, D. Coleman, T. Grimm and F. Brandeberry, "LEB Engineering Prototype Tuner and Cavity Center Conductor," URA/SSCL - Budker Institute for Nuclear Physics Interlaboratory Collaboration Agreement, SSC-92-W-11138, 1993.

[16] National Magnetics Group, "Garnets - Aluminum Doped," [Online]. Available: http://www.magneticsgroup.com/pdf/p8-13%20Magnetic.pdf.

[17] W. Smythe, T. Enegren and R. Poirier, "A versatile RF cavity mode damper," in *EPAC 90*, Nice, France, 1990.

[18] R. Madrak, G. Romanov and I. Terechkine, "TD-15-005," 2015. [Online]. Available: https://web.fnal.gov/organization/TDNotes/Shared%20Documents/2015%20Tech%20Notes/TD-15-005.pdf?Web=1.

[19] R. Madrak, G. Romanov and I. Terechkine, "TD-15-004," 2015. [Online]. Available: https://web.fnal.gov/organization/TDNotes/_layouts/15/WopiFrame.aspx?sourcedoc=/organization/TDNotes/Shared%20Documents/2015%20Tech%20Notes/TD-15-004.pdf&action=default.

[20] D. Pozar, Microwave Engineeering, 4th Edition ed., John Wiley & Sons, 2011, p. 276.

[21] V. Shapiro, "Magnetic losses and instabilities in ferrite garnet tuned RF cavities for synchrotrons," *Particle Accelerators,* vol. 44, no. 1, pp. 43-63, 1994.

[22] Henkel Adhesives, March 2015. [Online]. Available: http://www.henkel-adhesives.com/product-search-1554.htm?nodeid=8802585018369.

[23] MG Chemicals, "8616 - Super Thermal Grease II," MG Chemicals, 2018. [Online]. Available: https://www.mgchemicals.com/products/greases-and-lubricants/thermal-greases/super-thermal-grease-ii-8616.

[24] Wolfram Research, 2015. [Online]. Available: www.wolfram.com.

[25] Keysight Technologies, Oct 2015. [Online]. Available: http://www.keysight.com/en/pc-1297113/advanced-design-system-ads?cc=US&lc=eng.

[26] G. Romanov, "2nd harmonic RF perpendicular biased cavity update (02 Mar 2017)," 02 March 2017. [Online]. Available: http://beamdocs.fnal.gov/AD-public/DocDB/ShowDocument?docid=5342.

[27] G. Romanov and D. Sun, " 2nd harmonic RF perpendicular biased cavity update (16 June 2016)," 16 June 2016. [Online]. Available: http://beamdocs.fnal.gov/AD-public/DocDB/ShowDocument?docid=5175.

[28] G. Romanov, " 2nd harmonic RF perpendicular biased cavity update (30 June 2016)," 30 June 2016. [Online]. Available: http://beamdocs.fnal.gov/AD-public/DocDB/ShowDocument?docid=5183.

[29] W. Peter, R. Faehl, A. Kadish and L. Thode, "Criteria for vacuum breakdown in RF cavities," in *1983 Particle Accelerator Conference*, Santa Fe, NM, USA, 1983.

[30] G. Romanov, "2nd harmonic RF perpendicular biased cavity update (22 Jun 2017)," 22 June 2017. [Online]. Available: http://beamdocs.fnal.gov/AD-public/DocDB/ShowDocument?docid=5567.

[31] MDC Vacuum Products, LLC, "Del-Seal Mount -- Single ended (Part number 9242000)," 2014. [Online]. Available: https://www.mdcvacuum.com/DisplayPart.aspx?d=MDC&wr=US&p=9242000.

[32] U. Weinands and others, "The LEB Book," 1994.

[33] V. Paramonov, "The proposal of complex impedance termination for versatile HOM damper cavity," in *PAC 1995*, Dallas, TX, USA, 1995.

[34] Los Alamos Accelerator Code Group, 2013. [Online]. Available: http://laacg.lanl.gov/laacg/services/download_sf.phtml.

[35] C. Tan, "HOM_power_prequirements.pdf," 2018. [Online]. Available: http://beamdocs.fnal.gov/AD-public/DocDB/ShowDocument?docid=6113.

[36] R. Carter, "Review of RF power sources for particle accelerators," in *Proceedings RF engineering for particle accelerators*, Oxford, UK, 1991.

[37] R. Carter, "RF power generation," 2011. [Online]. Available: https://arxiv.org/ftp/arxiv/papers/1112/1112.3209.pdf.

[38] I. Terechkine and G. Romanov, "Reduction of the RF Loss in the Garnet Material of a Tunable Cavity by Optimizing the Magnetic Field Distribution Using Shimming," 08 March 2016. [Online]. Available: https://web.fnal.gov/organization/TDNotes/Shared%20Documents/2016%20Tech%20Notes/TD-16-007.pdf.

[39] I. Terechkine and G. Romanov, "Evaluation of Temperature Distribution in the Tuner of the FNAL Booster's Tunable Second Harmonic Cavity," 19 February 2016. [Online]. Available: https://web.fnal.gov/organization/TDNotes/Shared%20Documents/2016%20Tech%20Notes/TD-16-002.pdf.

[40] I. Terechkine, "Eddy Currents in the Tuner of the 2-nd Harmonic Booster Cavity," 10 April 2017. [Online]. Available: https://web.fnal.gov/organization/TDNotes/Shared%20Documents/2017%20Tech%20Notes/TD-17-003.pdf.

[41] I. Terechkine, *email dated 19 Jan 2018,* Batavia, IL, 2018.

[42] I. Terechkine, "Magnetic Bias System for the Second Harmonic Cavity of the FNAL Booster," 12 July 2016. [Online]. Available: https://web.fnal.gov/organization/TDNotes/Shared%20Documents/2016%20Tech%20Notes/T

D-16-012.pdf.

[43] Performance Controls Inc., "GA301, 1-Axis Gradient Amplifier," 2014. [Online]. Available: http://pcipa.com/products/mri/ga301-mri-gradient-amplifier.

[44] R. Best, Phase locked loops, design, simulation and applications, New York, NY: McGraw-Hill, 1999.

[45] G. Romanov, "2nd harmonic RF perpendicular biased cavity update," 18 August 2016. [Online]. Available: http://beamdocs.fnal.gov/AD-public/DocDB/ShowDocument?docid=5218.

[46] T. Berenc and J. Reid, 2001. [Online]. Available: http://rf.fnal.gov/global/technotes/TN/TN023.pdf.

[47] Tomco Technologies, "TOMCO 8kW CW RF amplifier model BT8K ALPHA," Tomco Technologies, Stepney, Australia, 2016.

[48] R. Madrak, J. Reid, M. Slabaugh and C. Tan, 22 March 2017. [Online]. Available: http://beamdocs.fnal.gov/AD-public/DocDB/ShowDocument?docid=5350.

[49] Richardson Electronics, July 2001. [Online]. Available: http://www.relltubes.com/products/Electron-Tubes-Vacuum-Devices/Tetrode/4CW150000E.html.

[50] J. Dey and D. Wildman, "Higher Order Modes of the Main Ring Cavity at Fermilab," in *Particle Accelerator Conference*, Piscataway, NJ, USA, 1995.

[51] G. Jackson, "Review of Impedance Measurements at Fermilab," Batavia, 1990.

[52] V. Yakovlev, "Experience with the ferrite tuner for LEB (1992-1993)," Fermilab, 15 April 2016. [Online]. Available: http://beamdocs.fnal.gov/AD-public/DocDB/ShowDocument?docid=5137.

[53] Spira Manufacturing Corporation, "EMI gaskets and shielding," Spira Manufacturing Corporation, 2017. [Online]. Available: http://www.spira-emi.com/.

[54] G. Romanov, "2nd harmonic RF perpendicular biased cavity update (09 Nov 2017)," 9

November 2017. [Online]. Available: http://beamdocs.fnal.gov/AD-public/DocDB/ShowDocument?docid=5924.

[55] Coorstek Inc, "Alumina 98% - 99.8%," Coorstek Inc, 2016. [Online]. Available: https://www.coorstek.com/english/solutions/materials/technical-ceramics/alumina/alumina-98-998/.

[56] Fermilab Technical Division, "Vector - Select Travelers - Read Only," 2018. [Online]. Available: https://vector-onsite.fnal.gov/SelectTravelerReadOnly.asp?sSeriesID=608&sSerialNoID=all&sReworkID=all&sSpecificationID=all&sRevisionID=all&sJobNo=all&sStatusID=all.

[57] Fermilab Technical Division, "Magnet Photos," 2018. [Online]. Available: http://www-tdserver1.fnal.gov/Project/ProEng/MagnetPhotos/pics.asp?qsPath=BSS/END%20PLATE%20STACKING.

[58] 2nd harmonic cavity group, "2nd harmonic RF perpendicular biased cavity update (19 Jul 2018)," 19 July 2018. [Online]. Available: http://beamdocs.fnal.gov/AD-public/DocDB/ShowDocument?docid=6534.

[59] F. Caspers, "Beam Impedance Measurements Using The Coaxial Wire Method," CERN PS/88-59 (AR/OP), Geneva, Switzerlland, 1988.

[60] P. Colestock, P. Chou, B. Fellenz, M. Foley, F. Harfoush, K. Harkay, G. Jackson, Q. Kerns, D. McConnell and K. Ng, "A critical survey of stretched-wire impedance measurements at Fermilab," in *Particle Accelerator Conference 1991*, San Francisco, CA, USA, 1991.

[61] Melexis, "Evaluation board for the MLX90632 (EVB90632)," Melexis, 2018. [Online]. Available: https://www.melexis.com/en/product/EVB90632/EVB90632.

[62] PTC Instruments, "Model 311C Celsius 20° to 180°C Fully Enclosed Sealed Surface Thermometer," PTC Instruments, 2018. [Online]. Available: http://ptc1-com.3dcartstores.com/Thermometer-311C.

[63] PTC Instruments, "Model 309F Fahrenheit -50° to 250°F Fully Enclosed Surface Thermometer," PTC Instruments, 2018. [Online]. Available: http://ptc1-

com.3dcartstores.com/Thermometer-309F.

[64] Ohmic Instruments, "Humidity Sensors," Ohmic Sensors, [Online]. Available: https://www.ohmicinstruments.com/humidity-sensors/.

[65] D. Edwards and M. Syphers, An introduction to the physics of high energy accelerators, New York, NY: John Wiley & Sons, 1993.

[66] T. Wangler, RF linear accelerators, 2nd edition ed., Verlag: Wiley-VCH, 2008.

[67] T. Enegren and R. Poirier, "Analysis of Booster amplifier design," in *Proceedings of the advanced hadron facility accelerator design workshop*, Los Alamos, NM, USA, 1988.

[68] F. Niell, *Private communication,* 2015.